The importance of scale structure in scattering from random, rough surfaces

by

Vincent Lupien

B.A.Sc., University of Toronto, 1992

Submitted to the Department of Ocean Engineering
in partial fulfillment of the requirements for the Degree of

Doctor of Philosophy in Acoustics

at the

MASSACHUSETTS INSTITUTE OF TECHNOLOGY

June 1998

Author .....
Department of Ocean Engineering
March 18, 1998

Certified by .....
Professor Arthur B. Baggeroer
Ford Professor of Ocean and Electrical Engineering
Thesis Supervisor

Accepted by .....
Professor J. Kim Vandiver
Chairman, Departmental Graduate Committee

The importance of scale structure in scattering from random, rough surfaces

by

Vincent Lupien

Submitted to the Department of Ocean Engineering
on March 18, 1998 in partial fulfillment of the
requirements for the Degree of
Doctor of Philosophy in Acoustics

Abstract

This thesis was motivated by analysis of scattering data at 228 Hz ($\lambda \simeq 6$ m) collected on the western flank of the Mid-Atlantic Ridge as part of the Acoustical Reverberation Special Research Program (ARSRP) using a range and azimuth-resolving sonar. The succession of echoes from pulses transmitted near the ocean surface results from interactions of sound with kilometer-tall bathymetric features at depths of up to five kilometers and ranges as high as hundreds of kilometers.

The backscatter statistics of match-filtered, beamformed envelopes collected from a selected bathymetric have a *target-like* character in the form of an enhanced tail in the probability density function compared with the Rayleigh density. Concurrently, visual observations of the wavelength-scale morphology of this region suggest that the stochastic roughness is *feature-like*, being composed of contributions at discrete scales associated with specific geological processes, in contrast to fractal Gaussian processes which are non-feature-like, receiving roughness contributions at all scales continuously. *Scale structure*, the stochastic spatial arrangement of roughness contributions at various scales, is proposed to be a parameter of importance in explaining the statistics of backscatter in the ARSRP data and in the general, theoretical problem of scattering from random rough surfaces.

These propositions are studied using an exact integral equation method for one-dimensional rigid surfaces. Surface models are developed with a common power spectral density but different scale structure. In particular, a new facet surface model is proposed which exhibits feature-like roughness and matches the power spectral densities commonly observed in natural interfaces such as the seafloor. The bistatic scattering strength and the time-domain statistics of backscatter are computed, revealing that given a common power spectral density, surfaces with feature-like roughness lead to enhanced target-like behavior and enhanced incoherent forward scatter compared to their non-feature-like counterparts.

Extending the surface models to a three-dimensional scenario, the closest match of numerically computed time-domain backscatter to ARSRP data is obtained when the scale structure of the seafloor is correctly represented, supporting the assertion

that scale structure is playing an important role in scattering from the Mid-Atlantic Ridge.

Scale structure is concluded to be an important new concept in characterizing those aspects of the stochastic roughness of surfaces which are relevant to scattering.

Thesis Supervisor: Arthur B. Baggeroer
Title: Professor, Department of Ocean Engineering

Acknowledgments

I invite everyone who has contributed to making this Ph.D. thesis happen to share with me deservingly in feeling a deep satisfaction at its successful completion. The required elements - a supportive and intellectually stimulating environment - were made possible by a community of people.

I have had the unique privilege of receiving the guidance of all of the faculty in the Acoustics Group of the Department of Ocean Engineering at one time or another during my time at MIT. Prof. Henrik Schmidt, who was my advisor formally for the first semester of my career at MIT, continued to be an indispensible source of technical advice until the very end of my studies as a committee member for this thesis. With a ligthspeed mind and unequaled intensity, Henrik helped me out of many difficulties in computational acoustics.

At the beginning of my second term at MIT, Prof. Robert Fricke encouraged me to come work with him; Rob's constant enthusiasm and optimism proved to be a fertile environment for new ideas and creative thinking. Rob's involvement began well before I arrived at MIT; he played a role during the admissions process in stimulating my interest in MIT and, along with Henrik, in my appointment as a Research Assistant.

Prof. Ira Dyer, who provided indispensible help both on administrative and scientific levels during my Doctoral Exams, has been a mentor and role model. His ideas on the role of facets in surface scattering were a major inspiration. I owe him thanks for the obvious attention he paid to any work I submitted and for his clear feedback, whether he delivered a verdict of "mediocre" or "excellent".

Prof. Arthur Baggeroer became my advisor after the departure of Prof. Robert Fricke in my third year at MIT. Our relationship has proved fruitful and long-lasting, and led to the inclusion of an entirely new set of concepts in the thesis - stochastic processes and signal processing - without which the thesis would not have had the same caliber. At the same time, I enjoyed a high degree of intellectual freedom which was necessary for the ideas in this thesis to bloom fully. Along with the guidance he has provided both technically and professionally, I am deeply grateful to Art for

finding alternative funding to permit the completion of this project when the original source of funding expired.

The arrival of Prof. Nicholas Makris and Dr. William Carey to the Acoustics Group towards the end of my studies at MIT provided fresh perspectives and new opinions on the subject matter and helped me strengthen and refine my arguments.

I am thankful for the contagious positive energy provided by Dr. Tim Stanton of the Woods Hole Oceanographic Institution, and for his guidance as a committee member and as an expert on scattering theory. Thanks also to Prof. Paul Sclavounos for his role as a committee member.

I feel a deep gratitude to Sabina Rataj who, through her boundless reserve of goodwill, has helped me resolve all types of difficulties over the years. Whenever I approached Sabina with a problem, the solution was immediate; whenever a special favor was asked, the answer was "yes". I had the feeling that someone was on the lookout for my well-being; the net increase in the quality of my life while at MIT is immeasurable. Thank you, Sabina. Thanks also to Robert Fadel, Patrick Preston, Taci Darnell, and Isela Cordova.

To my fellow students in the Acoustics Group throughout the years - whether it was through the relentless computer help you provided (Peter Daly), the review of a manuscript for a paper (Joseph Bondaryk and Pierre Elisseeff), heated debates on scattering theory (Dan Li and Eugene Dorfman), working out at the gym (Michael Klausbruckner and Matt Conti), friendship during very late nights at work (Peder Sverdrup), or camaraderie (Kyle Becker, Yuriy Dutko, Tarun Kapoor, Jaiyong Lee, Yi-San Li, Patty Manning, Dong Guk Paeng, Jeong-Ho Park, Brian Sperry, Brian Tracey, Kevin Xu), you contributed positively to my experience at MIT. Your intelligence, determination and drive are the reasons I came to this university.

I benefited greatly from accepting the generous offers of help by Caterina Stamoulis during the intense final two weeks of thesis writing and in preparing my thesis defense presentation. Beyond her sound technical advice, she has achieved a status of inestimable worth to me by becoming a good friend.

Thanks are owed to Prof. Ross Chapman at the University of Victoria who pro-

vided facilities for me to continue working on this thesis during the Chrismas holidays while visiting family. I am thankful to my friend Adrian Butscher from the Mathematics Department at Stanford University for help with the set notation of Chapters 2 and 3, and to my brother Bernard for helping with many figures in this thesis.

To Nancy, the word "thanks" would fall far short of expressing my feelings. You fill my life with joy! My love for you never ceases to grow. Together, we have enjoyed so much of what life has to offer over the past five years - our marriage, trips all over the world, constant learning, a love for cooking and physical fitness, and superb health and vitality. At the same time, we have seen our careers blossom. How could all this success be surpassed other than through the knowledge that such a heightened form of human existence is going to continue?

A mon père, qui m'a donné le réflexe de réussir. A ma mère, pour mille et une petites faveurs qui disent "je t'aime".

Contents

List of Figures

List of Tables

Chapter 1

Introduction

The topic of wave scattering from random rough surfaces is of interest in a wide variety of fields including sonar, radar and seismic imaging and detection, medical ultrasonics, optics, computer rendering of images, and ultrasonic non-destructive testing. After a century of effort, the solution of the general scattering problem is still not fully understood. For those of us who harbor a fascination for waves, it is fortunate that many questions remain to be answered and useful ways of applying acoustics remain to be discovered.

Although wave scattering is a branch of physics, developments are often brought about by the need to push the capabilities of the applications of wave physics to higher levels. Such is the case in this thesis; the advances presented here in the general topic of rough interface scattering were inspired by the need to push the capabilities of active sonar in the deep ocean to higher levels of performance. The focus is on both the sonar engineering application and the theoretical developments it has inspired.

1.1 Motivation

Sound is the most effective way to probe the ocean at long distances and is commonly used for mapping the ocean floor, measuring oceanographic parameters, communicating, and detecting targets.

In target detection, a key concern is reverberation noise which, unlike ambient

noise in the ocean, cannot be removed by increasing source level. Amidst reverberation noise, the ability to distinguish a target is a function of one's grasp of the character of reverberation versus that of the target. In an effort to improve the understanding of reverberation, the Office of Naval Research launched the Acoustical Reverberation Special Research Program (ARSRP) in 1989. A series of experiments were performed to study reverberation and scattering in the deep waters of the middle of the Atlantic Ocean on the Western flank of the Mid-Atlantic Ridge.

What poses the greatest challenge to long-range detection in this part of the world's oceans is the young, mountainous crust which forms the seafloor and with which sound waves interact. Rough features are found throughout a range of scales that span many orders of magnitude above and below the wavelength, from grains smaller than a millimeter in size to kilometer-tall abyssal hills. Variations in the types of roughness are also extensive, alternating between flat sediment ponds and steep scarps of exposed basalt, and between seafloor areas with distinct geological origin.

The reverberation from a pulse emitted near the surface can last up to 20 minutes and results from interaction of sound with bathymetric features as far as a hundred or more kilometers away. Match-filtered, beamformed envelopes of 55 Hz bandwidth pulses centered at 228 Hz exhibit lineations across range and azimuth which have been shown to be deterministically linked with large bathymetric features [41] [40] [58] [28]. For such lineations and features, a scattering interaction is taking place at an identifiable spot on the seafloor.

The next level of refinement is the understanding of the scattering process taking place at the seafloor. A feature of the ARSRP experiments which poses unique challenges is the use of range-resolving pulses. For such pulses, the seafloor region over which the sonar integrates energy (footprint) is small, and scattered pressures from separate features, which might occur at the same time in a large footprint, arrive temporally separated. Unlike reverberation, scattering in the context of ARSRP is not well-understood and has not been studied to the extent warranted by the extensive datasets collected. To shed light on this matter, scattering strengths and probability density functions of time-domain backscatter are extracted from the ARSRP data.

Inspired by these scattering data, rough surface scattering is then studied from a theoretical perspective.

On a theoretical level, it is a trivial fact that for any rough interface, its *roughness* and the material properties on either side of it govern the scattering process. What is not trivial is how to subsume the roughness into a manageable set of parameters that can be related to acoustical quantities of interest. With the advent of computational approaches, that "manageable" number has been growing rapidly, but there is still a need for the identification of only the most essential information about the roughness, for two reasons. First, it is usually impossible to know the shape of a scattering surface to sufficient accuracy for exact acoustical prediction. Second, even if the surface were known to high resolution, its complexity may render exact acoustical calculations prohibitively expensive. Both of these limitations exist in the context of the ARSRP experiment and highlight the need to efficiently characterize the roughness in useful ways. A pervasive concept in this characterization is that of scale.

1.2 The Tradition of Scale in Scattering

From the very beginning of the field of scattering from rough surfaces, the issue of *scale* has been identified as most vital to characterize roughness. In his consideration of scattering of a plane monochromatic wave from a sinusoidal surface in the late 19th century, Lord Rayleigh [55] identified the importance of the magnitude of the vertical excursions on the surface relative to the wavelength and the grazing angle. The parameter $R_a = k\Delta h \cos\theta_i$, where Δh is the amplitude of the sinusoidal surface and θ_i is the grazing angle of the incident wave, is used to evaluate the roughness of a surface and has come to bear Rayleigh's name [55].

Another powerful tool in simplifying the task of predicting scatter from rough surfaces is to use an acoustical model based on a probabilistic surface description which, instead of attempting to treat each surface and its details individually, treats an entire family of surfaces at once. In a statistical context, the notion of scale preserves its importance. In the Rayleigh parameter, Δh is replaced by the root

mean square (rms) height of the surface; its square represents the average energy in the random process.

As the applications of acoustics and electromagnetics have multiplied over the past century, the full correlation function of a surface has been found to provide useful information for the prediction of scattering [50]. This function embodies the notion that along with a surface's vertical scales, the horizontal scales over which variations take place are relevant. The equivalent of this full second-moment statistical characterization in the wavenumber domain is the power spectral density, which represents the expected value of the energy in the surface at each wavenumber component.

In a further refinement, the terms "single-scale" and "multi-scale" have evolved to create a distinction between surfaces which exhibit roughness in the form of features closely distributed about a single scale and surfaces which exhibit roughness in the form of features at many different scales. The organization of features at different scales in a stochastic process is referred to in this thesis as *scale structure*, and it is the focus of my research effort.

This refinement beyond merely describing the power spectral density of a random surface, towards a determination of scale structure, is proposed to be necessary to explain data such as those collected in the ARSRP experiments, because

1. Scattering occurs in response to features, not spectral components;

2. The geological processes that form the seafloor exhibit *feature-like* roughness; and

3. Second moment representations of the seafloor for power-law type power spectral densities are unable to model feature-like roughness.

The objective of this thesis is *to study the importance of scale structure in scattering from random, rough surfaces on a theoretical level to aid in bringing the predictive ability of scattering theories to the level warranted by current applications of acoustics.* One such application is the scattering of high-resolution range-resolving pulses from the rough ocean floor. Threrefore, the processing of data from the ARSRP experiment into a form conducive to interpretation is another major goal of this study.

1.3 Outline of Thesis

This thesis is divided into two major parts:

1. The analysis and interpretation of data from the ARSRP experiment.

    - Chapter 2 explains the ARSRP experiment and shows how reverberation can be modeled and, therefore, removed from the data to study scattering.
    - Chapter 3 extracts scattering data corresponding to a specific bathymetric feature from the reverberation data and demonstrates that intertwined areas as narrow as 500 m of distinct geological type can be resolved and studied separately. Evidence of target-like scatter and the importance of anisotropy are seen.
    - Chapter 4 analyzes the roughness of the seafloor from both a deterministic morphological point of view and from a stochastic point of view, revealing the existence of feature-like roughness which is not captured by second-moment statistical models. A composite seafloor model is proposed.

    The acoustical and bathymetric observations of Chapters 2, 3, and 4 lead to the proposal that scale structure as a characteristic of random surfaces which is distinct from the power spectral density is relevant to acoustic scattering. This proposal is explored in a theoretical study.

2. The theoretical modeling of acoustic scatter from random rough surfaces.

    - Chapter 5 develops feature-like one-dimensional stochastic models exhibiting power-law decay in their power spectral densities. These models, distinct in scale structure from Gaussian models having the same second moment, are proposed as fitting components in the composite seafloor model proposed in Chapter 4.
    - Chapter 6 employs a Monte-Carlo technique based on the exact integral equations for scatter from rigid, one-dimensional surfaces to compute bistatic scattering strength and the probability density functions of the

log-envelopes of backscatter from feature-like and non-feature-like surfaces with identical power spectral density, demonstrating the importance of scale structure in acoustic scattering.

Conclusions and suggestions for future work are contained in Chapter 7.

1.4 Summary of Contributions

This thesis makes four major contributions.

Contribution 1 The development of ARTIST, which is both a software package and a mathematical formalism, to help visualize the insonification process in physically intuitive ways, model reverberation, and extract scattering data originating from detailed seafloor regions in the context of a range and azimuth resolving sonar system.

With the goal of extracting useful information about scattering from the ARSRP data, a model is developed to keep track of the propagation and refraction of energy from the sonar arrays to the seafloor and back, the orientations and positions of the arrays, the array beampatterns, and the effect of local bathymetry in generating shadow zones and in modulating local grazing angles. Two data structures, insonification and intersection patterns, are defined which efficiently represent the combination of these factors and allow the insonification of the seafloor to be visualized in ways conducive to physical interpretation.

Using ARTIST, simulated reverberation is generated and compared with ARSRP data. Prominent events at 200 msec scales are successfully predicted, confirming that they result from the single seafloor interaction ray paths modeled by ARTIST. Other events, particularly at early times, are not adequately modeled by such ray paths; in these cases, ARTIST is a valuable tool for gaining insight into the dominant mechanisms responsible for the observed reverberation levels. For events which *are* correctly modeled, the formalism allows portions of the data corresponding to specific seafloor features to be extracted and analyzed.

Contribution 2 The analysis and interpretation of scattering and bathymetric data from a feature of O (10 x 40) km^2 in size known as site B'.

The elongated bathymetric feature of O (10 x 40) km^2 in size known as site B' is composed of alternating scarp and terrace areas. The areas of B' belonging to either category are identified using polygonal shapes. Using these polygons, ARTIST is able to separately extract detailed portions of reverberation data corresponding to scarps and terraces. Using data from seven different ship positions, backscattering strength curves are obtained for scarps and for terraces, revealing that terraces are stronger scatterers at grazing angles below 20 degrees. Both seafloor types are found to disagree with Lambert's law below grazing angles of 25 degrees.

The anisotropy of scarps is also investigated, revealing higher backscattering strengths normal to the scarps than at 30-50 degrees relative to the axis of anisotropy.

The log-envelope pdfs of time-domain backscatter are estimated and found to have a target-like or non-Rayleigh character at the highest levels for both seafloor regions, but the deviations from non-Rayleigh are found to be higher for scarps at normal incident azimuths with respect to the anisotropy, and at large grazing angles. The bathymetry is observed to be feature-like, and the target-like acoustic data are proposed to be linked to the feature-like nature of the roughness.

The bathymetry is then analyzed in more detail, revealing that the feature size distibution is distinct along scarp-parallel and scarp-normal directions. Concurrently, spectral estimates in the two orthogonal directions yield the same power spectrum. This observation suggests the inability of the power spectral density to capture feature-like roughness. A composite seafloor model is proposed which is the superposition of component models each acting at a specific scale and corresponding to a separate seafloor generating mechanism.

Contribution 3 The establishment of the concept of scale structure and its distinctness from the power spectral density.

One-dimensional stochastic surface models with feature-like roughness are developed. Their power spectral densities are derived analytically and are shown to exhibit

a power-law decay. In contrast, Gaussian models with the same power-law spectrum are not feature like, demonstrating the insufficiency of the power spectral density in describing the appearance of spatial domain realizations.

In this thesis, the spatial arrangement of a surface's component features at different scales is defined as "scale structure". It is proposed to be more descriptive than the power spectral density in determining a surface's scattering properties, because it directly describes the objects which cause scatter: surface features.

While scale structure remains largely a qualitative attribute, processes having identical power spectral density but different scale structure are successfully discriminated using the wavelet transform which suggests that a quantitative, mathematical definition of scale structure could be based on wavelets.

Contribution 4 The establishment that scale structure is a surface attribute of relevance to acoustic scatter and that second moment characterizations of random surfaces are insufficient for predictions of scattering.

Using an exact integral equation numerical approach, the potential impact of scale structure in scattering is investigated by comparing the scatter from feature-like and non-feature-like surfaces having identical power spectral density. The results show that scale structure is important both for bistatic scattering strength and for the pdfs of the log-envelopes of backscatter and demonstrate the insufficiency of second moment characterizations in describing the roughness of surfaces in acoustically relevant ways. Feature-like surfaces are found to behave considerably more target-like than multi-scale surfaces.

Surfaces with similar scale structure but different power spectral densities are also compared and are found to share some characteristics.

Finally, feature-like and multi-scale rough surfaces with variance and correlation length similar to the roughness normal to Site B' scarps are tested. The results demonstrate that scale structure preserves its importance in enhancing target-like scatter at the scales of roughness encountered in the ARSRP scenario, suggesting that proper analysis of the scale structure of the seafloor is worthwhile for improving

predictions of scattering statistics.

Chapter 2

Simulation of ARSRP Reverberation

2.1 Introduction

In this Chapter, I address the issue of reverberation from the Atlantic Natural Laboratory of the Mid-Atlantic Ridge, regarding which significant progress has been made since the Office of Naval Research launched the Acoustical Reverberation Special Research Program (ARSRP) in 1989. Previous efforts [41] [40] [58] [28] have clearly shown that there exists a deterministic link between large-scale features in the bathymetry and large-scale features in the beamformed reverberation time series. These studies have also shown that direct ray paths from the arrays to the seafloor play a dominant role in generating the most prominent returns.

Here, I study how reliably beamformed reverberation time series can be *simulated* using the ray paths that interact with the bottom only once. With the aid of the software package ARTIST [38] [37] [36], beamformed reverberation envelopes within 1/2 CZ are simulated at temporal resolutions of 200 msec and compared to actual reverberation data collected at two sites near the MAR. The two sites studied lie at either end of a set of deep interconnected valleys called the B'-C' corridor, shown on Fig. 2-1. The western site is referred to as B', and the eastern site is referred to as C'.

The purpose behind the reverberation simulations is to demonstrate that the propagation and array resolution effects can be accounted for by ARTIST and therefore removed from the data to isolate scattering. In particular, in Chapter 3 I am interested in identifying specific portions of data as resulting from scattering at selected seafloor regions. The reverberation modeling is flavored by this end goal in that it is carried out only to the degree necessary for the local scattering analysis; in particular, the only ray paths accounted for are those which interact with the seafloor once. In spite of this limitation, surprisingly good simulations of reverberation are possible in ARSRP. The degree of agreement between data and model is excellent for prominent events at intermediate to late times and fair at early times. The varying levels of agreement provide insight into the physical mechanisms that are in play over each data region.

In Section 2.2, I provide a brief description of the ARSRP experiment. This is followed in Section 2.4 by a theoretical description of ARTIST propagation modeling and data structures. Monostatic reverberation simulations at sites B' and C' and a bistatic simulation at site B' are presented in Section 2.5.

2.2 Experiment

The ARSRP experiments took place at the Office of Naval Research Atlantic Natural Laboratory, which occupies a 400 km by 200 km rectangular area centered around 47° W, 26° N, just West of the Mid-Atlantic Ridge (MAR) as shown in Fig. 2-1. The seafloor in this area is geologically young, ranging from 0 to 28 million years in age. At the largest scales, it is characterized by a series of mountains (abyssal hills) rising one to two kilometers from valleys at depths of 3500 m at the eastern end and 4500 m at the western end. The seafloor exhibits strong anisotropy, with mountain crests oriented nominally 60° counter-clockwise from an x-axis pointing East. Valleys are typically sedimented, but large portions of the abyssal hills display exposed acoustically-hard rock such as basalt. At any given frequency, roughness structures are present at scales ranging from thousandths of an acoustic wavelength

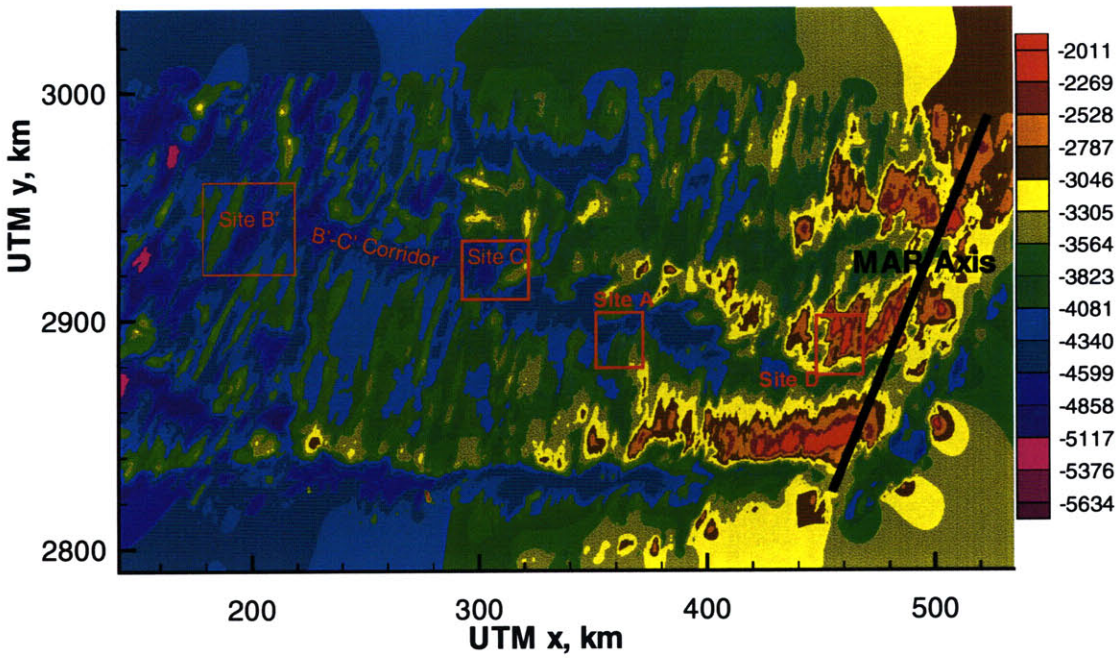

Figure 2-1: Bathymetry of the Atlantic Natural Laboratory collected in 1992 on the western flank of the Mid-Atlantic Ridge, having nominal horizontal resolution of 200 m.

or less to hundreds of wavelengths and higher. Reverberation and scattering from such seafloor are complex phenomena and the ARSRP experiments were designed to improve their understanding,

The data analyzed in this thesis were collected during the July 1993 ARSRP Cruise [48]. The experimental configuration and the angular co-ordinate system used are shown in Fig. 2-2. The *R/V Cory Chouest* towed a 10-element vertical line array (VLA) source with 2.29 m spacing and a 128-element horizontal receiving line array (HLA) with 2.5 m spacing. To permit bistatic observations of sites A, B', and C', a second ship, the *R/V Alliance*, towed a vertical pair flextensional source and a receiving array identical to the *Cory*'s.

Two of the elements of the receiving array were desensitized to permit analysis of the emitted signals and several others had significant gain reductions due to malfunction. These issues resulted in an increase of the sidelobe level of the wideband beampatterns from -30 dB to -25 dB, but had a minor impact on main lobe width. A

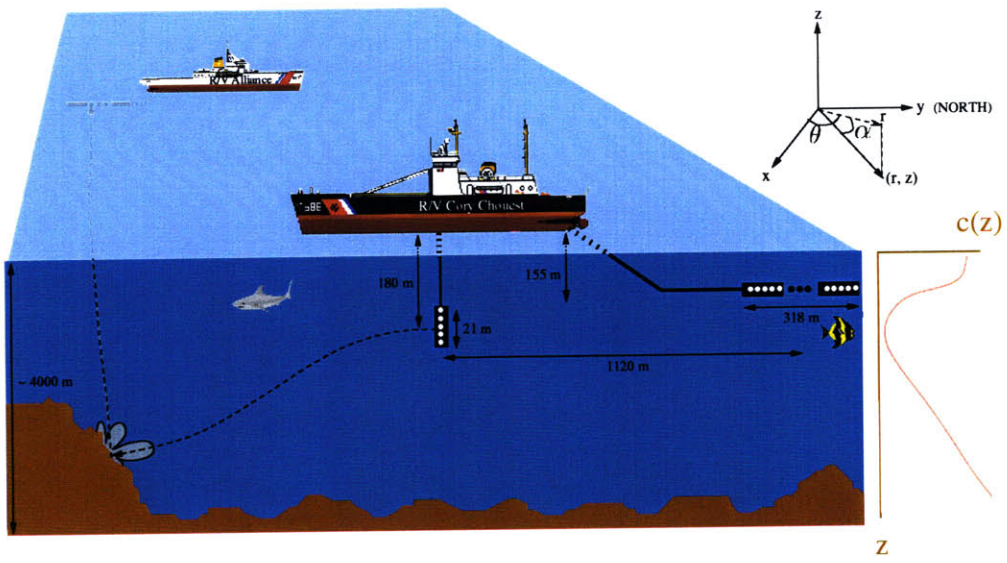

Figure 2-2: Experiment configuration. The *R/V Cory Chouest* towed a ten element VLA source and a 128 element HLA receiver. The *R/V Alliance* also towed a 128 element HLA, permitting bistatic observations of features insonified by the *Cory*'s source. The cartesian and angular co-ordinate systems used in the remainder of the chapter are as indicated.

potentially more important difficulty relates to the hydrodynamically-induced vertical array deformations with an amplitude of several wavelengths [14]. This has been shown to smear the main lobe of the receiving array over as much as ten degrees for vertical incidence directions, however the vertical array deformations have a negligible impact on the beampattern for the near-horizontal incidence directions considered here. Similar distortions in the *horizontal* plane could degrade the beampattern for near-horizontal look directions. In Ref. [12], the main lobe width of the receiver array is deduced by picking a particularly loud and impulsive event incident upon the array at near-horizontal angles and tracking its leakage into neighboring beams. The conclusions are that the main lobe is not discernably wider than for an ideal line array, suggesting that horizontal deformations were negligible. Near-broadside beamwidths were about 1°, leading to a lateral footprint size at 1/2 CZ ($\simeq$ 35 km) of about 600 m. The data were processed into 128 non-overlapping beams.

A range of acoustical signals were emitted including CW multitones, wideband

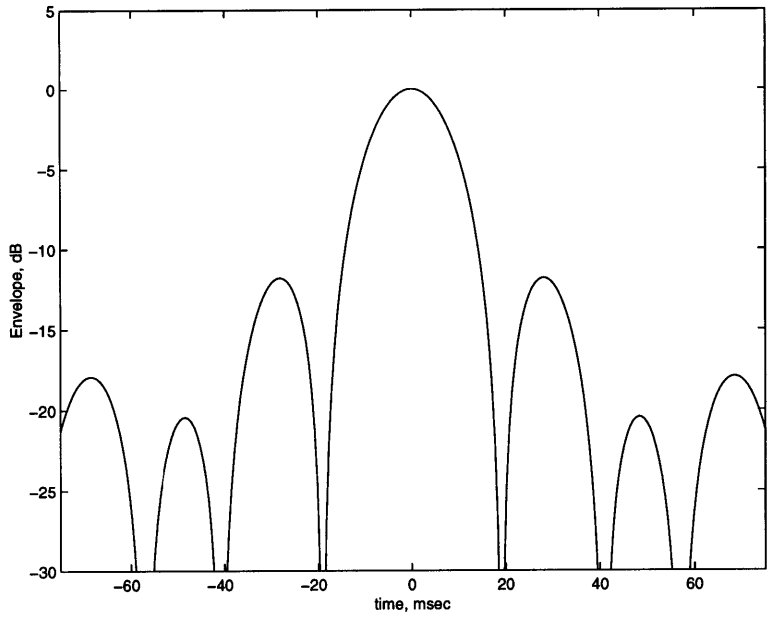

Figure 2-3: Match-filtered de-modulated pulse used in the wideband 200-255 Hz LFM experiments. The null-to-null width of the main lobe is about 35 msec; the 3-dB width is about 20 msec. The highest sidelobe level is about -12 dB.

LFM's, stepped LFM's and signals from SUS charges. The experiment was divided into "segments", which included 12 minutes of data acquisition using different "pings". Each ping corresponded to a different signal. In this thesis, no distinction is made between a segment and a ping since only the wideband LFM signals are analyzed. These were pulses with instantaneous frequency linearly varying between 200 Hz and 255 Hz over a 5-second duration, with a cosine amplitude taper over the first and last 0.3 seconds. The *Cory*'s source level at the center frequency of the pulse band was 232 dB re 1 μPa and the wavelength at this frequency was approximately 6 m at the seafloor.

The acoustic data analyzed in this thesis were the result of demodulating, down-sampling, match-filtering, and beamforming the raw data collected at the receiving arrays. The match-filtering compressed the wideband LFM signals into a pulse approximately 35 msec wide between nulls with relatively high sidelobes, as shown in Fig. 2-3. The 3-dB width of this pulse is approximately 20 msec. Its range resolution, depending on the definition of pulse width, ranges from 15 to 26 m.

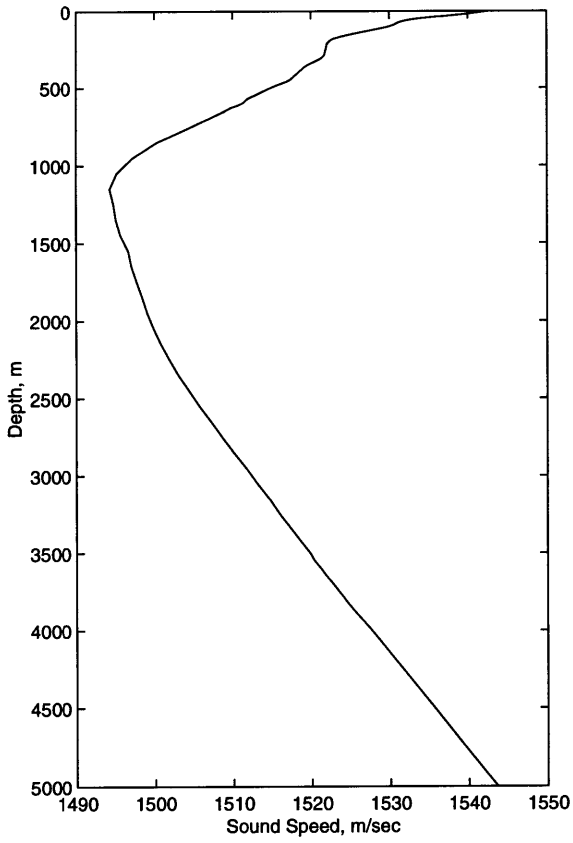

Figure 2-4: Sound speed profile used in the ARTIST simulations.

Supporting environmental data include frequently measured array positions and orientations, sound speed profiles from bathythermographs and CTD casts, and full-coverage bathymetry at 200 m lateral resolution. The bathymetry, shown in Fig. 2-1, was collected as part of the 1992 Reconnaissance Survey. The environmental data were used as input parameters to ARTIST for simulation of reverberation and extraction of scattering strength. The single sound speed profile used in all the simulations in this Chapter is shown in Fig. 2-4. It represents a smoothed version of the CTD casts.

Higher-resolution bathymetric data were collected at selected sites to provide an understanding of the fine-scale structure of the seafloor. These surveys include DSL-120 sidescan sonar data with a resolution of 5 m and observations from the remotely-operated vehicle Jason, including 1-m resolution pencil-beam mesotech sonar data and

video images [67] [18]. Although these datasets provide insufficient coverage and too high a resolution for productive deterministic simulations, they are extremely useful in revealing seafloor structure near the acoustic wavelength. Without this knowledge, the interpretation of observed scattering behavior would be impossible.

2.3 Full-field vs. Ray Models

Previous studies of acoustic data from the ARSRP experiments have used either ray-based models [22] [28], full-field Parabolic Equation (PE) models [58] [39], or both [41] [40]. Both techniques present advantages and disadvantages. Full-field models yield a more accurate picture of transmission loss in shadow zones because they naturally account for diffraction and multipath. This translates into more realistic reverberation simulations in shadow zones, provided that time-delays are available. These can be obtained either by carrying out computationally-intensive wideband full-field simulations, or more simply with a ray model. Full-field models also yield correct transmission loss values near caustics where ray theory breaks down, and they preserve phase in their calculations, thus accounting for the coherent effects of multipath.

On the other hand, ray models provide a more intuitive interpretation of the physics of reverberation and scattering. Each ray path corresponds to an energy bundle that can be followed through the water column, interacts with the seafloor at an identifiable grazing angle, and has a specific time delay associated with it. The knowledge of grazing angles makes the study of the scattering behavior of particular seafloor patches possible; a full-field model is incapable of this analysis because it always includes coherent multipath even when the true insonification picture is simple and well-captured by a ray analogy. With ray models, the easily-obtained time delays are especially convenient in a broadband, pulse-revolving effort such as ARSRP.

In the deep water scenario of ARSRP, dominant reverberation events at ranges greater than about 25 km are due to seafloor features which intersect ray paths emanating directly from the receiving and transmitting arrays. Thus, ray theory is

not only intuitive but a correct model of the physics for those events. The confirmation of this assertion was initiated in Ref. [28]; further confirmation is provided here in Sections 2.5.1 and 2.5.2.

The portions of the data at lower levels typically cannot be attributed to ray paths that interact with the seafloor only once; the received levels result from multiple seafloor bounces. In these areas, the inclusion of all multipath in full-field models leads to more realistic predictions. From an engineering perspective, the dominant events (where ray models are more appropriate) are more important than the background because they lead to clutter in active sonar systems and as such they are the motivation for ARSRP.

The above points should help clarify why a ray-based model was used instead of a full-field model. I now proceed to the description of the ray-based code Acoustical Ray-Tracing Insonification SofTware (ARTIST).

2.4 ARTIST

Existing ray models devoted to reverberation such as the Generic Sonar Model (GSM) [70] and BiRASP [11] account for ray paths interacting several times with the bottom, the surface, and volume scatterers. In these models, each portion of the reverberation data is considered to originate from a multitude of scattering areas either in the water column, the sea surface, or the bottom, insonified at varying grazing angles and incident energies.

The principal goal of ARTIST is the local study of scattering at the water-seafloor interface; a supporting goal is the prediction of reverberation. In modeling reverberation, ARTIST concentrates on that part which is useful for local bottom scattering studies, that is, the part for which the dominant contributors are direct and surface-reflected rays interacting *only once* with the bottom.

It is natural to ask about the price paid in simulation quality by neglecting multiple seafloor bounces, volume scattering, and sea surface scattering. In ARSRP, the sea surface was calm, major portions of the seafloor are acoustically hard, and

reverberation associated with multiple seafloor bounces is often significantly less energetic than that due to single seafloor interactions; ARTIST simulations are very good in this situation. ARTIST incorporates grazing angles with respect to local bathymetry in its simulations, providing it with a significant advantage with ARSRP data compared to a flat seafloor model such as GSM.

Another ray-tracing model used in the context of ARSRP to study scattering and reverberation is BISSM [5]. This model accounts for direct paths to the bathymetry to determine transmission losses and grazing angles with respect to local seafloor slopes. It allows for source-receiver separation and the specification of the source beampattern and arbitrary sound speed profiles, and has been used to simulate reverberation and extract Lambert's law coefficients in Ref. [28].

ARTIST is based on a rigorous theoretical framework in which data structures resulting from ray-tracing are manipulated as *insonification* and *intersection patterns.* These mathematical entities incorporate the full ambiguity function that results from the combined effects of the source and receiver beampatterns, the pulse shape, and the propagation process. Both direct *and* surface-reflected paths are included. As will be shown in Sections 2.5.1 and 2.5.2 and in Chapter 3, the benefits of the careful theoretical treatment are evident in the reverberation simulations, in the ability to visualize the insonification process, and in the capability to reliably extract scattering strength over detailed geographic areas.

The following Section is a mathematical description of ARTIST; the uninterested reader may skip to Section 2.5 for a look at the reverberation simulations.

2.4.1 Theory of Operation

The description of the theory behind ARTIST is divided into three sections. First, the modeling of propagation from the source to the seafloor and from the seafloor to the receiver is described. Second, a method is presented which combines the source and receiver data structures from the propagation modeling into a single data structure. Third, the generation of simulated reverberation is discussed. In Chapter 3, the theory is extended so that scattering data corresponding to selected seafloor features

can be extracted from the reverberation data.

Throughout Chapters 2 and 3, the subscripts s and r refer to the source and the receiver respectively, and $\mathbf{r}$ is used to specify two-dimensional vectors in the xy plane. Three-dimensional vectors are written $(\mathbf{r}, z)$.

Insonification Patterns

ARTIST models the propagation of direct and surface-interacting paths from the source to the seafloor by performing a ray-trace starting from the source location $(\mathbf{r}_s^*, z_s^*)$. If the source is an array, the center of the array is used. The sound speed $c(z)$ is assumed to depend only on depth z. Each ray is identified by its initial spherical launch angle pair $\phi = (\alpha, \theta) \in \mathcal{S}^2$ where

$$\mathcal{S}^2 = \{(\alpha, \theta) : \alpha \in [-\pi/2, \pi/2], \theta \in \mathcal{S}^1\} \tag{2.1}$$

is the set of points on the sphere and $\mathcal{S}^1 = [-\pi, \pi)$ is the set of points on the circle. Each ray is traced until it either makes contact with the seafloor as defined in a bathymetric input file, or until it exceeds a specified path length, whichever comes first. If the sea surface is encountered, the ray is assumed to reflect with no specular energy loss. If no seafloor contact is made, the ray is discarded. Let $\mathcal{P}_s$ be the set of all rays having made contact with the seafloor:

$$\mathcal{P}_s = \{\phi_1, \phi_2, \ldots, \phi_{P_s}\} \subset \mathcal{S}^2. \tag{2.2}$$

Upon contact, the following parameters are determined: horizontal contact position $\mathbf{r}_s = \mathbf{R}_s(\phi)$, bathymetric depth $z_s(\phi)$, local grazing angle with respect to the bathymetry $\gamma_s(\phi)$, time delay $t_s(\phi)$, and transmission loss $TL_s(\phi)$. These parameters are grouped into a single set

$$I_s^{\mathcal{P}} = \{(\mathbf{R}_s(\phi), \mathbf{q}_s(\phi), \phi) : \phi \in \mathcal{P}_s\}. \tag{2.3}$$

where the second factor is

$$\mathbf{q}_s(\phi) = (z_s(\phi), \gamma_s(\phi), t_s(\phi), TL_s(\phi)). \tag{2.4}$$

The numerical implementation of the ray-tracing imposes that ϕ be a discrete variable, but in reality there is some continuous subset $\mathcal{S}_s^2 \subseteq \mathcal{S}^2$ for which the seafloor is accessed by rays. The remainder of $\mathcal{S}^2$ is the space of rays that are discarded. I define the continuous set I_s such that it contains the result of the ray-trace over all of $\mathcal{S}_s^2$. The set $I_s^{\mathcal{P}}$ is merely a discretized version of the full set I_s:

$$I_s^{\mathcal{P}} \subset I_s = \{(\mathbf{R}_s(\phi), \mathbf{q}_s(\phi), \phi) : \phi \in \mathcal{S}_s^2\} \subseteq \mathcal{R}^2 \times \mathcal{Q} \times \mathcal{S}_s^2. \tag{2.5}$$

where

$$\mathcal{Q} = \mathcal{R} \times \mathcal{S}^1 \times \mathcal{R}^+ \times \mathcal{R} \tag{2.6}$$

and $\mathcal{R}^+$ is the set of real, positive numbers. The parameterization by ϕ is mathematically convenient in that each ray launch angle is mapped to unique $\mathbf{R}_s(\phi)$ and $\mathbf{q}_s(\phi)$. On the other hand, it is easier to gain physical insight into the parameters in $\mathbf{q}_s$ when they are represented graphically as functions of the horizontal position vector $\mathbf{r}$. If an inverse $\Phi_s(\mathbf{r})$ could be found for $\mathbf{R}_s(\phi)$ such that $\phi = \Phi_s(\mathbf{R}_s(\phi))$, I could write

$$I_s = \{\mathbf{r}, \mathbf{q}_s(\Phi_s(\mathbf{r})), \Phi_s(\mathbf{r})) : \mathbf{r} \in \mathbf{R}_s(\phi), \phi \in \mathcal{S}_s^2\}, \tag{2.7}$$

achieving the desired parameterization by $\mathbf{r}$. A single inverse can be found only when $\mathbf{R}_s(\phi)$ is one-to-one, but rays launched at seperate angles are often mapped to a single position. For example, consider the ARSRP scenario in which a given point on the seafloor can receive both a direct and a surface-reflected ray. In such cases, while a global inverse does not exist, the notion of *local* inverses is useful, as described in the following theorem.

Inverse Function Theorem: *When*

$$\det\left(\frac{\partial \mathbf{R}}{\partial \phi}\right)\Big|_{\phi=\phi_0} \neq 0, \tag{2.8}$$

$\exists$ a neighborhood A of ϕ_0, U of $\mathbf{R}(\phi_0)$ and a function Φ so that $\mathbf{R} : A \to U$ is one-to-one, onto and $\Phi : U \to A$ inverts $\mathbf{R}$ in these neighborhoods, i.e. $\Phi(\mathbf{R}(\phi)) = \phi$ or $\phi = \Phi(\mathbf{r})$.

For the current application, the vector condition in Eq. 2.8 can be simplified. When the sound speed depends only on depth, the azimuths of ray contacts about the source position are independent of declination launch angle α. In this case, Eq. 2.8 reduces to the one-dimensional condition

$$G(\alpha, \theta) \equiv \frac{\partial |\mathbf{R}_s - \mathbf{r}_s^*|}{\partial \alpha} \neq 0, \tag{2.9}$$

where $|\mathbf{R}_s - \mathbf{r}_s^*|$ is the horizontal range.

The parameterization of all factors in I_s by $\mathbf{r}$ can be realized by finding sets of neighborhoods $A_s^{m_s} \subseteq \mathcal{S}_s^2$ and $U_s^{m_s} \subseteq \mathcal{R}^2$, $m_s \in [1, 2, \ldots, M_s]$ such that $\mathbf{R}_s : A_s^{m_s} \to U_s^{m_s}$ is one-to-one and onto and has inverse $\Phi_s^{m_s} : U_s^{m_s} \to A_s^{m_s}$. There are infinitely many ways to break up $\mathcal{S}_s^2$ into subsets over which local inverses exist. I define the $A_s^{m_s}$ as the unique combination of subsets of $\mathcal{S}_s^2$ such that

$$\mathcal{S}_s^2 = \bigcup_{m_s=1}^{M_s} A_s^{m_s} \tag{2.10}$$

and M_s is the *minimum* possible number of subsets. This number is at least $O + 1$ where O is the maximum number of zeros of $G(\alpha, \theta_0)$ as a function of α for constant θ_0. The number M_s may be greater than $O + 1$ whenever a particular subset C of S_s^2 is totally disconnected from the rest of S_s^2 such that it is impossible for ϕ to vary continuously in passing from C to the remainder of S_s^2 without passing through regions where $\mathbf{R}_s(\phi)$ is undefined; these undefined regions can contain hidden sign changes. If they do, they constitute a boundary between some of the $A_s^{m_s}$. The

curves over which $G = 0$ are always boundaries between the $A_s^{m_s}$.

The original set I_s is divided into M_s subsets

$$I_s^{m_s} = \{(\mathbf{r}, \mathbf{q}_s(\Phi_s^{m_s}(\mathbf{r})), \Phi_s^{m_s}(\mathbf{r})) : \mathbf{r} \in U_s^{m_s}\}, \tag{2.11}$$

which I define as *insonification patterns*, each of which is uniquely parameterized by $\mathbf{r}$; note that

$$I_s = \bigcup_{m_s} I_s^{m_s}. \tag{2.12}$$

For a receiver located at $(\mathbf{r}_r^*, z_r)$, the same procedure is employed. The result of the ray trace is recorded in a discrete set

$$I_r^{\mathcal{P}} = \{(\mathbf{R}_r(\phi), \mathbf{q}_r(\phi), \phi) : \phi \in \mathcal{P}_r\} \tag{2.13}$$

which is a subset of the continuous set

$$I_r = \{(\mathbf{R}_r(\phi), \mathbf{q}_r(\phi), \phi) : \phi \in \mathcal{S}_r^2\}. \tag{2.14}$$

The parameterization by ϕ is transformed into a parameterization by $\mathbf{r}$ by finding the smallest number of neighborhoods B^{m_r} of ϕ and V^{m_r} of $\mathbf{r}$ such that for each B^{m_r}, the function $\mathbf{R}_r : B^{m_r} \to V^{m_r}$ is one-to-one and onto and has inverse $\Phi_r^{m_r} : V^{m_r} \to B^{m_r}$ and

$$I_r = \bigcup_{m_r} I_r^{m_r}. \tag{2.15}$$

The final product is the set of M_r insonification patterns

$$I_r^{m_r} = \{(\mathbf{r}, \mathbf{q}_r(\Phi_r^{m_r}(\mathbf{r})), \Phi_r^{m_r}(\mathbf{r})) : \mathbf{r} \in V_r^{m_r}\}. \tag{2.16}$$

The source's insonification patterns provide information as to how a listener moving along the seafloor would be illuminated by the source. Conversely, the receiver's

insonification patterns contain information about the receiving array's perception of a speaker standing at each seafloor point.

Intersection Patterns

With insonification patterns on hand for both the source and the receiver, information about the propagation from the source to the bottom and from the bottom to the receiver are known separately. The information from these processes is combined in the form of *intersection patterns.* The regions over which the intersection patterns are defined represent seafloor areas that are illuminated by both the source and the receiver. Such areas are expected to play a strong role in reverberation and are also the only ones of practical use for locally extracting scattering strength. Analogously to insonification patterns, intersection patterns consist of a number of single-valued functions of space defined on a subset of $\mathcal{R}^2$ that corresponds to an illuminated area. Intersection patterns are defined as:

$$X^n = \{\mathbf{r}, \mathbf{Q}^n(\mathbf{r}), \Phi_s^{m_s[n]}(\mathbf{r}), \Phi_r^{m_r[n]}(\mathbf{r}) : \mathbf{r} \in W^n\} \tag{2.17}$$

where the domain of definition for each intersection pattern, W^n, is the intersection of the domains of definition of its constituent insonification patterns:

$$W^n = U_s^{m_s} \bigcap V_r^{m_r}. \tag{2.18}$$

The index n is related to the insonification pattern indices through

$$n = (m_s - 1)M_r + m_r. \tag{2.19}$$

Conversely, m_s and m_r can be recovered from n using

$$m_s[n] = \text{floor}\left(\frac{n-1}{M_r}\right) + 1 \tag{2.20}$$

and

$$m_r[n] = n - M_r \text{floor}\left(\frac{n-1}{M_r}\right). \tag{2.21}$$

The second factor in Eq. 2.17 is

$$\mathbf{Q}^n(\mathbf{r}) = (z^n(\mathbf{r}), \gamma_s^n(\mathbf{r}), \gamma_r^n(\mathbf{r}), \eta^n(\mathbf{r}), t^n(\mathbf{r}), TL^n(\mathbf{r})), \tag{2.22}$$

where

$$z^n(\mathbf{r}) = z_s(\Phi_s^{m_s[n]}(\mathbf{r})) = z_r(\Phi_r^{m_r[n]}(\mathbf{r})),\ \mathbf{r} \in W^n, \tag{2.23}$$

$$\gamma_s^n(\mathbf{r}) = \gamma_s(\Phi_s^{m_s[n]}(\mathbf{r})),\ \mathbf{r} \in W^n, \tag{2.24}$$

$$\gamma_r^n(\mathbf{r}) = \gamma_r(\Phi_r^{m_r[n]}(\mathbf{r})),\ \mathbf{r} \in W^n, \tag{2.25}$$

$$t^n(\mathbf{r}) = t_s(\Phi_s^{m_s[n]}(\mathbf{r})) + t_r(\Phi_r^{m_r[n]}(\mathbf{r})),\ \mathbf{r} \in W^n, \tag{2.26}$$

$$TL^n(\mathbf{r}) = TL_s(\Phi_s^{m_s[n]}(\mathbf{r})) + TL_r(\Phi_r^{m_r[n]}(\mathbf{r})),\ \mathbf{r} \in W^n, \tag{2.27}$$

and $\eta^n(\mathbf{r})$ is the bistatic angle in the xy plane, given by

$$\eta^n(\mathbf{r}) = \angle((\mathbf{r} - \mathbf{r}_s^*), (\mathbf{r} - \mathbf{r}_r^*)),\ \mathbf{r} \in W^n, \tag{2.28}$$

where $\angle(\mathbf{r}_1, \mathbf{r}_2)$ is the angle between $\mathbf{r}_1$ and $\mathbf{r}_2$.

The intersection patterns reveal the manner in which seafloor areas are being insonified both geometrically and energy-wise from the combined effects of source and receiver, and the times at which they contribute to the received signals.

Simulated Data

Using the information in the intersection patterns, I seek to generate simulated reverberation time series $AL(t_j, b_k)$ representing the average energy collected at times t_j by beams b_k, where $j \in \{1, 2, \ldots, J\}$ and $k \in \{1, 2, \ldots, K\}$.

For each intersection pattern, the energy contributed to pixel (j, k) is found by integrating the energy at the seafloor, given by $10^{E^n(\mathbf{r},j,k)/10}$ where the quantity $E^n(\mathbf{r}, j, k)$, in dB units, includes the effects of the source beampattern $B_s(\phi)$, the receiver beampattern $B_r^{(k)}(\phi)$ for beam k, the pulse magnitude in dB $T(t)$, the transmission loss $TL^n(\phi)$ and the scattering strength $SS\left(\gamma_s^n(\mathbf{r}), \gamma_r^n(\mathbf{r}), \eta^n(\mathbf{r}), \mathbf{r}\right)$. The total energy received at t_j by beam b_k is the sum over the N intersection patterns, each corresponding to a different set of ray paths linking the source, the seafloor, and the receiver. The simulated data are given by:

$$AL(t_j, b_k) = 10 \log_{10} \left(\sum_{n=1}^{N} \int_{W^n} 10^{\frac{E^n(\mathbf{r}', j, k)}{10}} d\mathbf{r}' \right), \tag{2.29}$$

where

$$E^n(\mathbf{r}, j, k) = F^n(\mathbf{r}, j, k) + SS\left(\gamma_s^n(\mathbf{r}), \gamma_r^n(\mathbf{r}), \eta^n(\mathbf{r}), \mathbf{r}\right), \ \mathbf{r} \in W^n \tag{2.30}$$

and

$$F^n(\mathbf{r}, j, k) = B_s\left(\Phi_s^{m_s[n]}(\mathbf{r})\right) + B_r^{(k)}\left(\Phi_r^{m_r[n]}(\mathbf{r})\right) + T(t_j - t^n(\mathbf{r})) - TL^n(\mathbf{r}), \ \mathbf{r} \in W^n \tag{2.31}$$

is the ambiguity function for pixel (j, k). Since the integration in Eq. 2.29 is over all of W^n, the ambiguity function sidelobe energy is included in the calculation of the pixel level. In Eq. 2.30, an estimated scattering strength function must be used since there is usually no *a priori* knowledge of the true function. The presence of $\mathbf{r}$ as one of the arguments of SS emphasizes that local variations due to changes in seafloor geology could be specified.

2.5 Reverberation Simulations

In this section, simulated reverberation is compared to actual reverberation first for monostatic source-receiver geometries at sites B' and C' in Sec. 2.5.1 and then for a bistatic geometry at site B' in Sec. 2.5.2. The number of beams is $K = 128$. I used $J = 350$ time bins of 200 msec in duration yielding time series 70 seconds long from the onset of pulse transmission, which was sufficient to capture all 1/2 CZ reverberation for all segments considered.

In any of these simulations, it is necessary that some scattering model be applied at the seafloor. Because I have no *a priori* knowledge of the actual scattering characteristics, I employ reasonable phenomenological scattering functions having the desirable property of showing an increase in backscatter with grazing angle. This serves to enhance the features in the simulated reverberation and leads to better agreement with the data. The use of such rough approximations to the actual scattering relationship enables one to incorporate, if only approximately, the universal role of the grazing angle in affecting observed energy levels.

Later, in the scattering analysis of Chapter 3, the *actual* dependence of scattering strength on grazing angle is extracted from the data using ARTIST.

2.5.1 Monostatic Reverberation at B' and C'

In the monostatic configuration, I first consider segment 436 in which the *Cory Chouest* was located 20 km East and 10 km South of B'. Figure 2-5 (a) is a rendering of the bathymetry in the vicinity; the location of segment 436 is indicated by the black circle at the center. The arrow is the orientation of the receiving array. The configuration is only quasi-monostatic in that although both the source and receiving arrays are towed by the *Cory*, their centers are separated by over 1 km. The other six circles shown in red represent the ship locations for other segments used for the backscattering analysis of Chapter 3.

ARTIST reveals that $M_s = M_r = 2$ and that the sets I_s^1 and I_r^1 contain direct paths to the seafloor while I_s^2 and I_r^2 contain mostly surface-reflected paths. The

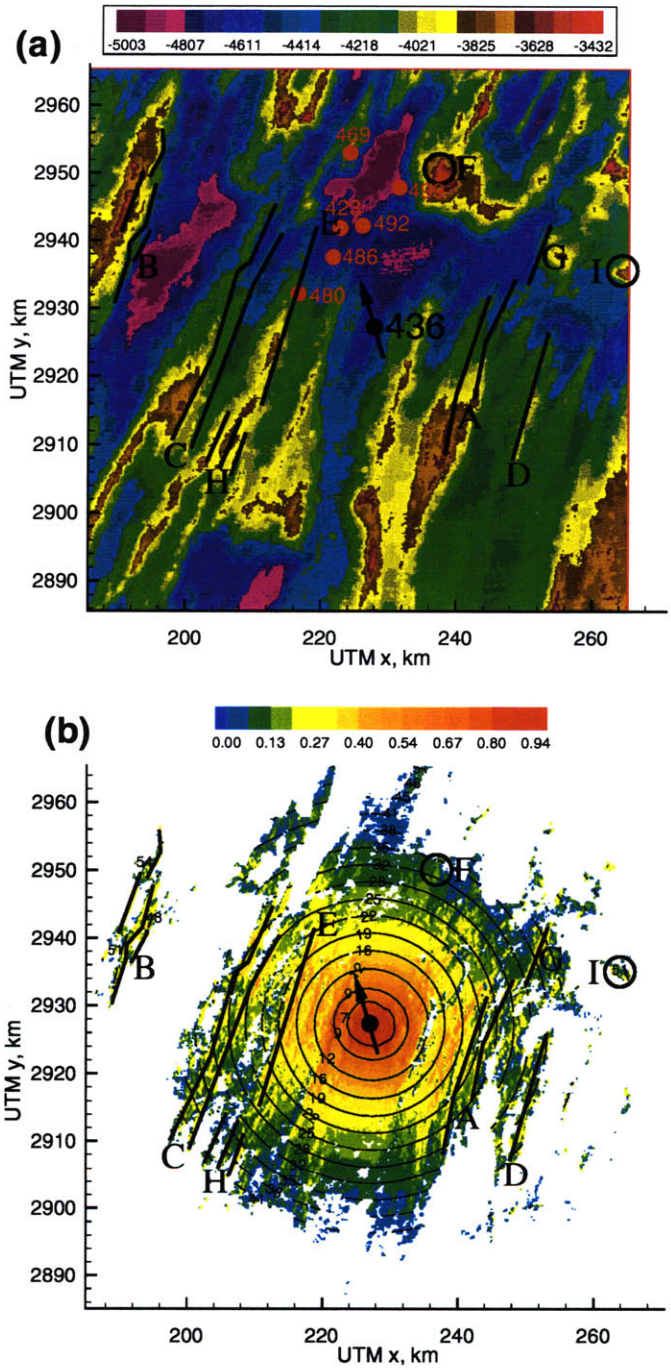

Figure 2-5: (a) Bathymetry in meters for monostatic segment 436, near site B'. The position of the *Cory* and the orientation of its receiving array are indicated by the black circle and arrow respectively. The six red dots represent the position of the *Cory* during the other experimental segments used in the scattering strength study. (b) Visualization of direct-path intersection pattern X^1, with color contours corresponding to $|\sin(\gamma_s^1(\mathbf{r}))|$, γ_s^1 being the grazing angle with respect to local bathymetry. The black contours represent $t^1(\mathbf{r})$, the two-way time delay in seconds.

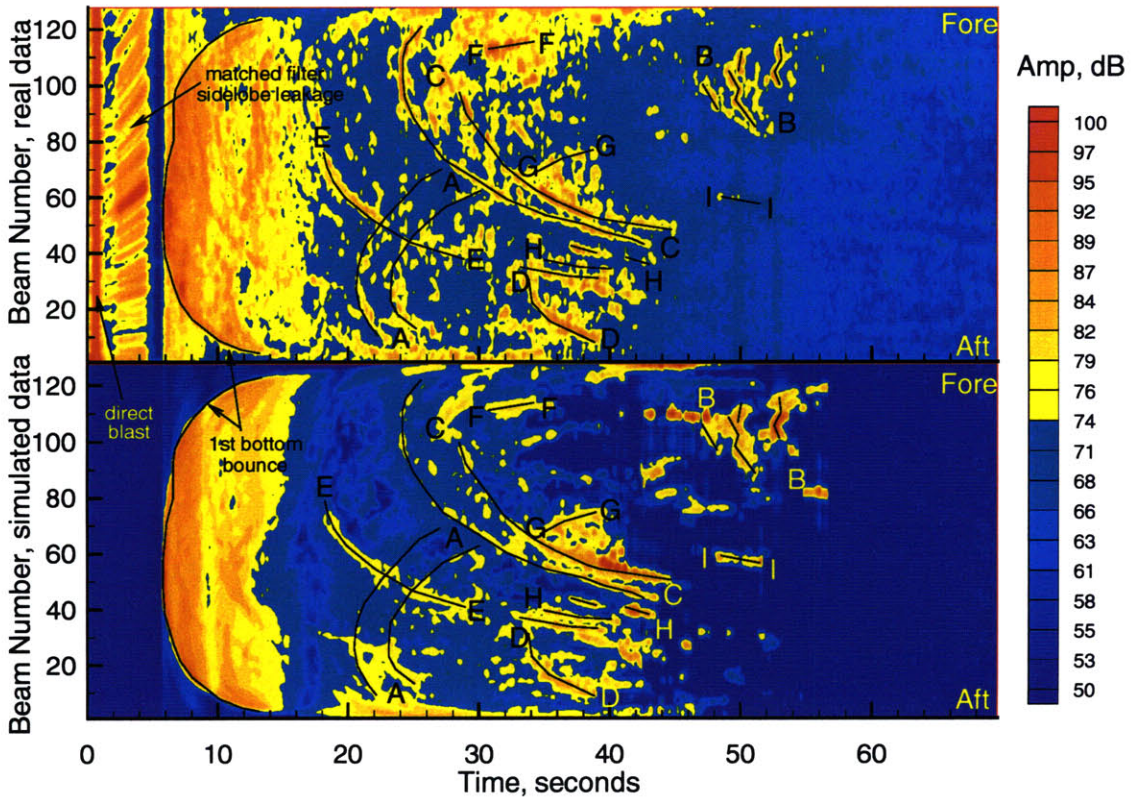

Figure 2-6: Actual (top) and simulated (bottom) data for segment 436. Labels A through I identify matching features. These labels are mirrored in Fig. 2-5 showing that the yellowish-orange lineations in the intersection pattern, corresponding to high grazing angles, are good predictors of hot spots in the reverberation.

insonification patterns will not be presented for the monostatic cases. I present only the first intersection pattern $X^1(\mathbf{r})$, which corresponds to the combination of the direct-path insonification pattern for both the source and the receiver, $m_s = 1$ and $m_r = 1$. In the monostatic configuration, little additional insight would be provided by presenting the insonification patterns or the other intersection patterns, although it will be seen that this is not the case for the bistatic geometry of Sec. 2.5.2.

In Fig. 2-5 (b), the colored area is W^1; the blank areas lie in shadow and are not accessible by rays. The black contours overlaid are isochrons representing $t^1(\mathbf{r})$,

and the color contours represent $|\sin(\gamma_s^1(\mathbf{r}))|$. This visualization of the intersection pattern provides considerable insight into the reverberation. Ridges surrounded by shadow or enhanced by an increased grazing angle are expected to lead to prominent features in the reverberation data.

Figure 2-6 shows real and synthetic data. The "real" data are the beamformed data averaged according to Eq. 3.12. The color corresponds to the amplitude of the averaged envelope in dB re 1 μPa as a function of time (horizontal axis) and beam number (vertical axis). The colormap, which has a discrete jump at 74 dB, was chosen to combine the event-selection feature of a threshold plot with the detailed rendering of structure at intermediate levels provided by a continuous colormap.

Those features which are well represented in both the simulated and the actual data are labeled A through I, and the corresponding seafloor areas in the intersection pattern and the bathymetry are marked using the same labels in (a) and (b). In relating features between Figs. 2-5 and 2-6, it is important to remember the right-left ambiguity associated with the receiving system. It explains why features A and E, which are on opposite sides of the *Cory*, intersect in the beam-time space of Fig. 2-6.

The phenomenological scattering relationship applied at the seafloor is Lambert's law,

$$SS = \mu + 10\log_{10}(\sin(|\gamma_s^n \gamma_r^n|)). \tag{2.32}$$

I emphasize that this relationship is not presumed to be correct, but a reasonable approximation [28] for the purpose of incorporating the effect of local grazing angles when no *a priori* information on the true scattering relationship exists.

As can be deduced from looking at Figures 2-6 and 2-5 (b), the most prominent reverberation events register with areas where local grazing angles are higher than 25 degrees. One of the principal objectives of the ARSRP experiment was to "... understand low grazing angle scattering." By "low grazing angle", one typically means angles between 0 and 15, perhaps 20 degrees. Interestingly, Figs. 2-5 and 2-6 show that such low grazing angles play a minor role in generating the loudest events

at 200 msec scales.

While the labeled features are self-explanatory in their agreement, areas where disagreement exists merit further discussion. The discrepancy between 0 and 5 seconds where the data show a red stripe extending across all beams followed by a yellow-orange band is associated with energy having propagated directly from the source to the receiver without interacting with the seafloor. The band corresponds to sidelobe leakage from the matched filter. From 6 to 10 seconds, considerably more beampattern sidelobe leakage is observed in the data than in the model. This discrepancy vanishes at higher ranges where the ray angles at the receiving array are closer to horizontal. The marked sidelobe leakage at early times is due to the high-amplitude vertical array deformations [14] which corrupt the beampattern for rays incident from directions away from horizontal. The effect of deformations was not included in the beampattern used by ARTIST.

Disagreements in hot spots before 20 seconds are generally associated with multiple seafloor bounce paths, which lead to reverberation of comparable magnitude to that from direct and surface-reflected paths at early times. Clearly, these areas are to be avoided in a study of backscattering strength versus grazing angle. Disagreements at early times also result from the unknown sidelobe structure of the transmitting array and the vertical deformations of the receiving array.

At late times near 1/2 CZ ($>$ 40 sec), smaller hot spots are difficult to predict reliably since their detection is highly sensitive to bathymetry at near-horizontal propagation directions.

At intermediate times, discrepancies are associated mainly with scattering phenomena. A good example is the beam-time space surrounding FF in Fig. 2-6. While ARTIST predicts the existence of returns in this beam-time area, levels above 74 dB are predicted only for feature F of Fig. 2-5 (a). On the other hand, the data show levels above 74 dB over a region 10 seconds long and 20 beams wide centered on FF. Based on Ref. [28], the coefficient of Lambert's law was chosen as -17 dB to provide the best match with all seafloor areas simultaneously. The observed discrepancy suggests that the scattering properties of the contributing seafloor around F differ

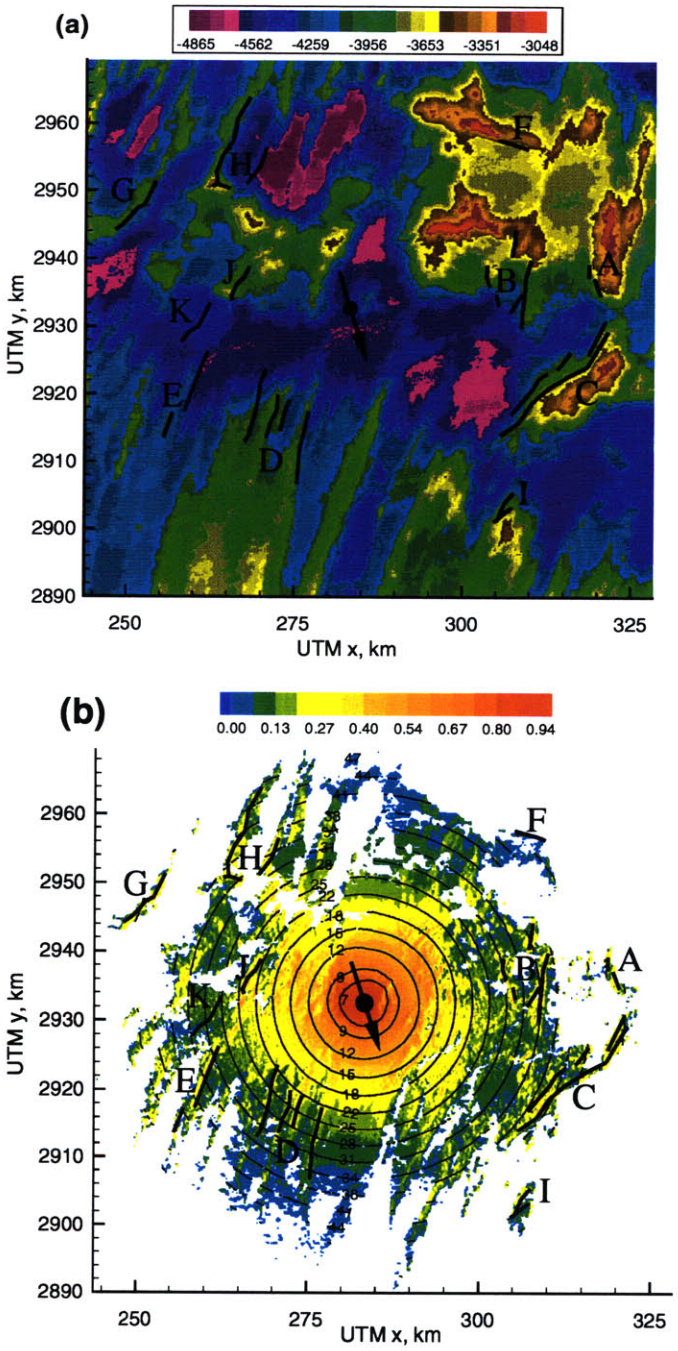

Figure 2-7: (a) Bathymetry in meters for monostatic segment 889, near site C'. The circle and arrow represent the position of the *Cory* and the orientation of its receiving array. (b) Visualization of direct path intersection pattern X^1, with color contours representing $|\sin(\gamma_s^1(\mathbf{r}))|$. The black contours represent the two-way time delay $t^1(\mathbf{r})$ in seconds.

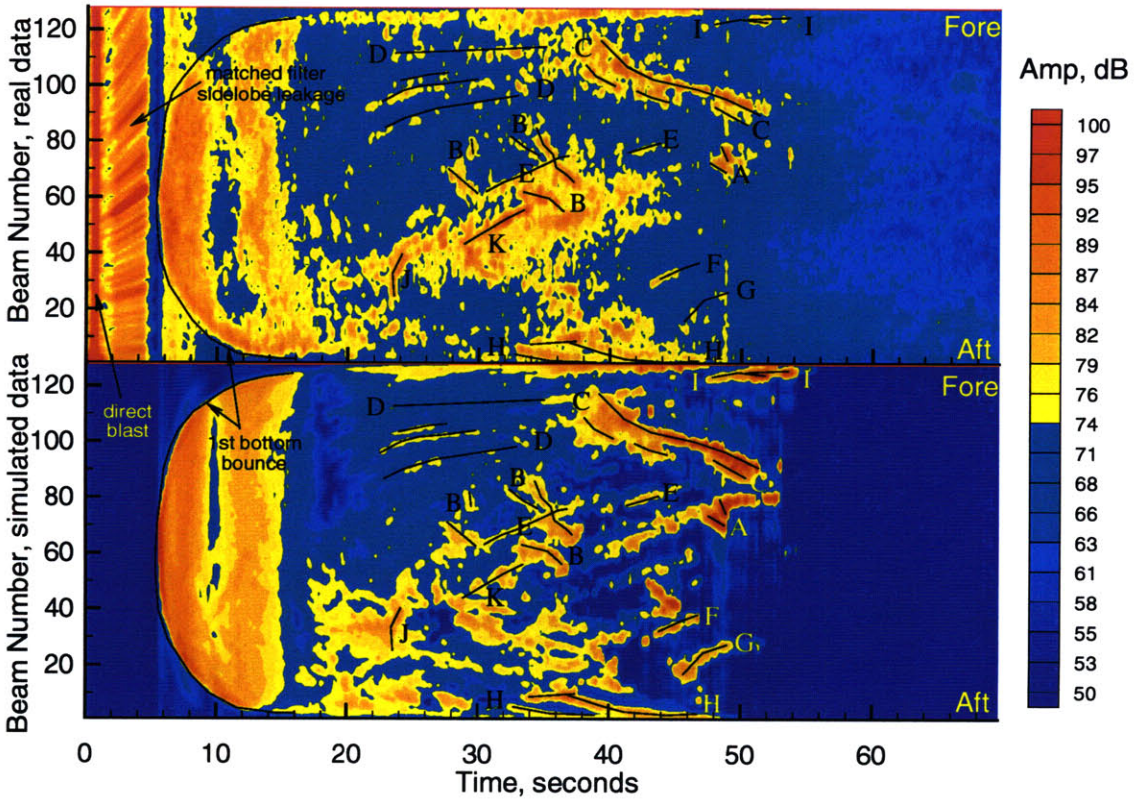

Figure 2-8: Actual (top) and simulated (bottom) data for segment 889 with labels A through K identifying matching features and mirrored in Fig. 2-7.

appreciably in the value of the Lambert's law coefficient and/or in the nature of the relationship of scattering strength to grazing angle.

The second example of reverberation simulation is segment 889 at site C'. The *Cory Chouest*'s position and orientation during segment 889 are shown in Fig. 2-7 (a). The feature C' itself is indicated by the letter C. Fig.2-7 (b) shows the quantity $\sin(\gamma_s^1(\mathbf{r}))$ in color overlaid on intersection pattern 1, highlighting the various ridges which are predicted to contribute strongly to the reverberation. Finally, Fig. 2-8 shows the actual and simulated data, with a number of correctly predicted features labeled A through K.

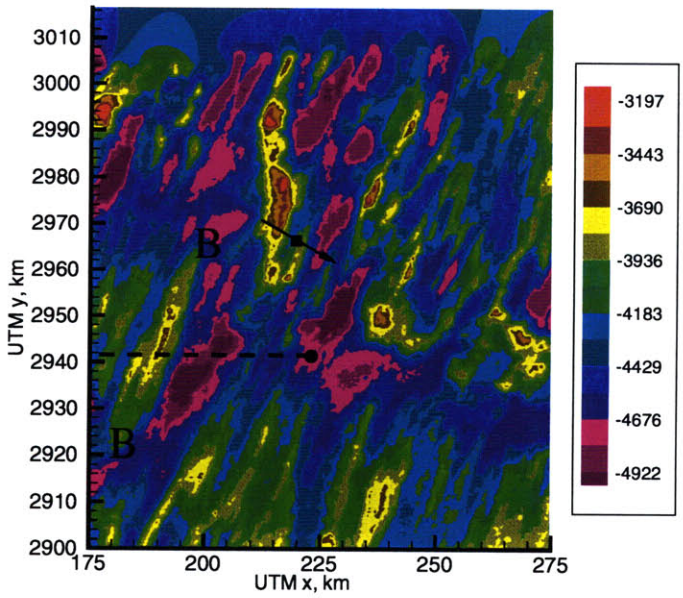

Figure 2-9: Bathymetry for bistatic configuration during segment 423, in meters. The *Cory* is represented by the circle. The position of the *Alliance* and the orientation of its receiving array are indicated by the square and arrow respectively. Feature BB corresponds to site B'.

2.5.2 Bistatic Reverberation Simulation at B'

In this section, I show bistatic reverberation data and modeling for segment 423. The source was on the *R/V Cory Chouest* about 35 km due East of B' and the receiver was on the *R/V Alliance*, located about 20 km North of the *Cory*. The *Cory*'s source is represented by the circle in Fig. 2-9 and the *Alliance*'s receiving array by a square. The source-receiver separation leads to distinct insonification patterns for the source and the receiver, as shown in Fig. 2-10.

As in the monostatic case, $M_s = M_r = 2$; I_s^1 and I_r^1 contain direct paths to the seafloor, and I_s^2 I_r^2 contain mostly surface-reflected paths. While the differences in source and receiver insonification patterns are expected due to physical separation, it is interesting that the insonification from surface-reflected paths should differ so significantly from the direct path insonification. The largest difference between direct and surface-reflected paths can be seen at the circumference of the plots, where the ray energy is going through the 1/2 CZ point and is propagating almost horizontally.

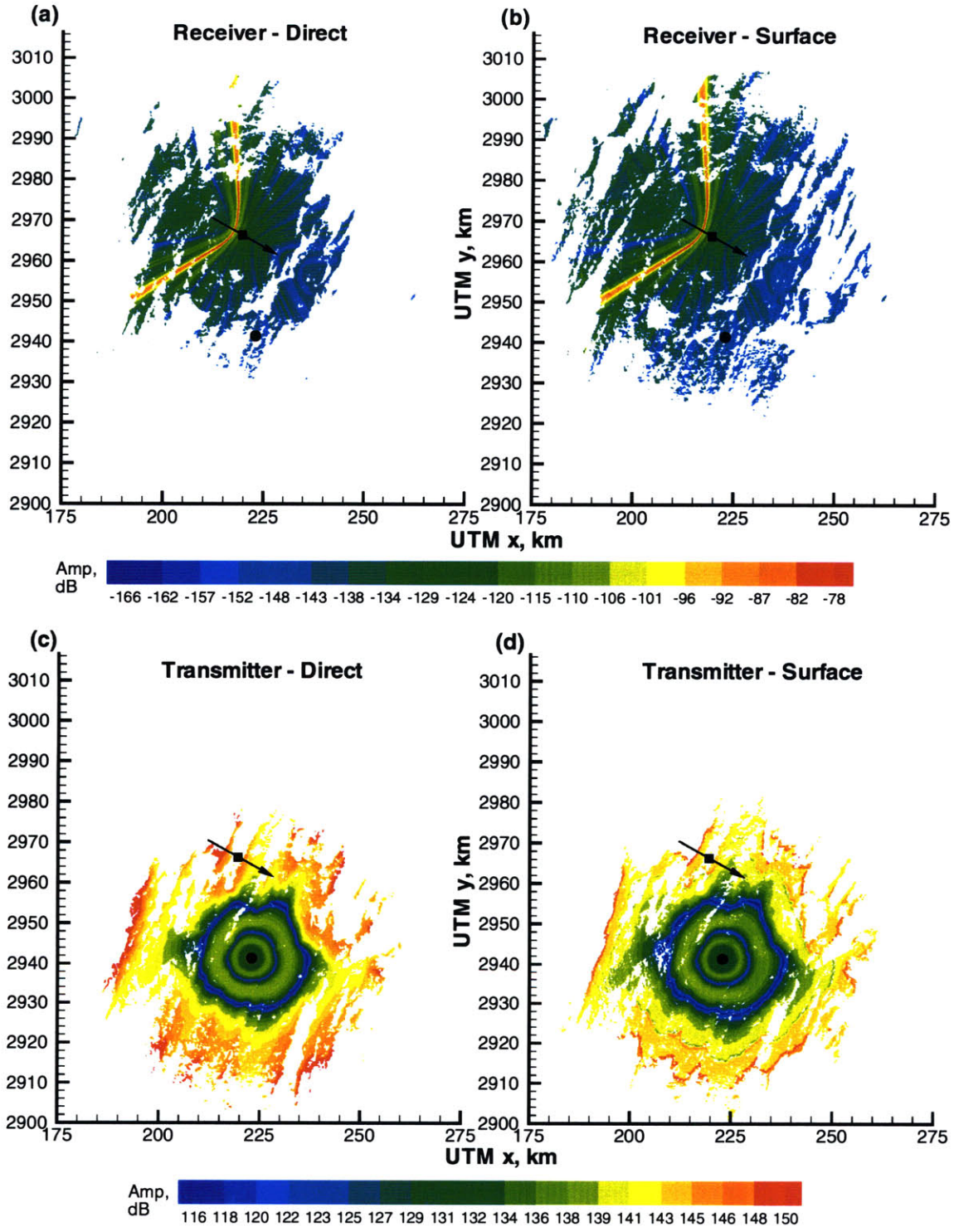

Figure 2-10: (a) Direct, I_r^1, and (b) surface-reflected, I_r^2, insonification patterns for the *Alliance* receiving array during segment 423. The color contours correspond to the sum of beampattern and TL for beam 30. In (c) and (d) I show direct I_s^1 and surface-reflected I_s^2 insonification patterns for the source array of the *Cory*.

Rays corresponding to the image contributions lie several hundred meters above their direct path counterparts and thus are likely to miss prominent bathymetric features and propagate farther.

The next step in the modeling consists in combining insonification patterns pairwise, taking one from the source and one from the receiver, into intersection patterns. Each combination represents one path from source to bottom to receiver. Figure 2-11 depicts all $N = 4$ intersection patterns.

The time contours represent the total travel time from the source to the seafloor to the receiver array, $t^n(\mathbf{r})$. The shape of these contours is nominally an ellipse, but deviations are especially evident in the earliest contour where the bathymetry, being of higher magnitude relative to range at small ranges, induces travel-time perturbations. The color represents the gain function

$$G^n(\mathbf{r}, k) = B_s\left(\Phi_s^{m_s[n]}(\mathbf{r})\right) + B_r^{(k)}\left(\Phi_r^{m_r[n]}(\mathbf{r})\right) - TL^n(\mathbf{r}),\ \mathbf{r} \in W^n \tag{2.33}$$

for beam number $k = 30$. The function G^n, in contrast to F^n in Eq. 2.31, excludes the pulse function $T(t)$. One can clearly distinguish the concentric contours centered around the *Cory Chouest* corresponding to the transmitting array's sidelobe structure, and the hyperbolic main lobe of beam 30 of the receiving array with focus at the *Alliance*. The contributions to the time series between times t and $t + \Delta t$ for beam 30 originate predominantly from seafloor lying on the red hyperbola between time contours t and $t + \Delta t$.

Depicted in Figure 2-12 (a) are the beamformed data collected by the *Alliance*. In Fig. 2-12 (b), I show synthetic data generated by ARTIST using only direct paths, that is, using only $n = 1$. In (c), both direct and surface-reflected paths are included, using all four possible intersection patterns. The immense bright spot labeled BB extending from 30 to 55 seconds and from beams 10 to 45 is caused by insonification of B', as can be confirmed by referring back to Fig. 2-11. There is a clear enhancement in the ability to model BB when surface-bounce paths are included. Enhancement is also observed in capturing the double ridge of AA and in reducing shadow zones

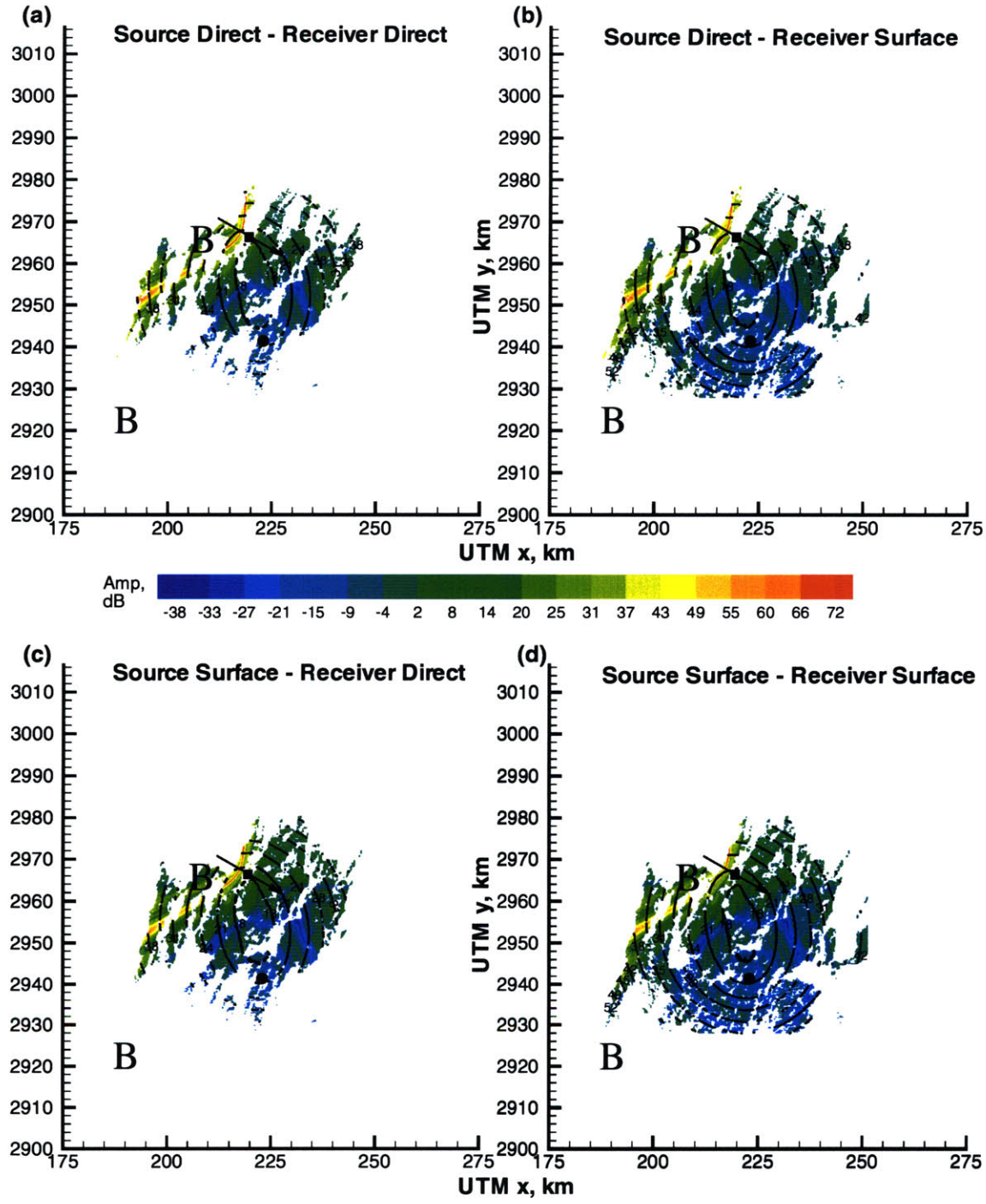

Figure 2-11: Intersection pattern visualization. (a) X^1, (b) X^2, (c) X^3, and (d) X^4. The color contour corresponds to total acoustic gain including both array beampatterns and two-way TL. The elliptical black contours represent two-way travel time $t^n(\mathbf{r})$ in seconds.

around CC and DD. Near DD, the surface-bounce prediction by ARTIST does not lead to sufficiently energetic returns to merit a bright color, but the light blue color indicates that the existence of a return is predicted. The fine-tuning of predicted energy levels would require an accurate knowledge of the dependence of scattering strength on grazing angle and variations in scattering behavior between different areas of the seafloor. Included in this local variation is the fact that some of the received energy comes from volume scattering *within* sediment ponds as opposed to scattering at the water-seafloor interface. Such detailed knowledge of local scattering physics is beyond the state of current research.

The greatest discrepancies between ARTIST simulations and actual data result from the effect of multiple seafloor bounces, which lead to reverberation of comparable magnitude to direct and surface-reflected paths during the first 10-15 seconds. Indeed, at feature EE, it is not known whether the disagreement between data and model is due to local scattering phenomena or paths having undergone multiple seafloor bounces. Such areas are to be avoided in a study of scattering strength.

2.6 Summary

The rigorous framework for propagation modeling and data structure manipulation embodied by ARTIST has been used to model reverberation in ARSRP. The concepts of insonification and intersection patterns have been shown to be useful tools both for visualizing the complex illumination of the seafloor and for data interpretation. I have shown that ARTIST is useful in capturing predominant reverberation features within 1/2 CZ in both bistatic and monostatic configurations. In this regard, the ability to account for surface bounce and source-receiver separation has been shown to be of significant value.

The disagreements between simulated and actual data are useful in suggesting that other mechanisms than those modeled by ARTIST are at play. Disagreements at early times are due to the fact that reverberation from multiple seafloor interaction paths is comparable to or higher in magnitude than that from direct and surface-

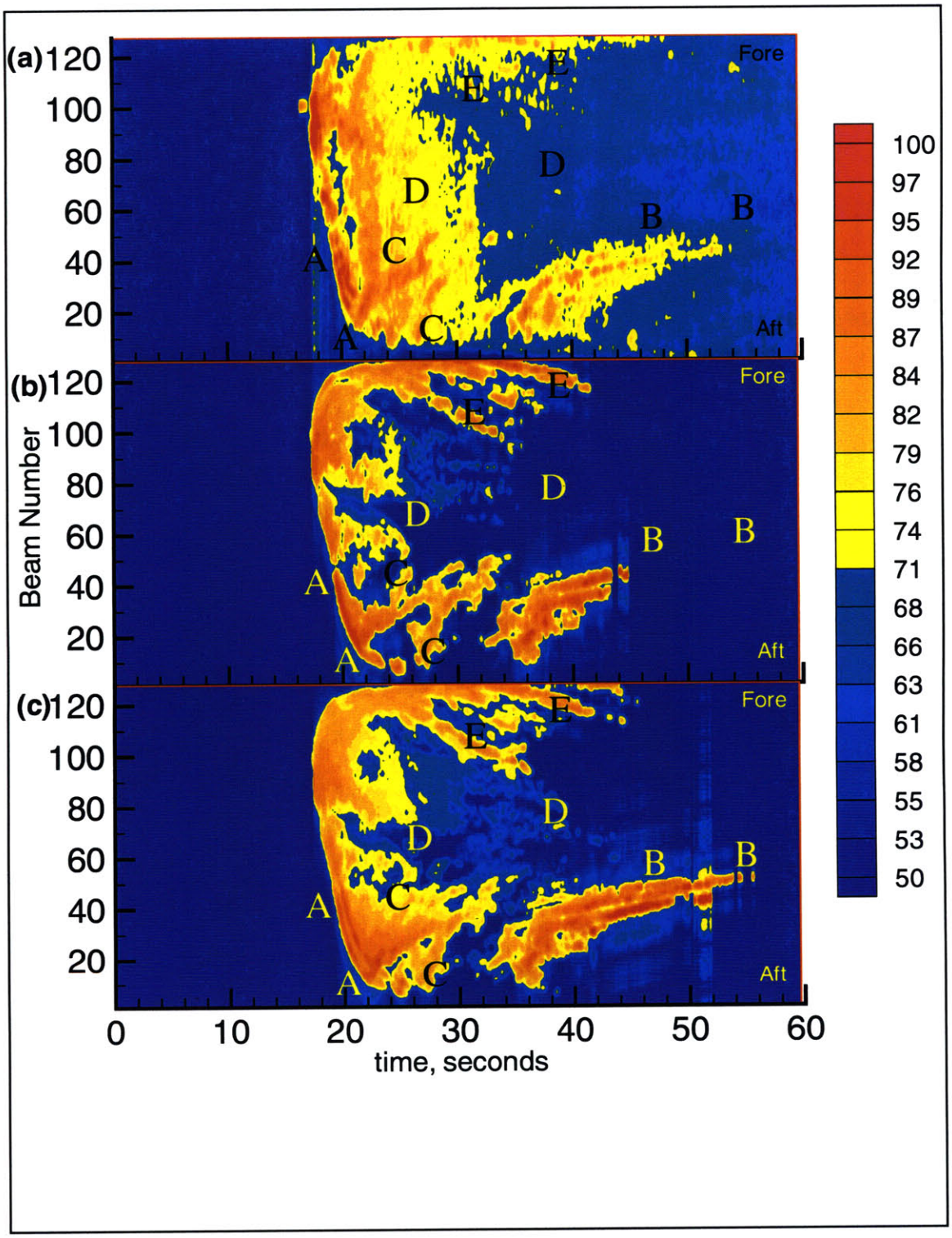

Figure 2-12: (a) Beamformed, match-filtered reverberation data collected at the *Alliance* during segment 423, averaged over 200 msec windows. (b) Synthetic data using only direct paths (X^1 only). (c) Synthetic data using both direct and surface-reflected paths (all X^n). Color contours are in dB re 1 μPa.

reflected paths. At late times, disagreements can be ascribed to uncertainties in the environment, and at intermediate times local scattering behavior can be the main cause of discrepancies between ARTIST simulations and data.

For those events in the reverberation simulations which *are* correctly modeled, such as feature B in Fig. 2-6 and Fig. 2-12, and feature C in Fig. 2-8 (c), one can conclude that the physics are adequately described by direct and surface-reflected ray paths. A more thorough analysis involving the extraction of the scattering strength of specific bathymetric features is then possible. Such an analysis is the subject of Chapter 3.

Chapter 3

Analysis of Backscatter From Site B'

The success of ARTIST in modeling the major features in the reverberation using direct and surface-bounce paths with a single bottom interaction indicates that for dominant events, scattering is taking place at isolated features insonified at clearly-defined grazing angles. This simple insonification picture opens the door to the next higher level in studying ARSRP data: the extraction of specific portions of data corresponding to selected bathymetric regions.

Previous studies of scattering in ARSRP include Ref. [28], in which Lambert's law coefficients μ were extracted at site A, shown on Fig. 2-1. One of the conclusions was that $\mu = -17dB$ provided the best fit to the entire ARSRP dataset, although values ranging from -10 to -20 dB were observed. More recently [22], the scattering behavior of site A was compared to that of crust 25 km to the north across a sediment pond, with an attempt to explain variations in backscattering strength by the seafloor dip distribution. The sites studied correspond to crust with distinct geological origin. It was concluded that seafloor dip distribution was insufficient in accounting for the observed differences in scattering behavior. Therefore, the differences were attributed to other factors such as fine-scale roughness.

In both of the above studies, the focus was on characterizing the global scattering properties of bathymetric features of order 10 km in diameter or larger. In contrast,

the scattering analysis presented here seeks to resolve scattering strength variations between different categories of seafloor *within* such a feature by making maximal use of available environmental data, resolving capabilities of the sonar system, and the unique capabilities of ARTIST. In particular, site B' is investigated, which is a highly anisotropic feature composed of steep, unsedimented scarps separated by flat, sedimented terraces. Using the full capabilities of ARTIST, a distinction in the scattering properties of scarps and terraces is sought by carefully "chiseling" out those portions in the reverberation data corresponding to individual scarps and terraces. The width of the geographical regions being resolved is as narrow as 500 m.

In Section 3.1, the ARTIST framework outlined in Section 2.4 is extended to the case of scattering data extraction. The extraction of scattering strength is discussed in Section 3.1.1, and the extraction of the log-envelope statistics is discussed in Section 3.1.2. In Section 3.2, I explore means specific to the ARSRP experiment to limit the errors in mapping portions of data to seafloor regions.

The scattering strength curves for scarps and terraces are presented in Section 3.3.1. This section also includes an investigation of the effect of the anisotropy of B' on backscattering strength, which is made possible by the wide range of azimuths relative to B' over the seven segments considered. Next, the full probability density functions (pdfs) of the backscattered waveforms are estimated for scarps and terraces in Section 3.4. As with scattering strength, the effect of scarp anisotropy is investigated. I also present density estimates for "noise" reverberation which cannot be ascribed to any portion of the bathymetry through a single bottom interaction.

Finally, the results are discussed in Section 3.5 and summarized in Section 3.6.

3.1 ARTIST Framework For Local Analysis of Scattering

3.1.1 Extraction of Scattering Strength

It is assumed that the data are pixels corresponding to average reverberation levels $RL(t_j, b_k)$ defined over the same time-beam grid as the simulated data $AL(t_j, b_k)$. The goal is to appropriately normalize the energy of pixels (j, k) to yield scattering strengths and to relate a single triad of angles $\gamma_s(j,k)$, $\gamma_r(j,k)$, and $\eta(j,k)$ to each pixel.

Normally, only a subset $\Lambda \subseteq \{(j,k) : j \in [1,2,\ldots,J],\ k \in [1,2,\ldots,K]\}$ of the available pixels contains information that can readily be used for scattering strength studies. Some pixels are dominated by paths having interacted several times with the bottom for which a single triad of angles and a localized seafloor area cannot be defined. The energy in some pixels may originate from portions of the seafloor not under study.

The first step in the scattering strength extraction is to explicitly define the set of pixels Λ that arises from single interactions of rays with seafloor lying within a bathymetric region of interest $\Omega \subseteq \mathcal{R}$. The usable set of pixels for scattering analysis is represented as the union of the usable pixels for each intersection pattern,

$$\Lambda = \bigcup_{n=1}^{N} \Lambda^n. \tag{3.1}$$

To find the Λ^n, let $j^n(\mathbf{r})$ and $k^n(\mathbf{r})$ be index functions which identify a unique pixel in the data as being dominantly contributed to by seafloor location $\mathbf{r}$ within W^n:

$$(j^n(\mathbf{r}), k^n(\mathbf{r})) = \arg \max_{j \in \{1,2,\ldots,J\},\ k \in \{1,2,\ldots,K\}} F^n(\mathbf{r}, j, k),\ \mathbf{r} \in W^n. \tag{3.2}$$

Letting the sonar footprint for time t_j and beam b_k be denoted by $Z^n_{j,k} \subseteq \mathcal{R}^2$, the

usable set of pixels for intersection pattern n is given by

$$\Lambda^n = \{(j^n(\mathbf{r}), k^n(\mathbf{r})) : Z^n_{j^n(\mathbf{r}),k^n(\mathbf{r})} \subseteq \Omega,\ \mathbf{r} \in W^n \bigcap \Omega\}. \tag{3.3}$$

Note that in Equ. 3.3, I require that the footprint lie entirely within the region of interest Ω. This is to prevent the possibility of contamination of the scattering strength estimates by contributions from outside Ω. This is especially relevant if the ambiguity function is near its maximum at distinct seafloor locations far from each other, which occurs, for example, in the case of a horizontal line array receiver. This type of array possesses a right-left ambiguity such that illuminated seafloor on opposite sides of the ship is insonified with comparable energy. The sonar footprint is defined explicitly for each pixel as

$$Z^n_{j,k} = \{\mathbf{r} \in W^n : F^n(\mathbf{r}, j, k) \geq F^{\max}(j, k) - TH\}, \tag{3.4}$$

where TH is a chosen threshold below the maximum value of the ambiguity function, given by

$$F^{\max}(j, k) = \max_{\mathbf{r} \in W^n,\ n \in [1,2,\ldots,N]} F^n(\mathbf{r}, j, k). \tag{3.5}$$

Note that this definition of footprint is more than just an area term; it specifies the actual physical seafloor locations as well. The scattering strength is then calculated using

$$SS(j, k) = RL(t_j, b_k) - 10\log_{10}\left[\sum_{n\ :\ (j,k) \in \Lambda^n} \int_{W^n} H^n_{j,k}(\mathbf{r}')d\mathbf{r}'\right],\ (j, k) \in \Lambda \tag{3.6}$$

where the function $H^n_{j,k}(\mathbf{r})$ is defined as

$$H^n_{j,k}(\mathbf{r}) = \begin{cases} 10^{F^n(\mathbf{r},j,k)/10} & \mathbf{r} \in Z^n_{j,k} \\ 0 & \text{otherwise.} \end{cases} \tag{3.7}$$

Defining the operator $\Upsilon_{j,k}$ as

$$\Upsilon_{j,k} \cdot f(\mathbf{r}) \equiv \sum_{n \,:\, (j,k) \,\in\, \Lambda^n} \int_{W^n} f(\mathbf{r}')d\mathbf{r}', \tag{3.8}$$

the grazing and bistatic angles are then computed as weighted averages over the selected areas and insonification patterns:

$$\gamma_s(j,k) = \frac{\Upsilon_{j,k} \cdot \left[H^n_{j,k}(\mathbf{r})\gamma^n_s(\mathbf{r})\right]}{\Upsilon_{j,k} \cdot H^n_{j,k}(\mathbf{r})}, \tag{3.9}$$

$$\gamma_r(j,k) = \frac{\Upsilon_{j,k} \cdot \left[H^n_{j,k}(\mathbf{r})\gamma^n_r(\mathbf{r})\right]}{\Upsilon_{j,k} \cdot H^n_{j,k}(\mathbf{r})}, \tag{3.10}$$

and

$$\eta(j,k) = \frac{\Upsilon_{j,k} \cdot H^n_{j,k}(\mathbf{r})\eta^n(\mathbf{r}')}{\Upsilon_{j,k} \cdot H^n_{j,k}(\mathbf{r})}. \tag{3.11}$$

The formulation presented here avoids the explicit specification of a footprint area; it is calculated for each pixel based on the threshold parameter TH and the full ambiguity function. In practice, this formulation is only feasible when the bathymetry is sampled at a higher rate than the Nyquist rate of the ambiguity function. In the case of ARSRP, the 200 m bathymetric resolution is sufficient to sample the cross-range variation in the ambiguity function caused by the receiver beampattern, but it is far from sufficient in capturing the $O(10\text{ m})$ variations in range modulating the match-filtered pulse.

In order to stabilize the scattering strength estimates, I average the data over a time window Δt large enough to yield a range resolution on the order of the 200 m lateral resolution of the bathymetry; I use $\Delta t = 200$ msec, which yields a spatial extent of about 150 m. Supposing that the complex received time series for beam k

is given by $r(t,k)$, the pixel energies are then calculated according to

$$RL(t_j, b_k) = 10\log_{10}\left[\frac{1}{\Delta t}\int_{t_j-\Delta t/2}^{t_j+\Delta t/2} |r(t,k)|^2 dt\right]. \tag{3.12}$$

The pulse shape to use in the ambiguity function in Eq. 2.31 is therefore the boxcar

$$T(t) = \begin{cases} 1 & -\Delta t/2 \le t < \Delta t/2 \\ 0 & \text{otherwise.} \end{cases} \quad y \tag{3.13}$$

The grazing and bistatic angles are then calculated as before using Eqs. 3.9, 3.10, and 3.11 but the scattering strength calculation of Eq. 3.6 becomes

$$SS(j,k) = RL(t_j, b_k) - 10\log_{10}\left[\Upsilon \cdot H^n_{j,k}(\mathbf{r})\right] - 10\log_{10}\left[\frac{\Delta t_p}{\Delta t}\right], (j,k) \in \Lambda \tag{3.14}$$

where Δt_p is the null-to-null match-filtered pulse resolution of 35 msec.

In the case where $|r(t,k)|$ in Eq. 3.12 is Rayleigh distributed, it can be shown [42] that the log-transformed variable RL has a mean which depends on the mean intensity $\overline{|r(t,k)|^2}$ and on the number of degrees of freedom μ in the average through the relation

$$\overline{RL} = 10\log(\overline{|r(t,k)|^2}) + F(\mu). \tag{3.15}$$

At a minimum of 1 degree of freedom ($\mu = 1$), $F(\mu) = 2.5$ dB; the log-transformed variable has a 2.5 dB augmentative bias compared to the log of the mean intensity. As μ increases, this bias tends to zero. In the processing of the data in this thesis for scattering strength analysis, 200 msec pixels are used containing about 10 pulse widths. Equation 3.12 therefore averages over about $\mu = 10$ degrees of freedom, yielding a negligible bias of about 0.2 dB [42].

The log-transformed variable has a standard deviation which depends only on the number of degrees of freedom. At $\mu = 1$ this value is 5.6 dB. The standard deviation decreases as μ increases. At $\mu = 10$, the standard deviation is approximately 1.4 dB.

While this poses a fundamental resolution limit on estimates of logarithmic quantities such as scattering strength using a *single* pixel $RL(t_j, b_k)$, the error on estimates of mean scattering strength can be made arbitrarily small by averaging over sufficiently many pixels.

3.1.2 Extraction of Log-Envelope pdfs

From Eq.3.12, each data pixel used in the scattering analyses is an average over 200 msec of the actual received envelopes. I define $r^*_{j,k}(t)$ to be the portion of the high-resolution envelope for beam k that lies between $t_j - \Delta t/2$ and $t_j + \Delta t/2$. Thus, in addition to grazing and bistatic angles, footprint physical locations $Z^n_{j,k}$ and normalization energy, each data pixel (j, k) is related to a high-resolution time subseries of 200 msec duration containing about six null-to-null pulse widths or ten 3 dB pulse widths. The extraction of scattering strength in Section 3.1.1 concerns the average values of each of the $r^*_{j,k}(t)$. I now seek to statistically characterize the fluctuations of the $r^*_{j,k}(t)$ within each 200 msec window.

A convenient way to characterize the fluctuations is through the use of histograms of the envelopes $r^*_{j,k}(t)$. Histograms are estimates of the complete one-point probability distribution function (pdf) of r, including all moments. They do not provide any information regarding the N-point joint pdfs of r for $N > 1$. These N-point joint pdfs will not be studied in this thesis.

Since the mean has already been discussed in the form of scattering strengths, it is removed from each time subseries so that only the higher moments are studied. I define $r_{j,k}$ to be the mean-corrected versions of the high-resolution subseries:

$$r_{j,k}(t) = r^*_{j,k}(t) - RL(j, k). \tag{3.16}$$

The question arises as to whether this mean subtraction affects the statistics. The number of pulse widths which lie within a processing window Δt defines the maximum number of independent observations of the underlying statistical process for each window. When this number is sufficiently large, the zero-mean operation in Eq. 3.16

does not alter the density of the process. In the current application, there are 10 pulse widths per processing window and the subtraction of the mean has a significant effect on the statistics. The effect has been characterized in the case where $r(t)$ is a log-Rayleigh process in Appendix B.

Before proceeding to the presentation of the scattering strengths and time-domain statistics for the ARSRP scenario, two key concerns are addressed (i) the effect of uncertainties in the environment, and (ii) the avoidance of seafloor areas where the direct and surface-bounce paths interfere coherently.

3.2 Issues in Local Scattering Analysis

3.2.1 Uncertainties in the Environment

The degree of agreement between the prominent features in the simulated and actual data is degraded by uncertainties in the environment. Careful treatment is necessary to prevent this degradation from inducing large errors into the scattering strength estimates.

Hot spots in the simulation are sometimes off by a few time indices or beam numbers. For example, feature BB in Fig. 2-6 does not have exactly the same outline in the actual and simulated data. The set Λ of pixels that would be selected by ARTIST in the scattering strength extraction phase is roughly those pixels which are yellow, orange or red. If a selected pixel does not in fact lie on a *data* hot spot, an abnormally low value of scattering strength is deduced. To avoid selecting these shadow zone pixels, a minimum threshold TH^* is applied to the data. Pixels lying below this level are not considered in the analysis. The threshold is set by considering the average reverberation levels at similar times along beams which are known to lie in shadow, for example beams 60-70 between 45 and 55 seconds in Fig. 2-6. Fortunately, it is always possible to find such shadow zone data in the analysis of B', therefore TH^* can always be defined.

3.2.2 Resolved or Unresolved Direct and Surface-reflected Paths

Were infinite-duration CW signals to be used, the direct and surface-reflected paths would interfere with one another at all points in the water column and lead to a Lloyd mirror TL pattern. At the other extreme, were a delta function signal to be employed, direct and surface-reflected arrivals would be temporally separated everywhere except along isolated singular surfaces, and a separate TL value would be experienced for each arrival. Clearly, the LFM pulse used in ARSRP lies between these two exteremes in that direct and surface-reflected arrivals are resolved or temporally separated over some portion of the water column, and are unresolved or temporally overlapping over the remaining portions. Over the resolved portions, the average energy in a window large enough to include both arrivals is given by the sum of the energies in each separate arrival. Over the unresolved portions, the two arrivals interfere coherently and the Lloyd mirror effect is experienced. Applying the Lloyd mirror pattern in the resolved region or an incoherent sum in the unresolved region could introduce significant errors in the evaluation of TL.

In Ref. [22], TL for the site A experiments was estimated at all points by applying a monochromatic Lloyd mirror pattern that explicitly included the 5 degree downward steering of the source, and then performing an incoherent average over bandwidth. The importance of the correct treatment of the surface contribution is reduced because the downward source steering significantly attenuates this path. The surface contribution for the site B' experiments analyzed here is not negligible since the source beampattern was steered to broadside. This requires that careful be paid to the summation of energy over the two paths. Either the correct amplitudes must be determined, or those portions of the seafloor where a coherent interaction takes place must be identified and excluded. Here, I choose the latter since the TL estimates obtained by ARTIST are only valid when direct and surface-reflected paths interfere incoherently.

In Ref. [58], wideband PE simulations were used to simulate the incident energy at

B' and it was suggested that an interference between direct and surface-reflected paths existed, however the ranges at which this effect became important was not specified. To determine these, I determine the minimum acceptable time delay between two pulses such that an incoherent sum is within 1 dB of the wideband coherent sum. The seafloor locations to exclude are then identified as those where surface and direct rays arrive within the minimum acceptable time delay.

Figure 2-3 depicts the pulse used in the ARSRP experiments. Figure 3-1 (a) shows direct and surface bounce arrivals combined coherently for three values of delay: 80 msec (black), 15 msec (blue), and 5 msec (red). At very low delay, the opposite sign of the arrival from the pressure-release surface begins to cancel out the direct arrival and a stark reduction in amplitude is visible. At the larger values of delay, one observes two separate arrivals which don't interfere with each other.

Figure 3-1 (b) shows the error in incoherently versus coherently computing the average energy over a 1 sec window as a function of time delay between direct and surface arrivals of equal amplitude. The two horizontal lines correspond to a ± 1 dB contour. From the figure, the smallest acceptable time delay to maintain a 1 dB error in the incoherent energy calculation is about 15 msec. If the amplitudes of the two pulses were not equal (which is usually the case), the minimum time delay would be reduced further as the ability of the weaker pulse to attenuate the stronger pulse would be diminished. This would increase ARTIST's region of validity.

The time delay between direct and surface arrivals generally decreases with range. The seafloor below a source at a depth of 150 m receives direct and surface bounce contributions which are separated by about 200 msec, or ten times the 3-dB width of the match-filtered pulse. At the edge of 1/2 CZ, the direct and surface arrivals are simultaneous. Thus, seafloor portions to exclude lie beyond some critical range.

Fig. 3-2 (a) depicts the function $t - R/c_0$ as a function of range R, where c_0 is a nominal value of sound speed (1500 m/sec). The variable t is the ray time delay from source to seafloor for segment 423 along a transect extending directly West from the *Cory Chouest*, as indicated by the dashed line in Fig. 2-9.

Beyond a range of about 30 km, the time separation between the two eigenrays

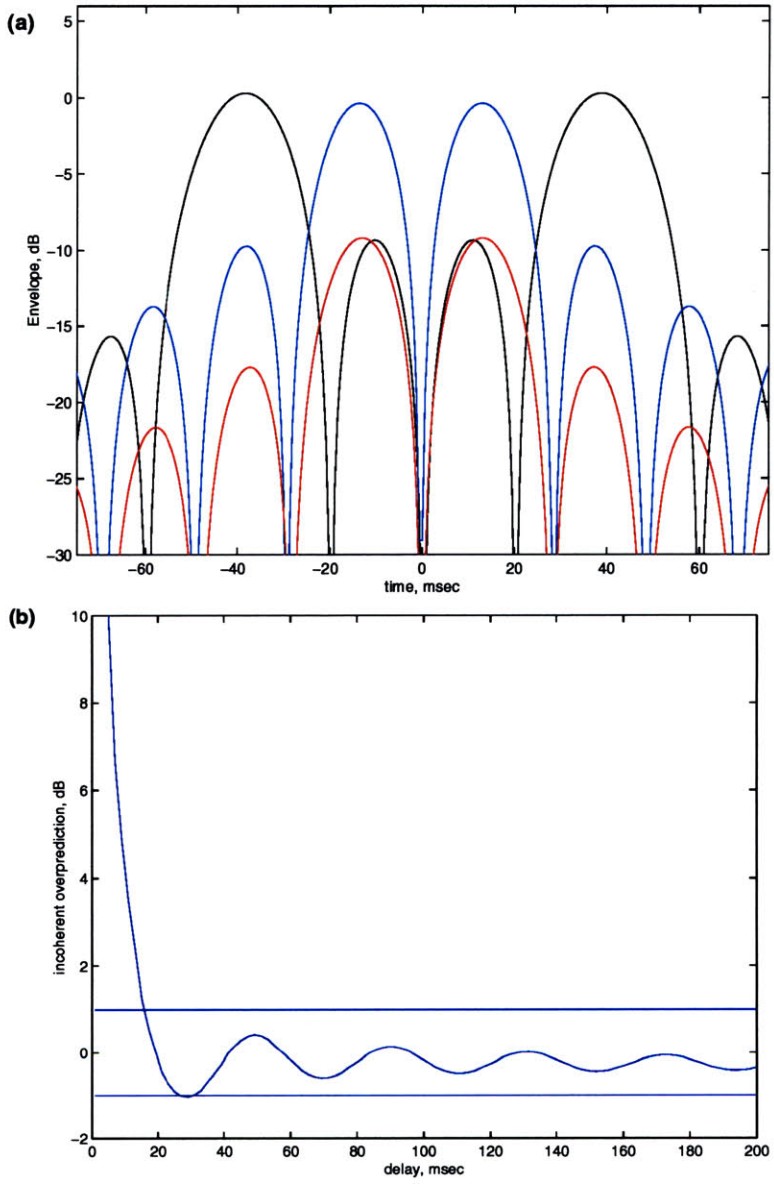

Figure 3-1: (a) Coherent combinations of direct and surface-bounce arrivals for 80 msec (black), 15 msec (blue), and 5 msec (red) delays. (b) Error associated with incoherently versus coherently combining direct and surface-bounce arrivals as a function of the time delay between them. The parallel lines delimit the $\pm$ 1 dB error region. The lower limit of time delay to maintain a 1 dB error is 15 msec.

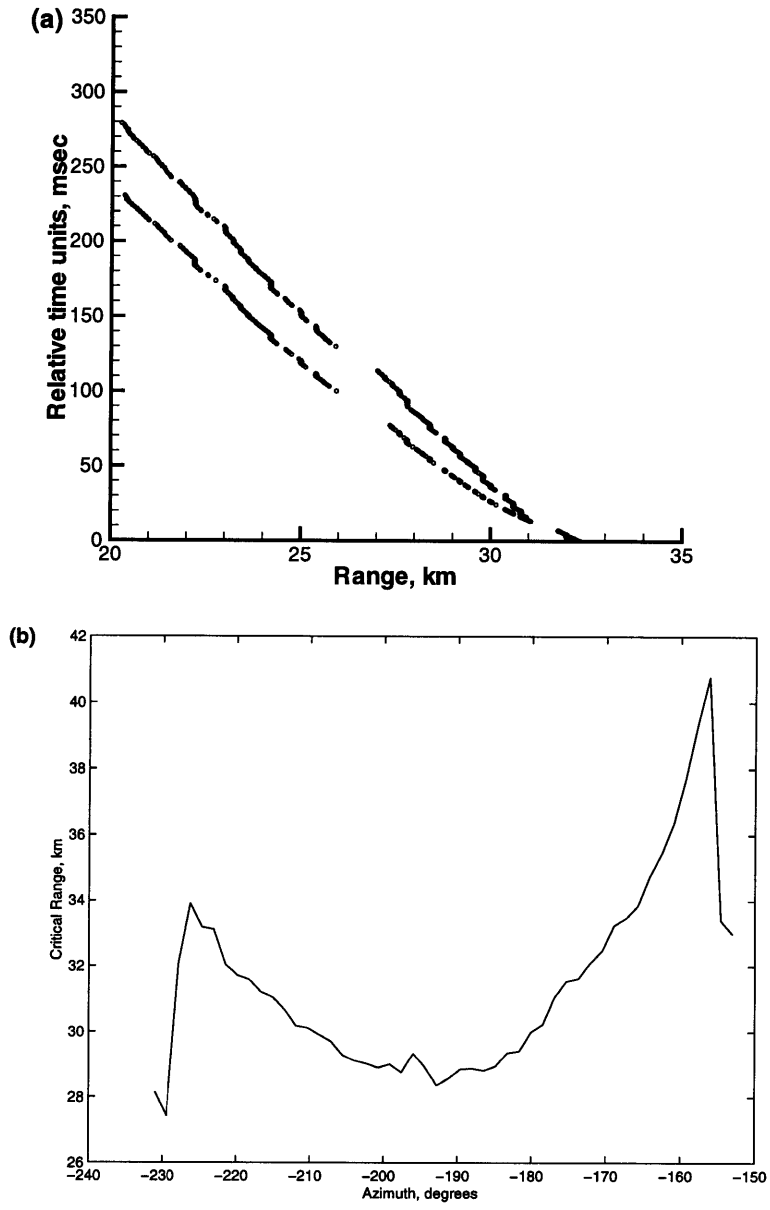

Figure 3-2: (a) The function $t - R/c_0$ as a function of range for a ray trace from the *Cory* along the dashed line of Fig 2-9 (segment 423). t is the travel time, R is the range in km, and c_0 is a nominal value of sound speed, set to 1500 m/sec. The top line of ray contacts has undergone a surface bounce, while the bottom one has not. The range at which the time delay between the two rays falls below 15 msec (critical range) is approximately 30 km. (b) Critical range as a function of azimuth θ for the *Cory* during segment 423. The case in (a) corresponds to $\theta = -180°$.

falls below 15 msec. The incoherent summation is no longer valid and the portion of the data corresponding to those ranges should be neglected in the scattering analysis. This affects a small subset of the data; of the 32 km of seafloor which are insonified along this azimuth, only the last 2 km are unavailable for incoherent processing. The decision to keep or throw away data points for further analysis must be made at each azimuth, and for each source-receiver geometry. Fig. 3-2 (b) shows the critical range as a function of azimuth for the *Cory Chouest* during segment 423.

A benefit of eliminating seafloor areas where coherent interaction occurs is that these are usually those where caustics are encountered; by neglecting such areas, ray calculations are kept simple. It is understood that caustics can be important practically, but they are a propagation phenomenon and therefore are not the focus of this scattering study.

3.3 Presentation and Analysis of Backscatter

Focusing on monostatic configurations at site B', I explore (i) variations in backscattering strength between scarps and terraces, and (ii) the effect of seafloor anisotropy for scarps. The data are extracted using ARTIST and the seven segments depicted in Fig. 2-5 (a). The segments insonify B' from different angles and at different ranges.

Based on Refs. [68], [67], and [18], I define scarps and terraces as follows. The sketch of Fig. 3-3 may be useful.

Scarp (blue) These seafloor areas are steep and lightly sedimented. They feature an eroded surface of exposed basalt cut by cross-scarp canyons which are 100-200 m wide and 30-50 m deep on average. These large canyons are in turn intersected by smaller scarp-parallel canyons 10-30 m wide and as deep as 10-20 m. The rough features on these scarps range in scale from centimeters to tens of meters.

Terrace (green) Mostly flat seafloor lying at the base of scarps or between scarps. Such areas are erratic in terms of roughness. Referring to Fig. 3-3, there is

talus near the base of a scarp, consisting of piles of loose basalt ranging from tens of centimeters to tens of meters in size. The central area of the terrace is heavily sedimented ($\simeq$ 25 m thick), with little exposed basalt. Finally, if there is a subsequent scarp, the area near the tip of the next scarp is exposed basalt.

Other (red) Seafloor which does not fit neatly into either of the two categories above and which may contain some of the characteristics of both. For example, slump blocks are segments of scarp which have detached from from rest of the scarp. While similar to scarps in their composition, they tend to be much more sedimented, hence also similar to terrace seafloor.

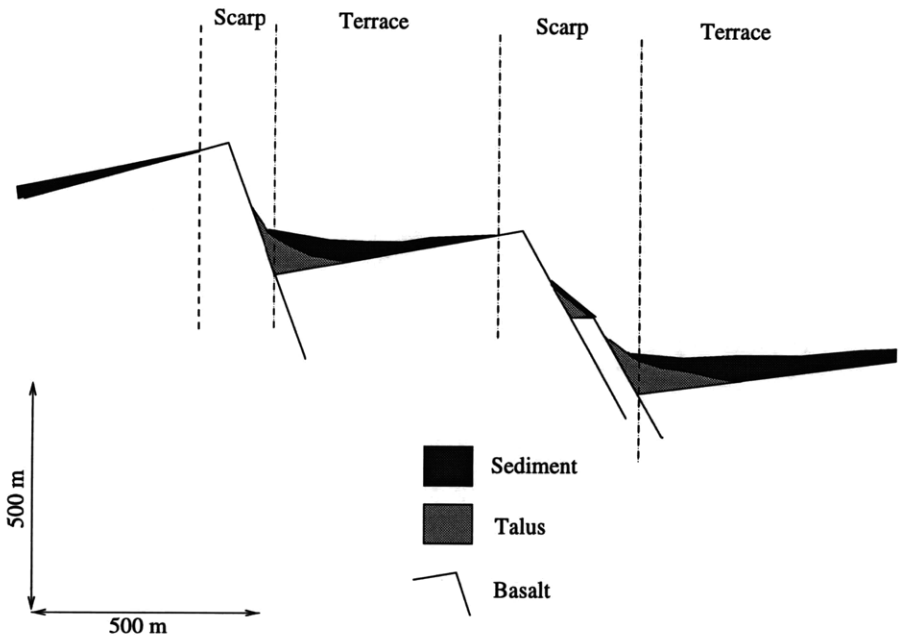

Figure 3-3: Sketch of the cross-section of B', showing the alternating scarp-terrace structure. The upper portions of the scarps are bare basalt while the lower portions are talus. The terraces, extending from the base of one scarp to the tip of the next, are heavily sedimented in the central portions but range from talus at one end to bare basalt at the other.

The backscattering analysis requires a detailed geographical delimitation of all areas on B' and their classification into one of the three categories. This is achieved using the color-coded polygons Ω_i shown in the three-dimensional view of B' in Fig. 3-4. Each Ω_i is analogous to the region of interest Ω in the scattering strength extraction

description of Sec. 3.1.1. Corresponding to each Ω_i is a set of pixels Λ_i in the reverberation data; thus, pixels are readily sorted into one of the three seafloor types and separate scattering strength curves can be obtained for each type.

3.3.1 Backscattering Strength for Three Seafloor Classes at B'

Armed with the knowledge of which data pixels and seafloor areas to avoid for each segment, a detailed backscattering analysis is possible. I perform ARTIST runs on all seven of the segments depicted on Fig. 2-5 (a) and establish a mapping between 200 msec reverberation data pixels and their normalization energy levels and grazing angles as described in the last part of Sec. 3.1.1. On Fig. 3-5 each dot corresponds to one of the selected pixels in one of the segments and is color-coded with its corresponding segment. The position of a dot co-incides with the peak of its corresponding ambiguity function $F_{\#}^{\max}(j,k)$, where (j,k) is the selected pixel and # is the segment number. The same polygons Ω_i as in Fig. 3-4 are overlaid on Fig. 3-5 so that the reader may identify the three-dimensional appearance of the seafloor features that each segment insonifies.

Using data from all seven segments, backscattering strength curves are estimated separately for the three seafloor classes. The results are shown on Fig. 3-6. I emphasize that each grazing angle is computed as the minimum angle between the incident ray direction and the best-fit plane at the point of contact of the ray with the 200-m resolution Hydrosweep bathymetry. The grazing angles are *not* computed with respect to a horizontal seafloor, and they are *not* merely vertical angles.

For grazing angles below 15 degrees, the blue curve, corresponding to scarp seafloor, lies 3-4 dB below the green curve for terrace seafloor. In this regime, other seafloor, shown in red, exhibits a behavior which lies in between scarp and terrace seafloor. Starting at around 20 degrees, all three curves converge.

In the case of scarp seafloor, the highest grazing angle contributions come from the steepest parts of the scarps, high enough above the terraces to lie above the

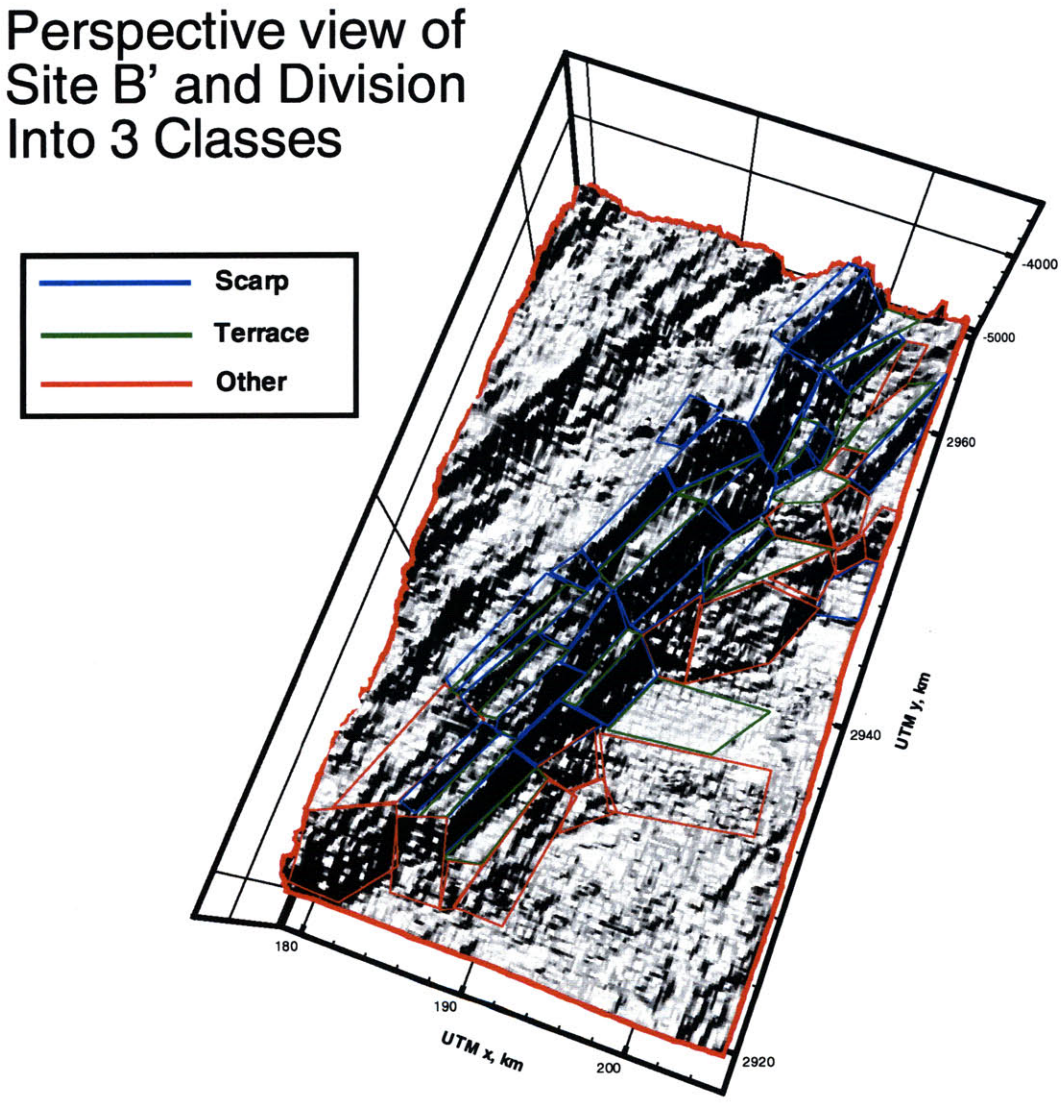

Figure 3-4: Three-dimensional view of the bathymetry at B', with overlaid color-coded polygons classifying each region into one of three seafloor types. The illumination for the shading is from the northwest; the scarps and terraces are easily distinguishable in this view.

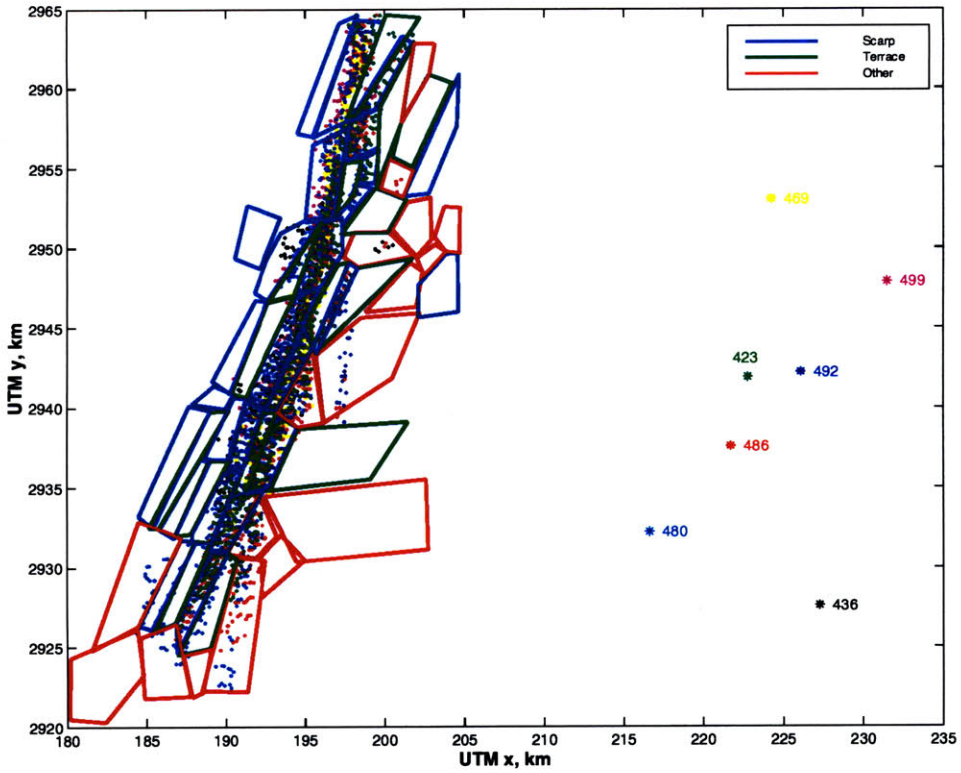

Figure 3-5: The positions of the seven segments used in the scattering analysis are indicated by the colored * symbols. Each dot corresponds to a selected pixel in the received data of one of the segments and is color-coded according to its segment. The polygons of Fig. 3-4 are overlaid.

start of talus slopes (see Fig. 3-3). The lowest grazing angles come mostly from the tops of the scarps, which are composed of relatively smooth exposed basalt. The middle grazing angle region comes mostly from the bases of the scarps where talus has accumulated and formed a less steeply-sloping bottom. This talus extends into the terrace seafloor, and so the middle grazing angle range for terrace seafloor also comes from talus, explaining the match in backscattering strengths between scarps and terraces in this regime.

The lower grazing angle contributions for the terrace curves generally come from the central portion of the terraces which are heavily sedimented. Volume scattering from loose basalt buried within the sediment is a potential cause of the enhanced backscattering strengths in this angular regime. The flat surface of the sediment

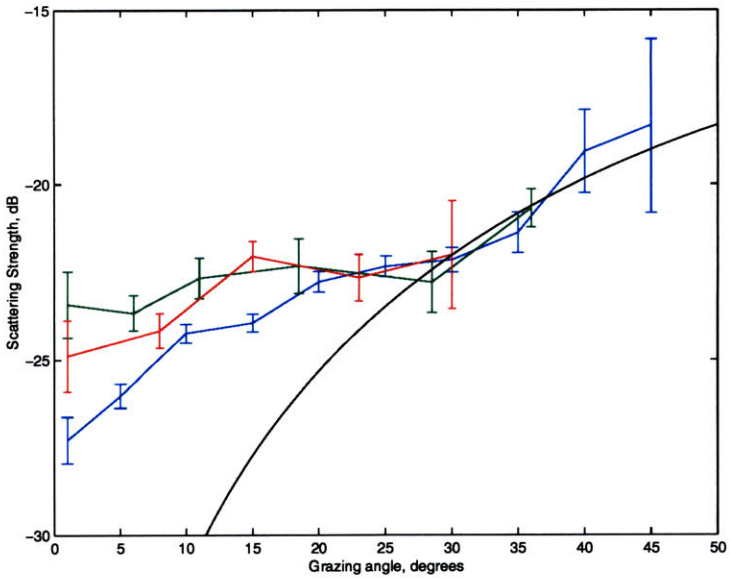

Figure 3-6: Backscattering strength as a function of grazing angle for scarp (blue), Terrace (green), and Other (red) seafloor. An enhancement of 4 dB in terrace seafloor as compared to scarp seafloor is observed at the lowest grazing angles, while all three curves agree at grazing angles above 20 degrees. The best-fit Lambert's law at the higher grazing angles has $\mu = -16$ dB (black curve), but this law fails at low grazing angles.

masks a much rougher underlying basalt basement. The grazing angles with respect to the basement may in some cases be much higher than those calculated using the water-sediment interface, which would also lead to enhaned low-grazing angle backscatter.

"Other" seafloor, manifesting a combination of the geological characteristics of scarp and terrace seafloor, lies in between the two previous curves at all angular regimes, as would be expected.

It is interesting to compare the data with the best fit Lambert's law. For the regime above 20 degrees, the best fit coefficient is $\mu = -16$ dB for all three seafloor classes. Fig. 3-6 shows that while Lambert's law can be made to match the data starting at 25 degrees, it fails at lower grazing angles.

3.3.2 The Effect of Anisotropy on Backscattering Strength at B'

The obvious large scale anisotropy in Mid-Atlantic Ridge seafloor and more specifically that encountered at site B', as seen from Fig. 3-4, naturally leads one to ask about scattering behavior at various azimuths relative to particular seafloor features.

I define the *axis of B'* as the line making an angle of 66 degrees with the x-axis, lying along the direction of the bathymetry's longest correlation length. By using the fact that the seven segments used in the previous section insonify B' from different directions, it is possible to study whether the anisotropy at B' translates into measurable differences in backscattering strength.

As mentioned earlier, I focus exclusively on scarp seafloor. There are three reasons for this; first, scarp seafloor is the category for which evidence of anisotropy is strongest. Second, since the $\simeq$ 228 Hz pulse penetrates the sediment cover of terraces, it interacts with an unknown underlying interface. In the case of scarp seafloor, the water-seafloor interface obtained using high-frequency sonar is more representative of the true scattering surface because the rigidity of basalt allows little penetration. Finally, I note that large volumes of data are required if reliable estimates are to be obtained at many azimuths; as can be seen from Fig. 3-5, scatter from scarps is much more common than scatter from terraces.

The four curves on Fig. 3-7 show the dependence of backscattering strength on grazing angle at four different values of the incident azimuth relative to the axis of B'. The dark blue curve corresponds to incident azimuths between 70 and 90 degrees. The light blue curve is for azimuths between 60 to 70 degrees, the green for 50 to 60 degrees, and the red for 30 to 50 degrees. The backscattering strength curves are shifted down by at least 5 dB at all grazing angles as the azimuth ranges from 90 to 30 degrees relative to the axis of B'. This Figure suggests re-interpretation of the scarp curve in Fig. 3-6 as a composite over many azimuths. Lambert's law curves were fit to the largest grazing angles yielding $\mu = -14$ dB from 60 to 90 degrees, $\mu = -17.5$ dB from 50 to 60 degrees, and $\mu = -22.5$ dB from 30 to 50 degrees. Lambert's law

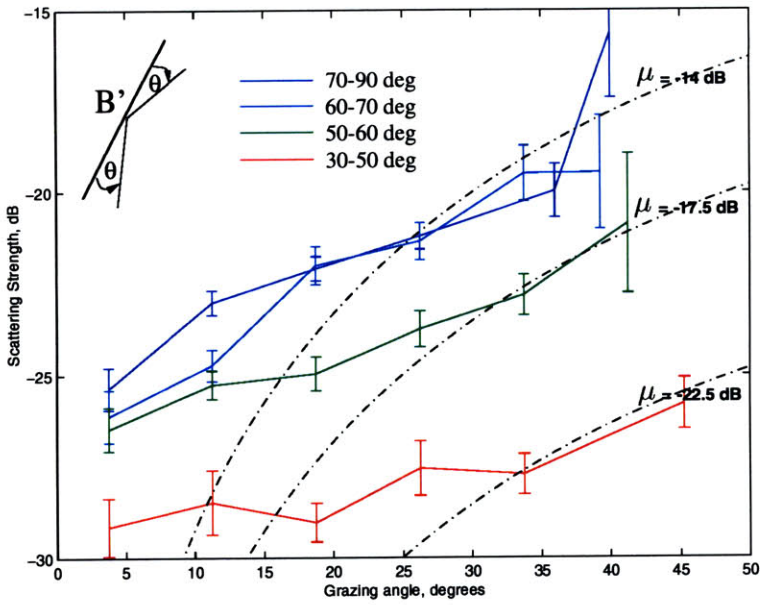

Figure 3-7: Backscattering strength as a function of grazing angle for various angles of incidence relative to the anisotropic axis of B': $70-90°$ (dark blue), $60-70°$ (light blue), $50-60°$ (green), and $30-50°$ (red). The best-fit Lambert's law curves are shown in black.

is seen to fail at all azimuths for low grazing angles due to the different functional relationship of the data.

3.4 Time-Domain Statistics of Backscatter at B'

In analyzing high-resolution envelopes backscattered from B', I choose a statistical approach because neither the knowledge of the bathymetry and the environment, nor current computational models are sufficient to deterministically relate obervations to data in the ARSRP application.

Through the data structures made available by ARTIST, it is possible to extract data histograms for specific regions of interest on the seafloor lying within particular grazing and bistatic angle regimes, and at desired incident azimuths with respect to the anisotropy of B'. Before presenting these, I present the log-envelope pdf estimate for the pixels that are deemed by ARTIST not to correspond to direct or surface-

Segment #	$J_{\min}$	$J_{\max}$	$K_{\min}$	$K_{\max}$	TH^* (dB)
423	110	170	50	120	68
430	100	170	60	120	66
436	80	140	80	128	64
492	110	170	70	125	66
499	120	190	80	128	64

Table 3.1: Values used to select noise subspace for each segment.

reflected paths. I shall call these pixels "noise pixels"; the energy in these pixels results from a large number of multiple-bottom interaction ray paths.

3.4.1 Pdf of Log-Envelope of Noise Pixels

The set of noise pixels is

$$\Lambda^* = \{(j,k) \in \Lambda^\dagger : RL(j,k) < TH^*\} \tag{3.17}$$

where $\Lambda^\dagger$ is the complement of the selected set Λ with respect to $\{(j,k) : j \in [J_{\min}, \ldots, J_{\max}], k \in [K_{\min} \ldots, K_{\max}]\}$. The latter subset is a rectangular area of pixels that was set manually for each segment and which is just large enough to include Λ. The threshold TH^* for each segment is set using the method of Sec. 3.2.1. Table 3.1 indicates the values of $J_{\min}$, $J_{\max}$, $K_{\min}$, $J_{\max}$, and TH^* that were used for each segment.

The total contribution to the histogram is the union over all segments of

$$r^{\text{noise}} = \bigcup_{(j,k) \in \Lambda^*} r_{j,k}(t). \tag{3.18}$$

Fig. 3-8 (a) is a plot of the histogram on a linear scale (y-axis). The x-axis is in dB, corresponding to the fact that the time series $r_j(t,k)$ (c.f. Eq. 3.12) are in dB. The thin solid curve is a plot of the log-Rayleigh distribution which results when the real and imaginary components of the underlying signal are Gaussian. It respresents the tranformed version of the Rayleigh pdf after the operation $10\log_{10}(r(t))$, which I refer

to as the log-Rayleigh pdf, as described in Appendix B. If, at each value of time, the signal is viewed as a sum over a number of degrees of freedom each corresponding to independent paths or independent scatterers, then a Rayleigh pdf is obtained in the upper limit of this number.

Each time subseries is 200 msec long and contains 10 independent observations of the underlying statistical process given that the 3-dB width of the pulses is 20 msec. As explained in Appendix B, when sets of I log-Rayleigh variables are normalized by their mean, the resulting variables are no longer log-Rayleigh. Taking the example case $I = 2$, we begin with two i.i.d. log-Rayleigh variables $\{E_1, E_2\}$ and end up with $\{\frac{1}{2}(E_1 - E_2), \frac{1}{2}(E_2 - E_1)\}$, a set in which the second variable is perfectly correlated with the first. Because E_1 and E_2 are i.i.d., the opposite signs of the variable $E_1 - E_2$ lead to a symmetric distribution. From this argument alone, I have already determined that this variable cannot be log-Rayleigh, since this pdf is not symmetric.

The thick solid curve on Fig. 3-8 (a) is the transformed version of the log-Rayleigh density that results from normalizing sets of $I = 10$ log-Rayleigh variables by their means. The data histogram agrees with this density of mean-corrected log-Rayleigh variables, indicating that the magnitude of the underlying signal envelope is Rayleigh. If the effect of mean normalization were not included, it might be incorrectly deduced from the difference between the histogram and the log-Rayleigh distribution near the peak that the process was non-Rayleigh.

In Fig. 3-8 (b), I show the same data with the y-axis in dB according to a relative scale chosen to make the peak of the density 50 dB. The log scale is useful to search for non-Rayleigh behavior at the high level tail which could be hidden in a linear display. The horizontal line is a reference showing the decibel level ascribed to a histogram bin having only one element. As in (a), the thin solid line is the log-Rayleigh pdf and the thick line is the density of log-Rayleigh variables mean-normalized in sets of 10. The noise data agree very well with the latter curve at levels above -30 dB.

Below -30 dB, the density estimates are unreliable. Such low levels, if they occur at all, usually result from sidelobe leakage of the higher levels; they are not independent estimates of a Rayleigh variable, but samples corrupted by linear dependence on

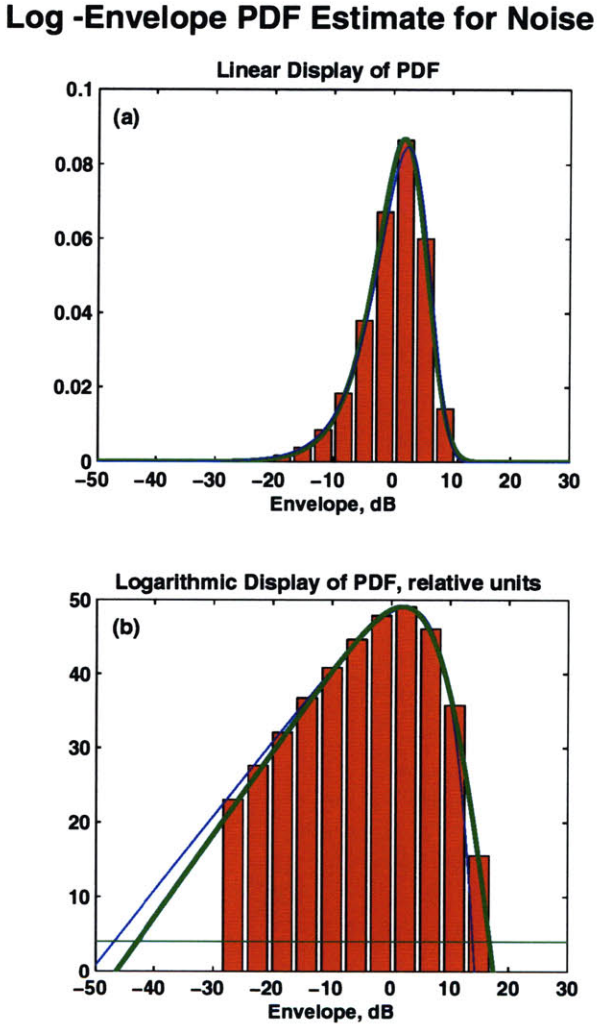

Figure 3-8: Estimate of the pdf of the log-envelope of noise pixels (red). The thin blue curve is the log-transformed Rayleigh distribution. The thick green curve includes both the log tranformation and the effect of mean subtraction from finite duration Rayleigh time series containing ten pulses. The agreement of the data with this curve indicates that the data are Rayleigh.

the higher level variables. I have observed by carrying out numerical simulations of complex Gaussian white noise convolved with different pulse types, that changing the pulse sidelobe structure changes the lower levels in the log-envelope density estimates in erratic and unpredictable ways. Given that the low levels do not form the basis for any conclusions in this thesis, they have been omitted entirely from all the histograms presented in this chapter. The high level density estimates, which *are* used to draw conclusions, are insensitive to pulse sidelobe structure.

The last histogram bin is clearly above the log-Rayleigh pdf. This might be interpreted as evidence of non-Rayleigh behavior, but the bin matches well with the mean-modified log-Rayleigh pdf, indicating that the noise pixels are in fact Rayleigh.

The log-Rayleigh curve would be encountered in the limit of increazing window size Δt. Excessively large windows would lead to non-stationary samples, thus it is preferred to use reasonable window sizes and account for the warping of the density by the zero-mean operation.

The standard deviation is estimated to be 5.39 ± 0.03 dB; the mean-corrected log-Rayleigh pdf for $I = 10$ (see Appendix B) has a standard deviation of 5.38 dB.

The result that the noise pixels are Rayleigh is intuitive, given that ARTIST simulations have identified them as correpsonding to shadow zones, deriving their energy from more than one path having reverberated up and down several times in the water column and also potentially from sidelobe leakage.

3.4.2 Pdf Estimates For Scarps and Terraces

The density estimate of $r_{j,k}(t)$ for terrace seafloor at all grazing angles is displayed on Fig. 3-9 in (a) linear and (b) logarithmic units. The green curves are the densities of log-Rayleigh variables zero-meaned in groups of 10. There is evidence of non-Rayleigh behavior near the peak in (a) and in the last two histogram bins in (b). The third last histogram bin, centered about 15 dB, is 10 dB above the Rayleigh case, so 15 dB events are ten times more likely from the terraces than from a perflectly Rayleigh process.

Turning now to scarps, I show density estimates of the log-envelopes for two

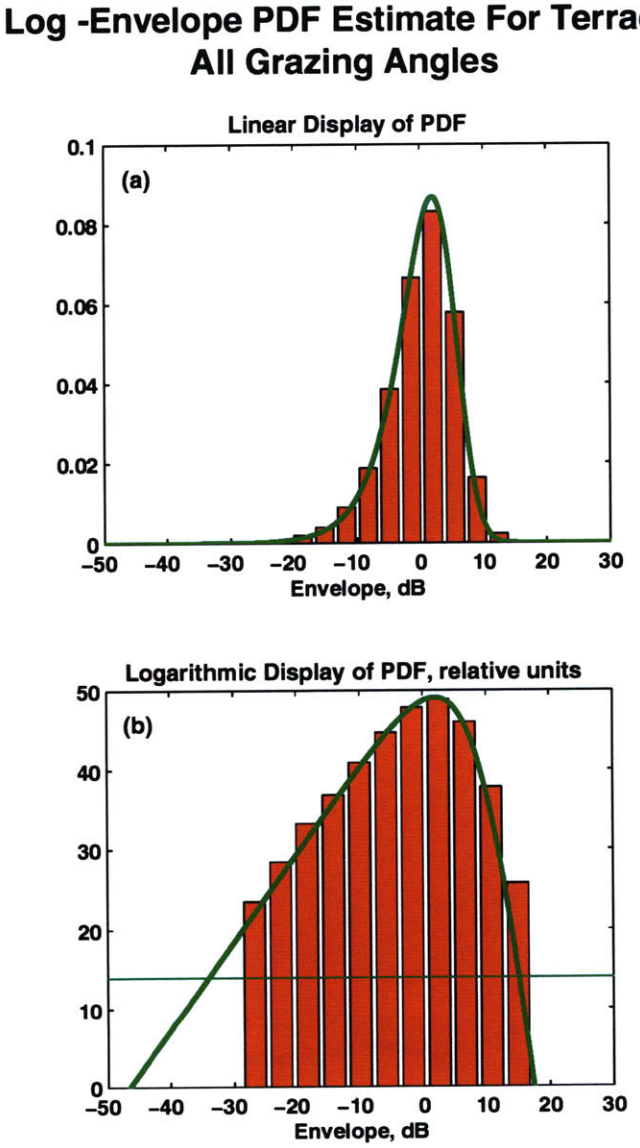

Figure 3-9: Log-envelope histograms for backscatter from terrace areas (red). Although all grazing angles are included in the estimate, very few data pixels are associated with grazing angles above 25 degrees. The depression from the peak in (a) and the enhanced upper tail in (b) indicate a departure from Rayleigh.

grazing angles regimes: smaller than 25 degrees in Fig. 3-10 (a) and (b) and greater than 25 degrees in Fig. 3-10 (c) and (d). In (a), the depression of the histogram peak from the peak of the curve for Rayleigh statistics is greater than for the terraces. Examining (b), the 15 dB histogram bin (third last) is slightly higher than for the terraces; more importantly, there is significant evidence of non-Rayleigh behavior above 15 dB. The last histogram bin lies approximately 40 dB above the curve for the Rayleigh case; these scarp events are 10,000 times more likely than from a Rayleigh process.

Examining grazing angles greater than 25 degrees, the linear plot in (c) reveals an even greater depression of the histogram from the Rayleigh case than in Fig. 3-9 and (a) of Fig. 3-10. In (c), the high-level tails show clear evidence of non-Rayleigh behavior, with the highest bin revealing a 50,000 higher likelihood of the strongest events than from a Rayleigh process.

It is interesting to ask how the enhanced high-level tails affect the second moment of the log-envelope pdfs. To reduce the error on this standard deviation estimate, I do not restrict the analysis to site B'; I use all data pixels which can be ascribed to scattering from bathymetric features through ray paths interacting with the seafloor only once. The result is a standard deviation of 5.90 ± 0.04 dB, which is to be compared to a value of 5.38 dB of the process were perfectly Rayleigh. Thus, there is an increase of about 0.5 dB in the standard deviation of the log-envelope pdfs compared to a Rayleigh process.

The observation that the received signals from scarps and terraces at all grazing angles are not fully-formed Rayleigh suggests that individual scatterers are occasionally glinted by the sonar system. This glinting enhances the high-level tails in the envelope pdfs as compared with the Rayleigh distribution. The fact that the glints become more likely at high grazing angles suggest that they are not caused by shadowing but by scattering by rare large facets oriented to reflect specularly in the back direction.

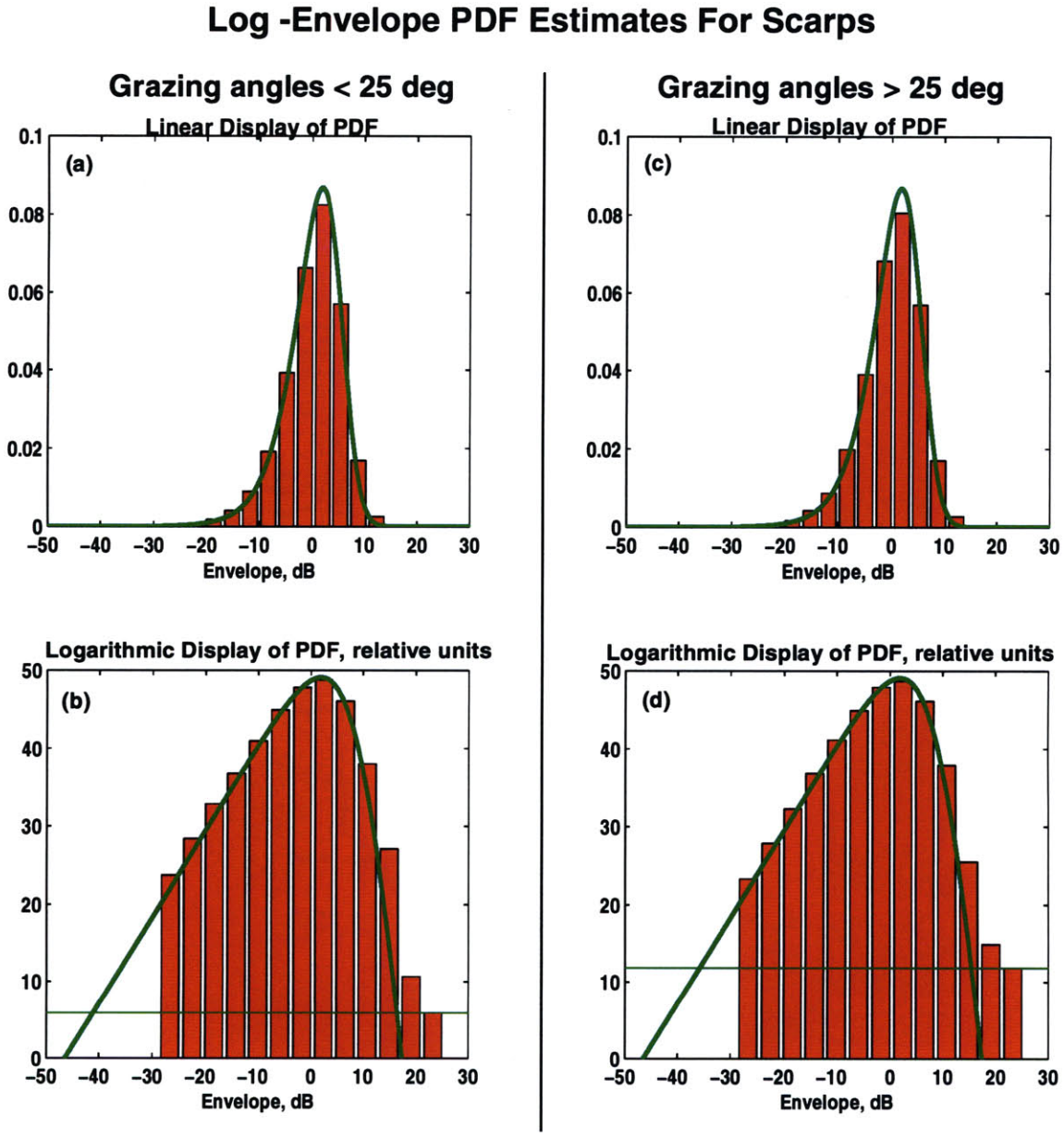

Figure 3-10: Estimates of the pdfs of backscatter from scarp areas (red). (a) and (b) The shallow grazing angles are comparable to those that dominate the terrace seafloor. Data from the scarps at low grazing angles exhibit a greater departure from Rayleigh than the terraces (c.f. Fig. 3-9). (c) and (d) The departure is accentuated further at the higher grazing angles.

3.4.3 Effect of Anisotropy on Scarp pdfs

Taking the analysis one step further, Fig. 3-11 examines the scarp time series for different incidence directions with respect to the anisotropy of B', for grazing angles less than 25 degrees. Fig. 3-11 (a) and (b) are for azimuths 70-90 degrees from the axis of B', that is, within a $\pm$ 20 degree cone of being normal to the scarps. Fig. 3-11 (c) and (d) show log-envelope density estimates for azimuths of incidence of 30-70 degrees with respect to the axis of B'.

Finally, in Fig. 3-12, I examine the effect of anisotropy as in Fig. 3-11 except that now I focus on grazing angles greater than 25 degrees. Both grazing angle regimes reveal the same observation: the departure from Rayleigh at the central peak of the linear density and at the tails of the logarithmic density is more dramatic normal to the scarps. The last bin of Fig. 3-12 (b) suggests that scarp events above 20 dB are more than 200,000 times more likely for normal incident azimuths and high grazing angles than from a Rayleigh process.

3.5 Discussion

3.5.1 Terraces

The comparisons of scattering strengths and envelope densities for scarp and terrace seafloor have revealed that terraces are stronger scatterers at low grazing angles while their time-domain backscatter is closer to being Rayleigh than scarps. Since there is little direct knowledge on the fine scale structure of the sediment and its underlying basement, it is difficult to ascertain the cause of this behavior.

The increase in backscattering strengths at lower grazing angles could be explained both by the presence of scatterers within the sediment, and by a scatterer-free sediment layer overlying a basalt basement. In the latter case, the flat surface of the sediment leads to shallow grazing angles, but the wave interaction is at a potentially steeper interface beneath, explaining the higher scattering strengths.

In the absence of volume scatterers, the time-domain statistics should be similar

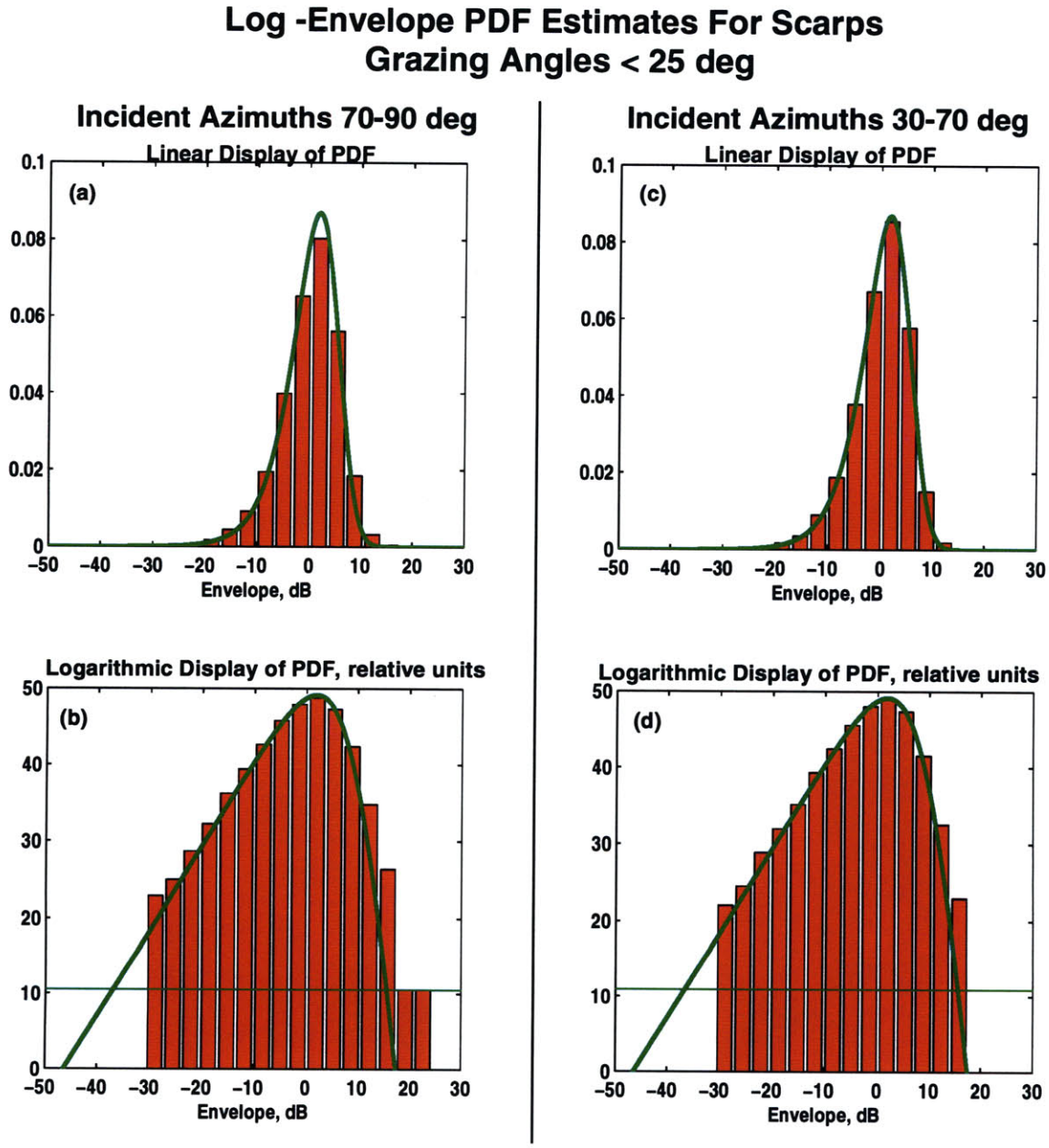

Figure 3-11: At low grazing angles, greater departures from Rayleigh are observed for data incident normal to the scarps (a) and (b) than at large angles to the scarps (b) and (c).

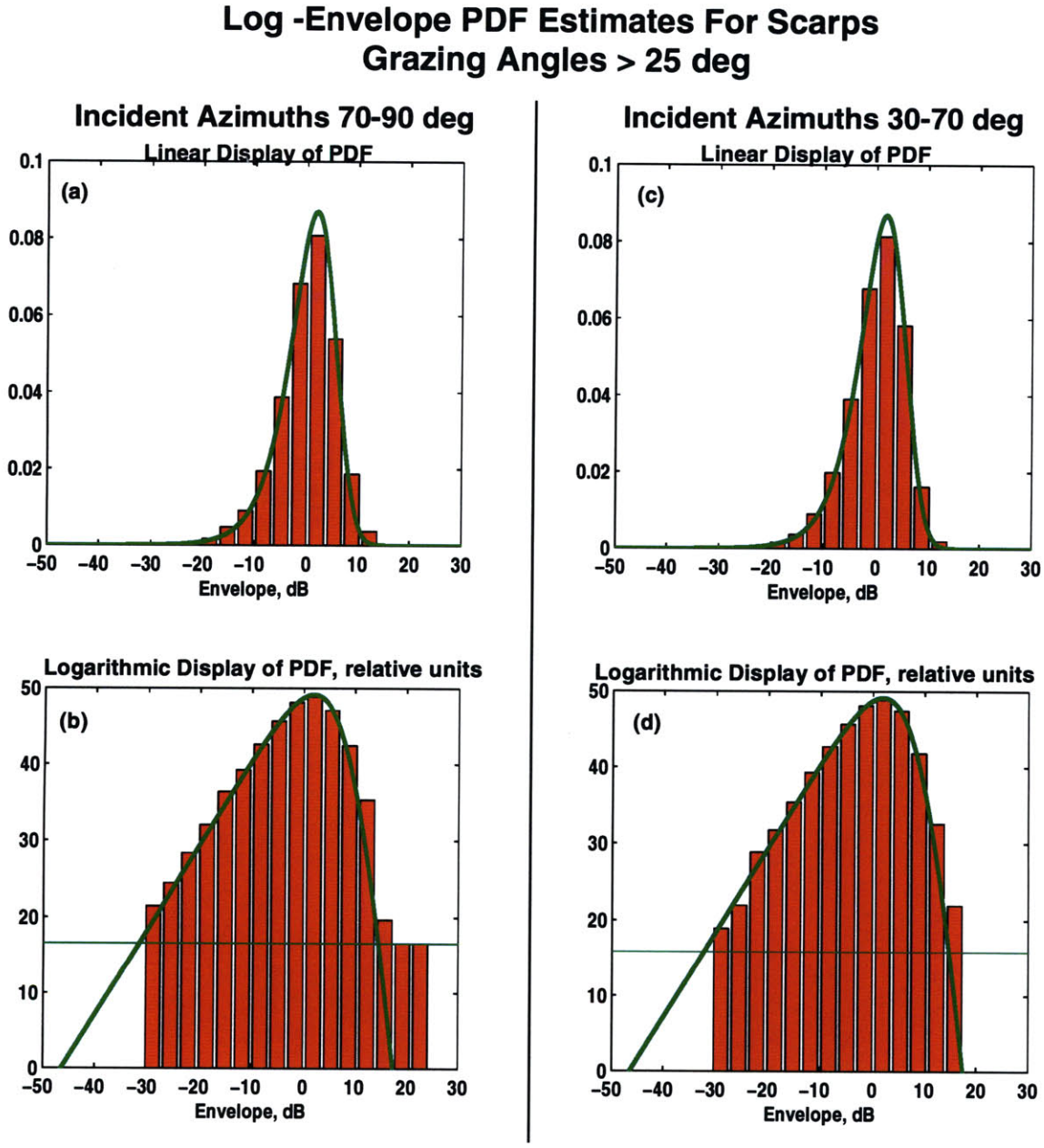

Figure 3-12: At high grazing angles, greater departures from Rayleigh are observed for data incident normal to the scarps (a) and (b) than at large angles to the scarps (b) and (c).

to those for scarps since interaction is with the same interface. It is likely that volume scatterers are contributing to the backscatter thereby increasing the number of degrees of freedom in the waveforms and resulting in statistics that are closer to being Rayleigh than for scarps. These issues will be explored no further in this thesis since I concentrate on scattering at the exposed water-basalt interface rather than scattering within or underneath sediments. The reader interested in volume scattering in ARSRP is referred to Ref. [33].

3.5.2 Lambert's Law

Agreement with Lambert's law is expected when the roughness within the footprint distributes acoustic intensity uniformily in solid angle. The energy, or scattering strength, radiated in any direction is then simply the projected area of the footprint in that direction. For an impenetrable boundary, conservation of energy fixes the value of the coefficient of Lambert's law, but is it customary in practice to account for energy lost through penetration or other mechanisms not accounted for by empirically fitting the coefficient to the data.

The best-fit Lambert's law has a coefficient μ of -16 dB for all three seafloor classes, and is found to fail at low grazing angles, which is also where the three seafloor types exhibit distinct scattering strengths. In the anisotropic study of scarps, best-fit Lambert's law coefficients range from -22.5 dB at 30-50 degrees relative to the axis of B' up to -14 dB for normal incident azimuths. In all cases, it is found to fail at grazing angles below 30 degrees. The failure of Lambert's law indicates that the seafloor and the footprint size in ARSRP violate the assumption of uniform intensity scattering.

3.5.3 Log-envelope pdfs

The deviation of the statistics from those of a Rayleigh process for all the seafloor areas analyzed imply that the number of degrees of freedom which sum up to make the backscattered signal is not sufficiently high for the real and imaginary parts of the signal to have converged to independent Gaussian processes by the Central Limit

Theorem. There are three plausible causes.

1. It is at least occasionally true that a small number of scatterers within the footprint dominates over the rest. A good example would be an occasional glint from a facet large compared to the wavelength oriented in the back direction.

2. The number of scatterers within the footprint is at all times large enough to cause fully-formed Rayleigh signals, but a shadowing function causes the mean energy levels to fluctuate over time as the pulse passes over shadowed and illuminated features within the 200 msec time windows used in data processing.

3. A combination of 1 and 2 is responsible for the non-Rayleigh behavior.

As the grazing angle increases, the effect of shadowing becomes less important. If shadowing were an important mechanism for generating non-Rayleigh scatter, deviations from Rayleigh would decrease with increasing grazing angle. The data exhibit the opposite behavior and therefore do not support option 2. This implies the intriguing result that a sufficiently small number of abnormally strong scatterers is encountered in the approximately 500 m x 25 m footprint.

3.5.4 Scarp Anisotropy: Evidence of Scale Structure Importance in Acoustic Scatter

Further insight can be gained by considering the observed dependence on incident azimuth with respect to B' anisotropy. It is helpful to make use of available knowledge regarding the fine-scale structure of B' scarps. Geophysical surveys at B' [67] reveal that scarp anisotropy exists at smaller scales. As mentioned earlier, the scarps are cut by canyons 100-200 m wide and 30-50 m deep along the direction normal to the axis of B'. This is the roughness that is experienced by a wave incident parallel to the scarps. Along the axis of B', or parallel to the scarps, one finds gullies 10-30 m wide and 10-20 m deep, which is the roughness that a wave incident normal to the scarps experiences. There are other forms of wavelength-scale roughness such as talus, but

these structures lead to isotropic roughness and therefore cannot be used to explain data dependence on anisotropy.

It is possible that the backscattered energy in ARSRP contains glints from relatively smooth features on the order of a wavelength or larger with high slopes ($> 45°$). According to this theory, backscatter from the scarp-parallel gullies is expected to be stronger than from the canyons since the gullies are more likely to present retro-reflecting features than the canyons.

It is appropriate at this point to mention a perplexing result from Ref. [18] presented in the next chapter. The estimates of power spectral density parallel and normal to B' scarps are very close to being identical in shape and amplitude, suggesting isotropy in spite of clear identification of anisotropy in visual observations of the bathymetry at the same scales. It appears that the spectral representation has lost information about the features in the bathymetry, features which are potentially relevant to scattering.

The explanation of scatter in terms of the statistical morphology of scattering surfaces is the central subject of this thesis. The spatial organization of a surface's features at different scales is defined as *scale structure.* The ARSRP data suggest that scale structure plays an important role in scattering.

3.5.5 Discrete Scatter

One of the proposed mechanisms for explaining scatter in ARSRP has come to be known as the *Dyer conjecture* [13]. Although no analysis of the time-domain statistics were performed in the original paper [13], the theory was formulated based on the statement that "Rough bottom acoustic backscatter observed in the 200-300 Hz frequency range has a discrete character." The theory proposes that scatter from isolated, smooth "facets" can lead both to discrete backscatter and high values of backscattering strength as observed in ARSRP, if their sizes are close to one acoustic wavelength. The reasoning is as follows: facets large compared to the wavelength scatter strongly but only in the forward direction, and facets much smaller than the wavelength scatter omnidirectionally but do so weakly. Only those facets which are of

comparable size to the wavelength lead to energetic backscatter. The discrete character of backscatter would persist at a range frequencies because the wavelength would self-select wavelength-sized features.

The events based on which I proclaim event-like or temporally discrete statistics are extremely rare, as can be seen from the histograms themselves. The frequency of these events is not sufficient to make them the dominant contributors of scattering strength, which is the mean energy of the envelope. The specific cause of such events, whatever it is, is itself rare, and it is not the same as that which causes the mean levels. For the Dyer conjecture to explain both the mean levels and the rare events, it is required that we regard the rare event of a wavelength-sized feature oriented to reflect specularly in the back direction as the cause of the high-level events and the common event of a wavelength-sized feature oriented in any other direction as the cause of the mean levels. However, any smooth feature oriented in the back direction of size equal to *or larger* than the wavelength leads to high-level events. The Dyer conjecture is thus not quite adequate in describing both the glinting and scattering strengths. Nevertheless, it was a powerful inspirational force in shaping the ideas to be presented in the remainder of this thesis about scale structure and its impact on acoustical scattering.

3.6 Summary

1. Focusing on monostatic configurations and site B', I have shown that in the context of ARSRP it is possible to classify scattering data according to a set of intertwined seafloor categories defined over regions as narrow as 500 m. The ability of ARTIST in incorporating the range and azimuth resolution capabilities of the sonar have proven invaluable in this respect.

2. The data analysis has revealed higher backscattering strengths for terraces than for scarps at grazing angles below 15 degrees. Lambert's law was found to fail at grazing angles below 20 degrees.

3. Backscattering strength curves for scarp seafloor were extracted for different incident azimuths relative to the anisotropic axis of B'. It was found that backscattering strengths for incident azimuths normal to the scarps were at least 5 dB higher than at 30 to 50 degrees relative to the scarps. Best-fit Lambert's law coefficients ranged from -22.5 dB at 30 to 50 degrees relative to the scarps, up to -14 dB normal to the scarps; Lambert's law was found to fail at grazing angles below 30 degrees at all azimuths.

4. In the estimates of high-resolution log-envelope pdfs, I have found that data associated by ARTIST with multiple seafloor interaction ray paths behave as samples from a Rayleigh process. In establishing this fact, it was important to account for the logarithmic transformation applied to the data as well as the effect of subtracting the mean from data segments ten pulses wide.

5. While exhibiting a variance which is only 0.5 dB different from that of a Rayleigh process, all of the pdf estimates for data which can be mapped to the seafloor by ARTIST through direct or surface-reflected paths differ from the pdf of a Rayleigh process in two important ways: they exhibit a lower peak value and enhanced tails. The enhancement of the tails is such that high-level events are many orders of magnitude more likely than from a Rayleigh process.

6. The extent of the disagreement with a Rayleigh process is higher for scarps than for terraces. For scarps, the disagreement is higher at large grazing angles, suggesting that shadowing is not the leading cause.

7. For a given range of grazing angles, the disagreement with a Rayleigh process is higher normal to the scarps. Concurrently, the fine scale roughness at B' exhibits features which are more elongated and have smaller slopes parallel to the scarps than normal to the scarps, although the power spectral density along both directions is the same (shown in Chapter 4). These observations lead to the suggestion that scale structure, or feature size distribution, may play an important role in scattering from random rough surfaces and that alternative

methods in statistical seafloor morphology are needed to represent them.

The high-level tails in the pdfs are relevant from an engineering perspective because they can lead to clutter in active sonars. They are also intriguing from a scientific point of view and provoke some thoughts regarding a possible connection with the stochastic morphology of the seafloor. In the next chapter, I take a closer look at the feature-like nature of the bathymetry by presenting a set of nested plots of increasing resolution centered on site B' and periodograms of high-resolution profiles normal to and parallel to B' scarps. This analysis of the bathymetry combined with the results of the present Chapter form the motivation for the theoretical exploration of scale structure and its role in scattering in Chapters 5 and 6.

Chapter 4

Seafloor Morphology

In the previous chapter, enhanced tails were observed at the high levels in the pdf's of time-domain backscatter across all grazing and anisotropic angles. The tails provide quantitative confirmation that time-domain backscatter has an event-like character. These events are proposed to result from scattering at localized seafloor features. It is then natural to pose questions regarding the features that are contained on the seafloor. These questions can only be answered by taking a closer look at available bathymetric surveys.

In this chapter, I concentrate solely on the seafloor and perform a deterministic, morphological analysis using a series of nested surveys to reveal dominant structures in each range of scales. This is followed by estimates of the power spectral densities of high resolution profiles normal and parallel to scarp seafloor at site B'.

The observations will inspire a new stochastic seafloor model which, in contrast to the Goff-Jordan model, can generate feature-like roughness.

4.1 Deterministic Observations

The coarsest dataset is the Hydrosweep bathymetry of the Atlantic Natural Laboratory depicted in Fig. 2-1, collected in 1992 and providing a 200 m horizontal resolution. The horizontal extent covered by this figure is several hundred kilometers, and the dominant feature of the roughness at these scales is the nominal 60° orientation of

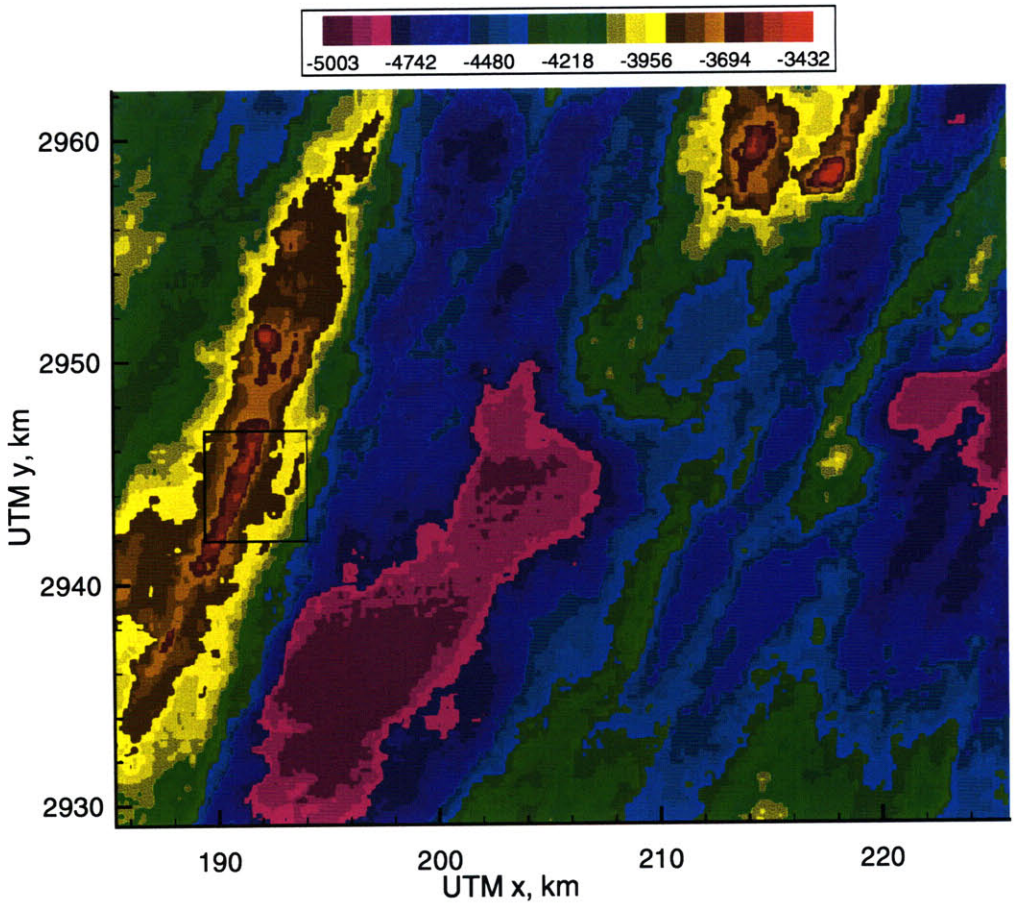

Figure 4-1: Zoom-in on the square at site B' in Fig. 2-1. At the range of scales in this plot, the bathymetry does not exhibit features at a predominant scale.

the quasi-periodic lineations with separation distance on the order of 20 km (abyssal hills). Also, there is a gradual subsidence of the mean seafloor depth from $\simeq$ 3500 m at the MAR to $\simeq$ 4500 at the Western end. The numerous abyssal hills evident in this view have a predictable impact on reverberation, as shown in Chapter 2.

The next higher level of detail is depicted in Fig. 4-1; it is a zoom-in on the rectangle labeled Site B' on Fig. 2-1 with a horizontal extent of 40 km. The view provided at this scale of magnification reveals no repeatable features. The steep scarps of B' change into a sedimented valley in the center. Partial ridges are scattered around the circumference of the plot, but with no clear pattern.

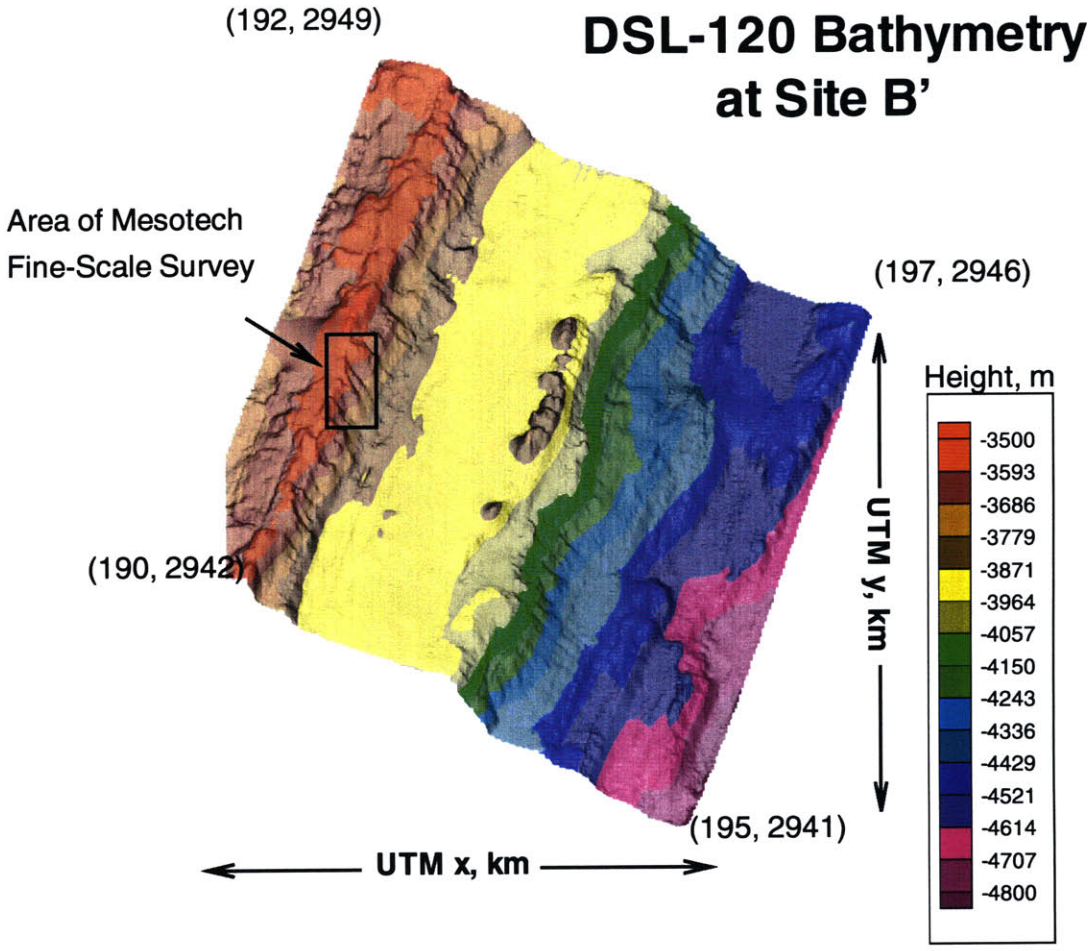

Figure 4-2: Vertically exagerrated view of bathymetry at site B' collected with DSL-120 sonar system at a lateral resolution of about 5 m. The color contours represent the depth in meters. In this view, a central sedimented terrace separates an upper scarp of exposed basalt from a lower scarp. These are the same two scarps that were used in the data analysis of Chapter 3 and which can be seen in the perspective view of Fig. 3-4. The region below the lower scarp contains of mix of exposed basalt and sedimented areas which was typically classified as "Other" seafloor in Chapter 3. The dominant form of roughness on the scarps at this scale comes from the cross-scarp canyons.

The next view, with horizontal extent of about 5 km, focuses on the B' rectangle of Fig. 4-1 to yield Fig. 4-2. These data were collected using the 120 kHz sonar system DSL-120 yielding a 5 m horizontal resolution. At this scale, one can see the re-emergence of repeatable, single-scale features. These are especially evident on the highest scarp; they take the form of canyons cutting normal to the scarp and are separated by an average distance of 100-200 m. This finding has been studied and related to mass wasting in Ref. [67]. These cross-scarp canyons are also visible in the lower scarp. The two scarps are separated by a sedimended terrace which shows little roughness in this view. In Ref. [67], the authors observe scarp-parallel gullies 10-30 m wide and 10-20 m in height on some of the lower scarps of B'. These gullies intersect the larger cross-scarp canyons at near right angles, yielding a trellis pattern.

A non-vertically exaggerated view of the DSL-120 bathymetry taken from Ref. [67] is shown on Fig. 4-3. The cross-scarp canyons are even more evident in this Figure.

Zooming in on the rectangle in Fig. 4-2 gives Fig. 4-4 with horizontal extent on the order of 500 m. These data were collected using the Mesotech 675 KHz pencil-beam sonar system of the ROV Jason, with horizontal resolution of 2 m. The smooth areas result from interpolation; data are only available along a set of tracks taken by the ROV. Shown on the figure is the size of the ARSRP sonar footprint, represented by the red rectangle. The canyons from the previous view are still visible, but a new finer-scale structure can now be distinguished. On the flanks and at the base of the scarp, there are cross-scarp corrugations with average spacing on the order of 20 m. Near the top of the scarp, a number of blocky features with diameter around 10 m is visible. Focusing in on these features using the black rectangle, it can be seen in Fig. 4-5 that they are comparable to the wavelength in size. They are labeled "facets" since they are morphologically consistent with the notion of the smooth localized features mentioned in the previous chapter and at the beginning of this chapter.

The ROV was equipped with video cameras, permitting an even more detailed view of the seafloor. The two still-camera images shown in Fig. 4-6 along with their interpretation were borrowed from Ref. [18]. They were taken at locations indicated by the black dots on Fig. 4-4. Fig. 4-6 (a) is from UTM location (191.410, 2944.65)

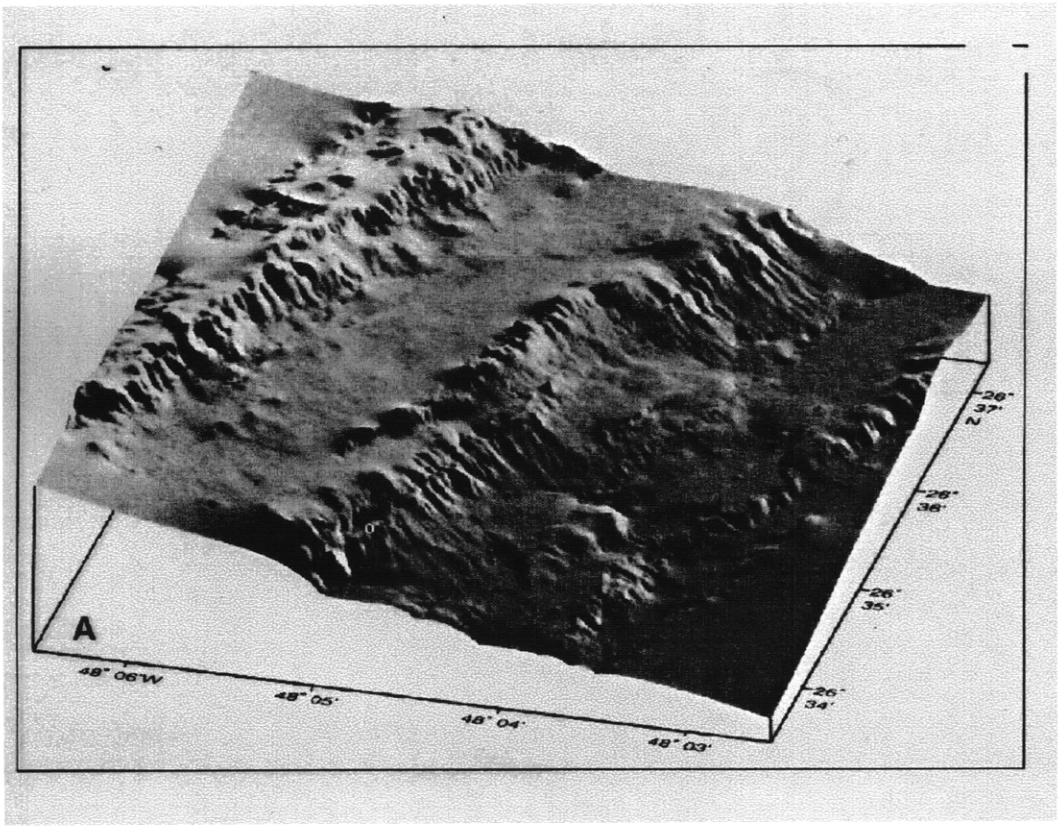

Figure 4-3: View of bathymetry from DSL-120 system taken from *Tucholke et al., Geology* 25(2), Ref. [67], over the same region as Fig. 4-2 but to scale. The shadowing provides a clearer view of the single-scale nature of the structures on the scarps. The axis running left to right is approximately 7 km long, that running bottom to top is approximately 4 km long, and the length of the vertical axis shown at the bottom left corner is approximately 1300 m.

km near the top of the scarp and (b) is from (191.320, 2944.3) km near the bottom of the scarp. In (a) the vertical extent of the picture is around 3 m and in (b) it is about 2 m. At (a), the angle of the scarp is approximately 45°. At this sub-wavelength scale, we see the appearance of yet another form of roughness due to manganese nodules around 10-20 cm in scale. There is an absence of roughness for scales from 30 cm up to the full size of the view, 3 m. The grayish matter between the nodules is a thin sediment cover over basalt. There is an absence of roughness over much of the range of scales between the sediment grain size and the size of the nodules. In (b), the slope is initially $70 - 90°$ at the left edge and abruptly settles to shallower angles at the top

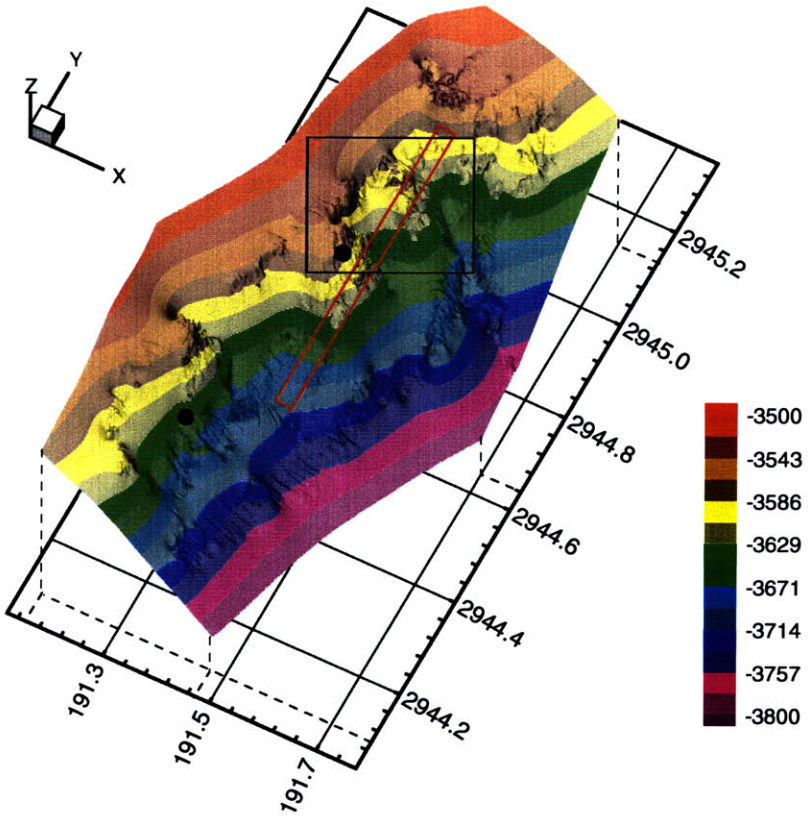

Figure 4-4: Zoom-in on rectangle of Fig. 4-2 using 2 m gridded bathymetry from Mesotech pencil-beam scanning system. Contours in meters.

right corner. This latter area consists of talus more heavily draped with sediment. Apart from this break in slope, the structure is similar to (a), where roughness is dominated by features 10-20 cm in diameter.

The observations from the nested views of the seafloor can be summarized as follows. Each of the nested views presents a wavenumber-filtered picture of the seafloor where the largest scale detectable is associated with the lateral extent of the view, and the smallest scale is associated with the smallest pixel in the image. In each case, the range of scales encompasses several orders of magnitude. In some of the views, a dominant form of roughness at a single scale is revealed. For example, in the 2 to 3 m views of the top scarp of B', this dominant roughness took the form of 20-30 cm manganese nodules. At the 5 km view of Fig. 4-2, there was a detectable roughness

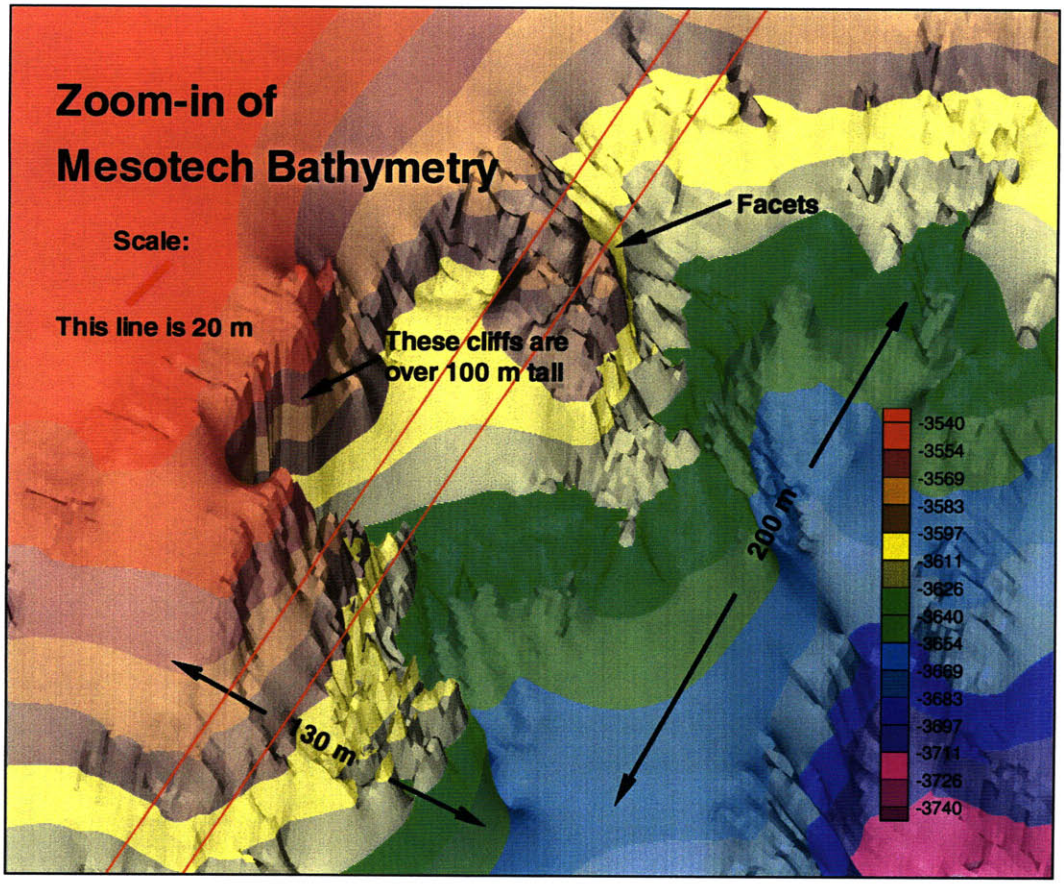

Figure 4-5: Zoom-in on rectangle of Fig. 4-5 showing some wavelength-scale structure on the scarps of site B'.

dominance by the cross-scarp canyons. On the other hand, in the view of Fig. 4-1, such single-scale patterns were not evident.

It is clear that the morphology of the seafloor, whether it reveals features at a dominant scale or not, differs from one range of scales to the next. It is therefore interesting to take a look at traditional spectral stochastic seafloor analysis to see how this variability across scales translates into energy density as a function of wavenumber.

4.2 Spectral Analysis

The most common technique for characterizing stochastic seafloor roughness is spectral analysis [17] [3]. A characteristic which is shared by seafloor from widely varying

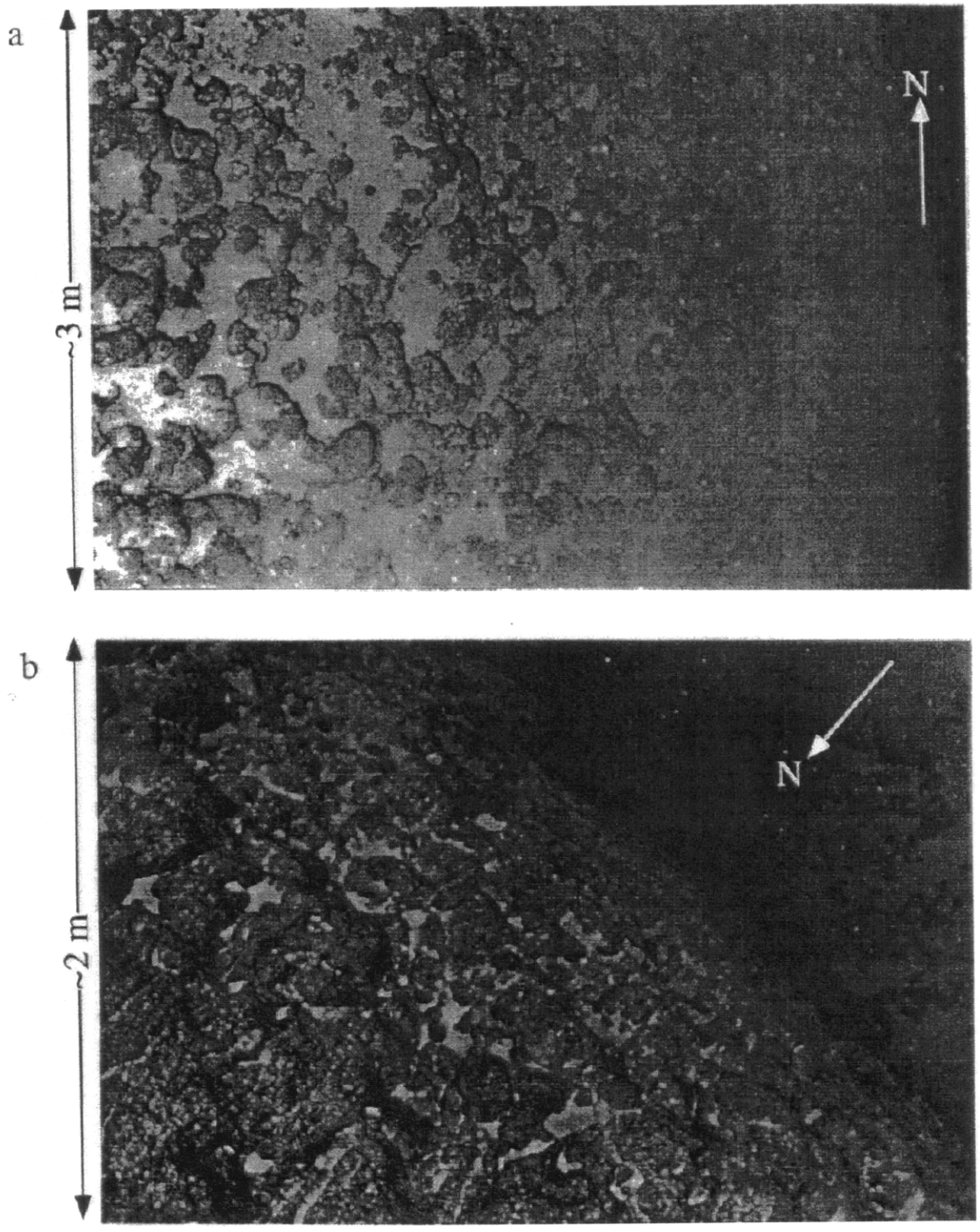

Figure 4-6: Video still images of bathymetry at sub-wavelength scales from *Goff et al.*, J. Geo. Res. 102(B7), Ref. [18], taken (a) at (191.410, 2944.65) km and (b) at (191.320, 2944.3) km, as indicated by the dots on Fig. 4-4. Both images show a dominance of features at a scale of 10-20 cm, with comparatively little roughness at any other scale.

parts of the world's oceans is that plots of their power spectral densities as a function of wavenumber yield straight lines in log-log space. This implies the relationship $S_{xx}(k) = A/k^b$, $A > 0$. In practice, the exponent b usually lies somewhere between 1 and 3. The parameters A and b (and their variants) have been used in the past both for classifying the seafloor and characterizing its roughness.

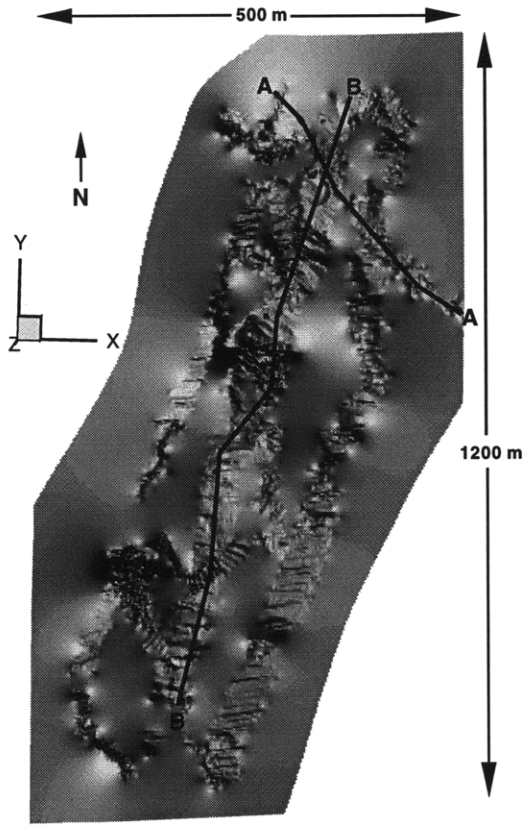

Figure 4-7: The cross-scarp (A-A) and scarp-parallel (B-B) profiles used in the spectral analysis, superimposed on a view from above of the interpolated Mesotech bathymetry.

Fig. 4-7 shows a top view of the 2 m Mesotech bathymetry shown previously in Fig. 4-4. In this view, it is easy to discern the tracks of the ROV, with characteristic width determined by the average swath width ($\simeq$ 30 m) of the mechanically swept sonar. Valid data are extracted from the bathymetry along polygonal lines passing through the ROV's tracks. The black line labeled A-A on Fig. 4-7 is used for a cross-scarp spectral estimate, and the line labeled B-B is used for a scarp-parallel

estimate. The estimates were obtained by removing the linear variation along the profile, applying a Kaiser-Bessel window of order 5, and Fourier transforming the magnitude squared of the result.

Fig. 4-8 (a) displays the resulting profile for the cross-scarp direction, and the spectral estimate along with the best-fit straight line are indicated in (b). Fig. 4-9 displays the analogous information for the scarp-parallel direction.

In both cases, the typical power-law decay is observed, with exponents b of 2.60 in (a) and 2.76 in (b). A similar spectral analysis was performed in Ref. [18]; the best-fit exponents b were found to be 2.44 ± 0.08 and 2.46 ± 0.14 for the cross-scarp and scarp-parallel directions, respectively, where the error estimates were taken from the periodograms themselves by considering their noisiness to be an empirically-defined error envelope.

This method of error estimation explains the discrepancy between the results of Ref. [18] and the values 2.60 and 2.76 obtained here. By using slightly perturbed paths for the profiles in Fig. 4-7 such that the new paths still lie on the valid, non-interpolated data within the swath width of the ROV, values of b have been found to vary by about ± 0.3. While for any given path the error estimate on the exponent may be adequately determined by the noisiness of the periodogram, this error is not representative of the uncertainty relative to other scarp-parallel or cross-scarp profiles lying within a swath width. The values presented here lie in the upper regime of the exponents encountered across different paths, because the paths were explicitly chosen to pass through 10-15 m facet-like features. The sharp slope variations in these features tend to increase the slope of the periodograms.

The *power law* form of seafloor power spectra has important mathematical implications. If a stochastic process has Gaussian statistics (refer to Chapter 5 for a rigorous definition of Gaussianity) and a power-law spectrum, it is a *fractal* random process for certain values of the decay exponent. The ensemble statistics of the process are fractal because the correlation function is self-similar, i.e $R_{xx}(a\tau) = a^{\gamma} R_{xx}(\tau)$, which implies that its full pdf is self-similar in the Gaussian case.

In the Gaussian case, individual realizations themselves have fractal properties;

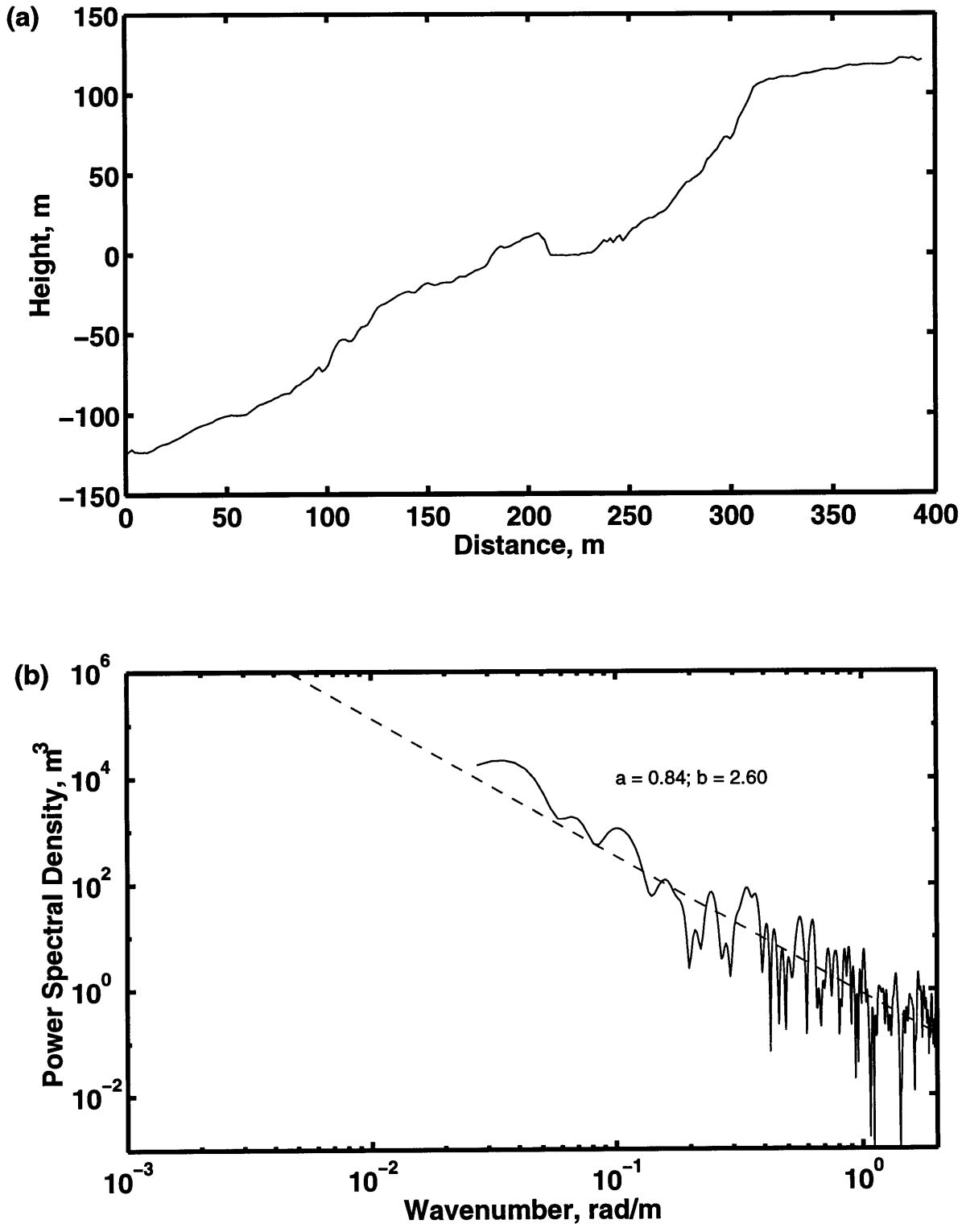

Figure 4-8: (a) Cross-scarp profile from Fig. 4-7. (b) Periodogram.

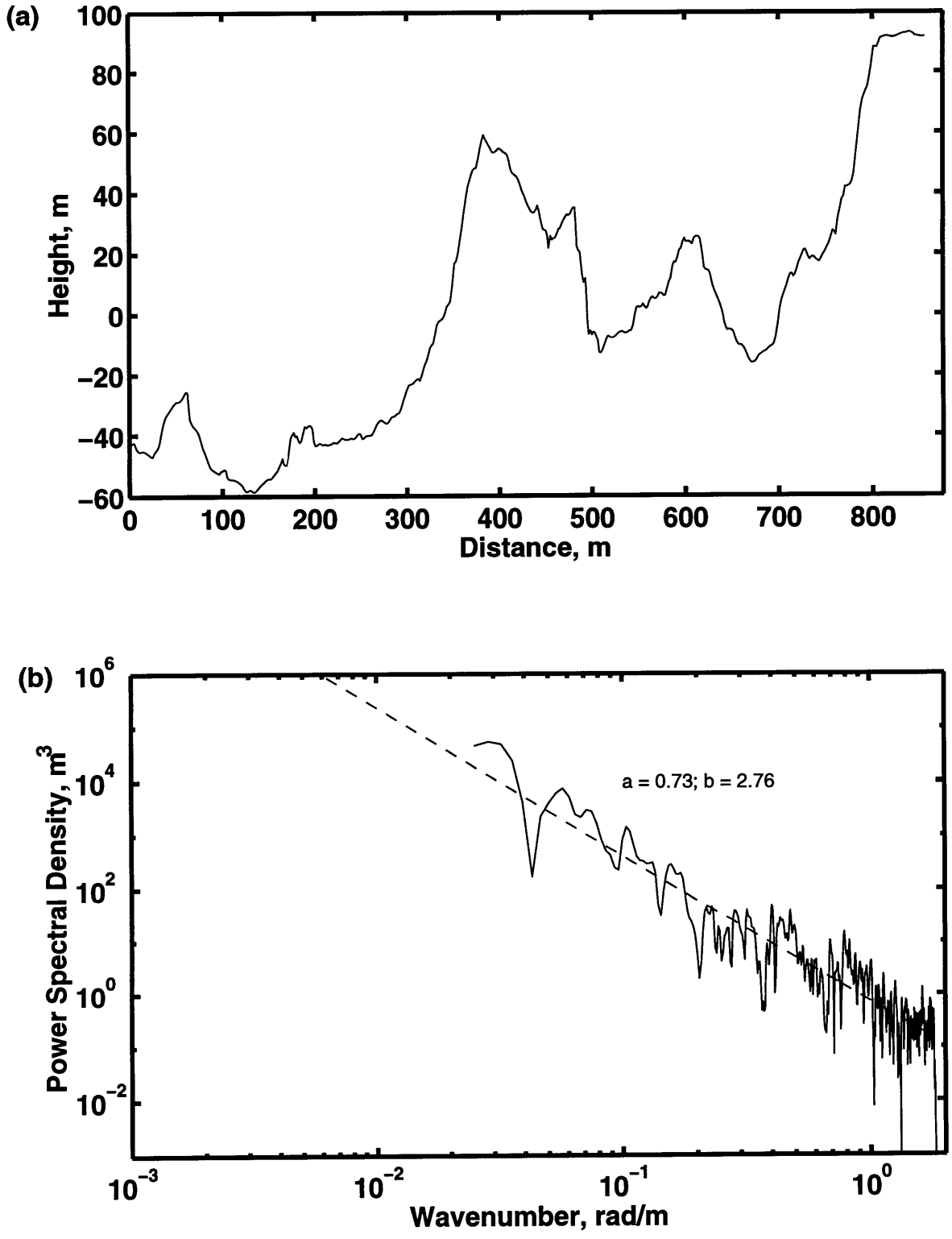

Figure 4-9: (a) Scarp-parallel profile from Fig. 4-7. (b) Periodogram.

they are non-rectifiable, i.e. the event that a disk of radius ε exists such that the surface is differentiable over this disk has probability zero for $\varepsilon > 0$. These nowhere-differentiable curves have the property of showing roughness at all scales simultaneously. Incidentally, this implies that the existence of locally smooth segments such as facets is impossible because a facet must exhibit no roughness at scales smaller than its width. Thus, a Gaussian fractal model with power-law spectrum is inadequate to model facets.

The most common stochastic model currently in use for modeling of the seafloor for acoustical purposes is the Goff-Jordan model [19] [20]. It is an anisotropic, two-dimensional, Gaussian, and fractal model which provides for a power-law decay at high wavenumbers with adjustable exponent.

One of the powerful ideas behind the Goff-Jordan model is that it can be used to extrapolate measured roughness into roughness at smaller scales. This approach is explored further for a particular realization. A 100 km by 100 km patch is generated with 60 degree anisotropy and a major to minor anisotropic axis of 4.5 and fractal dimension of 2.4. These parameters are comparable to measured values in ARSRP. The specific values of correlation length and variance were set graphically by manually scaling horizontal and vertical directions for best visual agreement with ARSRP bathymetry.

Fig. 4-10 shows a zoom-in on a 5 km x 5 km area of this patch to see how the predicted morphology at fine scales compares with the observations over similar horizontal dimensions in Fig. 4-2 and 4-3. The 60 degree large-scale anisotropy is extrapolated fully to the smaller scales by the Goff-Jordan model when in fact a different kind of anisotropy is clearly visible at the $\simeq$ 500 m scales of Fig. 4-3 in the cross-scarp canyons. The contour plot in (a) looks more like the plot of the large-scale bathymetry in Fig 2-1, based on which the model parameters were set, than 5 km scale roughness. Although specific "features" can sometimes be picked out, there is no dominant pattern and features of all sizes are equally likely to manifest themselves, as one would expect from this Gaussian model.

The fractal concept is useful in capturing the easily observable fact that the

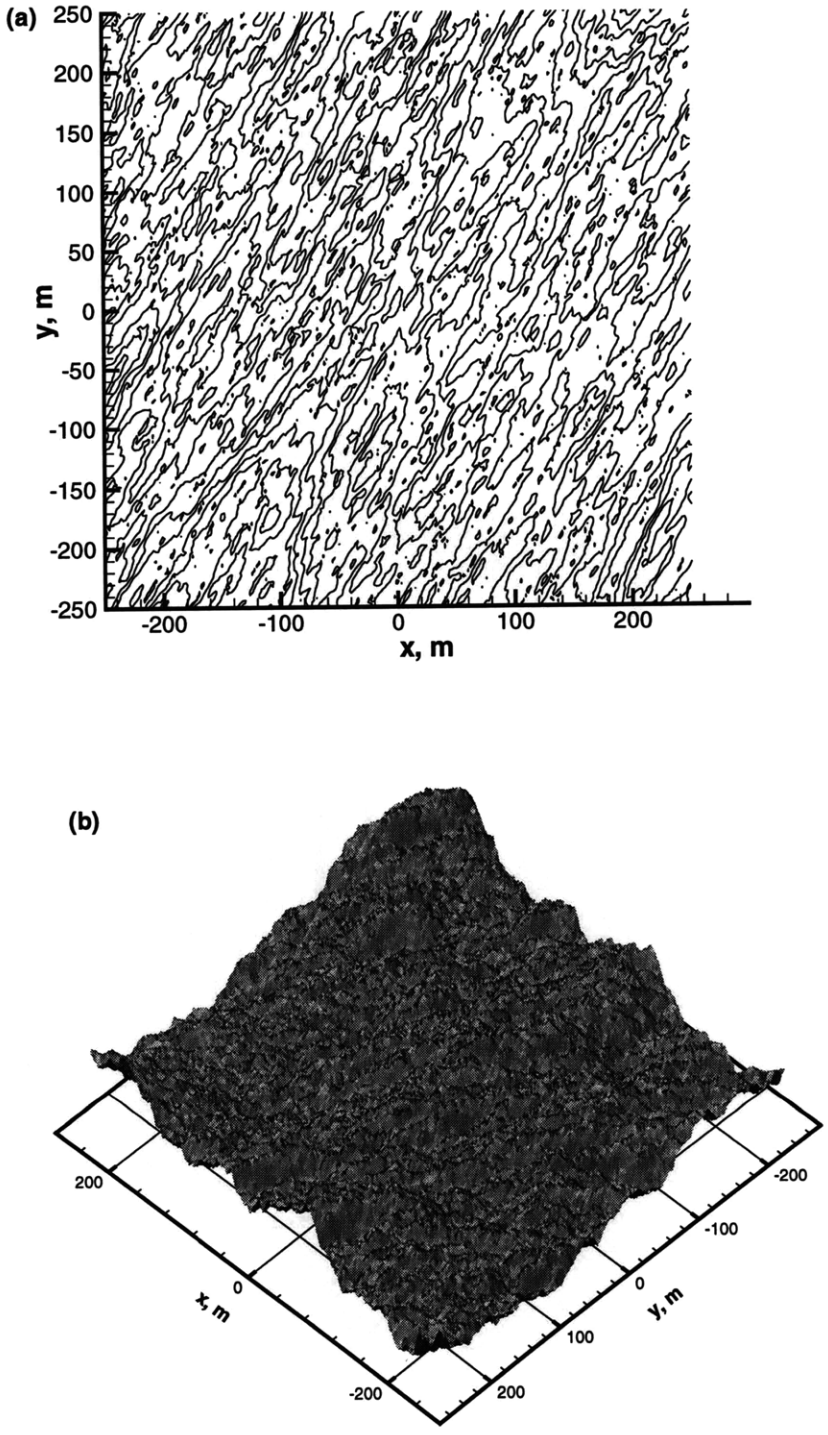

Figure 4-10: (a) Contour plot of a realization from the Goff-Jordan model with fractal dimension 2.4 and 60 degree anisotropy. (b) Carpet plot of same. The realizations of the Goff-Jordan model do not capture the canyons structures of Fig.4-3.

seafloor shows structure over a broad range of scales, from the width of the ocean's basins down to fractions of a millimeter and smaller. The difficulty with the Goff-Jordan model is that its realizations correspond to the superposition of randomized contributions at *each scale* continuously, while the seafloor emphasizes structure at a set of isolated scales.

This issue has been discussed in Ref. [24], where the variograms of profiles from the East Pacific Rise were analyzed and found to be inconsistent with self-similar and self-affine fractal models such as the Goff-Jordan model. This opens the door to proposals of seafloor models that might succeed better at matching observed scale structure.

In spite of the morphological differences, it is surprising but true that power spectral density estimates of the actual seafloor at scales of 5 km and below can match the extrapolated version of the 50-100 km scale Goff-Jordan spectrum to higher wavenumbers. This fact suggests that the power spectral density does not uniquely determine the scale structure of a random process. This subject is explored in a theoretical sense in the next chapter.

4.3 Conclusion

4.3.1 Summary of Observations

Two seemingly contradictory claims can be made about the bathymetric data. First, since structure is observed over scales spanning from centimeters to hundreds of kilometers, the data are consistent with the qualitative notion of a fractal. On the other hand, when looking over a particular range of scales, a single-scale form of roughness can be present which predominates over roughness components at adjacent orders of magnitude in scale. This kind of roughness cannot be explained by a Gaussian power-law model such as the Goff-Jordan model.

While such models may be successful in capturing the *existence* of structure over the 7 orders of magnitude considered here, it is not a useful concept in describing

seafloor morphology more precisely a few orders of magnitude about a particular scale. Since wave interactions with the seafloor impose a specific scale associated with the wavelength and the footprint, it appears more sensible to model the seafloor morphology about those scales than to attempt to simultaneously model its morphology at all scales between, say, 1/1000 th of a wavelenth and 10,000 times the wavelength.

One of the challenges of stochastic seafloor modeling is to analytically relate observed power spectral densities to proposed seafloor formation mechanisms such as faulting, erosion, sediment transport, and lava pillowing. Some of these mechanisms clearly occur at characteristic scales: faulting takes place every so many million years, and lava pillows are clustered about some characteristic mean size, as are manganese nodules. The idea that individual seafloor forming mechanisms at various scales can lead to non-fractal roughness can be found in Ref. [24] where "mathematical models of scale-dependent spatial structures are presented, and their relationship to geologic processes such as ridge evolution, crust formation, and sedimentation is discussed". On the other hand other, processes such as erosion might be expected to operate simultaneously over many scales, although clearly certain scales can be favored as evidenced by the canyons and gullies of B' scarps [67].

4.3.2 A New Seafloor Model

I entertain an alternative to the Goff-Jordan model for modeling stochastic seafloor morphology which is consistent both with the visual appearance of the bathymetry showing single-scale structures and the observed power-law spectra. The model is depicted in Fig. 4-11 for the case of one-dimensional profiles. The top part of the plot shows the logarithm of the seafloor power spectral density versus the logarithm of the wavenumber as being a straight line. This total power spectrum is seen as the superposition of a set of random processes each of which is associated with its own geological formation mechanism. Each of the individual random processes operates over a finite range of scales and either generates identifiable features clustered about some mean size or multiscale roughness over that range of scales, depending on the

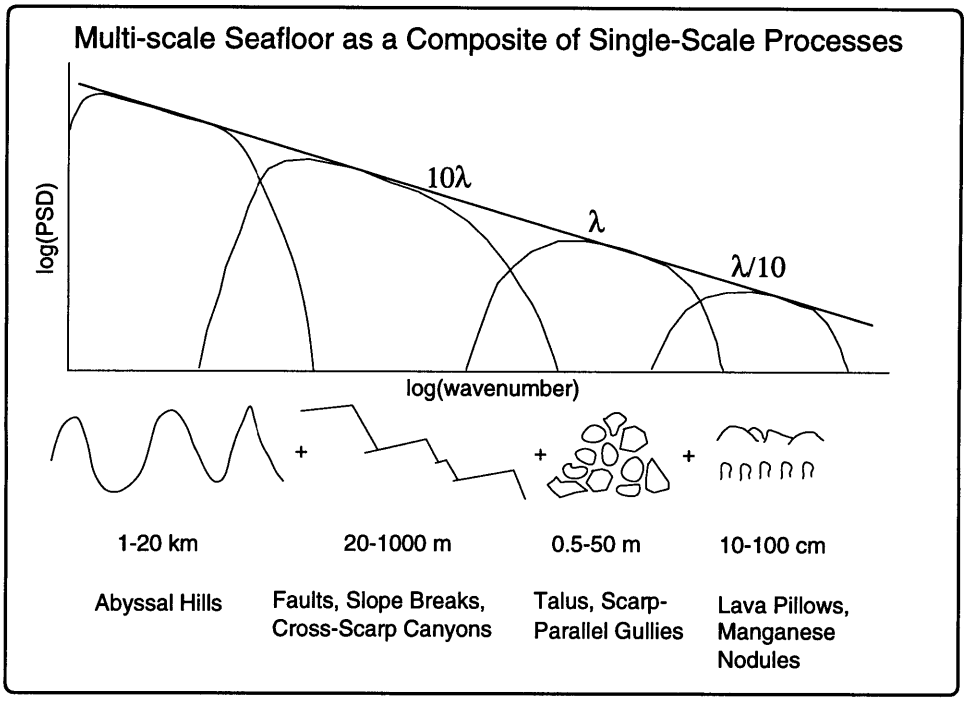

Figure 4-11: In the composite seafloor model, the existence of roughness over a range of scales spanning many orders of magnitude is explained as the superposition of single scale processes each corresponding to a specific geophysical mechanism.

underlying geophysical process. Although the example shown is for a one-dimensional profile, the idea that seafloor is composed of component single-scale processes acting at distinct scales extends to two-dimensions.

It should be apparent that an assumption was made in superimposing the individual processes: that there is a consistent scaling in going to smaller and smaller scales. This assumption is necessary in order to satisfy the observation that seafloor periodograms often exhibit a power-law decay over many orders of magnitude in wavenumber. The assumption is not without physical motivation since it is generally true that natural features which have a larger horizontal extent are also taller, although this does not prescribe a *constant* scaling. In the context of the composite model, the constant scaling would imply that totally different seafloor forming mechanisms have a common, natural length-to-width ratio.

Those readers who find this suggestion preposterous may find comfort in the fact

that there are many examples of spectra in which the decay rate abruptly changes at a certain value of wavenumber [17] [18], tending to support the intuitive idea that single-scale seafloor forming mechanisms at vastly differing scales do not operate with exactly the same height to width ratio.

Leaving this debate for another forum, I proceed to the rest of this thesis with a view of the seafloor as a composite over individual single-scale processes. The composite model as discussed so far has left the appearance of the realizations nebulous. The next chapter proposes some specific tentative models for the component single-scale processes. These processes are one-dimensional so that time-domain acoustic scatter may be computed exactly numerically in Chapter 6.

4.3.3 The Next Step

The motivation for looking at the seafloor in terms of features was the theory that acoustical glints in ARSRP are explained by locally-smooth features. It was shown in this chapter that there appear to be morphological differences between actual bathymetry and realizations of a Gaussian power-law model even when the power spectral densities match, suggesting that the power spectral density may be insufficient in describing scale structure. This proposition is verified formally in Chapter 5.

The possibility that a connection exists between the acoustical and bathymetric observations is the main focus of this thesis. The establishment of a connection requires the demonstration that surfaces with differing scale structure have different scattering properties.

In attempting this demonstration, the tone now switches from being heavily data-oriented to being highly theoretical. In particular, surfaces are modeled as one-dimensional profiles made of rigid material so that exact time-domain numerical simulations, presented in Chapter 6, can be performed on today's computers. The idealized modeling allows one to focus on scale structure from a general, theoretical perspective so as to establish its potential impact on scattering. The assumption of one-dimensionality poses some limitations on the applicability of the results to

ARSRP scattering. There are also potential effects from other mechanisms such as elastic waves. These limitations are a necessary trade-off to enable the study of scale structure from a general, conceptual perspective.

The developments in Chapters 5 and 6 provide valuable insights into the physics of scattering from feature-like and non-feature like surfaces and help interpret the ARSRP data. By applying the composite seafloor model developed here, using the feature-like surface models presented in Chapter 5 as the component single-scale processes, and extending the models to the full three-dimensional scenario of site B' scarps, it is found that including feature-like roughness gives the best match to the observed statistics of time-domain backscatter. This result supports the theory that feature-like roughness of Mid-Atlantic Ridge seafloor is an important factor in generating enhanced high-level tails in the log-envelope pdfs in a range-resolving scenario.

Chapter 5

Surface Models

In the previous chapter, it has been suggested that there is a parameter totally independent of the power spectral density in describing statistical surface morphology; this parameter was described as scale structure. In this chapter new surface models are proposed to (i) help refine the concept of scale structure, differentiating it from other attributes of a random process such as the power spectral density and Gaussianity, and (ii) generate one-dimensional realizations that capture the feature-like appearance observed in natural interfaces from which exact acoustical scatter can be computed in Chapter 6.

Two prototype feature-like models are presented and their correlation function and power spectral densities are derived analytically. The derivations reveal that in both cases, the power spectral density has a power law decay and the processes are non-Gaussian. Sample realizations of these processes are compared to Gaussian realizations having the same power spectral density and are shown to be morphologically different in spite of the identical second moments.

The feature-like processes in isolation are found to have an unnatural appearance. Two methods are proposed to bring the appearance closer to natural-looking interfaces. The first is the execution of the seafloor model laid out at the end of the last chapter involving the superposition of component single scale processes. The second is the addition of a small amount of the Gaussian, multiscale process to the feature-like realizations.

With these more natural-looking interfaces, it becomes difficult for the eye to make out the differences between the composite feature-like case and the Gaussian case. Spectral analysis is no help since by construction the Gaussian case has the same second moment as the feature-like case. Wavelets are proposed as ideal tools for differentiating scale structure where other methods fail.

5.1 On Gaussianity

Throughout this chapter and the next, references are often made to Gaussianity and to Gaussian power spectra or correlation functions. This section is intentended to define the two, establish that they are in no way connected, and point out that they make quite different statements about a random process.

The complete specification of a one-dimensional random process $f(x)$ requires the N-point joint probability density of heights $p_{\mathbf{f}}(\mathbf{F})$, where $\mathbf{f} = [f_1, f_2, \ldots, f_N]^T = [f(x_1), f(x_2), \ldots, f(x_N)]^T$ is a column vector of heights at arbitrary locations $\mathbf{x} = [x_1, x_2, \ldots, x_N]^T$ for any N. Specification of the mean $\mu(x) = \mathcal{E}[f(x)]$ and correlation function $R_{ff}(x', x'') = \mathcal{E}[f(x')f(x'')]$ fixes the first and second moments of the N-point joint probability density:

$$\boldsymbol{\mu} = \int \mathbf{F} p_{\mathbf{f}}(\mathbf{F}) d\mathbf{F}, \tag{5.1}$$

$$\mathbf{R} = \int \mathbf{F}\mathbf{F}^T p_{\mathbf{f}}(\mathbf{F}) d\mathbf{F}, \tag{5.2}$$

where $[\boldsymbol{\mu}]_i = \mu(x_i)$ and $[\mathbf{R}]_{ij} = R_{ff}(x_i, x_j)$. The expectations of products of three or more (possibly repeated) elements of $\mathbf{f}$ are unknown. In particular, none of the moments greater than two for even the *one*-point probability density are known. The unspecified moments leave room for enormous variability.

All the stochastic processes used in this thesis for surface modeling are zero-mean and wide-sense stationary. The latter condition implies that $R_{ff}(x_1, x_2) = R_{ff}(\chi)$

where $\chi = |x_2 - x_1|$. The power spectrum $S_{ff}(k)$ is then defined as the Fourier transform of $R_{ff}(\chi)$:

$$S_{ff}(k) = \int_{-\infty}^{\infty} R_{ff}(\chi) e^{-ik\chi} d\chi \tag{5.3}$$

where k is the wavenumber.

A random process is *Gaussian* if, for all sample locations $\{x_i\}$ and arbritrary dimensionality N,

$$p_{\mathbf{f}}(\mathbf{F}) = \frac{1}{(2\pi)^{N/2}|\mathbf{\Lambda}|^{\frac{1}{2}}} \exp(-\frac{1}{2}\mathbf{F}^T\mathbf{\Lambda}^{-1}\mathbf{F}). \tag{5.4}$$

where the elements of the covariance matrix $\mathbf{\Lambda}$ are given by $[\mathbf{\Lambda}]_{ij} = \mathcal{E}[(\mathbf{f}-\boldsymbol{\mu})(\mathbf{f}-\boldsymbol{\mu})^T]$, and in this case $\mathbf{\Lambda} = \mathbf{R}$ since $\boldsymbol{\mu} = \mathbf{0}$. In wide-sense stationary Gaussian processes, specification of the mean and correlation function is a complete probabilistic description. The first and second moments determine all higher order moments in the N-point density.

It is easy to get confused between a Gaussian process and a process with Gaussian spectrum. The term "Gaussian process" is used when Eq. 5.4 applies. A process has Gaussian spectrum when $R_{ff}(\chi)$, or equivalently $S_{ff}(k)$, has a Gaussian shape, as in

$$\frac{S_{ff}(k)}{\sigma_{ff}^2 l_c} = \sqrt{\pi} e^{-\frac{(kl_c)^2}{4}}. \tag{5.5}$$

where l_c is the correlation length and σ_{ff} is the variance. Neither description implies the other.

5.2 A First Attempt at a New Stochastic Surface Model

In an attempt to capture the morphology which has been observed in seafloor at various levels of resolution and which has been described as feature-like, it is neces-

sary to find some random process that will impart a feature-like appearance to the realizations. Consider the Poisson Process

$$Pr\left[N(x'') - N(x') = k\right] = \frac{\left[\lambda_r(x'' - x')\right]^k}{k!} e^{-\lambda_r(x''-x')}, \tag{5.6}$$

where $N(x'') - N(x')$ is the count of the number of transitions between x' and x''. It describes a staircase in which the length between each step is random with mean $1/\lambda_r$ and variance $1\lambda_r^2$, and the height of each step is 1, as shown in Fig. 5-1 (a). The larger λ_r, the more quickly new arrivals occur. Such a process might be a good building block for defining the horizontal dimensions of component features. Let $\{x_i\}$ be the locations of the transitions of $N(x)$, ordered by increasing size, and let $h(x)$ be a piecewise constant function defined by

$$h(x) = z_i \quad x_i \leq x < x_{i+1} \tag{5.7}$$

where the heights $\{z_i\}$ are independent, Gaussian and zero-mean with variance σ_{zz}^2, i.e. with probability density

$$p_{z_i}(Z_i) = \frac{1}{\sqrt{2\pi}\sigma_{zz}} e^{-\frac{z_i^2}{2\sigma_{zz}^2}}. \tag{5.8}$$

A sample path of this process is shown in Fig. 5-2 (a). The realization is piecewise constant over segments whose lengths are determined by the simple Poisson process, and displays smooth features of varying sizes. Incidentally, the process $h(x)$ can be represented as the derivative of the *compound Poisson process* [54]. It is intriguing to ask about the correlation function and power spectral density of $h(x)$.

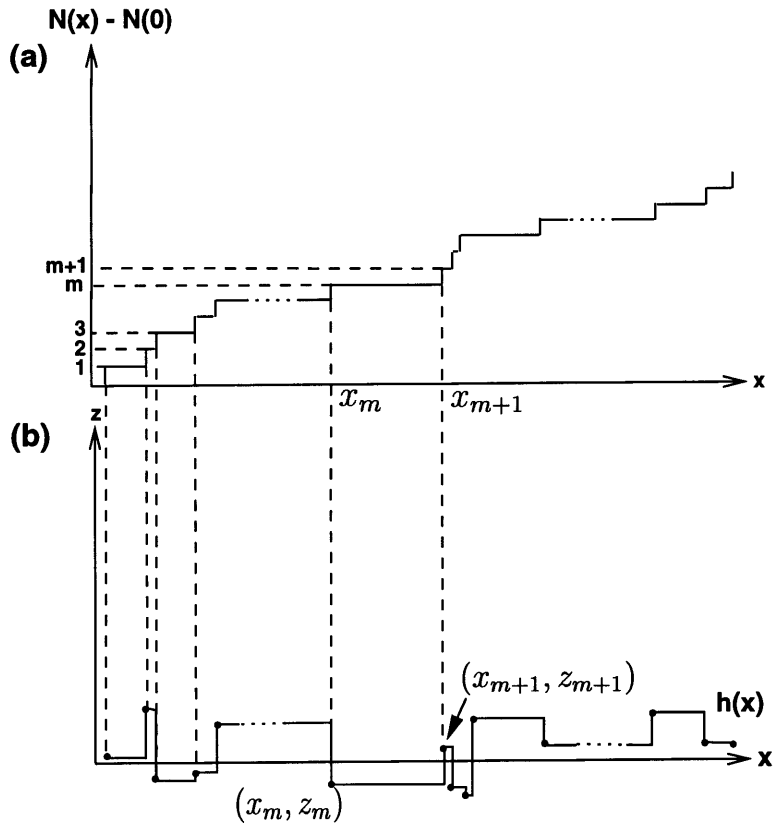

Figure 5-1: (a) A Poisson counting process $N(x)$ defines a set of transition locations x_m. (b) The process $h(x)$ is constant at height z_m between the arrivals x_m and x_{m+1}. The z_m are uncorrelated, zero-mean, and Gaussian.

The correlation function of $h(x)$, $R_{hh}(\chi)$, is given by

$$\begin{aligned} \mathcal{E}[h(x')h(x'')] &= \mathcal{E}[z_i^2]Pr[N(x'') - N(x') = 0] \\ &\quad + \sum_{|j-i|=1}^{\infty} \mathcal{E}[z_i z_j]Pr[N(x'') - N(x') = |j-i|] \end{aligned} \tag{5.9}$$

$$= \sigma_{zz}^2 e^{-\lambda_r \chi} \quad \chi = |x'' - x'|. \tag{5.10}$$

The variance is

$$\sigma_{hh}^2 = R_{hh}(0) = \sigma_{zz}^2. \tag{5.11}$$

The correlation length $l_c = 2/\lambda_r$ can be computed using Eq. C.58 in Appendix C.

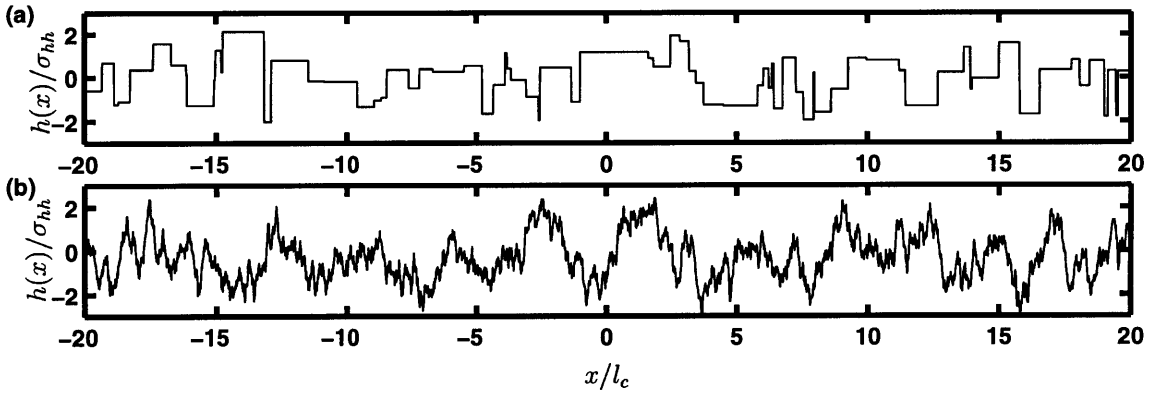

Figure 5-2: (a) Realization of piecewise contant feature-like process. (b) Realization of Gaussian process having the same second moment as the piecewise constant process, demonstrating that two processes with identical power spectral density can have vastly differing scale structure.

The power spectral density is readily obtained by Fourier transforming the correlation function:

$$\begin{aligned} S_{hh}(k) &= \int_{-\infty}^{\infty} R_{hh}(\chi) e^{-jk\chi} d\chi \\ &= \frac{1}{\lambda_r} \frac{2\sigma_{zz}^2}{1 + (k/\lambda_r)^2} \end{aligned} \tag{5.12}$$

As shown in Fig. 5-3 (a), the spectrum is effectively a low-pass filter with cutoff wavenumber of $k_c = \lambda_r = 2/l_c$ and a rolloff of 20 dB per decade. The high frequency asymptote is given by

$$S_{hh}(k) \sim 2\sigma_{zz}^2 \lambda_r / k^2 = 4\sigma_{zz}^2 l_c / (k l_c)^2 \tag{5.13}$$

as $k \to \infty$, and the limiting value of the spectrum at $k = 0$ is

$$\lim_{k \to 0} S_{hh}(k) \sim 2\sigma_{zz}^2 / \lambda_r = \sigma_{hh}^2 l_c. \tag{5.14}$$

The power-law spectrum of Eq. 5.12 and plotted on Fig. 5-3 should be familiar. It is generally associated with a one-dimensional Goff-Jordan type model, which is

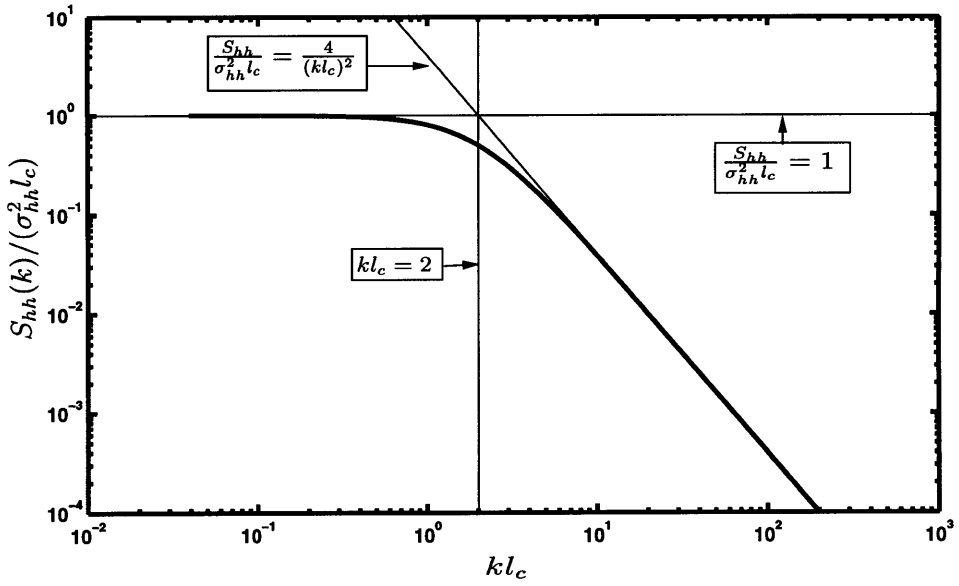

Figure 5-3: Power spectral density of the piecewise constant process, showing a power-law decay with exponent 2 past a corner wavenumber.

Gaussian and exhibits uniformily distributed independent phase components; a realization is shown in Fig.5-2 (b). It also has fractal properties; in particular, the Hausdorff dimension of its realizations is greater than the topological dimension, which implies non-rectifiability (non-differentiability) everywhere [71]. In comparison, the piecewise-constant function is non-rectifiable (non-differentiable) at a countably infinite set of points defined by the vertices.

In general, the unique Gaussian process $f(x)$ which has prescribed power spectral density $S_{ff}(k)$ can be obtained from the operation

$$f(x) = R(x) * w(x), \tag{5.15}$$

where

$$R(x) = \mathcal{F}^{-1}\left\{ |\, [S_{ff}(k)]^{\frac{1}{2}} \,| \right\}, \tag{5.16}$$

where $w(x)$ is a zero-mean stationary white Gaussian noise process with unit vari-

ance, $*$ denotes convolution and $\mathcal{F}^{-1}$ is the inverse Fourier transform operator. The resulting process is Gaussian because all LTI-filtered zero-mean Gaussian white noise signals are Gaussian processes [53].

The realizations in Fig. 5-2 (a) and (b) have identical correlation function, hence identical correlation length, variance and power spectral density, yet there are immense differences in their morphology: the two processes have different scale structure.

The Gaussian surface exhibits roughness which is evenly distributed in space at all wavenumbers as opposed to the piecewise constant process, in which the high-wavenumber roughness comes from the slope discontinuities and is concentrated at discrete points. The vertices allow the piecewise constant surface to possess as much high-wavenumber energy as the Gaussian surface while simultaneously exhibiting smooth features.

The piecewise constant process is non-Gaussian because the unique process which has Gaussian statistics *and* the power spectral density in Eq. 5.12 has fractal scale structure; the piecewise constant process, on the other hand, is non-fractal.

This idealized study of a one-dimensional profile helps in interpreting the previously troubling result that the power spectral densities of the Goff-Jordan model and actual bathymetry in Chapter 4 can be identical even when realizations appear quite different; the power spectral density of a random process does very little to constrain scale structure.

While the realizations of the piecewise-constant process may be totally adequate in principle to proceed to calculations of acoustical scatter, they have an unnatural look compared to the fractal ones, resembling more city skylines than mountain flanks.

This situation is partially alleviated when a process is designed as the superposition of a set of single-scale processes as was suggested in Chapter 4.

5.2.1 Composite Piecewise-Constant Process

Let there be N independent piecewise-constant component processes $h_i(x)$ with different rate parameters λ_r^i. The composite process $h_c(x)$ is defined as

$$h_c(x) = \sum_{i=1}^{N} h_i(x), \tag{5.17}$$

implying

$$S_{h_c h_c}(k) = \sum_{i=1}^{N} S_{h_i h_i}(k). \tag{5.18}$$

To ensure that $S_{h_c h_c}(k)$ has a power-law decay, two conditions are imposed:

1. The variance of each process is normalized so that the high wavenumber asymptotes overlap. From Eq. 5.13, this is achieved when $(\sigma_{zz}^i)^2 \lambda_r^i = \text{const.}$

2. Assuming the $\{\lambda_r^i\}$ are ordered by increasing size, the tail of $S_{h_c h_c}(k)$ at wavenumbers just beyond λ_r^i receives i contributions, while at wavenumbers lying between λ_r^{i-1} and λ_r^i, it receives only $i-1$ contributions. A jump is experienced at the corner wavenumbers of each component process. To avoid this difficulty, each component surface $h_i(x)$ is passed through a filter with a cutoff wavenumber of λ_r^{i+1}. This smooths the sharp features of component process $h_i(x)$ up to a characteristic scale determined by the subsequent process $h_{i+1}(x)$.

Fig. 5-4 shows an example in which there are three component processes with rate parameters separated by a factor of 10, i.e. $\lambda_r^{i+1} = 10\lambda_r^i$. The curve in (b) is the power spectral density of the composite process, which has the desired power law decay apart from minor ripples.

A sample realization is shown on Fig. 5-5. The top three plots are realizations at each of the component scales, and the fourth plot is the composite. The bottom plot in Fig. 5-5 shows a realization for the Gaussian case, obtained from Eq. 5.15 using the composite power spectral density on Fig. 5-4 (b).

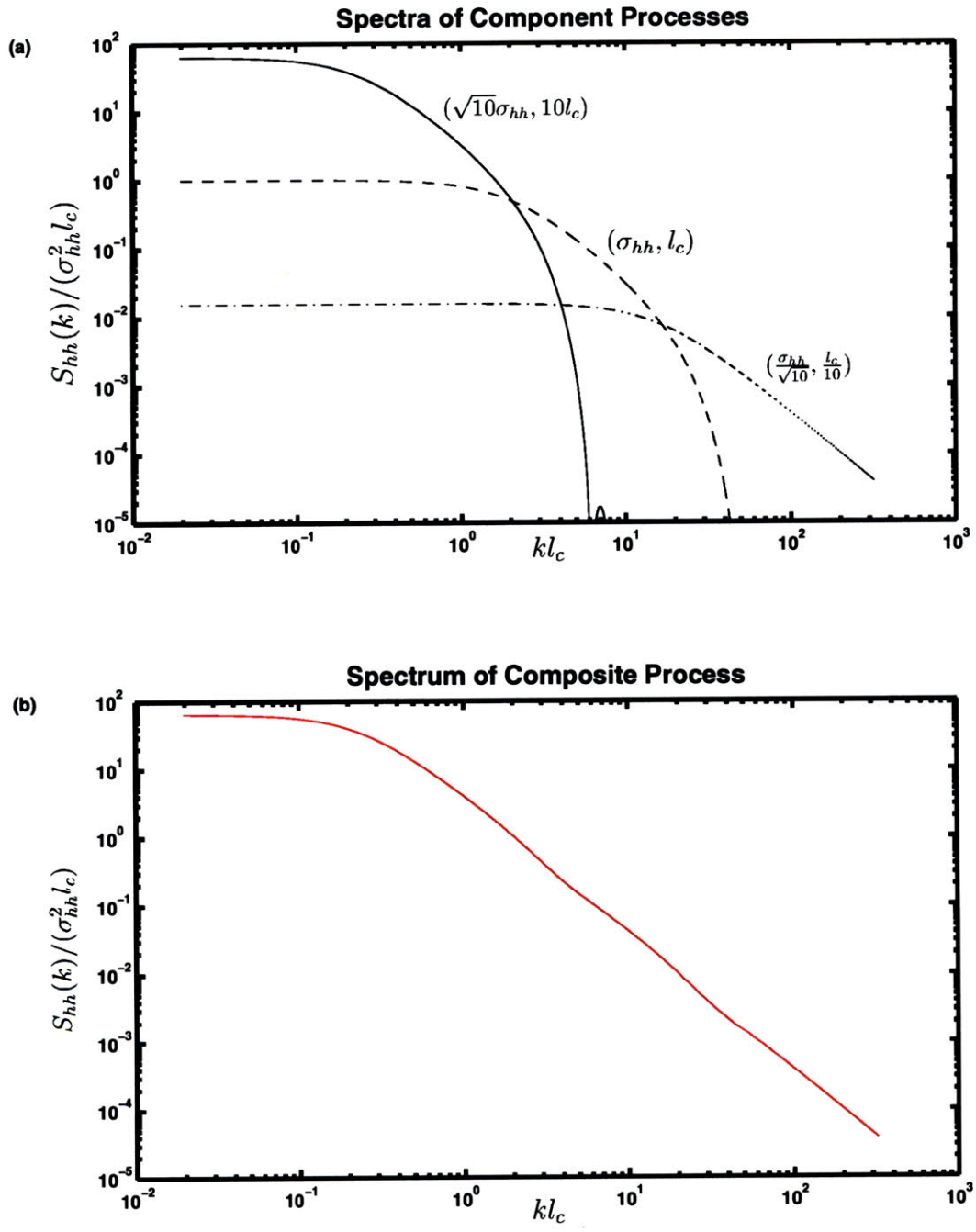

Figure 5-4: (a) Power spectra of three component single-scale processes separated by a factor of 10 in scale. The first two spectra are low-pass filtered to avoid overlap of the tails. (b) Spectrum of composite process, showing the desired power-law decay over many orders of magnitude in wavenumber. There are slight ripples where one single-scale process takes over from the previous one.

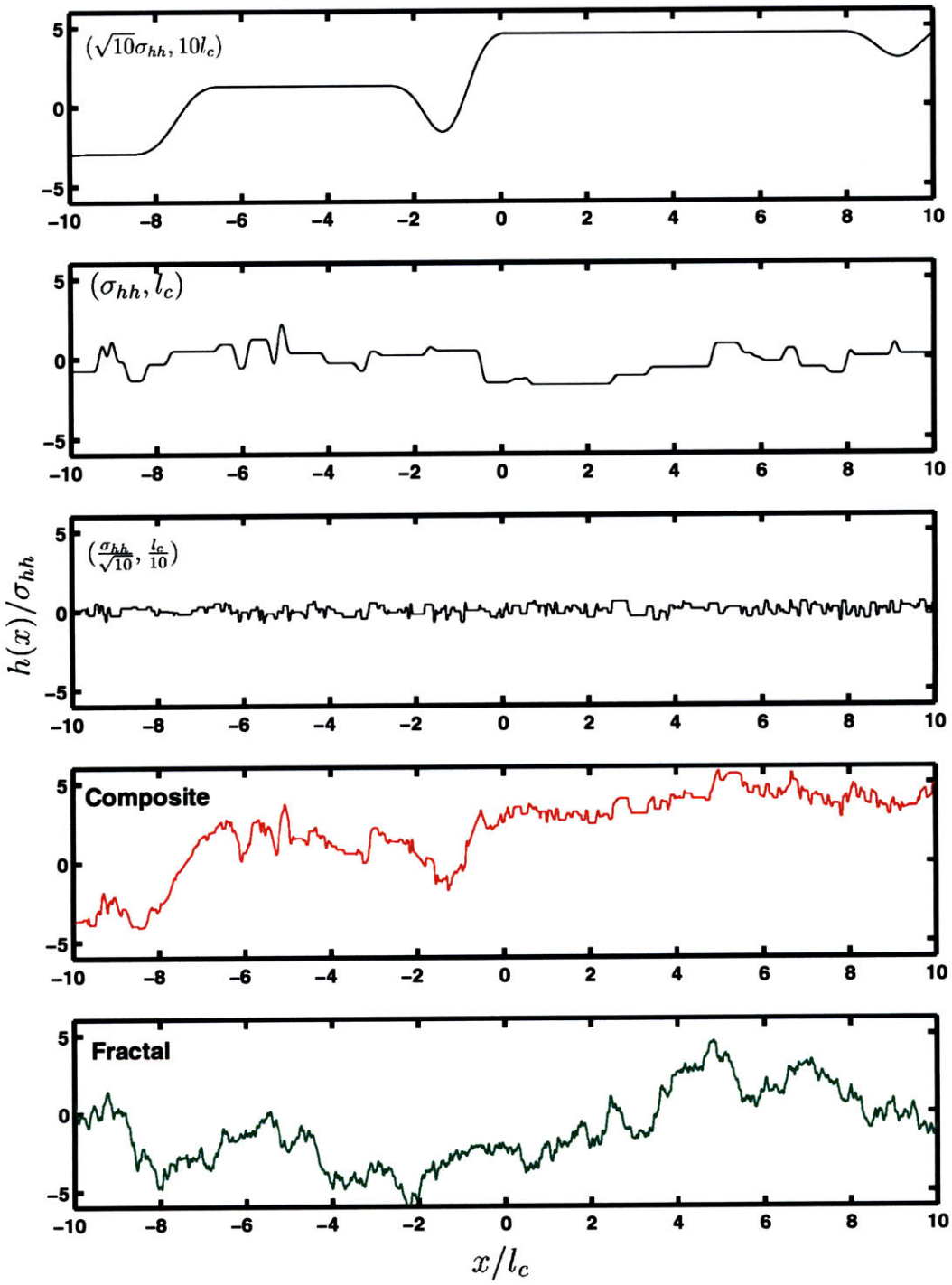

Figure 5-5: The top three plots show sample realizations of the piecewise-constant process at three scalings. The red curve in the fourth plot is the sum of the three single-scale realizations. The green curve at bottom is a fractal (Gaussian) realization having the power spectral density in Fig. 5-4 (b). The composite process has a similar natural look to the fractal case.

While the composite process's components are unnatural-looking, the composite itself appears almost as natural as the fractal case.

The fractal case with spectral decay of $\frac{1}{k^2}$ can be interpreted as the superposition of infinitely many low-pass filtered piecewise-constant processes across all scales *continuously*, that is, with inter-rate parameter ratios approaching 1. With this interpretation, one can see that any composite process assembled as described in this section gains a natural look when there is a sufficient number of component processes and if their rate parameters are sufficiently close, but if this approach is taken too far, the feature-like nature of the composite process is lost. This method of superposition is reminiscent of techniques for the synthesis of fractal $1/f$ processes using wavelets in Ref. [71]. See Appendix E for a definition of $1/f$ processes.

It is to be noted that other fractal composite processes than the Gaussian one mentioned above can be created. The case $\lambda_i = A\lambda_{i+1}$ where A is not small and $N \to \infty$, is fractal both in the sense of Hausdorff dimension and in the sense of self-similarity, but its scale structure is different from the Gaussian case; it remains feature-like.

5.2.2 Summary

This section has developed a framework for stochastically modeling surfaces in such a way as to respect naturally observed power law spectra and simultaneously incorporate the notion of aggregate single-scale processes, each possibly stemming from a unique physical mechanism. By comparison with Gaussian processes with identical spectra, it has been established that the power spectral density does not fix the scale structure of surfaces.

The simplified model investigated here to represent the component single-scale processes has the disadvantage of having a fixed rate of decay in wavenumber, with energy decaying as the wavenumber to the negative second power. One is also constrained to representing all features as piecewise-constant. As such, this model is not as versatile as the Goff-Jordan model in which decay rates can be matched empirically to data. As discussed in Section 5.5, filtering techniques can help attain different

inter-vertex shapes and rates of decay, but there are limitations. These limitations lead to a new effort, called the Facet random process. It is analogous to the process presented in this section except that the variation is linear between the vertices.

5.3 The Facet Random Process

In the hopes of generating more realistic-looking realizations and being able to model one more rate of decay at high wavenumbers, I now explore the case where a linear variation exists between vertices.

The Facet random process $h(x)$ is defined as follows:

$$h(x) = z_m + \left(\frac{x - x_m}{x_{m+1} - x_m}\right)(z_{m+1} - z_m), \quad x_m \leq x < x_{m+1} \tag{5.19}$$

where the $\{x_i\}$ are given by the Poisson process in Eq. 5.6 and the heights $\{z_i\}$ are Gaussian as before, but with a potentially non-white stationary discrete correlation function $R_{zz}[k] = \mathcal{E}[z_j z_i]$ where $k = |j - i|$.

5.3.1 Uncorrelated Vertices

In this section, the focus is on $h^{(0)}(x)$, defined as the case of $h(x)$ where the set $\{z_i\}$ is a discrete Gaussian white noise sequence:

$$R_{zz}^{(0)}[k] = \begin{cases} \sigma_{zz}^2, & k = 0 \\ 0, & k \neq 0. \end{cases} \tag{5.20}$$

A realization of this process is shown in Fig. 5-6 (a). The Facet process has the following correlation function which is derived fully in Appendix C:

$$\begin{aligned} R_{hh}^{(0)}(\chi) &= \mathcal{E}[h(x')h(x'')] = \mathcal{E}\left[\left(z_m + \left(\frac{x' - x_m}{x_{m+1} - x_m}\right)(z_{m+1} - z_m)\right) \times \right. \\ &\quad \left. \left(z_n + \left(\frac{x'' - x_n}{x_{n+1} - x_n}\right)(z_{n+1} - z_n)\right)\right] \\ &= \sigma_{zz}^2 \left(2E_4(\lambda_r \chi) + E_2(\lambda_r \chi) * E_2(\lambda_r \chi)\right). \end{aligned} \tag{5.21}$$

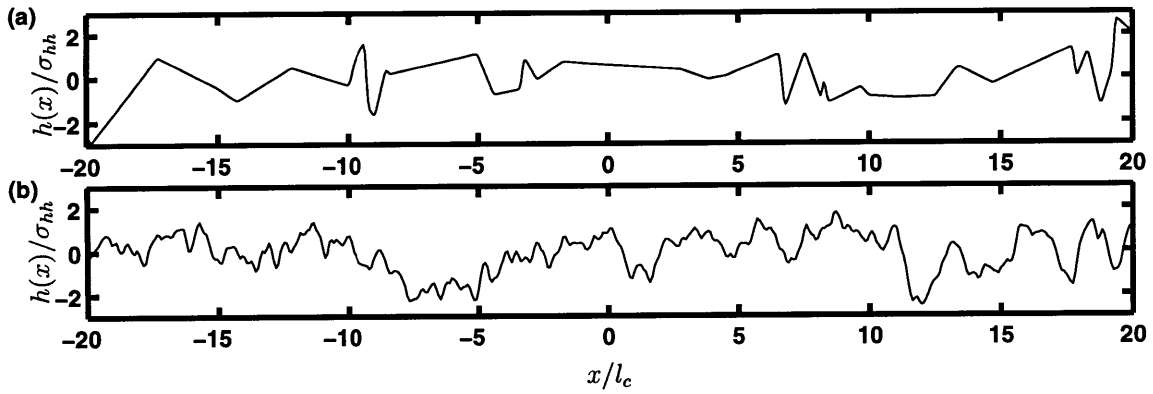

Figure 5-6: (a) Realization of the uncorrelated vertex Facet process. (b) Realization of the Gaussian process with second moment identical to the Facet process, demonstrating once more that second moment characterizations are insufficient to fix scale structure in random processes.

where $*$ denotes convolution and $\chi = |x'' - x'|$. $E_n(x)$ is the n-th order exponential integral for $x \geq 0$ and is zero for $x < 0$:

$$E_n(x) = \begin{cases} \int_1^\infty e^{-xu} u^{-n} du, & x \geq 0 \\ 0, & x < 0. \end{cases} \tag{5.22}$$

The resulting power spectrum, also derived in Appendix C, is:

$$\begin{aligned} S_{hh}^{(0)}(k) &= \frac{2\sigma_{zz}^2}{\lambda_r} \left[\frac{2\arctan(k/\lambda_r)}{(k/\lambda_r)^3} \right. \\ &\left. + \frac{1}{(k/\lambda_r)^4} \left(\ln^2(\sqrt{1+(k/\lambda_r)^2}) - \ln(1+(k/\lambda_r)^2) - \arctan^2(k/\lambda_r) \right) \right]. \end{aligned} \tag{5.23}$$

The variance of $h^{(0)}(x)$ is $(\sigma_{hh}^{(0)})^2 = \frac{2}{3}\sigma_{zz}^2$, and its correlation length is:

$$l_c^{(0)} = \frac{1}{\lambda_r} \frac{10}{3\sqrt{3}}. \tag{5.24}$$

The Facet surface has a power-law spectrum as can be seen by its asymptotic

behaviour at large k.

$$\text{As } k \to \infty, S_{hh}^{(0)}(k) \to 2\pi \frac{\sigma_{zz}^2 \lambda_r^2}{k^3} = \pi \left(\frac{10\sigma_{hh}^{(0)}}{3l_c^{(0)}} \right)^2 \frac{1}{k^3} \tag{5.25}$$

This expression shows that Facet process provides a rigid rate of decay of the power spectral density with wavenumber equal to 3. Methods for obtaining other rates of decay are discussed in Section 5.5.

The value of the spectrum at $k = 0$ is

$$\lim_{k \to 0} S_{hh}^{(0)}(k) = \frac{3}{2} \frac{\sigma_{zz}^2}{\lambda_r} = \sqrt{3} \frac{27}{40} (\sigma_{hh}^{(0)})^2 l_c^{(0)}. \tag{5.26}$$

The spectrum of $h^{(0)}(x)$ is essentially a low-pass filter with a gain of $\frac{3}{2}\frac{\sigma_{zz}^2}{\lambda_r}$, a rolloff of 30 dB per decade and a corner wavenumber of $\left(\frac{4\pi}{3}\right)^{\frac{1}{3}} \lambda_r$. The corner wavenumber is calculated as the intersection point of the high-frequency asymptote with a line of zero slope passing through the spectrum's origin in log-log space, as shown in Fig. 5-7.

As with the piecewiese-constant case, there is a Gaussian counterpart to the Facet process having identical power spectral density. Realizations can be generated using Eq. 5.15 with $S_{ff}(k)$ set to $S_{hh}^{(0)}(k)$. Such a realization is shown in Fig. 5-6 (b). emphasizing once more the important point that scale structure is not determined by the power spectral density.

5.3.2 Arbitrary Inter-Vertex Correlation

The correlation function, power spectral density, correlation length and variance for the case of arbitrary inter-vertex correlation function are derived in Appendix C. As a means of numerically validating the derivations, this section presents Monte Carlo estimates of the power spectral density of the Facet process in the general case of correlated vertices. The estimates are compared to the analytical form in Eq. C.54.

In particular, the special case of a Gaussian inter-vertex correlation function is

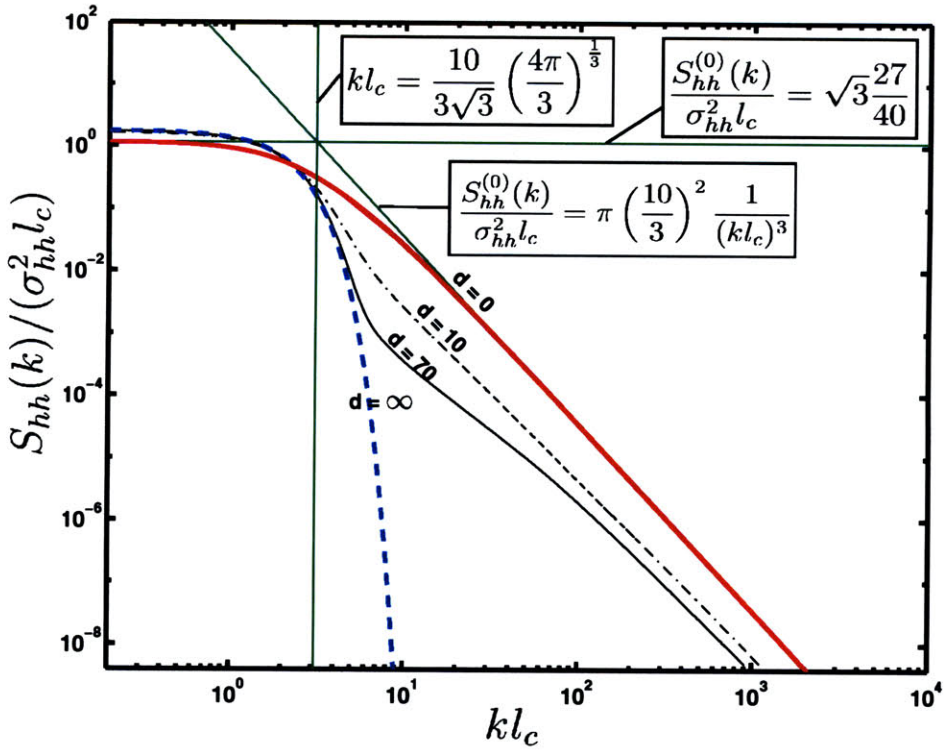

Figure 5-7: Non-dimensionalized Facet spectra with Gaussian inter-vertex correlation having d correlated vertices. $d = 0$ (red) corresponds to uncorrelated vertices. The corner wavenumber for this case, along with the high and low frequency asymptotes, are shown in green. $d = \infty$ yields a Gaussian spectrum (light blue). Intermediate values of d tend to match the Gaussian spectrum at low wavenumbers while maintaining a $1/k^3$ rolloff at high wavenumbers.

adopted:

$$R_{zz}[k] = \sigma_{zz}^2 e^{-\frac{k^2}{d^2}}, \tag{5.27}$$

where the parameter d is roughly the number of adjacent vertices which are correlated. The case $d = 0$ corresponds to the uncorrelated vertex process $h^{(0)}(x)$. As can be seen in Fig 5-7, when d is non-zero and finite, the spectrum of $h(x)$ has a Gaussian shape at low wavenumbers but retains the characteristic power-law decay with exponent -3 at high wavenumbers. As d increases, the facets have to be made progressively smaller to maintain constant correlation length and variance, and at the limiting value of

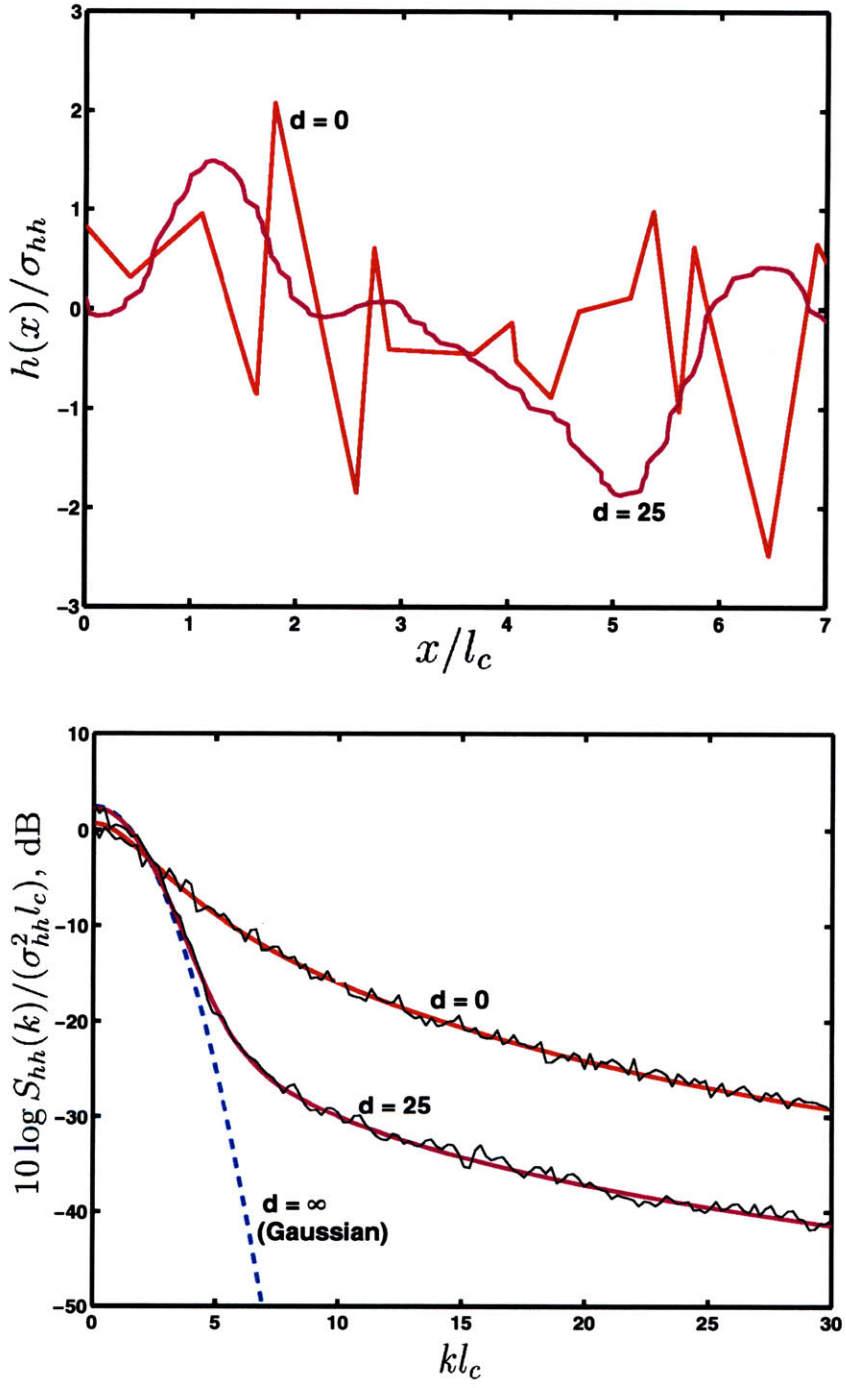

Figure 5-8: (a) Non-dimensional sample realizations of the Facet process with Gaussian inter-vertex correlation function for $d = 0$ (red) and $d = 25$ (magenta). (b) Monte Carlo spectral estimates for $d = 0$ and $d = 25$ (black lines) compared to analytical expressions for the spectra (colored lines).

$d = \infty$, the facets have infinitesimal length. The case of $d = \infty$ leads to $h(x)$ being a Gaussian process with no slope discontinuitites having the Gaussian spectrum in Eq. 5.5. Similarly, all Gaussian processes can be represented as a Facet process with vanishing facet size. This is due to the fact that the vertex heights $\{z_i\}$ are Gaussian.

For the Monte Carlo spectral estimates, two cases are studied, $d = 0$ and $d = 25$. The spectral estimates are obtained through the formula

$$\hat{S}_{hh}(k) = \frac{1}{N} \sum_{i=1}^{N} |\mathcal{F}(q(x)h_i(x))|^2 , \tag{5.28}$$

where $\hat{S}_{hh}(k)$ is the spectral estimate, $\mathcal{F}$ is the Fourier transform operator, $h_i(x)$ is the ith of a total of $N = 50$ independent surface realizations, and $q(x)$ is an appropriately chosen taper. Figure 5-8(a) shows one surface realization for both $d = 0$ and $d = 25$ and 5-8(b) demonstrates the excellent agreement between the Monte Carlo estimated spectra and the analytical results. The case of nonzero d is not studied further in this thesis, so references to the Facet process can be assumed to mean the uncorrelated vertex Facet process.

5.3.3 The Composite Facet Process

Remembering that the motivation for proposing feature-like processes was to capture observed structure in a natural interface, I now study how qualitatively "natural" the superposition of single-scale processes appears compared to the fractal case. As in the piecewise constant case, the component processes are normalized so that their high-wavenumber asymptotes overlap, and they are low-pass filtered and separated by a factor of 10 in scale.

The three first plots in Fig. 5-10 show the component realizations; the fourth plot shows the composite. The fifth plot is a realization from the Gaussian process generated using Eq. 5.15 and the composite process's spectrum shown in Fig. 5-9 (b).

It can be concluded that the unnatural-looking isolated single-scale process gains a much more natural look when viewed as but one of several single-scale processes

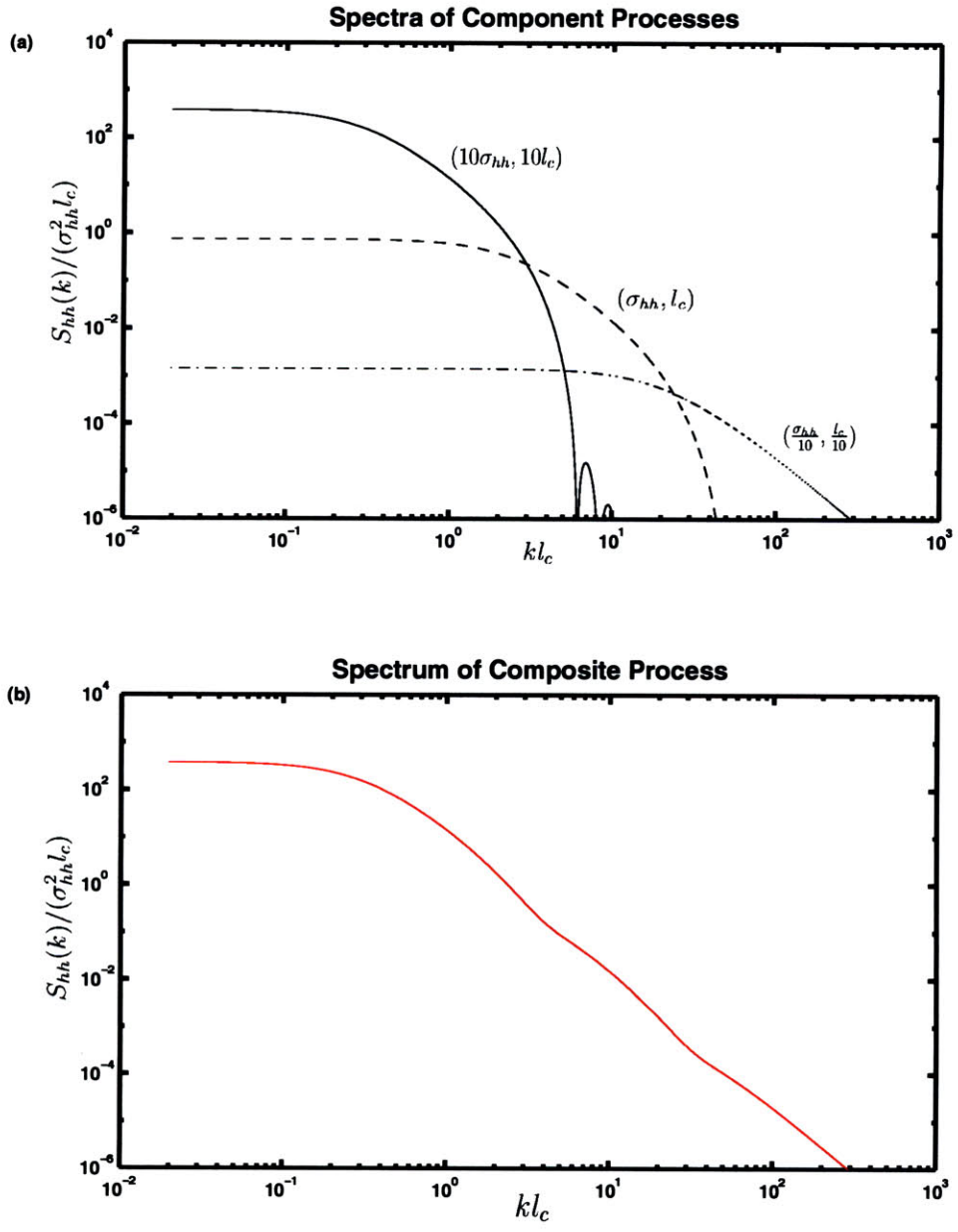

Figure 5-9: (a) The spectra of three Facet processes differing by a scale factor of 10. (b) The spectrum of the superposition of the three Facet processes in (a).

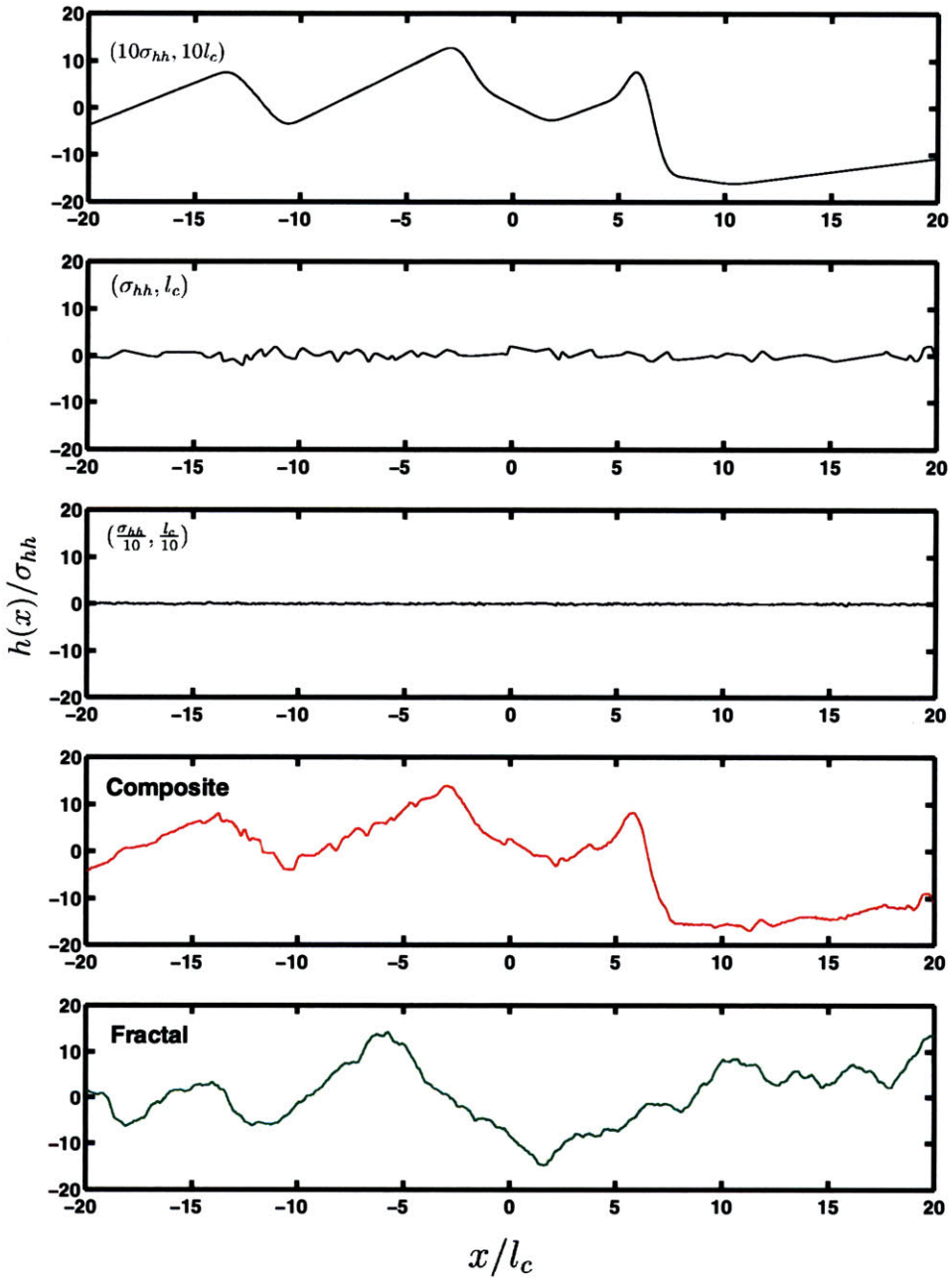

Figure 5-10: The top three plots are the realizations of low-pass filtered Facet processes at three scalings. The red curve is the superposition of the three Facet realizations, and the green curve is a Gaussian realization using the power spectral density in Fig. 5-9 (b). The composite and Gaussian realizations qualitatively look similar but nevertheless differ in scale structure.

acting in concert at different scales. It is not necessary to give up the satisfying look of fractal realizations when viewing the seafloor as a result of composite single-scale formation mechanisms.

5.3.4 Hybrid Facet Process

In conceding to the possibility that certain seafloor-forming mechanisms could be truly multi-scale as opposed to composite feature-like, it is interesting to consider the case in which some multi-scale roughness is added to the Facet process. Multi-scale effects in seafloor shaping could result from the cumulative of effects of erosion and sedimentation occuring over millions of years, gradually eroding the clarity of the original feature-like character.

In this section, I consider three random processes $f^1(x)$, $f^2(x)$, and $f^3(x)$ where $f^1(x)$ is the Facet Process with uncorrelated vertices, $f^2(x)$ is the corresponding Gaussian process with identical power spectral density which I define as the GPL process, and $f^3(x)$ is a power-conserving linear combination of the first two:

$$f^3(x) = \frac{af^1(x) + bf^2(x)}{\sqrt{a^2 + b^2}}. \tag{5.29}$$

The process $f^3(x)$ is termed Hybrid. As an example case the values $a = \sqrt{3}$ and $b = 1$ are picked such that 3/4 of the roughness energy comes from the Facet process and only 1/4 from the multi-scale process. A realization of each of these processes is displayed on Fig. 5-11; all three functions have the same power spectral density.

Given that 3/4 of the energy comes from the Facet process, it is not surprising that some of the prominent features in the Facet realization are visible in the Hybrid realization. What is surprising is that the eye has a tendency of seeing the GPL and Hybrid processes as qualitatively most similar. Looking at the Hybrid realization in isolation, one might be ready to concede right away that it appears fractal and therefore well-represented by something like the Goff-Jordan model. Amazingly, 75% of the energy comes from a process which is far from being fractal. The fact that the human eye can't always be relied on in detecting non-fractal roughness is not

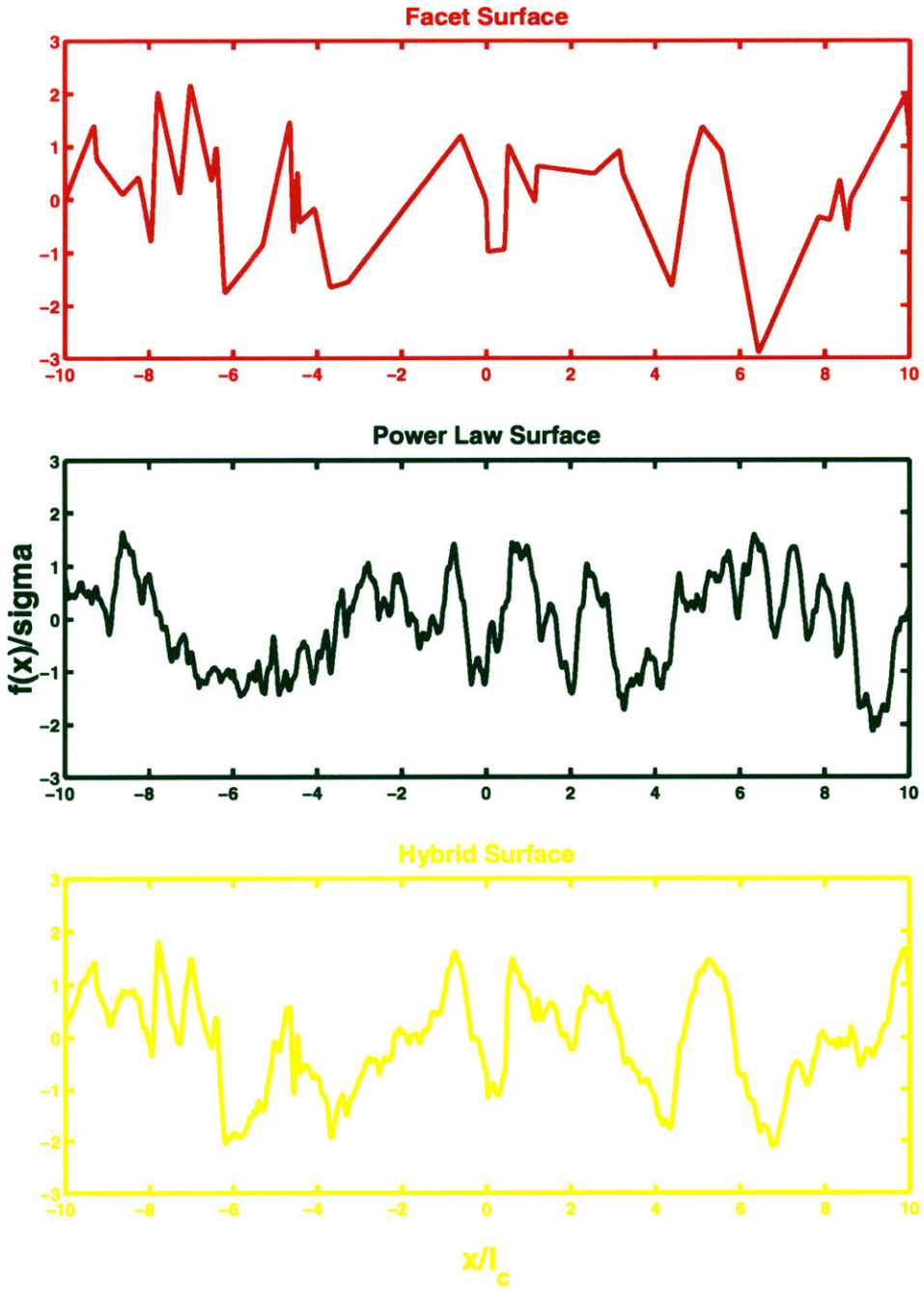

Figure 5-11: Realizations from three processes with identical power spectral density. The red plot is a Facet realization, the green plot is of the corresponding Gaussian process, and the yellow plot is of a Hybrid surface obtaining 75% of its energy from the Facet process and 25% from the Gaussian process. The Hybrid and Gaussian surfaces appear more similar than any other choice of two surfaces.

palliated by spectral analysis since all three processes have identical spectrum.

In the quest to understand how a single-scale seafloor-forming mechanism could contribute to an overall profile, it is important to be able to detect the "signal" corresponding to the feature-like roughness amidst the "noise" of fractal roughness. The non-detection of underlying feature-like processes has the potentially serious consequence of not being able to link statistical seafloor models and seafloor-forming processes.

As will be shown in the next chapter, proper characterization of scale structure is also important to predict mean scattering strengths and time-domain statistics of acoustic scatter.

If neither the qualitative look of the profiles nor conventional spectral analysis can be relied on to detect scale structure differences, which tool could succeed at this task? I propose that statistical wavelet analysis is ideal and show how it may be used in the next section.

5.4 Wavelet Analysis

In the preceding sections, scale structure was shown not to be determined by the power spectral density. This was primarily due to the fact that the power spectral density is a second moment quantity and that the differences in scale structure in the functions considered were attributable to differences in the higher moments.

The power spectral density is an awkward choice to characterize scale structure not only because it is a second-moment quantity, but also because it has no spatial localization ability. The concept of scale structure attempts to capture the spatial arrangement of features at different scales; it is a space-scale, or time-frequency concept. The complex exponential eigenfunctions functions used in Fourier analysis have infinite spatial extent. On average, a feature with sharp edges generates the same high-wavenumber energy as a series of smaller features distributed evenly in space.

The shortcomings of the Fourier transform do not doom scale structure to remain a qualitative concept. Multiresolution analysis, and in particular the Wavelet

tranform (Appendix E, [59] [71] [49] [9] [16] [69] [26] [32] [15] [66]), have introduced rigorous mathematical frameworks that enable localization in both space and scale. The wavelet transform is used in this section to demonstrate that scale structure *can* be characterized quantitatively. In particular, the continuous wavelet transform of single realizations and the statistics of wavelet transform coefficients for ensembles of realizations are presented for the thre Facet, GPL, and Hybrid processes defined in the previous section.

Unlike conventional spectral analysis, wavelet analysis allows a choice of many eigenfunctions each of which leads to a different decomposition. For the purposes of differentiating processes that may or may not contain piecewise-linear segments, the Daubechies 2 wavelet is a good candidate because it is orthogonal to linear variations.

5.4.1 Deterministic Continuous Wavelet Transform

Figure 5-12 is a depiction of the same three realizations as in Fig. 5-11 with a color contour plot in the background representing the logarithm of the energy in the continuous wavelet transform as a function of scale (y-axis) and space (x-axis). Note that the y-axis applies to the contour plots of the wavelet transform and not to the plots of the realizations. Both axes are normalized to correlation length. The scale parameter is roughly the length of the analyzing wavelet and the x-axis indicates where on the surface that analyzing wavelet is centered.

The dark areas in the case of the Facet realization in red corresponds to those areas where the wavelets lie entirely within one of the facets and yield zero energy. If a wavelet at a given scale is smaller than a facet, all smaller-scale wavelets centered at that position also yield zero energy. The larger facets yield zero energy beginning at larger scales, as would be expected.

On the other hand, neither the fractal nor the Hybrid cases show an obvious dependence across scale. Instead, the loci where the wavelets yield zero energy form a complex pattern of fractal bifurcations. Overall, the three plots in Fig. 5-12 demonstrate that the continuous wavelet transform of an individual realization does not provide any more information than could have been obtained just by looking at the

surfaces.

This example suggests that a statistical wavelet analysis might be better suited for differentiating scale structure in stochastic processes. This endeavor is undertaken with advance warning that along with conventional spectral analysis, qualitative perusal of realizations, and deterministic wavelet methods, statistical measures based on wavelets will *also* fail to detect differences between processes having identical second moment but different scale structure unless moments greater than 2 are considered. This is demonstrated in Appendix E and results from the fact that the wavelet transform is a linear operator.

5.4.2 Statistics of Wavelet Transform Coefficients

Whereas the continuous wavelet transform was used in the deterministic case, I now turn to the wavelet transform proper, which yields a set of wavelet coefficients evaluated at discrete intervals in scale and space, as explained in Appendix E.

Among the many combinations of higher moments from the general N-point probability density function, only one is analyzed here: the full one-point pdf of the wavelet coefficients at one scale. The pdfs are obtained by forming histograms from the wavelet coefficients using 50 independent realizations of each process. In Fig. 5-13, the histograms for the coefficients at a scale of approximately one tenth of a correlation length are presented.

The histograms are normalized to unit variance, and the blue curves in each plot represent a zero-mean, unit variance Gaussian pdf. The GPL case yields nearly-Gaussian wavelet coefficients and the Facet case yields highly non-Gaussian coefficients. The Hybrid surface lies between the two extremes, signifying that the statistical wavelet decomposition has differentiated the scale structure of all three surfaces.

For the GPL surface, it has been shown [71] that Gaussian processes with power-law power spectral densities are fractal and yield wavelet coefficients which are Gaussian and quasi-independent of one another across both scale and space. In light of this fact, the Gaussian result in the GPL surface is not surprising.

The wavelet coefficients are non-Gaussian in both the Hybrid and Facet cases in

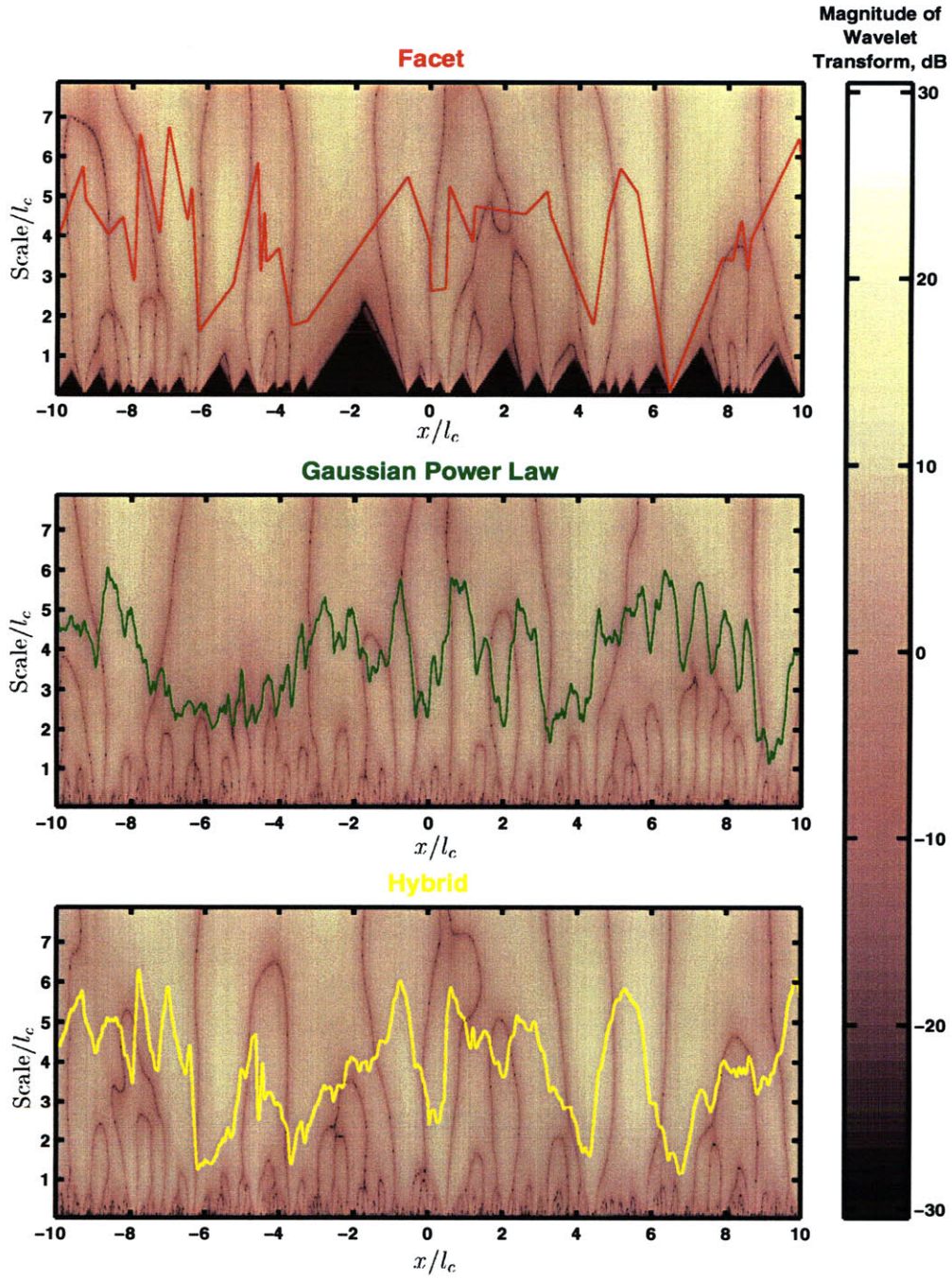

Figure 5-12: Contour plot of the magnitude of the Continuous Wavelet Transform using a Daubechies 2 wavelet, in dB. The x-axis is spatial position along the surface and the y-axis is the scale parameter corresponding to the spatial extent of the analyzing wavelet. At the top of each figure, the analyzing wavelet is 8 correlation lengths long, and at the bottom, its length is infinitesimal. The CWT does not significantly enhance one's ability to distinguish between the Hybrid (yellow) and Gaussian (green) realizations. The dark areas in the Facet case (red) occur when the size of the wavelet is smaller than the horizontal extent of a facet.

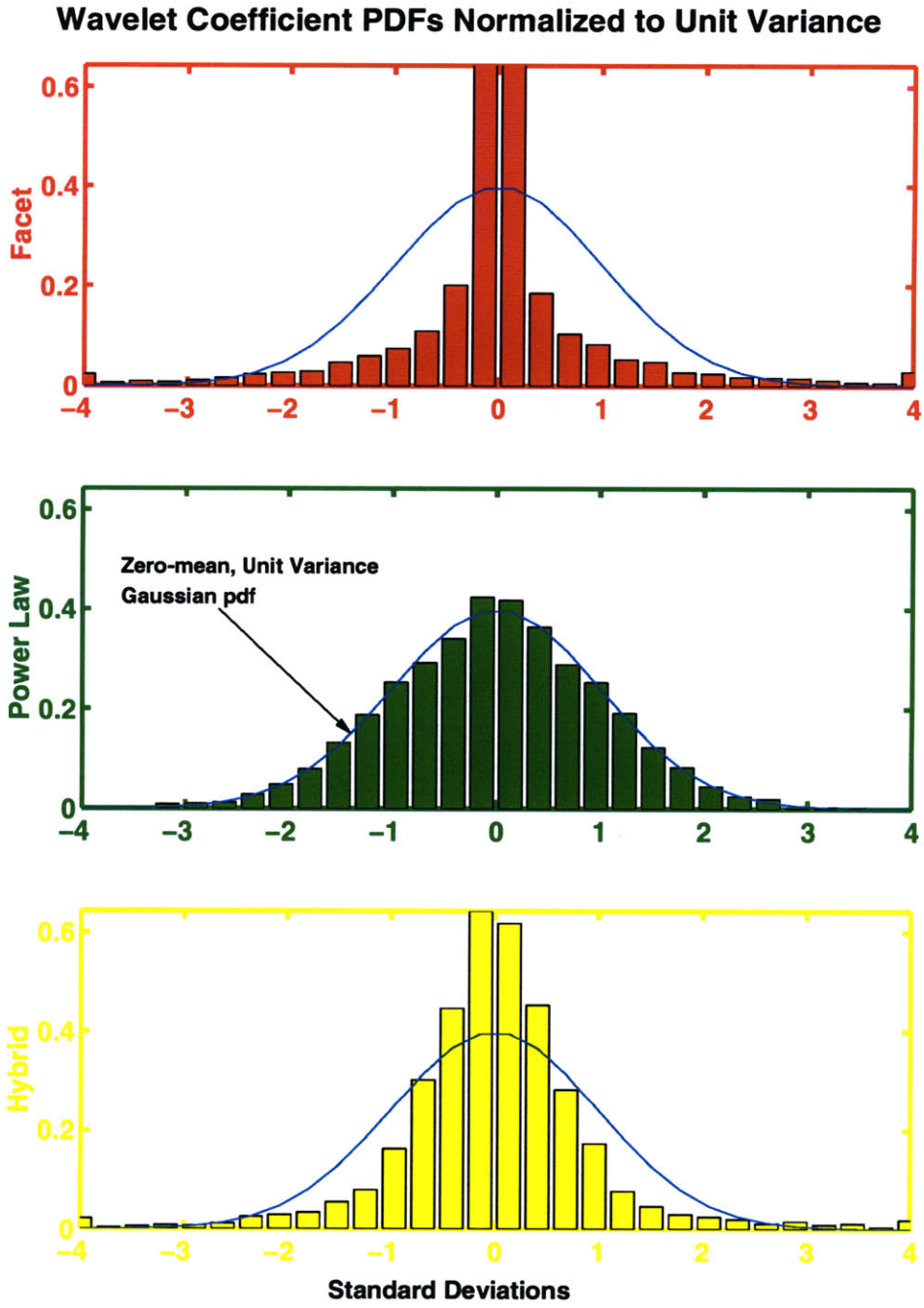

Figure 5-13: Estimated PDF's of the wavelet coefficients at a scale of 1/10 of a correlation length, normalized to unit variance. The Gaussian (green) process has Gaussian coefficients, but the other two processes yield non-Gaussian coefficients. The statistical wavelet analysis has successfully differentiated the scale structure of the three processes.

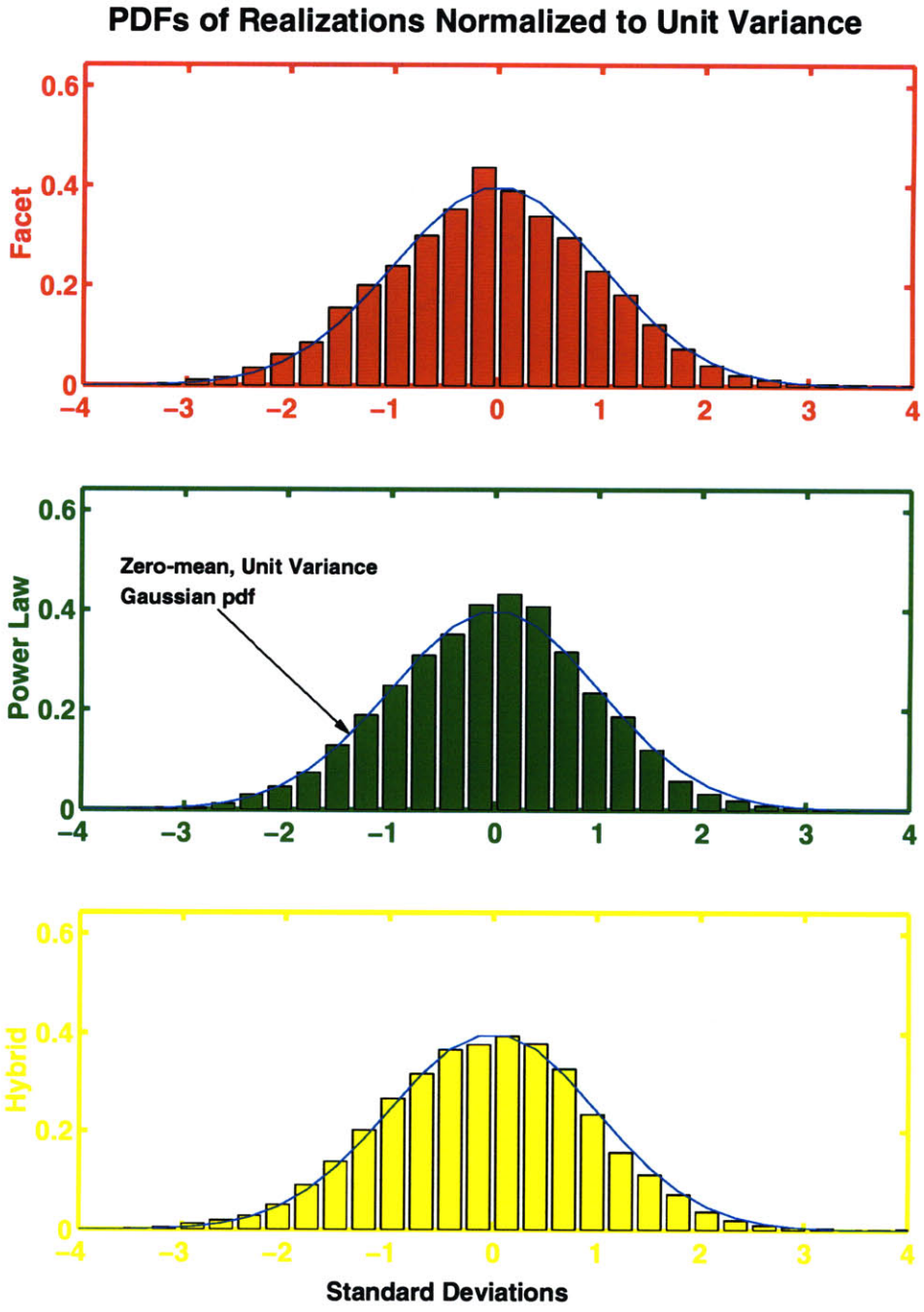

Figure 5-14: For comparison with Fig. 5-13, histograms of the realizations themselves showing that all three processes have a Gaussian one-point PDF.

spite of the fact that all three processes studied have a Gaussian one-point pdf. This can be readily verified by plotting histograms of the realizations themselves, as shown in Fig. 5-14. It can also be concluded from considering the fact that each point on the Facet surface is a linear combination of two Gaussian variables and is therefore Gaussian. The Hybrid surface is a linear combination of two Gaussian surfaces and is therefore also Gaussian.

Fig. 5-13 identifies statistical wavelet analysis as a tool for characterizing the statistical morphology of surfaces or, to be more precise, their scale structure. Several other densities could be examined in the future, such as conditional densities across scale. Clearly, in the Facet case, the wavelet coefficients at small scales are not independent of higher-scale coefficients. In particular, when the energy in co-located coefficients at higher scales is zero, the conditional density of the smaller-scale coefficients will be peaked about zero.

Any wavelet coefficient non-Gaussianity or prolonged dependence across scale and space indicates a departure from fractal scale structure and might constitute a starting point for demonstrating the inappropriateness of fractal models in describing seafloor areas with suspected feature-like morphology.

In the ARSRP scenario, such wavelet analysis is not necessary since the feature-like morphology is evident to the eye in the two-dimensional representations of the bathymetry in the previous chapter. It is also not possible at the scales of the two profiles in Figs.4-8 and 4-9, since statistical stability would require a larger number of profiles than are available. Nevertheless, the idea constitutes an exciting possibility for future study.

5.5 Other Rates of Decay

Seafloor profiles from around the world's oceans show decay exponents that range anywhere from 1 to 3.5 or higher. In the fractal model of Goff and Jordan, [19] the exponent can be adjusted to empirically fit the data. In the models proposed here there are only two possible values of the exponent, 2 or 3 corresponding to

piecewise constant or piecewise linear segments. Other values could surely be attained by considering other processes than Gaussian and Poisson for the vertices and by considering other functional forms between the vertices.

A simple way to achieve other rates of decay is to employ generalized derivatives:

$$\frac{d^\alpha h(x)}{dx^\alpha} = \mathcal{F}^{-1}\left\{(jk)^\alpha H(k)\right\}, 0 \leq \alpha \leq 1. \tag{5.30}$$

This operation decreases the rate of decay of the power spectral density by 2α. Starting from the Facet process, it allows all exponents from 3 to 1 to be attained. The variation between the vertices then consists of asymmetric cusps instead of straight lines. Starting from the piecewise constant process, exponents from 2 to 0 can be attained, but the realizations look even more unrealistic, exhibiting spikes at the vertices which become delta functions for $\alpha = 1$.

The case $\alpha = 1$ leads to piecewise-constant realizations in which the vertex heights are determined by the slopes of the Facet process and for which the power spectral density decays as $\frac{1}{k}$. The only difference in construction between this process and the piecewise constant process described at the beginning of this chapter is that the vertex heights are non-Gaussian.

This example demonstrates that changing the vertex statistics changes the rate of decay in the power law. It also suggests that there is a wide range of surface types with differing scale structure but identical rates of decay at high wavenumbers that remains to be explored.

5.6 Summary

The main conclusion of this chapter is that the scale structure of a stochastic surface is *not* determined by its power spectral density. Gaussian stochastic processes with power-law decay exhibit roughness at all scales which is uniformly distributed in space, leading to realizations with no feature-like behavior. Several alternatives have been presented which are capable of capturing feature-like morphology while

respecting the power-law decay of naturally observed power spectral densities.

As models of interfaces such as the seafloor, the realizations of the proposed feature-like processes were found to look unnatural. Composite models formed by superimposing component single-scale models acting at different scales have four desirable qualities: (i) they do not look unnatural; (ii) their power spectral densities have power-law decay; (iii) they lead to feature-like roughness, and (iv) they allow each section of the wavenumber spectrum to be accounted for by a separate seafloor-forming mechanism, taking statistical seafloor modeling one step closer to directly connecting observed spectra with geophysical processes. Qualities (i) and (ii) are shared by Gaussian models but qualities (iii) and (iv) are not.

It was demonstrated that it is easy for feature-like roughness to go undetected when accompanied by Gaussian multi-scale roughness. The wavelet transform has shown itself to be a valuable tool in differentiating the scale structure of random surfaces in situations where neither the power spectral density nor qualitative appearance can succeed. The tool is not the sole requirement; wavelet moments higher than the second must be considered when surfaces with identical power spectral density are compared.

While only one-dimensional surface models were investigated here, the concept of scale structure and its distinctness from the power spectral density extend to two dimensions. The development of two-dimensional stochastic surface models with feature-like structure would enhance the ability to describe the scale structure of realistic surfaces such as the seafloor. In Appendix C, the extension of the Facet seafloor model to the two-dimensional case is discussed.

The issue of scale structure and its applicability to seafloor modeling is both exciting and profound, perhaps too profound to be exhaustively investigated in a thesis on acoustics. Returning to acoustics, more excitement is added in the next chapter by investigating acoustical scattering from one-dimensional random rough surfaces with differing spectra and scale structure.

Chapter 6

Acoustic Scatter From One-Dimensional Surface Models

6.1 Introduction

In Chapter 3, a potential connection was proposed between the non-Rayleigh time-domain statistics in the ARSRP experiment and the feature-like roughness of the seafloor. The deeper investigation of seafloor morphology in Chapter 4 confirmed the existence of feature-like structure and inspired a new stochastic seafloor model consisting of the superposition of single-scale processes. In Chapter 5, one-dimensional models for the component single-scale processes were developed with the goal of generating realizations that would allow exact calculations of scattering in the time-domain, which forms the subject of the present chapter.

At the same time, the refinement of the concept of scale structure and its distinctness from the power spectral density has provoked some questions as to the appropriateness of second moment characterizations in describing morphology. The second moment description fixes the power spectral density of the process, which determines the expected value of the energy at each wavenumber. The previous chapter has established that an enormous range of scale structures is permitted by specifying only the power spectral density because the manner in which the energy at each wavenumber is organized spatially into features is left unspecified.

From a physical point of view, it is clear that what causes scattering are *features* and not wavenumber components, therefore it is enticing to study the potential implications in acoustics where it is customary to model only the second moment of rough scattering surfaces. Often, this is accompanied by the implicit assumption that the second moment is a *complete* description, implying that the surfaces are realizations of *Gaussian* processes. This is the case of the standard formulations of the perturbation and Kirchhoff approximations which form the backbone of scattering models in many numerical codes.

This chapter is thus a juncture where the proposal inspired from Chapters 3 and 4 that event-like statistics and feature-like morphology are related can be tested on a theoretical level using the surface models of Chapter 5.

The four surfaces types used in the scattering study are:

Gaussian-Gaussian (GG) A Gaussian process having Gaussian power spectrum, for which Eqs. 5.4 and 5.5 both apply.

Facet The Facet process of Section 5.3, which is a non-Gaussian, stationary process constructed by joining random vertices $\{x_i, z_i\}$ with straight line segments. The power spectrum of this non-Gaussian process exhibits a power law decay at high wavenumbers of the form A/k^b where $b = 3$.

Gaussian-Power Law (GPL) A Gaussian process whose sample surfaces are generated by filtering zero-mean Gaussian white noise through a filter with frequency response equal to the positive square root of the Facet process's spectrum.

Hybrid A non-Gaussian process created by a linear combination of Facet and GPL processes, with 75% of the energy coming from the Facet process.

These surfaces are used in three sets of numerical experiments.

1. The most pressing question is whether the Facet surface and its Gaussian counterpart, the GPL surface, have distinct scattering properties. If so, second

moment characterizations of random surfaces are not sufficient in acoustic scattering. It is also intriguing to ask whether the smooth features of the Facet process impart scattering properties that are similar to those of so-called single-scale processes, such as the GG process, which also exhibit smooth features but show little energy at high wavenumbers. These questions are addressed in Section 6.4, where the bistatic scattering strength and the time-domain statistics of backscatter are compared for Facet, GPL, and GG surfaces.

2. The next intriguing question is whether acoustics are capable of distinguishing the Hybrid and GPL processes given that neither qualitative perusal of the realizations nor spectral methods can. Section 6.5 addresses this question by comparing the bistatic and time-domain scatter for Facet, GPL, and Hybrid surfaces.

3. In Section 6.6, values of variance and correlation length closer to those encounted in the ARSRP scenario are tested to examine whether the conclusions from the first two sets of numerical experiments could apply to rougher interfaces.

All results are presented in non-dimensionalized form and are independent of center frequency and sound speed; they are thus applicable in a wide range of physical settings.

To ensure that any acoustical differences between the surfaces results from their properties and not from the approximations used in computing the scatter, an exact Monte Carlo integral equation method from Ref. [60] is employed. The theory behind the integral equation technique is presented in Section 6.2, and in Section 6.3 some of the issues in numerically implementing it are discussed but first, the characteristics of the model surfaces are described in more detail.

6.1.1 Surface Properties

A normalized sample path for each surface type is shown in Fig. 6-2, and the surfaces' properties are summarized in Fig. 6-1, showing that the first triad of surfaces defines

the poles of an aesthetic triangle with respect to Gaussianity, scale structure, and power spectral density.

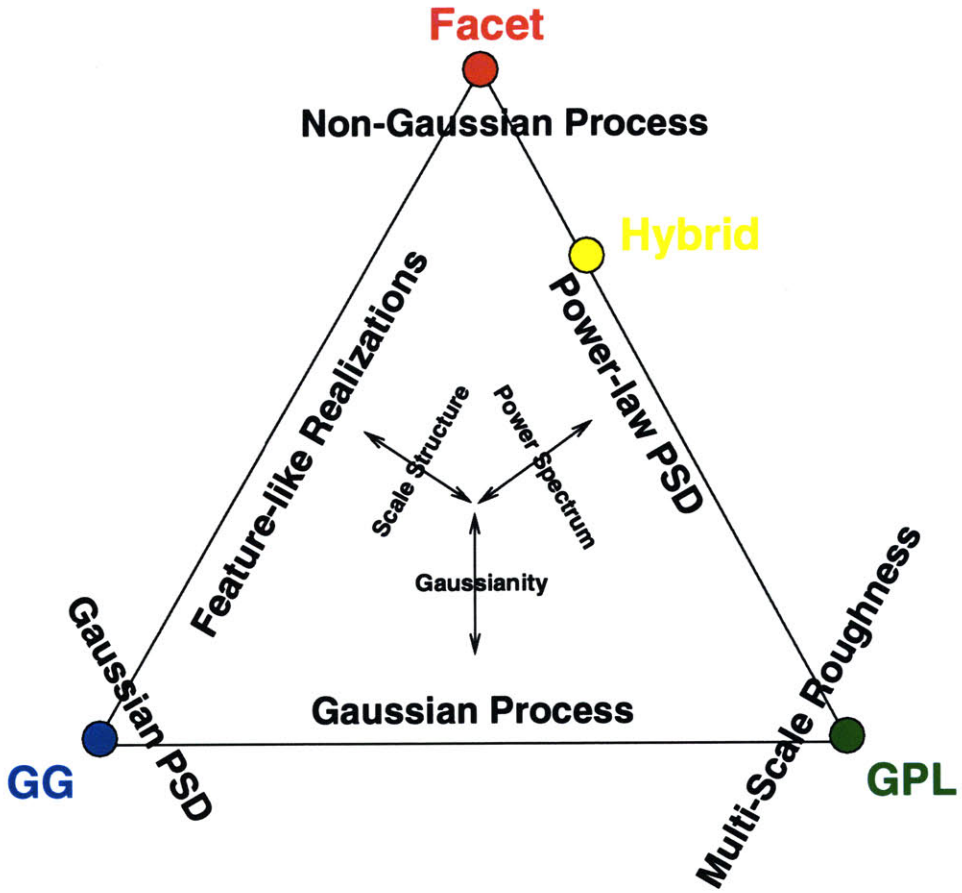

Figure 6-1: The Facet, GPL and GG surfaces define the three poles of a surface property triangle. The three arrows in the center define the three axes along which surface properties can vary. The GG surface is Gaussian, has Gaussian spectrum, and has feature-like roughness. The GPL surface is Gaussian, has power-law spectrum and is multi-scale. The Facet surface is non-Gaussian, has power-law spectrum, and has feature-like roughness. The Hybrid surface lies along a constant value of the power spectrum axis between the GPL and Facet poles.

This triangle is useful in discussing proper usage of the terms "single-scale" and "multi-scale". As discussed in Chapter 1, these terms are currently used both as statements of the qualitative appearance of realizations in the spatial domain (scale structure) and as statements about the power spectral density. Since language already exists to describe where a function lies in terms of Gaussianity and power spectrum, I

propose that the most reasonable use of these terms is along the scale structure axis. Single-scale then takes the meaning "feature-like", implying the existence of large, smooth features. The opposite is "multi-scale", meaning that the roughness is both spatially scrambled and arises from contributions at many scales.

The definition of the surfaces constitutes a complete statistical characterization in which the variance σ and correlation length l_c are parameters. Ideally, this study would present results spanning the entire $\sigma - l_c$ plane, but the computational cost of this complete study using the exact numerical method would be too high on today's machines.

The first two sets of numerical experiments involve only two points in this plane, which were chosen so as to lie away from the infinitesimal and away from the infinite, in a region in which features are likely to be of the same order of magnitude as the wavelength. This region is interesting because it leads to complex scattering behavior and is neither fully understood nor adequately predicted by any current analytical scattering theory in the general case. The two points are far enough from each other for their scattering properties to be distinct and to permit some general conclusions about the physics of surface scattering. The values are (i) $(\sigma, l_c) = (0.2, 1.0)\lambda$ and (ii) $(\sigma, l_c) = (0.3, 4.0)\lambda$. The incident field is a tapered plane wave at 45 degrees.

A third value of (σ, l_c) is considered in Section 6.6, where the objective is for the realizations to more closely resemble seafloor from the ARSRP scenario. In this set of experiments the incident field is a plane wave at a grazing angle of 30 degrees, to match the median grazing angle for backscatter from the scarps of site B'.

While penetrable fluid boundaries could readily be handled, the impenetrable case involves half as many unknowns. To minimize computational requirements the surfaces are modeled as impenetrable, and more specifically, as rigid in tribute to the basalt seafloor of ARSRP scarps that has inspired this study.

6.1.2 Previous Work

The second set of numerical experiments, involving the comparison of scatter from three surface types differering in scale structure but having identical power spectral

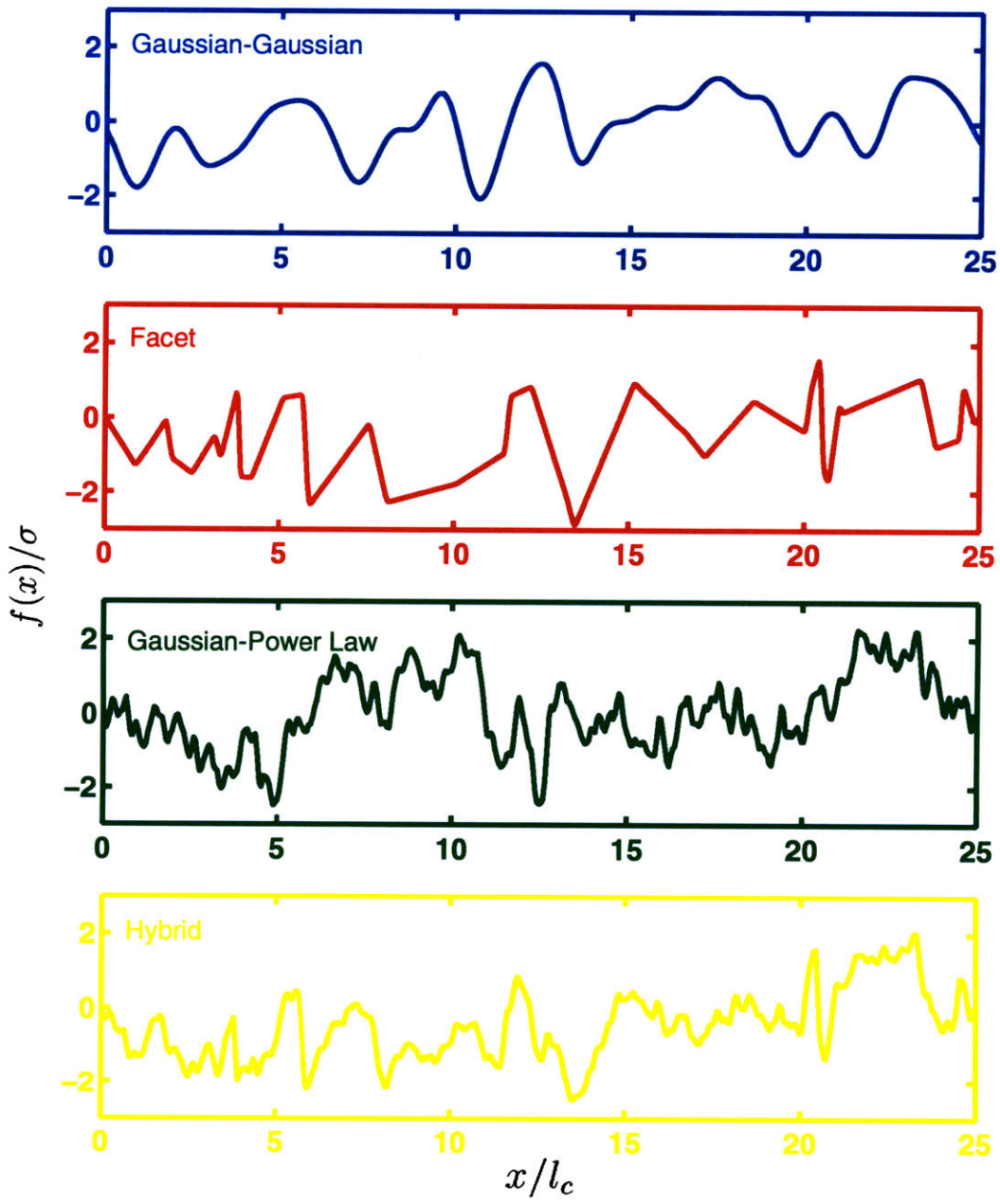

Figure 6-2: Normalized sample paths for the GG, Facet, GPL and Hybrid processes. The GG and Facet surfaces show feature-like roughness while the GPL surface shows multi-scale roughness. Although the Hybrid, Facet and GPL surfaces have the same power spectrum, the high-wavenumber energy is maximally concentrated in space for the Facet surface, while it is maximally distributed for the GPL surface; the Hybrid surface is a combination of the two but is qualitatively most similar to the GPL surface.

density, is reminiscent of the studies performed in Ref. [30]. In this article, the authors numerically compute coherence and scattering strength in the forward and back directions for an incident wave scattered by different rough surfaces. In the first study, a sawtooth surface realization is generated; its power spectrum is calculated and three new surface realizations are generated by scrambling the phases at each wavenumber. The three scambled-phase realizations are less feature-like than the sawtooth realization but have the same energy at each wavenumber. The scattering strength and coherence are found to be distinct for all three surfaces. In the second study, scatter from a water-wave realization is compared to scatter from three realizations having identical spectra but scrambled phases, yielding identical conclusions to the first study.

The distinction of the work presented in this thesis from that of Ref.[30] is that here, the computed quantities are *ensemble* averages over a large set of surface realizations having identical statistics. For a given surface model, the Fourier transforms of individual realizations differ both in amplitude and phase, resulting in distinct scattering characteristics for each realization. I do not focus on individual realizations; rather, I investigate the effect of a change in the statistics of surface models on the ensemble statistics of scatter.

With regards to this focus on ensemble statistics rather than individual realizations, this thesis resembles the work of Thorsos [60] [61] in which exact average bistatic scattering strengths from pressure-release Gaussian surfaces with Gaussian (GG) and Pierson-Moskowitz (GPL) spectra are compared. Here, the concept of scale structure is studied by introducing a new surface model which has the feature-like characteristics of the GG surface but the power-law decay at high wavenumbers exhibited by the GPL surface. Along with the bistatic scattering strength, the time-domain statistics are evaluated for rigid rather than pressure-release surfaces.

In Ref. [51], sea reverberation is modeled as a shot noise process consisting in the superposition of impulsive returns from discrete scatterers. In the limit of a large number of scatterers, the carrier amplitude is shown to be Gaussian. The author indicates how the coefficient of excess of the envelopes may be related to the scatterer

density. A large coefficient of excess indicates a depressed peak and enhanced tails in the carrier amplitude pdf relative to a Gaussian, which occurs when individual scatterers are resolved. In this chapter, it is shown numerically that certain surfaces exhibit such target-like characteristics. In characterizing the extent of the target-like behavior, I choose to depict the full pdfs of the logarithmic intensity of the carrier amplitudes instead of presenting values for the coefficient of excess, since the latter relate only to the departure of the *fourth* moment of a given pdf from a Gaussian pdf.

6.2 Integral Equation Method

In this Section, I describe the exact integral equation solution method adapted from [60] which is used to compute the scatter from each realization. The statistics of scatter are obtained by a Monte Carlo approach in which the exact solution to each realization is found and averaged over a number realizations. First, the matrix equations embodying the Helmholtz-Kirchhoff integral in the case of a finite, rigid boundary are developed. This is followed by a discussion of the choice of the monochromatic incident field in Section 6.2.2 and a discussion of wideband incident fields in Section 6.2.3.

6.2.1 Theory

The Helmoltz-Kirchhoff integral formula gives the total acoustic pressure in a volume V as an integral of source terms distributed over a smooth closed surface S_v bounding V. For the one-dimensional finite-length surfaces used here, S_v is the union of a circular contour at infinity $S_\infty + S'_\infty$ and two contours which surround the surface infinitesimally close to it, S_0 on the illuminated side and S_2 behind it. The contribution over $S_\infty + S'_\infty$ is equal to $p_{inc}(\mathbf{r})$, and the portion over S_2 is zero if one assumes that $p(\mathbf{r}) = \partial p(\mathbf{r})/\partial \mathbf{n} = 0$ behind the surface. A full explanation of the choices of contour integration for finite surfaces is found in Appendix D. For rigid surfaces, the

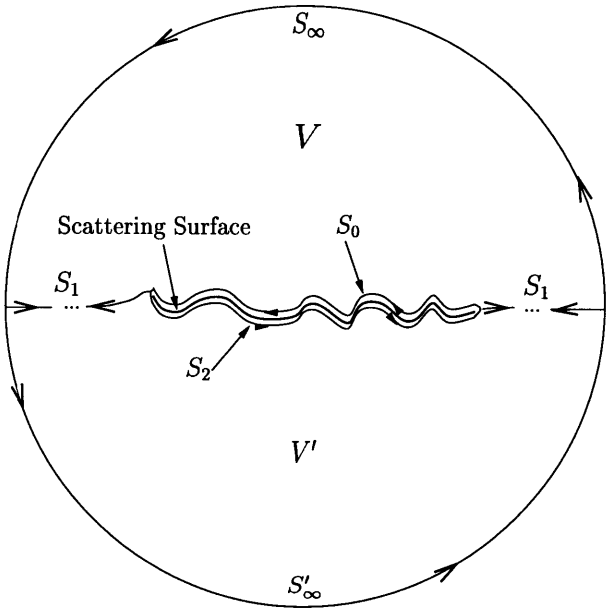

Figure 6-3: Integration paths for the Helmholtz-Kirchhoff integral equation as used to compute the scatter from a finite-length rough surface.

Helmholtz-Kirchhoff formula reduces to:

$$p(\mathbf{r}) = p_{inc}(\mathbf{r}) + \frac{1}{4i}\int_{S_0} p(\mathbf{r}')\frac{\partial H_0^{(1)}(k|\mathbf{r}-\mathbf{r}'|)}{\partial \mathbf{n}'}dS'. \tag{6.1}$$

Equation 6.1 is valid for any $\mathbf{r}$ not on S_0. In the limit where $\mathbf{r} \to \mathbf{r}'' \in S_0$, and given that S_0 is a smooth surface, Eq. 6.1 becomes

$$\frac{1}{2}p(\mathbf{r}'') = p_{inc}(\mathbf{r}'') + \frac{1}{4i}\int_{S_0} p(\mathbf{r}')\frac{\partial H_0^{(1)}(k|\mathbf{r}''-\mathbf{r}'|)}{\partial \mathbf{n}'}dS'. \tag{6.2}$$

Equation 6.2 is a Fredholm integral equation of the second kind for the total pressure on the surface, $p(\mathbf{r}'')$. For arbitrary S_0, this equation must be solved numerically by discretization. It can be proven that the discretized version of a Fredholm equation of the second kind converges to a unique and correct result as the discretization interval tends to zero [25].

The surface is sampled at equal intervals Δx and Eq. 6.2 becomes a matrix equa-

tion:

$$\mathbf{a} = \mathbf{H}\mathbf{b} \tag{6.3}$$

where $\mathbf{b}_l = p(\mathbf{r}_l)$ is the unknown vector, $\mathbf{a}_k = p_{inc}(\mathbf{r}_k)$, and

$$\mathbf{H}_{kl} = \begin{cases} \frac{i}{4}\Delta x \gamma(\mathbf{r}_l) \left. \frac{\partial H_0^{(1)}(k|\mathbf{r}_k - \mathbf{r}'|)}{\partial \mathbf{n}'} \right|_{\mathbf{r}'=\mathbf{r}_l} & k \neq l \\ \frac{1}{2} - \frac{\Delta x}{4\pi\gamma(\mathbf{r}_k)^2} \left. \frac{d^2 f(x')}{dx'^2} \right|_{\mathbf{r}'=\mathbf{r}_k} & k = l, \end{cases} \tag{6.4}$$

where $\gamma^2(\mathbf{r}') = 1 + (df(x')/dx')^2$ and $f(x)$ is the function defining the surface S_0. The normal derivative of the Hankel function in Eq. 6.4 is

$$\frac{\partial H_0^{(1)}(k|\mathbf{r}'' - \mathbf{r}'|)}{\partial \mathbf{n}'} = \frac{k H_1^{(1)}(k|\mathbf{r}'' - \mathbf{r}'|)}{\gamma(x')|\mathbf{r}'' - \mathbf{r}'|} \left[(f(x') - f(x'')) - f'(x')(x' - x'') \right]. \tag{6.5}$$

For the diagonal elements of $\mathbf{H}$ where $\mathbf{r}'' = \mathbf{r}'$, $f(x'')$ is expanded in a Taylor series about x' as suggested in [60], and the limit is taken as $\mathbf{r}'' \to \mathbf{r}'$, yielding

$$\lim_{\mathbf{r}'' \to \mathbf{r}'} \frac{\partial H_0^{(1)}(k|\mathbf{r}'' - \mathbf{r}'|)}{\partial \mathbf{n}'} = \frac{i f''(x')}{\pi \gamma^3(x')}. \tag{6.6}$$

The scattered pressure, defined as $p_s(\mathbf{r}) = p(\mathbf{r}) - p_{inc}(\mathbf{r})$, is computed at any location $\mathbf{r}$ in the fluid from the discretized version of Eq. 6.1:

$$p_s(\mathbf{r}) = \sum_k \frac{\mathbf{b}_k \Delta x \gamma(\mathbf{r}_k)}{4i} \left. \frac{\partial H_0^{(1)}(k|\mathbf{r} - \mathbf{r}'|)}{\partial \mathbf{n}'} \right|_{\mathbf{r}'=\mathbf{r}_k} \tag{6.7}$$

6.2.2 Narrowband Fields

A tapered plane wave incident field identical to that in Ref. [60] is used:

$$p_{inc}(\mathbf{r}) = \exp\left\{ i\mathbf{k}_{inc} \cdot \mathbf{r}\left[1 + w(\mathbf{r})\right] - (x - z\cot\theta)^2/g^2 \right\}, \tag{6.8}$$

where $w(\mathbf{r}) = [2(x - z\cot\theta)^2/g^2 - 1]/(kg\sin\theta)^2$. This pulse has Gaussian amplitude taper perpendicular to the incidence direction. The taper parameter g is set to

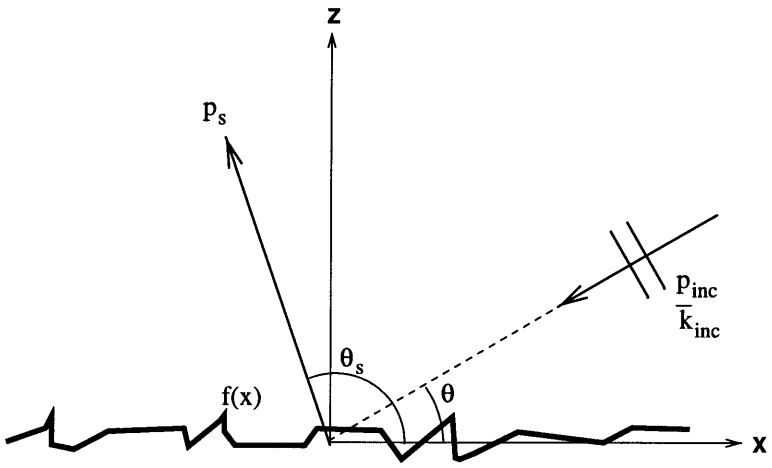

Figure 6-4: Scattering geometry. The surface is rigid.

$L/4$ for all surfaces considered here, where L is the horizontal extent of the surface and is chosen such that the incident beam illuminates a representative sample of the roughness. The angle of incidence is θ and the incident wavenumber is $\mathbf{k}_{inc} = k(\cos(\theta+\pi), \sin(\theta+\pi))$ as shown in Fig. 6-4. The taper suppresses the edge effects caused by assuming that the total field and its normal derivative are identically zero behind the surface in Eq. 6.1. A consequence of the chosen taper is that the incident field is only an approximate solution to the Helmoltz equation. The particular form used satisfies the Helmholtz equation to order $1/(kg\sin\theta)^2 \ll 1$ [60].

A useful quantity in distinguishing the angular dependence of narrowband scatter from various one-dimensional surfaces is the scattering cross section, defined as the mean-square scattered pressure evaluated in the far field normalized by the incident energy and a cylindrical spreading factor. The far-field scattering strength SS is ten times the logarithm of the scattering cross section. For the incident field in Eq. 6.8,

$$SS(\theta,\theta_s) = \lim_{|\mathbf{r}|\to\infty} 10\log \frac{|\mathbf{r}|\mathcal{E}[|p_s(\mathbf{r})|^2]}{\sqrt{\pi/2}g[1-0.5(1+2\cot^2\theta)/(kg\sin\theta)^2]}, \tag{6.9}$$

where $p_s(\mathbf{r})$ is found from Eq. 6.7 numerically. Since the sample surfaces scale with wavelength, the scattering strength is independent of frequency and sound speed.

6.2.3 Wideband Fields

Central to this thesis is an exploration of the time-domain statistics of scatter. The incident field in Eq. 6.8 is generalized to include frequency dependence:

$$p_{inc}^{WB}(\mathbf{r},\omega) = p_{inc}(\mathbf{r})G(\omega). \tag{6.10}$$

In this chapter, real band-limited pulses $g(t)$ are considered such that

$$G(\omega) = \begin{cases} G_b(\omega), & 1-\Gamma/2 \leq \omega/\omega_c < 1+\Gamma/2 \\ G_b^*(-\omega), & -1-\Gamma/2 \leq \omega/\omega_c < -1+\Gamma/2 \\ 0, & \text{otherwise.} \end{cases} \tag{6.11}$$

The quantity Γ is the proportional bandwidth, defined as the ratio of bandwidth to center frequency ω_c. The time-domain response of each surface realization is obtained from the inverse Fourier transform of $p_s(\mathbf{r},\omega)$

$$p_s(\mathbf{r},t) = \frac{1}{2\pi}\int_{-\infty}^{\infty} p_s(\mathbf{r},\omega)e^{-i\omega t}d\omega, \tag{6.12}$$

where $p_s(\mathbf{r},\omega)$ is obtained by solving Eq. 6.3 at each frequency using the wideband incident field in Eq. 6.10.

As a time-domain analog to the scattering strength, the zero-mean log-envelope $E(t,\theta,\theta_s)$ is defined as:

$$E(t,\theta,\theta_s) = \lim_{|\mathbf{r}|\to\infty}\left(10\log|p_s(\mathbf{r},t)|^2 - \mathcal{E}[10\log|p_s(\mathbf{r},t)|^2]\right). \tag{6.13}$$

Since a single angle of incidence is considered in each study, the notation for the log-envelope is simplified to $E(t)$. Note that the definition in Eq. 6.13 implies that the log-envelope is *zero-mean.*

Of interest is the probability density of E, $p_E(E)$ which is estimated directly from all the realizations of $E(t)$ using histograms. These density estimates form the basis for comparing the acoustic properties of the surfaces. The significance of differences

in estimated pdf's is always tested using the chi-square test.

It can be shown that all $p_s(\mathbf{r}, t)$ evaluated in the far-field are scaled versions of one another for independently varying ω_c and c. The log-envelope one-point probability density functions are insensitive to scalings, hence independent of ω_c and c.

The scenario in which $p_s(\mathbf{r}, t)$ is the sum over a large number of independent, identically distributed variables is a limiting case for the statistics of $E(t)$. By the central limit theorem, the quantity $r(t) = |p_s(t)|$ has a Rayleigh density at all values of t:

$$p_r(R) = \frac{R}{\sigma_r^2} e^{-R^2/2\sigma_r^2} u(R), \tag{6.14}$$

where $u(R)$ is the unit step function. The probability density of the resulting envelope, $E_R(t)$, is

$$p_{E_R}(E_R) = \frac{\ln 10}{20\sigma_r^2} 10^{\frac{E_R}{10}} e^{-\frac{10^{E_R/10}}{2\sigma_r^2}}. \tag{6.15}$$

This density will be referred to as log-Rayleigh. The fact that E_R is zero mean constrains the value of σ_r^2 as follows:

$$0 = \mathcal{E}[E_R] = \int_0^\infty 20 \log R \frac{R}{\sigma_r^2} e^{-R^2/2\sigma_r^2} dR = 10 \log e (\ln 2\sigma_r^2 - C), \tag{6.16}$$

implying that $\sigma_r^2 = e^C/2 \simeq 0.89$ where C is Euler's constant (0.577215 ...) [21].

Physically, this limiting case is achieved when $p_s(t)$ is the sum of a large number of scatterers that can be considered independent and identically-distributed, which occurs when the pulse insonifies a sufficiently large segment of a stationary random surface. At sufficiently small values of proportional bandwidth Γ, the pulse experiences the random-phase combination of many scatterers instead of the target-like scatter from individual scatterers. In each estimation of the log-envelope pdfs, the results are compared to the limiting case to gain a feeling for how target-like the surfaces behave at each bandwidth.

The integral equations were solved on a DEC Alpha 600 5/333 with 256 Mb

of RAM. The leading order of the algorithm was M^3NQ where M is the number of surface sample points, N is the number of surfaces, and Q is the number of frequencies. In all the simulations, $N = 50$ was found to provide sufficiently small error bounds on estimates of scattering strength and time statistics. For narrowband scattering, the highest number of samples used was $M = 1900$. For the wideband case, $M = 800$ and $Q = 100$ required a week of run time and were considered the upper limit of practicality. An advantage of the integral equation method is that the matrices are well-conditioned.

6.3 Numerical Implementation Issues: An Example

In this Section, some of the issues in numerically implementing the Monte Carlo integral equation method are discussed for an example case consisting in the computation of scatter from GG, Facet and GPL surfaces with $L = 80\lambda$, $(\sigma, l_c) = (0.2, 1.0)\lambda$, and $\theta = 45°$; the number of realizations is $N = 50$. This example corresponds to one of the cases that are studied in the first set of numerical experiments in Section 6.4.

6.3.1 Surface Filtering

Recall from Sec. 6.2.1 that the integral equation formulation requires that each scattering surface be smooth. A curve is said to be smooth if its first derivative exists and is continuous everywhere. The Facet surface has a countable number of slope discontinuities and is not smooth. The GPL surface has *uncountably* many slope discontinuities since it is non-differentiable at every point. Any surface with countably or uncountably many slope discontinuities can be made smooth by low-pass filtering. Although the acoustic properties of a low-pass filtered surface $f_d(x)$ differ from those of the original surface $f(x)$, the difference vanishes at high enough corner wavenumbers in the low-pass filters. This fact enables one to compute the scatter from a surface with slope discontinuities as the limit of integral equation solutions from a

sequence of smooth, low-pass filtered surfaces with increasing corner wavenumber.

In every set of experiments, all three surface types were filtered using the same low-pass filter $D(k)$ for consistency.

$$f_d(x) = \int_{-\infty}^{\infty} f(x')d(x - x')dx'. \tag{6.17}$$

The surface filters $D(k)$ were chosen carefully. A filter with sharp cutoffs in the wavenumber domain exhibits significant rippling in the spatial domain; these ripples are imparted to the surface and, when large enough, distort its scattering properties. Small-amplitude ripples can also significantly alter the scattered field if they lead to large distortions in the first or second derivative. By using conventional signal processing windows as impulse responses $d(x)$ for the filters, these problems were avoided; Kaiser-Bessel windows of order 5 [23] were used. The corner wavenumber k_c was defined as the location of the first null of $D(k)$. The spatial extent L_{KB} of the Kaiser-Bessel window of order 5 is related to the corner wavenumber k_c through the approximate formula $L_{KB} \simeq 3.8\pi/k_c$.

6.3.2 Convergence

If the filtered surfaces $f_d(x)$ are not sampled finely enough, the error on the computed scatter is unacceptably large. With each increase in sampling resolution, the error is diminished. The scatter is said to have "converged in sampling" when a doubling in resolution leads to changes in scattering strength which are smaller than or equal to 0.2 dB over all angles of scatter for a given angle of incidence.

Convergence is also an issue with regards to k_c. Beyond a critical value of k_c, negligible changes in the computed pressures are incurred by doubling k_c, and the smoothed surfaces are acoustically equivalent to their unsmoothed versions. In these situations the scatter is said to have "converged in k_c". At each value of k_c, the surfaces must be sampled sufficiently finely to have converged in sampling. The sampling rate required for convergence in sampling increases with k_c.

Define M to be the number of surfaces samples spaced a uniform distance of

$\Delta x = L/M$ apart. At the (σ, l_c) value of $(0.2, 1.0)\lambda$ in this example, convergence in k_c for the GG surfaces occured at $k_c = 2.5k$, where k is the acoustic wavenumber, requiring $\Delta x = \lambda/5$ ($M = 400$). The GPL and Facet surfaces were considerably slower to converge, requiring $k_c = 8k$ and $\Delta x \leq \lambda/16$ ($M = 1300$), as shown in Fig. 6-5(a). This value of k_c corresponds to an averaging width of $L_{KB} \simeq \lambda/4$. Fig. 6-5 (b) shows the appearance of a filtered 45 degree corner at each cutoff wavenumber.

While Fig. 6-5 only shows results for the Facet surface, the convergence pattern for the GPL surface was almost identical. What explains the more rapid convergence in k_c for the GG surface is that it does not possess much energy at wavenumbers above $2.5k$, so filters with cutoff wavenumbers above this value do not alter its shape. Higher cutoff wavenumbers are required for the Facet and GPL surfaces because they contain significant roughness up to much higher wavenumbers, leading to small features.

6.3.3 Wideband Case

In a numerical setting, obtaining results over a band of frequencies requires discrete frequency sampling. A judicious choice of frequency spacing Δf is such that no time-domain aliasing occurs. Strictly, this condition is achievable only if $\Delta f \leq 1/2T_m$ where T_m is the time between the first and last non-zero contributions. Since multiple scatter occurs forever along the surface after the initial interrogation by the incident pulse, T_m is infinite, but in practice a Δf corresponding to the reciprocal of the time required for the pulse to travel two to three times the surface length is sufficient to avoid aliasing.

For the time-domain results the computational cost of solving at a large number of frequencies restricted the investigation to backscattering and M to a maximum of 800. In the example of this Section, the highest cutoff wavenumber for which 800 samples are sufficient to attain convergence in sampling is $k_c = 4k$. Referring back to Fig. 6-5(a), the backscattering strength at $k_c = 4k$ has not quite converged to its value for an unrounded surface, which is attained at $k_c = 8k$. However, the rms error is on the order of 1 dB and is acceptably low. Given computational hardware many times faster, the ideal value of $M = 1300$ could be used, which would have permitted

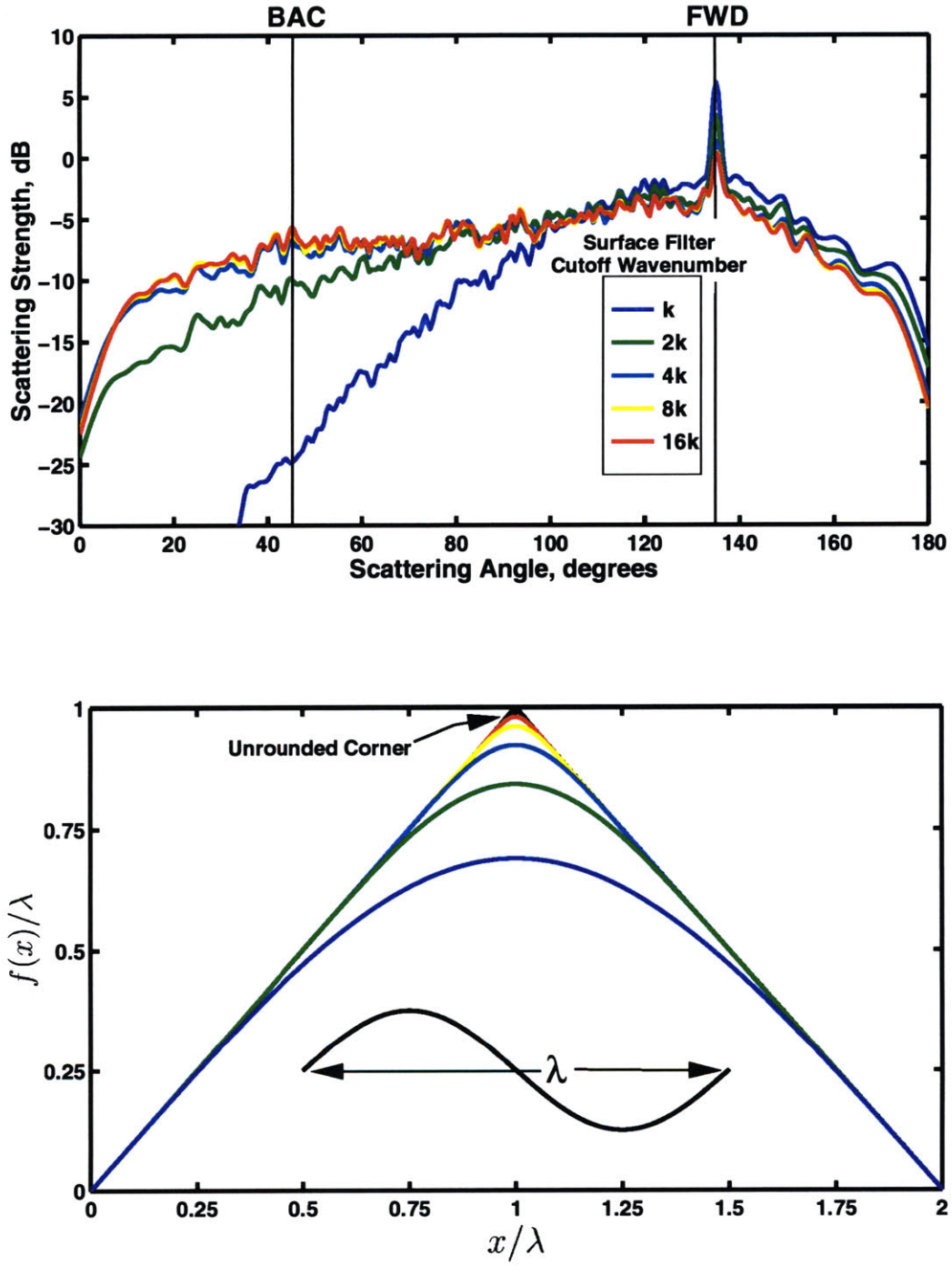

Figure 6-5: (a) Monte Carlo estimates of average scattering strength for 50 Facet surfaces with $(\sigma, l_c) = (0.2, 1.0)\lambda$ and increasing values of k_c. Convergence occurs at $k_c = 8k$. (b) Size of a rounded corner relative to the wavelength for increasing values of k_c. At $k_c = 8k$, the rounded corner is acoustically equivalent to a perfect corner.

$k_c = 8k$.

Explicit reference is made to the degree of convergence in k_c for the time-domain simulations in each set of experiments.

6.3.4 Accuracy of pdf Estimates

The number of pulse widths fitting within the length of the surface, $L/\Delta x_p$, is an indication of the number of independent observations of the random process $E(t)$. As the pulse length increases and covers larger portions of the surface, longer observation times are needed to achieve representative envelopes, which in turn requires the use of longer surfaces. In each set of numerical experiments, the surface lengths were not increased as a function of pulse length. Consequently, the accuracy of the pdf estimates decreased as the bandwidth was decreased. By concatenating the 50 realizations used in each experiment, one gets a minimum of 50 independent observations of $E(t)$. This minimum is achieved when the the pulse's spatial resolution on the surface is greater than or equal to L. All comparisons in this paper involving estimated pdf's are warranted by a chi-square test of the histograms using the number of independent observations as the number of degrees of freedom.

6.3.5 RMS Slope

A useful quantity in the discussion of the results is the angle of the rms slope. For the GG surface this quantity is $s = \sqrt{2}\sigma/l_c$. For the Facet GPL, and Hybrid surfaces, s is undefined. The $1/k^3$ decay of the height spectrum causes a $1/k$ decay of the slope spectrum, leading to a divergent integral. Low-pass filtering the surface eliminates this logarithmic singularity such that the rms slope exists and is given by:

$$s = \left(\mathcal{E}[(df(x)/dx)^2]\right)^{\frac{1}{2}} = \left(\frac{1}{2\pi}\int_{-\infty}^{\infty} k^2 S_{ff}(k)|D(k)|^2 dk\right)^{\frac{1}{2}}. \qquad (6.18)$$

Each member of the surface filter family $D(k)$ is the Fourier transform of a Kaiser-Bessel window of order 5. For each value of cutoff wavenumber Eq. 6.18 is solved

$(\sigma, l_c)/\lambda$	Gaussian-Gaussian	Facet, GPL and Hybrid
$(0.2, 1.0)$	$15.8°$	$k_c = 4k : 27.7°; k_c = 8k : 35.2°$
$(0.3, 4.0)$	$6.1°$	$k_c = 4k : 18.2°; k_c = 8k : 21.1°$
$(2.0, 8.0)$	N/A	$k_c = 2k : 41.2°; k_c = 4k : 45.9°$

Table 6.1: Value of the rms slope angle γ for the surfaces used in this study. Each surface has been low-pass filtered using a Kaiser-Bessel window of order 5 with varying cutoff wavenumber.

numerically and the corresponding values of $\gamma = \arctan(s)$ are shown in Table 6.1 for all the surfaces used in this study.

Note that while s increases without bound as the corner wavenumber tends to infinity, the existence of a corner wavenumber beyond which all surfaces are acoustically identical suggests a physical definition of the rms slope which can be used for non-integrable slope spectra.

6.3.6 Angular Resolution

Figure 6-5 may be used to remark on an issue not related to convergence. A consequence of using finite length surfaces is that scatter at neighbouring angles is smeared together. For example the coherent component, which would be a delta function at $\theta_s = 135°$ for an infinite length surface, is transformed into a contribution of non-zero angular width and finite amplitude. The smearing effect becomes increasingly important at low grazing angles where the projection of the surface's length on the scattering wavenumber is very small.

Angular resolution must sometimes be traded for increased computational speed. In the first two sets of numerical experiments, $L = 80\lambda$ is used and provides ample angular resolution. In the third set of experiments, a higher sampling rate is needed to achieve convergence at $k_c = 4k$, so shorter surfaces having $L = 35\lambda$ must be used for the wideband simulations to maintain $N = 800$, leading to a decrease in angular resolution, although not excessively so.

6.4 Scatter From Facet, GG and GPL Surfaces

With the theoretical approach and numerical issues clearly established, it is now possible to proceed to the computation of scattering from rough surfaces. The metrics through which scattering properties are assessed are the bistatic scattering strength and the one-point pdfs of backscattered envelopes for a plane wave at 45 degree incidence. In this first set of experiments, the triad of surfaces lying at the poles of the triangle in Fig. 6-1 are studied.

The bistatic scattering strength results are presented and discussed in Section 6.4.1, and Section 6.4.2 presents the log-envelope histograms at proportional bandwidths of 1.8%, 9%, and 36%. Note that in the wideband case the normalization wavelength λ is the wavelength at the *center frequency.*

6.4.1 Narrowband Results

The expected value of the bistatic scattering strength was estimated for all three surface types for two cases: $(\sigma, l_c) = (0.2, 1.0)\lambda$ and $(0.3, 4.0)\lambda$. Each sample surface was low-pass filtered at a cutoff wavenumber of $16k$ (twice the convergent cutoff of $8k$), and thus the computed scatter was the same as would be calculated for unfiltered surfaces. The results are presented on Figs. 6-6 (a) and (b). In both (a) and (b) what is most obvious is the enhanced scatter in the back quadrant for the two surfaces with power law spectra compared to the GG surface. It should be noted that the integral of scattered energy across all bistatic angles was within 1% of the incident energy for all cases shown.

While the Facet and GPL surfaces have identical spectra, Fig. 6-6 shows their scattering strengths to be distinct. This is proof that the second moment is insufficient to predict the average scattering strength from a random rough surface. On the other hand, the figure also shows that for the values of (σ, l_c) considered, the power spectrum gives a coarse idea of the energy in backscatter. It is hard to imagine surfaces more opposite in their manifestation of a given power spectrum. In the extreme case of the Facet surface, all of the high-wavenumber roughness is concentrated at discrete

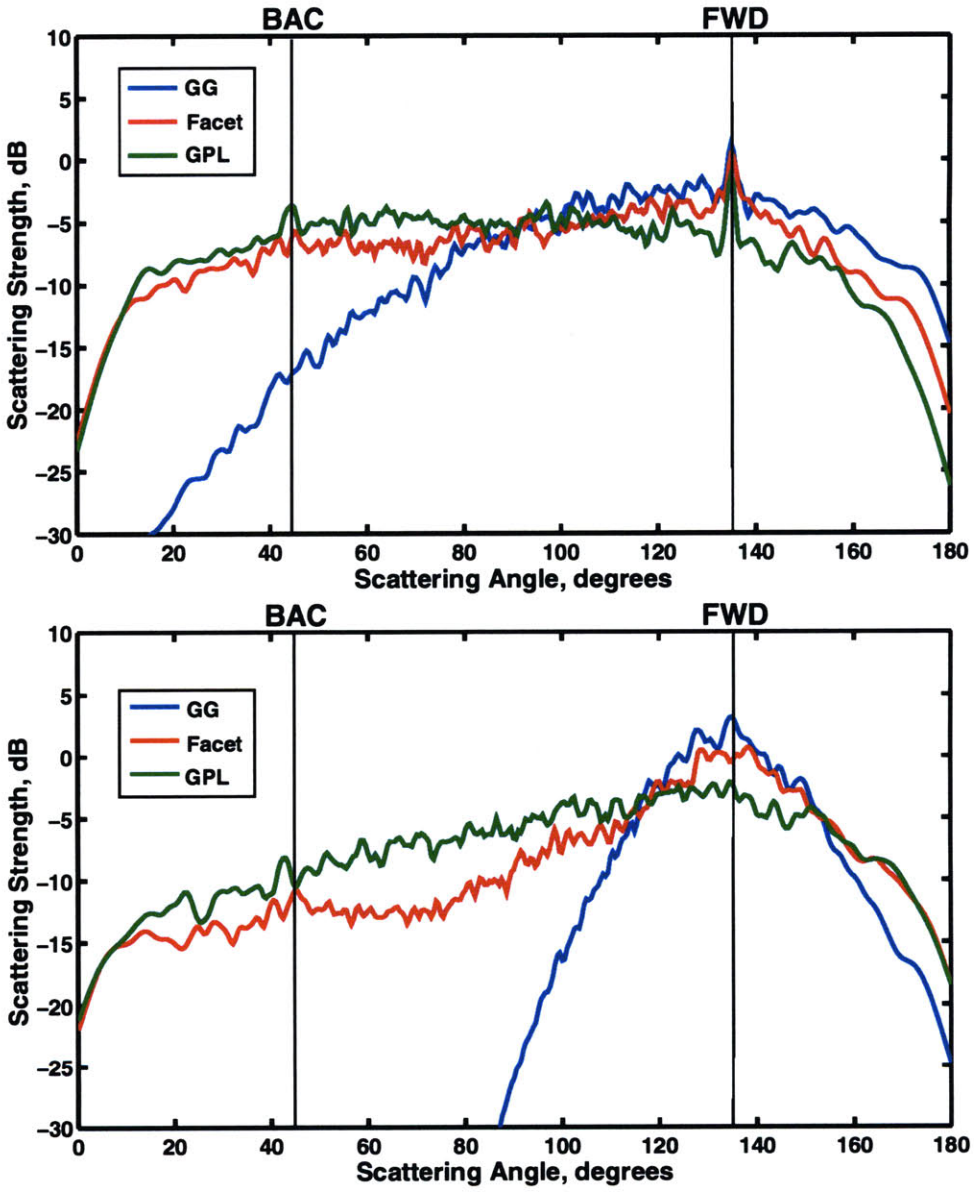

Figure 6-6: Monte Carlo estimates of scattering strength for $(\sigma, l_c) =$ (a) $(0.2, 1.0)\lambda$ and (b) $(0.3, 4.0)\lambda$. The Facet and GPL surfaces possess highly enhanced backscatter compared to the GG surface due to high-wavenumber roughness. The Facet and GG surfaces, being single-scale, show an enhanced forward scatter lobe compared to the GPL surface. In all cases, energy conservation is satisfied to within 1%.

points, while in the GPL surface it is distributed as evenly as possible. Any other surface with the same power spectrum is bound to lie in between these two extremes and thus it should be the case that all surfaces with a power-law spectrum with exponent not far from the present value of 3 will lead to enhanced scatter in the back quadrant for the values of (σ, l_c) considered here.

The Facet surface exhibits a different functional dependence than the GPL surface, manifesting a 3-5 dB increase about the specular direction which is especially evident in Fig. 6-6 (b). It appears to behave like the GG surface within ± 20 degrees of the specular direction, and like the GPL surface (although at reduced levels) everywhere else.

A physical interpretation of this phenomenon is as follows. In the GG surface, the incident energy encounters a curve each part of which is sufficiently smooth compared to the wavelength to act like a reflector. This is confirmed by the validity of the Kirchoff approximation for this surface and these values of (σ, l_c) [60]. The total scattering strength in any direction is dominated by the likelihood that locally-plane segments of the curve will reflect the incident energy in that direction. The average slope of the reflecting segments is zero, hence there is a bulge of incoherent energy about the specular direction. In Fig. 6-6 (b) the angle of the rms slope (from Table 6.1) is less than half of its value in (a), and thus the likelihood of slopes large enough to reflect energy into the low grazing angles of backscatter is lower. This explains the decreased backscattering strength in (b).

On the other hand, the GPL surface never presents locally plane segments because it contains structure down to infinitesimal scales. Each infinitesimal feature is a tiny diffractor which radiates in all directions, and the total scatter is the cumulative effect of these diffractors. This explains the quasi-omnidirectional beampattern of the GPL surface, in which backscatter is no more than 5 dB weaker than incoherent forward scatter.

The Facet surface is unique in that it consists of a combination of reflectors (the facets) and diffractors (the vertices). The diffractors lead to enhanced backscatter as in the GPL surface, and the reflectors lead to enhanced scatter about the forward

direction, as in the GG surface. The vertices diffract into directions unlikely to receive energy from reflective contributions, and the facets contribute more energy in the foward direction than would be possible for the diffractors alone. The facets are also contributors to energy in the back direction through their relatively high slopes. Of course, by conservation of energy, the scatter in the Facet surface cannot be as high in backscatter as the GPL surface while being as high in the forward direction as the GG surface.

In reality, all rough surfaces combine multiple reflections and diffractions but the physical interpretation above is representative of the dominant phenomena in each case and leads to the following general propositions:

1. The ability to produce a forward scatter lobe in a surface with zero mean slope is determined by the presence of single-scale features which must be large enough to act as local reflectors. The *scale structure* and average feature size are thus good predictors of the existence or inexistence of a foward scatter lobe.

2. The ability to produce high scatter in the back quadrant is governed by high-wavenumber roughness, which takes the form of sharp corners and short steep slopes. Thus, the *power spectrum* is an indicator of high energy in backscatter.

An important task in future efforts will be to see how these propositions hold at other values of (σ, l_c), θ, and for other types of random surfaces. At sufficiently small values of σ, the differences in the statistics of various surface types are not expected to play as important a role in the acoustics.

The variance and correlation length seem to be good predictors of energy in coherent scatter relative to incoherent specular scatter. All three surfaces show a coherent specular peak in Fig. 6-6 (a) while neither show it in (b) as it is buried in the incoherent component.

Lastly, it appears that the acoustics are indifferent to surface Gaussianity for the surfaces studied here, because Gaussianity is largely redundant once the scale structure and the power spectrum are known.

6.4.2 Wideband Results

The incident pulse used in the numerical calculations had spectrum $G_b(\omega)$ (see Eq. 6.11), equal to a Chebyshev window of order 50 and bandwidth $\Gamma\omega_c$. This pulse has constant sidelobe level equal to -50 dB and its time-bandwidth product is approximately $\Delta t \Delta\omega/(2\pi) \simeq 4.2$. From this, one can deduce the spatial extent of the pulse in wavelengths: $\Delta x_p/\lambda = c\Delta t/(2\lambda\cos\theta) \simeq 2.1/(\Gamma\cos\theta)$.

Three values of proportional bandwidth Γ were used: 1.8%, 9%, and 36%, for each of the two values of (σ, l_c) in the previous section. Recall that in the wideband case, λ is defined as the wavelength at the centre frequency.

For each set of 50 surfaces, average onset and extinction times were determined for the log-envelopes, corresponding to the average time at which the response first rises above a noise threshold and the average time beyond which it stays indefinitely below the theshold, respectively. All envelope data lying outside these times were rejected since they were associated with sidelobe leakage.

The quantity of interest is the zero-mean log-envelope defined in Eq. 6.13, which is formed by concatenating the selected portions of individual log-envelopes and subracting the mean. Histograms of these global envelopes were then formed, representing numerical estimates of their probability density functions. These pdf estimates are independent of center frequency and sound velocity.

At $\Gamma = 36\%$, there are 9.7 pulse widths per surface; this value decreases to 2.4 at $\Gamma = 9\%$, and at $\Gamma = 1.8\%$, the pulse is longer than the surface. In the latter case, because the pulse never insonifies to its fullest capacity, one is not observing the true statistics of a $\Gamma = 1.8\%$ pulse. The true statistics of $E(t)$ for this case would be *more* log-Rayleigh than those presented because the envelope would be the sum over a larger number of scatterers.

Case (i) $(\sigma, l_c) = (0.3, 4.0)\lambda$

Pdf estimates for the Facet and GPL surfaces are presented in Fig. 6-7. The pdf's of the GG surface were not calculated because at this value of (σ, l_c) and horizontal

extent L, the backscatter is dominated by edge effects.

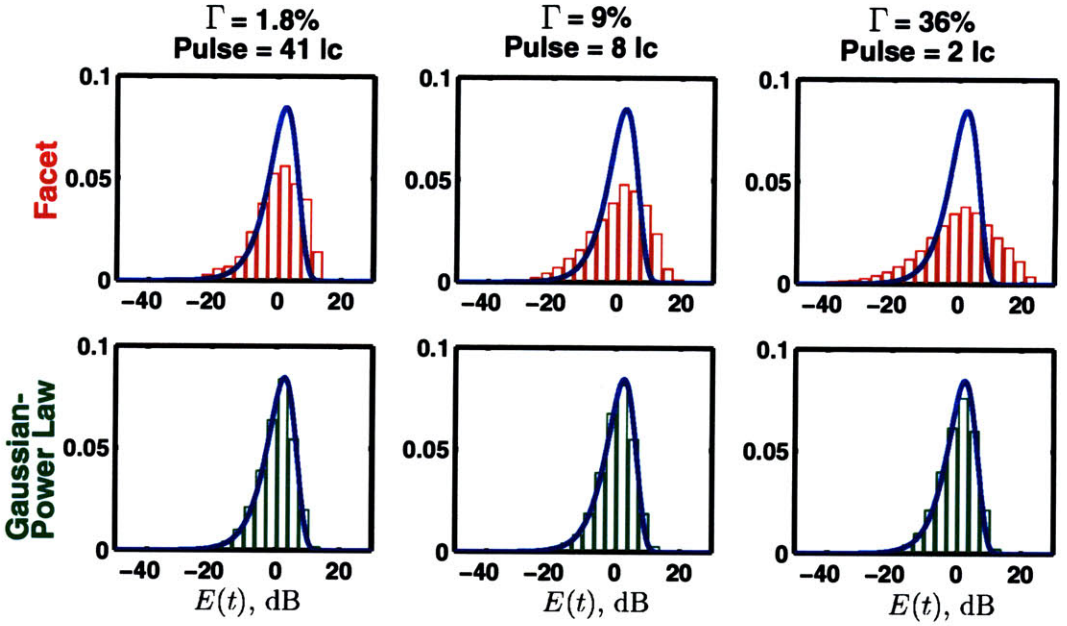

Figure 6-7: Estimates of the pdf's of the log-envelope for $(\sigma, l_c) = (0.3, 4.0)\lambda$. $E(t)$ is nearly log-Rayleigh at all proportional bandwidths Γ for the GPL surface. In the Facet surface, the deviation from log-Rayleigh is accentuated as the bandwidth is increased and the pulse resolves individual targets. This does not occur for the multi-scale GPL surface because many scatterers are included within the pulse width even at the highest resolution considered here. The log-Rayleigh distribution is shown in dark blue, and the pulse resolution is shown in correlation lengths for each bandwidth.

In each of the histograms in the figure, the solid line represents the log-Rayleigh distribution given by Eq. 6.15. The first row of the figure shows that for the Facet surface, the envelope statistics are increasingly non-Rayleigh as the bandwidth is increased from 1.8 % to 36 % and the pulse length is decreased from 41 to 2 correlation lengths. The sample paths of Fig. 6-2, which are normalized by the rms height and correlation length, may be useful to gain an intuitive feel of how much of the surface is included by the pulse at each bandwidth. Note that the ratio of pulse length to correlation length is related to the average number of facets per pulse. The average horizontal extent of a facet (range-wise) is $1/\lambda_r$, so the average number of facets per

pulse is $\Delta x_p \lambda_r$. From Eq. 5.24,

$$\Delta x_p \lambda_r = \frac{10}{3\sqrt{3}} \frac{\Delta x_p}{l_c}. \tag{6.19}$$

The nature of the deviation from the log-Rayleigh distribution for the Facet surface is that levels below -10 dB are more likely to occur, levels between -10 dB and 10 dB are less likely to occur, and more importantly, levels above 10 dB are significantly more likely to occur. The log-Rayleigh distribution shows a sharp cutoff at 10 dB but the 36% bandwidth case for the Facet surface shows a high value of the pdf for amplitudes as high as 25 dB.

To explain this bandwidth-dependent result, it is insightful to look at the two sample log-envelopes for the 36% case shown in Fig. 6-8. Scatter from the Facet surface shows short high-amplitude bursts separated by quiescent periods, representing the pulse's ability to resolve individual features. This is in sharp contrast to the sample envelope from the GPL surface in which one cannot clearly distinguish events. The pulse at this high value of Γ, being $2l_c$ long (see Fig. 6-2) includes roughly 4 facets on average. The target nature of the envelope is due to the fact that on occasion a facet with slope angle of 45° gives rise to a glint in the back direction.

Looking at the second row of Fig. 6-7, the envelope statistics of the GPL surface at proportional bandwidths of 1.8% and 9% are perfectly log-Rayleigh while at 36% they are nearly so. This suggests that even at the largest Γ the pulse includes many scatterers. This is in fact true as the GPL surface is multi-scale and presents features down to infinitesimal sizes.

The reflectors of the Facet surface occur at a single characteristic scale and are responsible for the non-Rayleigh envelope statistics. Still, as the bandwidth is decreased, the envelope statistics become more log-Rayleigh since the response at any given time includes contributions from a growing number of features.

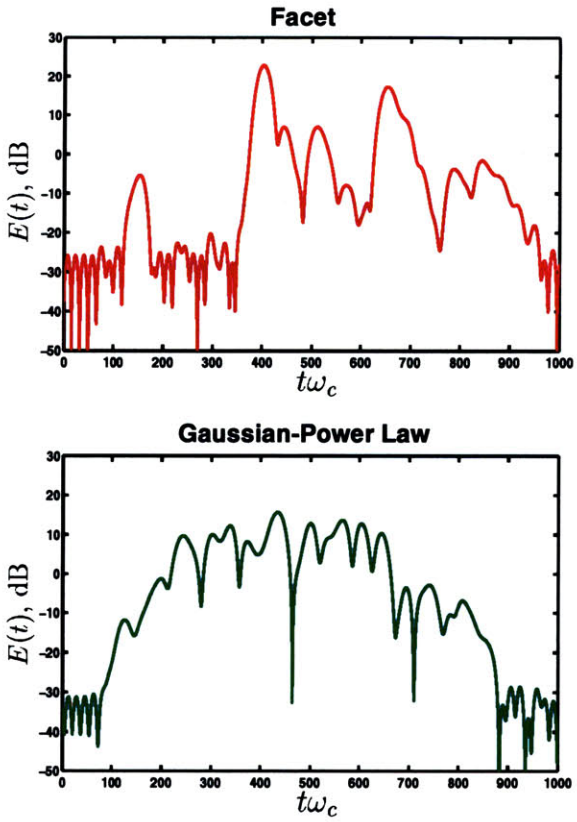

Figure 6-8: Sample realizations of the log-envelope for $(\sigma, l_c) = (0.3, 4.0)\lambda$. The Facet surface leads to log-envelopes with strong peaks separated by quiescence. The GPL surface does not give rise to distinct events.

Case (ii) $(\sigma, l_c) = (0.2, 1.0)\lambda$

It can be seen from Fig. 6-9 that the GPL surface is log-Rayleigh at all bandwidths. The second column shows that while the Facet surface is still largely log-Rayleigh at $\Gamma = 9\%$, the GG surface is already exhibiting event-like statistics. Only in the third column, at $\Gamma = 36\%$, does the Facet surface begin to deviate from log-Rayleigh, while the GG surface has already reached a strongly non-Rayleigh character.

It is perplexing at first to observe that the GG surface achieves non-Rayleigh scatter at lower proportional bandwidths than the Facet surface. Both surface types have the same variance and correlation length and are single-scale, and it is reasonable to expect event-like scatter to occur at around the same bandwidth. There are two factors which explain why this is not so. First, the GG surface, with $\gamma = 15.8°$, presents

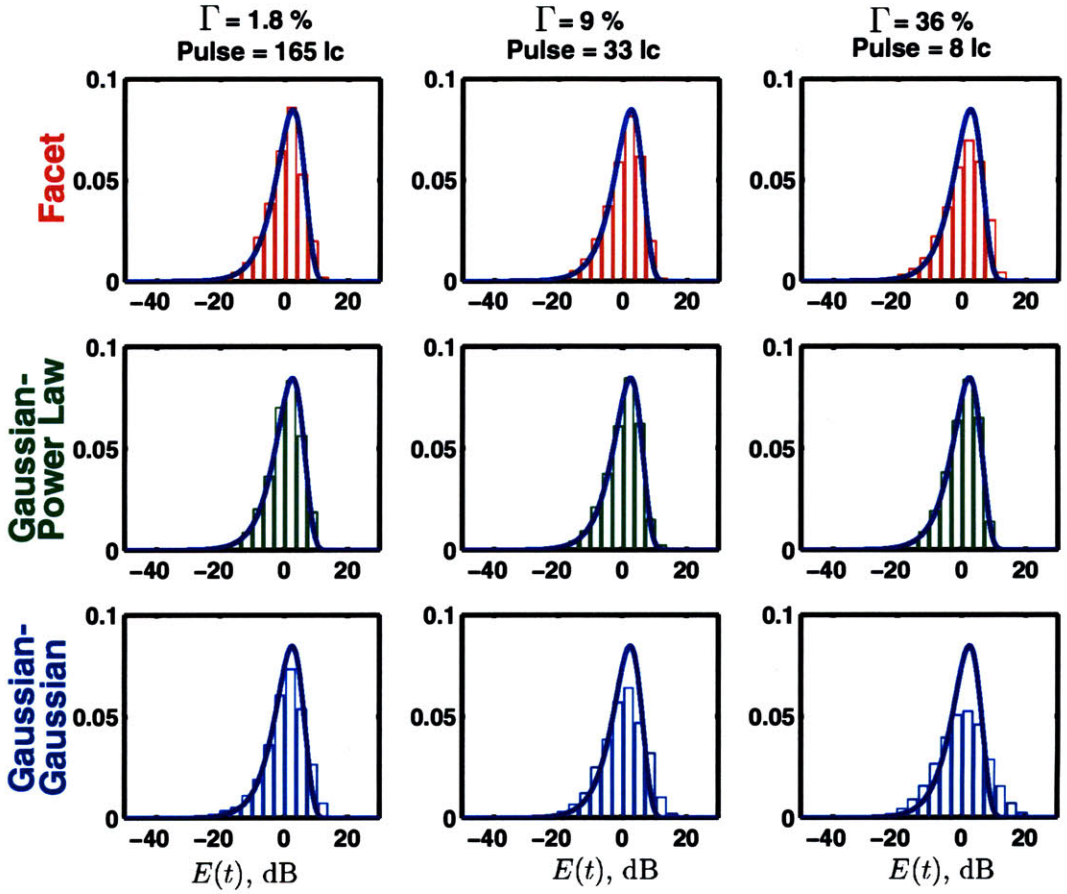

Figure 6-9: Estimates of the pdf's of the log-envelope for $(\sigma, l_c) = (0.2, 1.0)\lambda$. The GG surface is event-like at lower proportional bandwidths Γ than the Facet surface because of its lower rms slope γ and the larger size of its features. The log-Rayleigh distribution is shown in dark blue, and the pulse resolution is shown in correlation lengths for each bandwidth.

back-facing slopes much less frequently than the Facet surface, for which $\gamma = 28.1°$. It was observed in Case (i) that the non-Rayleigh scatter for the Facet surface was associated with *occasional* glints from facets in reflection. If back-reflecting segments become too likely, the envelope is not likely to experience quiescence in between glints, and is likely to include more than one glint at a time. This summation over n independent targets leads to log-Rayleigh envelopes for sufficiently large n.

The lower value of γ for the GG surface is partly responsible for its higher deviations from log-Rayleigh than the Facet surface. A second reason is that the average

width of a feature for the GG surface, being equal to l_c, is about twice that of an average facet ($1/\lambda_r \simeq 0.52 l_c$), so there are half as many features per pulse.

Perplexing differences also exist within the Facet surface family. While there are 16 facets per pulse for both $\Gamma = 36\%$ of Case (ii) and $\Gamma = 9\%$ of Case (i), the pdf estimates for these two cases are quite different. The difference is explained by the rms slope which is 28.1° in the former and 18.4° in the latter. This leads to more a log-Rayleigh behavior in Case (ii). Another consequence of the higher likelihood of back-facing facets is the higher backscattering strength by about 7 dB in Case (ii) as compared to Case (i) (Fig. 6-6).

6.5 Scattering From Hybrid Surfaces

The perfectly smooth features of the GG and the Facet surfaces lead to realiations that appear unnatural because most natural interfaces, including those for which a single-scale component dominates, exhibit some degree of roughness at all scales. In answer to this fact, Hybrid surfaces were introduced in the previous chapter as a combination of GPL and Facet roughness. The realizations of this process were found to have as natural a look as their GPL counterparts yet derived 75% of their energy from the Facet process. A realization of each of these processes is shown on Fig. 5-11.

In this second set of experiments, the bistatic scattering strength and the time-domain statistics of backscatter are compared for Facet, GPL, and Hybrid surfaces for the case $(\sigma, l_c) = (0.3, 4.0)\lambda$ to investigate whether the differences in the results obtained so far between Facet and GPL processes are merely an artifact of the perflectly smooth features. As in Section 6.4, the surfaces are 80 wavelengths long and are filtered at a cutoff of $4k$. The pulse used in the wideband results has a spectrum given by a Chebyshev winddow of order 50, and three values of proportional bandwidth are used: 1.8%, 9% and 36%.

In spite of drawing 75% of its energy from the Facet process, the Hybrid process appears qualitatively fractal. If this were a real profile collected from the seafloor, one would probably not suspect from its appearance that a single-scale process lurks

beneath, and spectral methods would not detect it because the power spectral density is power-law. It was shown that the statistics of the wavelet coefficients provided one means of detecting the differences in scale structure from both the Facet and GPL cases. The fascinating question that is about to be answered is whether the acoustical scattering process can detect what only the wavelets could.

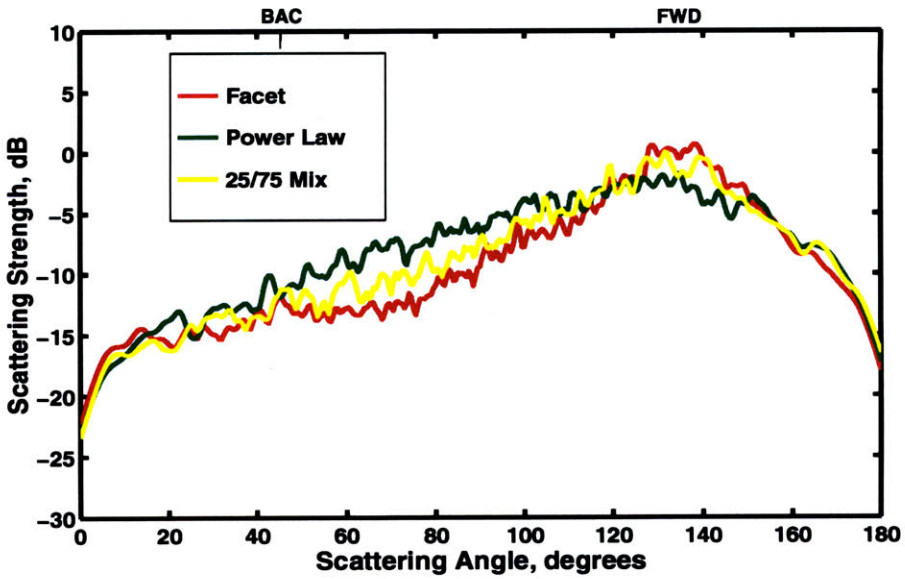

Figure 6-10: Monte Carlo estimates of scattering strength from Facet, GPL, and Hybrid surfaces for $(\sigma, l_c) = (0.3, 4.0)\lambda$.

Figure 6-10 shows that the bistatic scattering strength curves are distinct for the three surface types, with the Hybrid curve lying roughly half way between the Facet and GPL cases. The maximum deviation of the Hybrid curve from either of the two other curves is about 3 dB. It demonstrates that properly establishing the scale structure of a random surfaces for the purpose of scattering predictions goes beyond spectral analysis and qualitative perusal of a few sample profiles.

Turning now to time-domain statistics, Fig. 6-11 show the log-envelope histograms of backscatter at proportional bandwidths of 1.8%, 9% and 36%. As with the scattering strength results, the statistics of backscatter for the Hybrid surface lie somewhere in between those of the GPL and Facet surfaces, showing some deviation from the log-Rayleigh curve, but not as much as the Facet case. The deviation is most appar-

ent at the 36% bandwidth but is distinguishable even at the lowest bandwidth in the form of a lower peak.

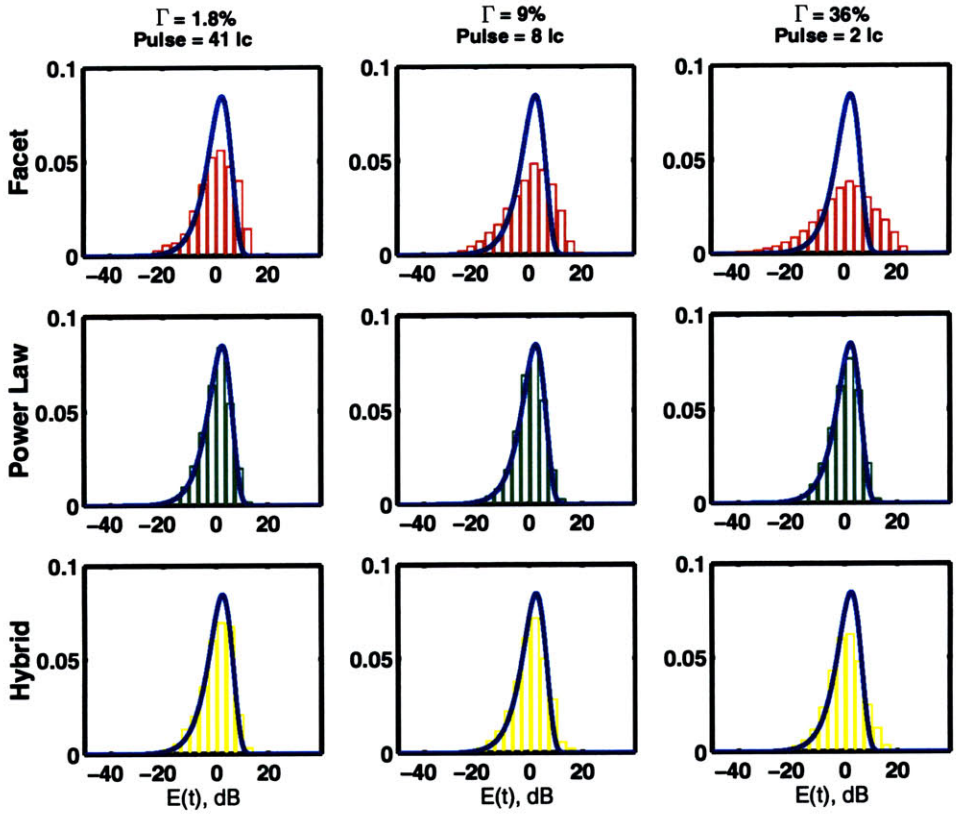

Figure 6-11: Estimates of the log-envelope pdf of backscatter from Facet, GPL, and Hybrid surfaces for $(\sigma, l_c) = (0.3, 4.0)\lambda$. The presence of 25% fractal energy in the Hybrid surface leads to a reduction in the deviations from log-Rayleigh. Nevertheless, at all three values of bandwidth the underlying Facet process of the Hybrid surface leads to non-Rayleigh behavior in spite of being invisible to the eye and undetectable through spectral methods.

It can be concluded that the obervation of a power-law power spectral density and a fractal qualitative appearance are not sufficient to default to a Gaussian model; feature-like roughness, even when hidden beneath a multi-scale "noise" signal, is detectable by the acoustics in both narrowband and wideband scenarios.

6.5.1 Effect of Scale Structure

At the conclusion of this second in a series of three numerical investigations, the following has been learned. The non-Rayleigh behaviour of the Facet, Hybrid, and GG surfaces suggests that single-scale roughness behaves as a collection of targets, however feature-like roughness is not *sufficient* to ensure target-like envelope statistics; the pulse width, the center wavelength, and the surface variance and correlation length must satisfy some critera.

The multi-scale roughness of the GPL surface makes it considerably harder for the surface to possess areas of strong scatter separated by areas of weak scatter, but this is not to say that Gaussian surfaces with power-law spectra can *never* produce non-Rayleigh time statistics. The lower peak in the histogram for the 36% bandwidth case in Fig. 6-11 shows that the GPL surface is beginning to act non-Rayleigh. Using the number of independent observations of the envelope as the number of degrees of freedom, a chi-square test shows that while the deviation from log-Rayleigh is small, it is statistically significant. This trend can only increase as the bandwidth is increased further. Therefore, not only is feature-like roughness insufficient for target-like scatter, it is not *necessary* either. However, it should be the case that for single-scale and multi-scale surfaces with identical correlation length and variance, target-like scatter will occur at much lower bandwidths in the single-scale surfaces. The next Section allows this theory to be tested in the context of much rougher surfaces than have been considered so far.

6.6 Scattering From Higher-Variance Surfaces

6.6.1 Variance and Correlation Length

While the surfaces studied so far have established the insufficiency of the power spectral density in predicting scatter, only two points in the (σ, l_c) plane have been tested. It is natural to ask whether similar conclusions would be reached at other values of variance and correlation length.

Since the ARSRP experiment was the motivation for this study, it seems fitting to attempt cases that resemble Mid-Atlantic Ridge bathymetry more closely. This endeavor comes with advance knowledge that a one-dimensional model cannot hope to obtain realistic values of scattering strength in a two-dimensional scenario. The ability to characterize the time-domain statistics of scatter from a two-dimensional surface with a one-dimensional model is also questionable. It was shown in previous Sections that a prime cause of non-Rayleigh time-domain backscatter is glinting from retroreflecting smooth features. In the two-dimensional case, the orientation of the features has an out-of-plane component that is expected to make glinting more rare than in the 1-D case. In spite of these limitations, the examination of a case with roughness parameters closer to those of ARSRP one-dimensional profiles can only bring one closer to fully understanding scattering in this experiment.

Recall that in Chapter 3, scarp-parallel corrugations on the order of 10-20 m high and 20-30 m wide were observed, and it was when incidence azimuths were normal to these corrugations and when grazing angles were high that maximum departures from Rayleigh were observed.

Here, I apply the composite seafloor model, viewing the faulting pattern that defines the scarps and terraces at Site B', shown in Fig. 3-3, as a single-scale form of roughness at large scales, on which I superimpose a form of roughness at the scale of the scarp-parallel corrugations. I assume that little roughness is present at scales between corrugation-scale roughness and the scale of the scarp-terrace roughness. Focusing on the scarps is then equivalent to focusing on one of the facets of the scarp-terrace process. The only form of roughness that exists on one of these facets is due to the single-scale process at the corrugation scale, and possible roughness at smaller scales. I investigate whether a difference in scattering behavior occurs depending on whether the roughness at the scales of the corrugations and below is modeled as being feature-like through the Facet process, multi-scale through the GPL process, or a combination of both through the Hybrid process.

An estimate of the ratio of rms height to correlation length to be used in the surface models can be obtained from the best-fit power law a/k^b of the power spectral density

of the profile normal to B' scarps in Fig. 4-9, where I found $a = 0.73$ and $b = 2.76$. I assume that the value of b is close enough to 3 to allow use of the Facet seafloor model. The choice of the ratio of rms height to correlation length fixes the position of the high-wavenumber asymptote, as can be seen from Eq. 5.25, which becomes

$$S_{hh} \sim \pi \left(\frac{10}{3}\right)^2 \left(\frac{\sigma^2}{l_c^2}\right) \frac{1}{k^3}, \tag{6.20}$$

implying

$$\frac{\sigma}{l_c} = \sqrt{\frac{a}{\pi}} \frac{3}{10} \simeq 0.14. \tag{6.21}$$

I choose a value of correlation length equal to 8 wavelengths, and a ratio of rms height to correlation length of 0.25, i.e. $(\sigma, l_c) = (2.0, 8.0)\lambda = (12.0, 48.0)$. The focus is not on matching the values exactly but on obtaining roughness which is credibly similar to the face of one of the B' scarps. The rms slopes of Facet, GPL, and Hybrid surfaces with these values of variance and correlation length are approximately 45 degrees, as shown in Table 6.1, and are therefore compatible with the slopes that are expected in the roughness from the cross-scarp corrugations. Simultaneously, the ratio of variance to correlation length is sufficiently near the values predicted from spectral estimates of the seafloor and the values of variance and correlation length themselves are comparable to the heights and widths of the corrugations.

The bistatic scattering strength results for 30 degree grazing incidence are shown in Fig. 6-12. The observation in the two previous sets of numerical experiments that feature-like roughness leads to enhanced incoherent scatter in the forward direction is seen to apply here, with the Hybrid and Facet surfaces showing an enhancement in the forward direction.

The results show that at values of variance and correlation length comparable to the ARSRP scenario, the bistatic scattering strength is distinct for one-dimensional surfaces with different scale structure but identical power spectral density. The scattering strengths for each surface type cannot be directly compared to those observed in ARSRP because increasing the dimensionality of the surfaces leads to radical changes

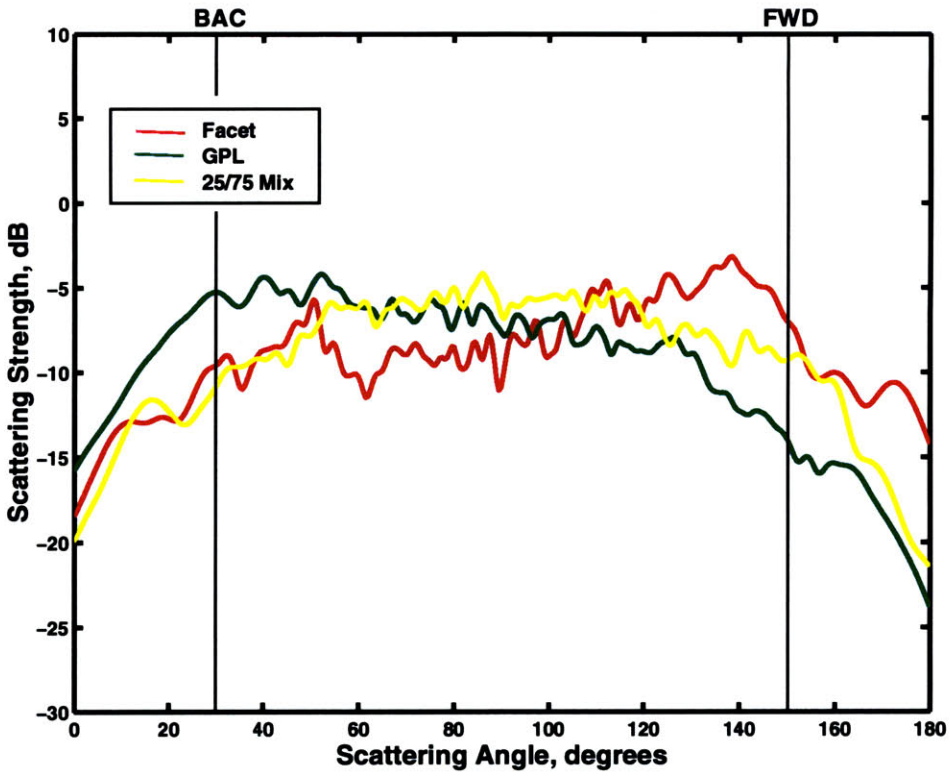

Figure 6-12: Estimates of scattering strength for Facet, GPL and Hybrid surfaces with $(\sigma, l_c) = (2.0, 8.0)\lambda$.

in scattering behavior. Nevertheless, the one-dimensional simulation presented here suggests that scale structure is likely to be an important factor in the two-dimensional scenario as well.

6.6.2 Pulse

In an effort to emulate the ARSRP scenario, the same pulse spectrum $G(\omega)$ is used:

$$A(t) = \begin{cases} \frac{1}{2}\left(1 - \cos(\frac{\pi(t+T/2)}{\tau})\right), & -\frac{T}{2} \leq t < -\frac{T}{2} + \tau \\ 1, & -\frac{T}{2} + \tau \leq t < \frac{T}{2} - \tau \\ \frac{1}{2}\left(1 + \cos(\frac{\pi(t-T/2)}{\tau})\right), & \frac{T}{2} - \tau < t < \frac{T}{2}. \end{cases} \tag{6.22}$$

$$G(\omega) = \mathcal{F}\left[A(t)\cos\left(\omega_{\rm lo}\left(t+\frac{T}{2}\right)+(\omega_{\rm hi}-\omega_{\rm lo})\left(t+\frac{T}{2}\right)^2\right)\right] \tag{6.23}$$

The values of the pulse parameters in the ARSRP scenario were $T = 5$ sec, $\tau = 0.3$ sec, $\omega_{\rm lo} = 200$ Hz, and $\omega_{\rm hi} = 255$ Hz. The log-envelope of the pulse is depicted in Fig. 2-3 of Chapter 2. The time-bandwidth product of this pulse is $\Delta t \Delta\omega/(2\pi) \simeq 2$, giving a ratio of pulse width to wavelength of $\Delta x_p/\lambda \simeq 1/(\Gamma\cos\theta)$, where an incident grazing angle θ of 30 degrees is used.

As in other Sections in this chapter, the results are presented in non-dimensionalized form; the case studied here has a proportional bandwidth of $\Gamma = 24\%$. Thus, the spatial resolution of the pulse is about 5 wavelengths, or 0.6 correlation lengths. In the case of the Facet process, this corresponds to there being, on average, about one facet per pulse.

This new choice of pulse for the numerical simulations raises the issue of the effect of pulse shape on the statistics. Having experimented with several pulse shapes, a summary of general trends can be presented. First, note that low-amplitude portions of the envelope are the result of weak scattering and/or sidelobe leakage from numerous higher-amplitude portions of the response. Thus, the lower the amplitude level, the higher the number of degrees of freedom which sum to form the total signal. For this reason, increases in pulse sidelobe level tend to reduce deviations from log-Rayleigh at lower levels. Deviations from the log-Rayleigh distribution at the highest levels beyond 10 dB are insensitive to changes in sidelobe level, because these high levels are due to peaks in the envelope which are unaffected by leakage from lower-amplitude portions. A widening of the main lobe of the incident pulse decreases deviations from log-Rayleigh at all amplitude levels. Although the use of a different pulse alters the pdf estimates, the conclusions drawn in this paper are not affected by the choice of pulse.

6.6.3 Wideband Results

The pdf estimates of the log-envelopes of backscatter for an incident grazing angle of 30 degrees are shown in Fig. 6-13. At these values of variance and correlation length, most of the facets of the Facet surface are much larger than the wavelength and act as perfect reflectors. The occurence of a strong return in the back direction then co-incides with the rare event that the facet slope is almost exactly back-reflecting or that multiple reflections send energy in the back direction. The behavior of this surface is thus extremely target-like.

The GPL surface is exhibiting significant non-Rayleigh behavior at these values of bandwidth, correlation length, variance, and incident angle. This behavior can be ascribed to the existence of significant portions of the surface which are shadowed by large vertical excursions. Thus, non-Rayleigh behavior is exhibited even if the scatter from illuminated portions of the surface is the sum over a large number of small scatterers. The current example clearly emphasizes that feature-like roughness is not a requirement for target-like scatter. The Hybrid surface, as before, manifests a behavior which lies in between that of the Facet and GPL surfaces.

I now simulate a two-dimensional scenario by considering the lateral size of the sonar footprint, about 600 m, to be composed of approximately ten correlation lengths in the scarp-parallel direction. The scatter from the two-dimensional footprint is then viewed as the superposition over 10 independent one-dimensional surfaces. To simulate the backscattered envelopes, the envelopes from the one-dimensional surfaces are first combined coherently in sets of 10, then processed as usual.

Fig. 6-14 demonstrates the result with the pdfs plotted on a log-scale as in the pdf estimates of data in Chapter 3. The summation over 10 processes considerably reduces the deviations from log-Rayleigh, but a significant deviation persists at the high levels in the case of the Facet and Hybrid surfaces. The deviation is not sufficient to match that of scarp-normal log-envelope pdfs at high grazing angles in Fig. 3-12, however this example shows how two-dimensionality shapes the histograms - the lower levels converge to Rayleigh, and the highest levels persist in their non-Rayleigh behavior,

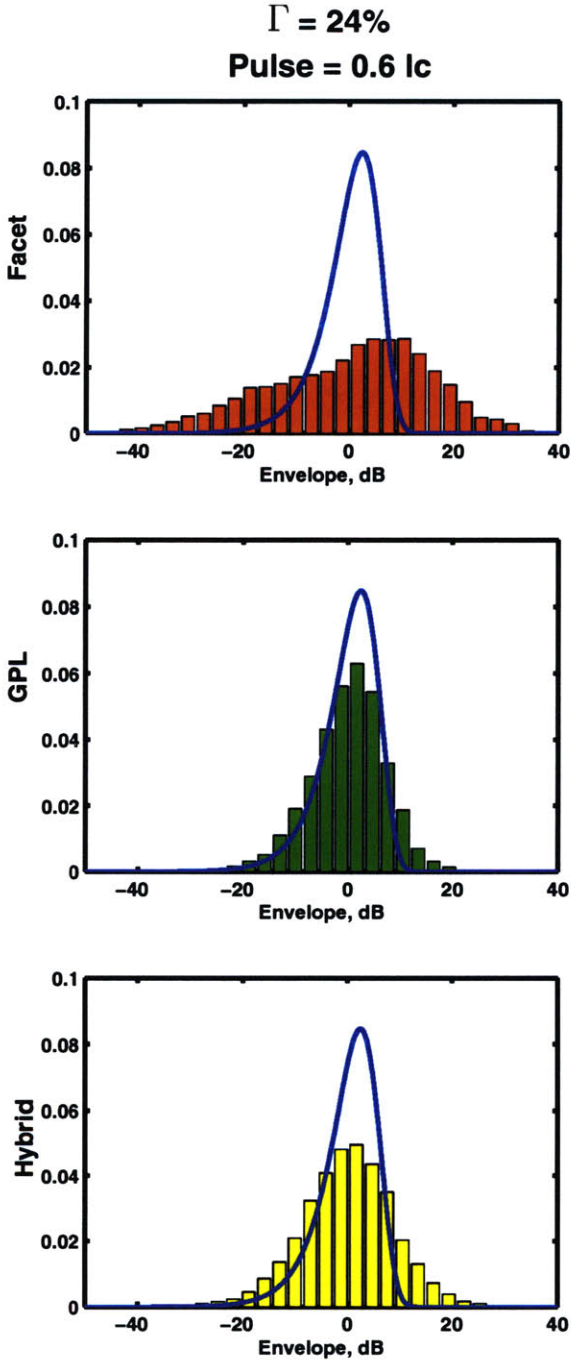

Figure 6-13: Log-envelope pdfs for Facet, GPL and Hybrid surfaces with $(\sigma, l_c) = (2.0, 8.0)\lambda$. The blue curve is the log-Rayleigh distribution. The match-filtered pulse of the ARSRP experiment was used, having proportional bandwidth of 24%. The Facet surface exhibits extreme target-like behavior. The scattering properties of Hybrid surface are distinct from those of the Facet and GPL surfaces.

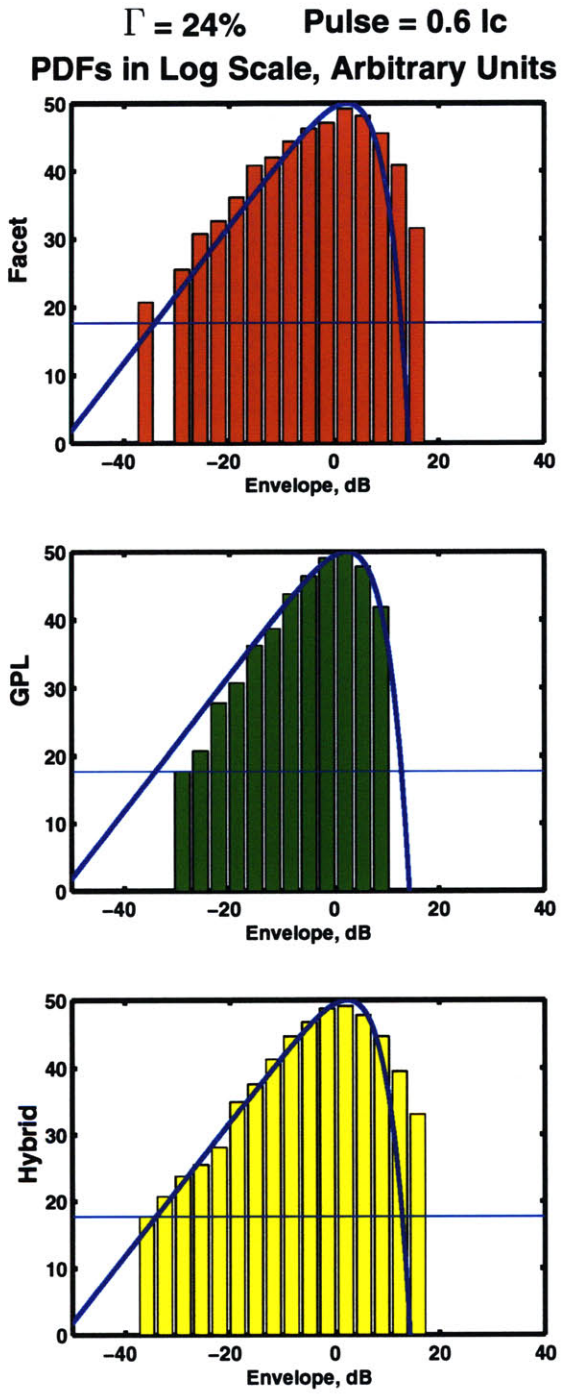

Figure 6-14: Log-envelope pdfs for simulated two-dimensional Facet, GPL and Hybrid surfaces in ARSRP scenario. The blue curve is the log-Rayleigh distribution.

even if just slightly.

The pdf estimates are sensitive to the number of correlation lengths that are deemed to exist within the sonar footprint. At a smaller value, the GPL surface would maintain its non-Rayleigh character at high levels. At larger values, all three surfaces would lead to Rayleigh statistics. Since the correct value to use is a matter of debate it is not possible based on this experiment to prove that in backscatter from the scarps of site B', feature-like roughness is the *cause* of non-Rayleigh statistics. Using the best estimates of variance and correlation lengths from the bathymetric data, I find that the surface models with feature-like roughness provide the closest match with the observed statistics of backscatter from site B' scarps (see Figs. 3-11 and 3-12).

This example *does* demonstrate that for roughness comparable in magnitude to the scarps of ARSRP, scale structure plays an important role in enhancing target-like statistics of time-domain backscatter, *supporting* the assertion that the feature-like nature of bathymetry in ARSRP can play a role in the observed non-Rayleigh behavior of the acoustic data and showing that it would be necessary to characterize the two-dimensional scale structure of ARSRP scarps to explain the data.

6.7 Summary

1. Scatter from the Facet process provides proof that second moment characterizations of random rough surfaces are *not* sufficient for predicting either the bistatic scattering strength or the time-domain statistics of backscatter.

2. Feature-like roughness is neither sufficient nor necessary for target-like scatter. Both feature-like and multi-scale surfaces behave as a collection of resolvable targets and lead to non-Rayleigh log-envelope statistics at sufficiently high proportional bandwidths. In multi-scale surfaces, whose component targets are much smaller and thus not easily resolved by the incident pulse, the onset of non-Rayleigh statistics occurs at higher proportional bandwidths than in feature-like surfaces. With decreasing bandwidth, log-envelope statistics are

increasingly log-Rayleigh for all random surfaces due to the simultaneous contribution of an arbitrarily large number of targets. Shadowing may prevent the log-Rayleigh distribution from ever being attained in some surfaces.

3. Scatter from the Hybrid process demonstrates that feature-like roughness is detectable by acoustic waves even when it is undetectable by either the qualitative appearance of realizations or spectral methods. The distinctness of the statistics of the Hybrid surface from those of the GPL and Facet surfaces suggest that the values of scale structure that are relevant to scattering are more numerous than simply "feature-like" or "multi-scale"; the values vary continuously between the two extremes. Accurate prediction of scattering strength and the statistics of log-envelopes require that along with a surface's power spectral density, its scale structure be determined. This may be accomplished using a variety of multi-scale transform techniques such as the wavelet transform.

4. It appears that Gaussianity is a redundant parameter and is important in scattering only to the degree to which it affects the scale structure and the power spectrum as suggested in Fig. 6-1.

5. In all the numerical experiments, the Facet surface features strong scatter in the back direction as the GPL surface does while exhibiting a forward scatter lobe (similar to that of the GG surface in the first experiment), which supports the assertions that the power spectral density has a dominant role in determining scattering strengths in the back direction and that scale structure plays an important role in determining incoherent scattering strengths about the specular direction and the degree of target-like behavior.

6. The calculations using values of variance and correlation length comparable to roughness on Site B' scarps support the theory that the feature-like nature of the bathymetry in ARSRP plays a role in enhancing observed target-like scatter in acoustic data. Surface models with feature-like roughness provide the closest match to the statistics observed in backscatter from the scarps of site B' in

ARSRP.

Chapter 7

Conclusion

7.1 Contributions

The contributions, results and conclusions in this thesis can be grouped into two categories: (i) those resulting from the analysis of acoustic and bathymetry data from the ARSRP experiment, and (ii) those associated with the theoretical investigation of scale structure in stochastic surfaces and its role in acoustic scattering. Each of these areas is discussed in turn.

7.1.1 Analysis of ARSRP Acoustic and Bathymetric Data

The ARSRP acoustic reverbation data collected near the Mid-Atlantic Ridge are the result of a complex physical process that involves propagation through the water column and scattering with a highly rough seafloor with variable geophysical characteristics. Buried within the resulting reverberation is information about scattering, which is the component of interest in this thesis.

Contribution 1 The development of ARTIST, which is both a software package and a mathematical formalism, to help visualize the insonification process in physically intuitive ways, model reverberation, and extract scattering data originating from detailed seafloor regions.

- Visualization of seafloor insonification

The development of the mathematical entities of insonification and intersection patterns have proved ideal in visualizing the combined effects of propagation, shadowing, bathymetry, time delays, and source-receiver geometry and beampatterns. Graphical representations of intersection patterns allow the identification of bathymetric features expected to play a major role in reverberation, the time windows and beam numbers in which they will contribute, and the combined insonification effects due to source and receiver beampatterns, transmission loss, and local grazing angles with respect to the bathymetry.

- Modeling of Reverberation

The intersection pattern data structure is readily used to generate simulated reverberation. 1/2 CZ reverberation simulations at 200 msec scales in both monostatic and bistatic source-receiver geometries showed excellent agreement with the prominent features in actual reverberation data at intermediate to late times. Reverberation at early times is dominated by mutiple seafloor interaction paths, which are not modeled by ARTIST. The success of the simulations emphasizes the deterministic connection between reverberation and bathymetry and the fact that prominent events are associated with single seafloor interactions. Areas where agreement is poor between model and data provide valuable information about the physical mechanisms at play, be they multiple seafloor interactions or local variations in scattering behavior not modeled by ARTIST.

- Extraction of scattering information

The dominance of surface-bounce and direct ray paths interacting with the seafloor only once for the most prominent events in ARSRP data, along with the capabilities of ARTIST, allow the extraction of portions of the reverberation data that specifically correspond to detailed geographic regions. The energy in each pixel in the data is normalized by TL and beampattern values and related to unique grazing and bistatic angles and a footprint area that is based on the sonar's spatio-temporal ambiguity function.

Using the 200 m resolution bathymetric data, the capabilities of the sonar system, and the capabilities of ARTIST, the scatter from intertwined seafloor areas as narrow as 500 m with distinct geology was resolved.

Contribution 2 The analysis and interpretation of scattering and bathymetric data from a feature of O (5 x 5) km in size known as site B'.

- Establishment of distinctness of backscattering strengths and time-domain statistics from scarps and terraces and failure of Lambert's law at low grazing angles

Site B' is composed of alternating scarp and terrace areas which were explicitly identified using polygonal shapes as narrow as 500 m and used as input to ARTIST for the extraction of scattering strength. Backscattering strength curves were then obtained separately for scarps and terraces and were shown to be distinct from each other, with terraces showing higher backscattering strengths by about 3-4 dB at grazing angles below 20 degrees. The best-fit Lambert's law has a coefficient μ of -16 dB but fails dramatically at angles below 25 degrees, a result which is consistent with well-known properties of seafloor scattering at low grazing angles.

The probability density functions of high-resolution log-envelopes exhibit a lower peak value and enhanced tails as compared with the log-Rayleigh pdf. This is true for both geological categories, but scarps show a higher deviation from Rayleigh. While the variance of the log-envelope pdfs from scarps and terraces is within 0.5 dB of the value associated with a Rayleigh process, the observed deviations from the Rayleigh distribution are significant in the context of target detection and provide useful information about the scale structure of the seafloor.

- Demonstration of the importance of anisotropy in scattering from B' scarps

Using seven different ship positions with respect to site B', the effect of the anisotropy of B' scarps was investigated, revealing that backscattering strengths are at least 5 dB higher normal to the scarps than 30 to 50 degrees relative to the scarps. The best-fit Lambert's law coefficients range from -22.5 dB between 30 and 50 degrees

with respect to B' scarps, to -14 dB normal to the scarps. Again, Lambert's law is found to fail at low grazing angles. The deviations of the time-domain statistics of high-resolution log-envelopes from Rayleigh are found to be accentuated for normal azimuths to the scarps, and at large grazing angles.

- Proposal of a composite stochastic seafloor model

Nested views of the bathymetry at increasing resolutions have revealed that the roughness at smaller scales cannot be extrapolated from the roughness at larger scales. At the range of scales defined by the views, the roughness exhibits repeatable feature-like structures such as abyssal hills, canyons, gullies, and manganese nodules which cannot simultaneously be explained with Gaussian seafloor models. A new model of the seafloor was proposed which is the composite of many single scale processes each of which is potentially associated with a specific geophysical mechanism. The new model satisfies observed power spectra which have a power-law decay over many orders of magnitude in wavenumber but can model feature-like roughness.

- Interpretation of scattering data using bathymetric observations and proposal of theories

Estimates of the power spectral densities of profiles normal and parallel to B' scarps are very close, suggesting isotropy, however visual observations of B' scarps at the same scales reveal a distinctness in morphology in the two directions. In both directions, the morphology is feature-like, but parallel to the scarps the features are canyons 100-200 m wide and 30-50 m tall and normal to the scarps the features are gullies 10-20 m tall and 20-50 m tall. The distinctness of the scatter for different anisotropic directions is proposed to result from the distinctness of the roughness along both directions. The distinctness cannot be explained by the power spectral density since it is equal in both directions. The linked acoustic and bathymetric observations have led to two proposals:

1. The power spectral density is inadequate in specifying feature-like roughness; and

2. There is a link between the scale structure of the roughness and its scattering strength and log-envelope pdfs. Specifically, the presence of feature-like roughness at certain scales can enhance backscatter and target-like behavior in the time-domain.

These two proposals have led to a theoretical exploration of the sufficiency of the power spectral density in describing feature-like roughness and in predicting acoustic scatter.

7.1.2 Surface Scale Structure and its Impact On Acoustic Scattering

Contribution 3 The establishment of the concept of scale structure and its distinctness from the power spectral density.

- Qualitative definition of scale structure

The scale structure of a stochastic process is defined as the statistical spatial arrangement of features at different scales.

- Development of single-scale models with feature-like scale structure and power-law power spectral density

Two prototype one-dimensional surface models have been proposed which generate feature-like roughness: a piecewise-constant process and a piecewise-linear process defined as the Facet process. The power spectral densities and correlation functions have been derived analytically and verified numerically in both cases; they exhibit a power-law decay. Comparison of realizations from these processes with realizations of Gaussian processes having identical second moment has demonstrated that the scale structure of stochastic processes is not determined by the power spectral density.

As models of seafloor, both processes are found to look unnatural, however when the models are used as the single-scale components of a composite process, the unnatural look disappears. Realizations of the composite seafloor model have four desirable qualities: (i) they do not look unnatural; (ii) their power spectral densities

have power-law decay; (iii) they lead to feature-like roughness, and (iv) they allow each section of the wavenumber spectrum to be accounted for by a separate seafloor-forming mechanism, taking statistical seafloor modeling one step closer to directly connecting observed spectra with geophysical processes. Qualities (i) and (ii) are shared by Gaussian models but qualities (iii) and (iv) are not.

- Usefulness of wavelet transform for detecting differences in scale structure

Scale structure has been shown to be quantifiable using wavelet transforms. Whereas qualitative methods invariably end up concluding that a realization is either "feature-like" or "not feature-like", the statistics of wavelet coefficients can detect subtle difference in scale structure. For a set of surfaces with identical power spectral density but differences in scale structure, all second moment characterizations fail in detecting differences, be they spectral or wavelet. Therefore, higher moments than the second must be used to characterize scale structure. A variation on the proposed feature-like seafloor models was the Hybrid surface which was defined as a linear combination of Facet and Gaussian power-law processes. The resulting process is qualitatively and spectrally indistinguishable from the Gaussian power-law process, but wavelets successfully distinguish all three processes.

Contribution 4 The establishment that scale structure is a surface attribute of relevance to acoustic scatter and that second moment characterizations of random surfaces are insufficient for predictions of scattering.

A Monte Carlo numerical implementation of the exact Helmholtz-Kirchhoff integral equation for scatter from a one-dimensional rigid surface was used to estimate mean bistatic scattering strengths and the one-point probability density functions of backscattered log-envelopes. The results of three numerical experiments led to the following conclusions.

- The power spectral density is insufficient in predicting scattering

The bistatic scattering strengths and log-envelope statistics of Facet and GPL surfaces, having identical power spectral density but different scale structure, were compared at two values of variance and correlation length: $(\sigma, l_c) = (0.3, 4.0)\lambda$ and $(0.2, 1.0)\lambda$. The scattering strengths were found to be distict by as much as 5 dB and the time-domain statistics of backscatter were found to deviate considerably from Rayleigh for the Facet surface and only marginally so for the GPL surface. These observations confirm the intuitive notion that surface *features*, not wavenumber components, are responsible for scattering and that since a given power spectrum allows many different scale structures, the power spectral density is not in general sufficient to make predictions about the scattering properties of a random rough surface.

- Feature-like surfaces are more prone to behaving as a collection of resolvable targets than multi-scale surfaces, but feature-like roughness is neither necessary nor sufficient for non-Rayleigh envelope statistics to occur.

Common scattering characteristics can be found between surfaces having vastly different power spectral densities but similar scale structure, as was found by comparing the scatter from Facet surfaces and Gaussian surfaces with Gaussian power spectral density (GG). The proclivity for an enhanced incoherent forward scatter lobe and for target-like statistics was noted for the above two values of variance and correlation length. It is not generally true that feature-like surfaces necessarily imply target-like scatter since pulses with large spatial extents can include a sufficient number of statistically independent scatterers for the log-envelopes to be Rayleigh for all surface scale structures, assuming that shadowing does not play a major role, and pulses with sufficiently small spatial extents can begin to resolve individual scatterers for all surface types.

- Scale structure is a continuous parameter of relevance to acoustic scattering

Hybrid surfaces, considered more realistic as models of natural interfaces, were found to have distinct scattering properties from both the Facet and Gaussian power law (GPL) processes, in spite of looking qualitatively similar to the latter. The distinctness of scatter from the Facet process compared to the GPL process is not an artifact

of the perfectly smooth facets; scattering properties are distinct throughout the continuum of scale structures between the Facet and GPL cases, and potentially for a wide set of other processes with identical second moment not studied here, emphasizing the importance of the use of a technique such as the wavelet transform to identify scale structure.

- Feature-like roughness at the scales encountered in the ARSRP experiment *does* enhance target-like behavior

At the large values of variance and correlation length characteristic of roughness on the scarps of site B' normal to the anisotropic axis, Facet and Hybrid one-dimensional surfaces were shown to significantly enhance the high-level tails in the pdfs of backscattered log-envelopes compared to GPL surfaces thereby improving the match with ARSRP data and supporting the theory that feature-like roughness in ARSRP scarps plays a role in the non-Rayleigh behavior of the data.

This research has demonstrated the importance of going beyond second moment characterizations of rough surfaces in making predictions of acoustic scatter. It proposes that a view of random rough surfaces in terms of the distribution of physical features at various scales is both more natural and more effective in understanding scattering than wavenumber representations and second moment statistics. Wavelet transforms appear to be ideal for this task, as they naturally embody the ability to detect features.

This thesis has made important contributions in modeling of reverberation, understanding of acoustic scattering, modeling of surfaces stochastically, and statistical representations of seafloor morphology. The three last areas appear fertile at the moment for further exploration.

7.2 Suggestions For Future Research

There are three lines of questioning that show considerable promise for future research. The first is in random rough surface scattering, the second is in stochastic surface modeling, and the third is in geophysics. Each of these areas is discussed in turn.

7.2.1 Scattering from Random Rough Surfaces

This thesis has established that scale structure is not congruent with the power spectral density in establishing the properties of a rough surface which are relevant for acoustic scattering. Although the simulations presented in this thesis have provided insight into the role of scale structure, a great many questions remain unanswered about its role in rough surface scattering. Obtaining the answer to any of these questions will constitute an advancement in the field:

- What is the role of scale structure at other values of variance and correlation length?

Using only three values of variance and correlation length, considerable progress has been made in this thesis in understanding the importance of scale structure. It is unclear what are the boundaries in the (σ, l_c) plane, if any, outside which or within which scale structure can be neglected and the dependence of these boundaries on pulse width. Can a general understanding of the scale structure effect at all values of variance and correlation length be attained for arbitrary power spectral density or does each case need to be investigated in isolation? These questions could be answered by sampling the (σ, l_c) plane more finely using exact computational methods.

- What are the scattering properties of the other surface models proposed in Chapter 5?

Models with different values of spectral exponent were presented: the piecewise constant model, fractional derivative model, and models with different vertex statistics. Also, a composite model made of feature-like processes acting at different scales was introduced. These models should be studied to gain a better undertanding of how the range of possible scale structures affects scattering.

- Can the effects of scale structure on acoustics be accounted for in the Kirchhoff and perturbation approximations?

Clearly, this thesis has demonstrated that the standard form for random rough surfaces [50] involving only the second moment is doomed to fail in predicting either the bistatics scattering strength of the time-domain statistics of scattered envelopes, but perhaps the methods can be extended satisfactorily by adding a small number of higher moments.

- Do the conclusions drawn using one-dimensional surfaces carry over to the two-dimensional case?

The three-dimensional rough surface scattering problem, involving surfaces defined over two-dimensional domains, cannot always be understood from one-dimensional surface examples. Azimuthal angles outside the plane of incidence have no equivalent in one-dimensional surfaces. Two-dimensional rough surfaces present a variability in the lateral dimension which has significant impact on scattering that cannot be modeled correctly using only one dimension. Anisotropy is unique to two-dimensional interfaces. Since the concept of feature-like versus multi-scale roughness clearly applies in two dimensions, it is interesting to ask how scale structure affects scatter in the three-dimensional scattering problem, where additionally to the unique characteristics mentioned so far, two-dimensional feature-like surfaces would have smooth features with arbitrary slope and azimuthal orientation. Given the numerical intensiveness of the three-dimensional wideband problem, this issue is particularly well-suited for experimental study. An experiment would involve the design of prototype one-dimensional and two-dimensional surfaces from which acoustic scatter would be collected and compared in a controlled environment.

- What is the role of scale structure in three dimensions?

There are many examples of natural three-dimensional processes through which sound propagates which lead to power-law spectra. Some examples are volume inhomogeneities in sediments, internal wave fields, and turbulence.

- Can exact numerical methods be improved to accelerate computations?

In fact, this question is already answered. Iterative solutions of the integral equation solution have a computational time of order N^2, where N is the number of surface samples [62]. Tsang, Chan and Pak (1994) have developed a sparse-matrix flat-surface iterative approach (SMFSIA) whose computational time is of order $N \log N$. It may be fruitful to benchmark these approaches against the integral equation method used here in the case of feature-like surfaces such as the Facet surface. If as accurate, these methods could allow more rapid investigation. In the case of the Facet and other feature-like surfaces, solutions based on the exact solution of Biot and Tolstoy [4] [64] [65] [63] are promising. This solution has been used both for one-dimensional and two-dimensional rough surfaces and also for three-dimensional objects [44] [43] [45] [27] [46] [47] [31] [29] [7] [35] [6] [8] [34].

- What is the role of scale structure in the general case of an interface between two elastic media?

There is no reason to believe that the distinctness of the scattering properties of multi-scale and feature-like surfaces in the rigid case does not carry over to scattering at an arbitrary elastic interface, but this remains to be verified. Elastic media support many more wave types, each of which could be affected in unique ways by scale structure. Scale structure could have an important role to play in the coupling between wave types, for example.

7.2.2 Stochastic Surface Modeling (Applied Mathematics)

I have identified three areas meriting further study.

- Development of the two-dimensional Facet process

Feature-like two-dimensional surface models with power-law spectra need to be developed. As described at the end of Appendix C, the natural extension to two-dimensions in the case of the Facet process is to use triangular Facets between vertices which are Poisson distributed in the plane with Gaussian heights. This would allow numerical investigation of the effect of scale structure in the three-dimensional scattering problem.

- Analytical definition of scale structure

Of the three properties in the triangle of Fig. 6-1, both Gaussianity and the power spectral density can be defined analytically, but the definition of scale structure remains largely qualitative. As demonstrated by the Hybrid surface, there is a need for an analytical definition that will identify surfaces which lie somewhere between being feature-like and multi-scale. While it was shown in this thesis that space-scale methods such as the wavelet transform can differentiate between surfaces that, by construction, are known to differ in scale structure, this quantity has not been defined explicitly so that given a surface with unknown statistics, its scale structure can be determined quantitatively.

I believe that a definition in terms of the statistics of wavelet coefficients may prove fruitful. The wavelet decomposition includes the information contained in the power spectral density and information about Gaussianity, but also provides information about *features*. The characterization of surfaces in terms of their wavelet statistics would therefore be more complete than using spectral methods. It would also allow the design of surface models in the wavelet domain with prescribed power spectral density and scale structure.

- Formulation of acoustic scatter in terms of wavelet statistics

With a characterization of stochastic surface models in terms of wavelet coefficients, the door is opened to test new ideas for analytical formulations of stochastic surface scattering. Such formulations are typically based on the power spectral density, but a formulation based on wavelet coefficient statistics may be able to accurately predict the effects of scale structure along with the commonly modeled effects of variance, correlation length, and the shape of the power spectral density. Such a formulation could be designed to inherently incorporate some of the ideas on separation of scales that are being used at the present time.

7.2.3 Geophysics and Oceanography

The composite seafloor model and the concept of scale structure proposed in this thesis open a new door to studying statistical seafloor morphology. Analyzing the scale structure of bathymetric data, using wavelets for example, would allow any feature-like component processes to be identified and potentially related to a specific geological process. If a link is established, the marine geologist's ability to study the various processes which form the ocean floor using statistical datasets of bathymetry is enhanced.

Once each seafloor-forming process is identified and the manner in which it contributes to roughness is understood, seafloor models could be developed which are parameterized by physical variables such as spreading rate, mass wasting, etc. as opposed to a phenomenological parameterization. The advantage of the parameterization in terms of physical processes is that a single model would apply in many parts of the world's oceans.

A variety of 1, 2, and 3-dimensional geophysical, oceanographic, and atmospheric stochastic processes exhibit power spectra with power-law decay. In all these fields, it is common either to use a deterministic characterization or a statistical one. In the former case, the scale structure of specific features can be studied individually but global study is not feasible for small features ($<$ 1 km for example). In the latter case, global study is possible but second-order characterizations are often used which cannot model scale structure. There is a need for a tool that can characterize feature-like roughness stochastically so that this vital physics-rich information can be included in global models.

Appendix A

A Note on Beampatterns

In Chapters 2 and 3, each array was modeled as a directive point source, as implied by Equation 2.31. The directivity results from applying the isovelocity far-field beampatterns $B_s(\phi)$ or $B_r^{(k)}(\phi)$ to a point source at the center of the array. For monochromatic insonification, the amplitude of the pressure experienced at the seafloor results from the coherent interaction of separate ray paths from individual elements in the source array. Since each ray path has its own phase and TL, the question arises whether the resulting amplitude is well approximated by ARTIST. The accuracy of the approximation depends on how well the refractive medium preserves the relative phases between the array elements. The results of Ref. [52] suggest that the relative phases are well preserved in ARSRP, since identical amplitudes are obtained whether the calculation is performed element by element or using a directive point source.

A second question relates to the calculation of beampatterns in the wideband case. Here, additionally to the coherent interaction of array elements that forms the beampattern, the incident amplitude at the seafloor is affected by coherent interference across the frequency band. The proper beampattern to use is therefore the coherent wideband far-field beampattern of the array in an isovelocity medium. In Ref. [22], the wideband scenario is handled by summing the squared of monochromatic beampatterns at each frequency, corresponding to a phase-neglecting incoherent average. The choice of frequency integration method affects mostly the sidelobe level, which is lower (and correct) in the coherent case. It is not felt that coherent wideband

integration would change any of the conclusions of Ref. [22].

Appendix B

Manipulation of Rayleigh Variables

As the number of independent, identically distributed (i.i.d.) variables which make up a complex signal $p_s(t)$ grows, the real and imaginary components of $p_s(t)$ are Gaussian by the Central Limit Theorem. Then, the quantity $r(t) = |p_s(t)|$ has a Rayleigh density:

$$p_r(R) = \frac{R}{\sigma_r^2} e^{-R^2/2\sigma_r^2} u(R), \tag{B.1}$$

where $u(R)$ is the unit step function. The probability density of the resulting log-envelope,

$$E_R(t) = 20 \log_{10}(r(t)), \tag{B.2}$$

can be found from the Rayleigh density using the Jacobian of transformation B.2 [53]:

$$p_{E_R}(E_R) = \frac{\ln 10}{20\sigma_r^2} 10^{\frac{E_R}{10}} e^{-\frac{10^{E_R/10}}{2\sigma_r^2}}. \tag{B.3}$$

This density will be referred to as log-Rayleigh. In all of the results presented in this thesis, the log-envelope mean is subtracted out. The fact that $E_R(t)$ is zero-mean

contrains the value of σ_r^2 as follows:

$$0 = \mathcal{E}[E_R] = \int_0^\infty 20 \log R \frac{R}{\sigma_r^2} e^{-R^2/2\sigma_r^2} dR = 10 \log e (\ln 2\sigma_r^2 - C), \tag{B.4}$$

implying that $\sigma_r^2 = e^C/2 \simeq 0.89$ where C is Euler's constant (0.577215 ...) [21]. This result is valid if the mean is known as an independent parameter, however in the data processing, each processed waveform is of finite length. The mean is estimated from the finite-length samples; its subtraction removes a degree of freedom from the samples and modifies the distribution of the samples.

The number of degrees of freedom for each finite-length chunk of $E_R(t)$ is determined by the ratio of pulse width to sample window width, I.

Suppose we have I i.i.d. log-Rayleigh variables E_i. Grouping them together and subtracting their mean, we now have I partially correlated variables $\hat{E}_i = E_i - \frac{1}{I}\sum_{j=1}^{I} E_j$. Whereas there were I degrees of freedom before subtraction, there are now $I-1$ degrees of freedom. Further, each variable is no longer log-Rayleigh.

Taking the example case $I = 2$, we begin with the set $\{E_1, E_2\}$ and end up with $\{\frac{1}{2}(E_1 - E_2), \frac{1}{2}(E_2 - E_1)\}$, a set in which the second variable is perfectly correlated with the first. Because E_1 and E_2 are i.i.d., the opposite signs of the variable $E_1 - E_2$ lead to a symmetric distribution. From this argument alone, I have already determined that this variable cannot be log-Rayleigh, since this pdf is not symmetric.

For arbitrary I, the pdf of the mean-corrected variables is obtained from

$$p_{\hat{E}}(\hat{E}) = p_E(E) * \underbrace{Ip_E(-IE) * \cdots * Ip_E(-IE)}_{I}. \tag{B.5}$$

I have not endeavored to solve this analytically, but a numerical solution is readily implemented, and the resulting pdf's are presented on Fig. B-1 for the cases $I = 2, 4, 7, 10$ and 15. On the linear scale of Fig. B-1 (a), it can be seen that the mean-corrected variables quickly converge to the log-Rayleigh density. In (b), the logarithmic scale provides an expanded view which reveals that the tails still haven't quite converged even at $I = 15$.

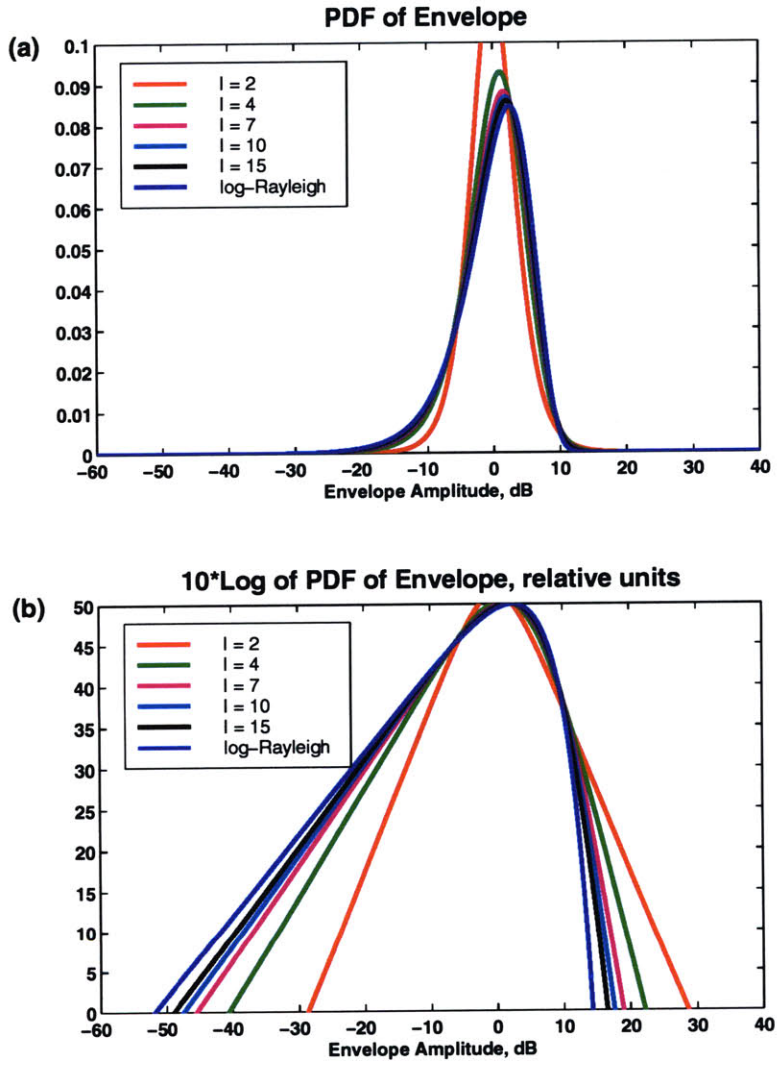

Figure B-1: Probability density functions of Rayleigh variables normalized to zero mean in sets of I. The log-Rayleigh case is attained for $I = \infty$.

Since logarithmic views of the upper tail in the pdfs are used in this thesis to establish whether or not collected envelopes are Rayleigh, it is important to determine the number of degrees of freedom from the window sizes and pulse lengths in question, and employ the correct formula in Eq. B.5. For example, in the data analysis of Chapter 2, I employ 200 msec data segments containing ten 20 msec 3-dB pulse widths. This corresponds to the light blue curve, which lies several orders of magnitude above the log-Rayleigh pdf at the high-level tail. Were the pdf estimates to be compared directly with the Rayleigh curve, it might be incorrectly deduced that the data are non-Rayleigh.

Finally, I would like to address some issues regarding the mean and variance of intensity measurements. The background for this discussion is Ref. [42], in which the statistics of averaged intensity measurements are studied.

All log-envelope histograms in this thesis are obtained from instantaneous (non-averaged) intensity. It is shown in Ref.[42] that instantaneous intensity measures which obey a Rayleigh pdf lead to a log-envelope with fixed standard deviation of 5.57 dB. In the processing of Chapter 3 in which mean-corrected 200 msec time windows are used (the mean being estimated from the 200 msec sample itself), the standard deviation can be computed numerically from the pdf in Eq. B.5 using the case $I = 10$; it is 5.38 dB. Any statistically significant deviation of the standard deviation of the data from this value of 5.38 dB indicates non-Rayleigh behavior. However, the focus in this thesis is on the high-level tails in the pdfs which, while they are often orders of magnitude greater than the tails of the Rayleigh process, may not affect the standard deviation by more than 1 dB.

Appendix C

The Facet Seafloor Process: Derivations

This appendix contains derivations for the correlation function, power spectral density, correlation length, and variance of the random process $h(x)$ defined by

$$h(x) = z_i + \left(\frac{x - x_i}{x_{i+1} - x_i}\right)(z_{i+1} - z_i) \tag{C.1}$$

where i and $i+1$ are the indices of the vertices whose abscissae lie just before and just after the current position x, respectively. The $\{x_i\}$ are Poisson arrivals, defined as the transition locations of

$$Pr[N(x'') - N(x') = k] = \frac{[\lambda_r |x'' - x'|]^k}{k!} e^{-\lambda_r |x'' - x'|}. \tag{C.2}$$

The $\{z_i\}$ are zero-mean and Gaussian with variance σ_{zz}^2 and discrete correlation function $\mathcal{E}[z_i z_j] = R_{zz}[k]$, $k = |j - i|$. The processes generating the $\{x_i\}$ and the $\{z_i\}$ are independent. Proceeding to the derivation of the correlation function, we define two arbitrary locations on the x-axis, x' and x'', with $x'' \geq x'$. We also define x_m and x_{m+1} as the abscissae of the vertices lying just before and just after x' respectively, and x_n and x_{n+1} as those lying just before and just after x'' respectively. The correlation

function is

$$R_{hh}(x',x'') = \mathcal{E}[h(x')h(x'')] = \sum_{k=0}^{\infty} \mathcal{E}\left[\left(z_m + \left(\frac{x'-x_m}{x_{m+1}-x_m}\right)(z_{m+1}-z_m)\right)\times \right. \tag{C.3}$$
$$\left.\left(z_n + \left(\frac{x''-x_n}{x_{n+1}-x_n}\right)(z_{n+1}-z_n)\right)\middle| N(x'')-N(x')=k\right] Pr[N(x'')-N(x')=k]$$

where we have conditioned on the number of events between x' and x''. Recall that for $\overline{x}$ and $\overline{y}$ both vectors in R^n, the conditional density of $\overline{x}$ given $\overline{y}$ is

$$p_{\overline{x}|\overline{y}}(\overline{X}|\overline{Y}) = p_{\overline{x},\overline{y}}(\overline{X},\overline{Y})/p_{\overline{y}}(\overline{Y}) \tag{C.4}$$

Another form of this relation applies when y is a variable taking discrete values:

$$p_{\overline{x}|y=k}(\overline{X},k) = p_{\overline{x},y=k}(\overline{X},k)/Pr[y=k]. \tag{C.5}$$

Distributing the elements within the parentheses in Eq. C.3, and using the independence of the $\{x_i\}$ and the $\{z_i\}$,

$$\begin{aligned} R_{hh}(\chi) = \sum_{k=0}^{\infty} \frac{[\lambda_r(x''-x')]^k}{k!} e^{-\lambda_r(x''-x')} \Big\{ & R_{zz}[k] \\ & +(R_{zz}[k-1]-R_{zz}[k])\mathcal{E}\left[\left(\frac{x'-x_m}{x_{m+1}-x_m}\right)|N(x'')-N(x')=k\right] \\ & +(R_{zz}[k+1]-R_{zz}[k])\mathcal{E}\left[\left(\frac{x''-x_n}{x_{n+1}-x_n}\right)|N(x'')-N(x')=k\right] \\ & +(2R_{zz}[k]-R_{zz}[k-1]-R_{zz}[k+1])\times \\ & \mathcal{E}\left[\left(\frac{x'-x_m}{x_{m+1}-x_m}\right)\left(\frac{x''-x_n}{x_{n+1}-x_n}\right)|N(x'')-N(x')=k\right]\Big\} \end{aligned} \tag{C.6}$$

The terms within each of the three expectation operators in the above equation are evaluated separately. Some background equations are necessary before this can be attempted.

C.1 Probability Densities for x_{m+1}, x_m, and $\overline{x'}$

The probability density function for x_{m+1} (the first arrival after x') is given by:

$$\begin{aligned} p_{x_{m+1}}(X_{m+1}) &= \frac{d}{dX_{m+1}} Pr[x_{m+1} \leq X_{m+1}] && \text{(C.7)} \\ &= \frac{d}{dX_{m+1}}(1 - Pr[N(X_{m+1}) - N(x') = 0]) && \text{(C.8)} \\ &= \lambda_r e^{-\lambda_r(X_{m+1}-x')} U(X_{m+1} - x'). \end{aligned}$$

where

$$U(x) = \begin{cases} 1, & x \geq 0 \\ 0, & x < 0. \end{cases} \qquad \text{(C.9)}$$

The pdf of the first arrival beyond x' depends only on the distance from x'. In general, the pdf of an arrival given a sequence of prior arrivals depends only on the distance from the latest of the arrivals. This results from the fact that the generating Poisson process is an independent increments process [53].

$$p_{x_j|x_1,x_2,\ldots,x_i}(X_j|X_1, X_2, \ldots, X_i) = \lambda_r e^{-\lambda_r(X_j - X_i)} U(X_j - X_i), j \geq i. \qquad \text{(C.10)}$$

Applying this rule, we see that

$$p_{x_{m+1}|x_m}(X_{m+1}|X_m) = p_{x_{m+1}}(X_{m+1}). \qquad \text{(C.11)}$$

Because the Poisson process is symmetric, the above arguments also apply to the pdf of an arrival given a sequence of *later* arrivals. In particular, the pdf of the first arrival before x' is given by:

$$p_{x_m}(X_m) = \lambda_r e^{-\lambda_r(x' - X_m)} U(x' - X_m). \qquad \text{(C.12)}$$

For notational convenience, we define $\overline{x'} \equiv (x_m, x', x_{m+1})$ and $\overline{x''} \equiv (x_n, x'', x_{n+1})$. Note that x' and x'' are not random variables. They are the current observation

points on $h(x)$ and as such appear in the pdf's of $\overline{x'}$ and $\overline{x''}$ as parameters. The pdf of $\overline{x'}$ is:

$$\begin{aligned} p_{\overline{x'}}(\overline{X'}) &= p_{x_{m+1}|x_m}(X_{m+1}|X_m)p_{x_m}(X_m) \\ &= \lambda_r e^{-\lambda_r(X_{m+1}-X_m)}U(X_{m+1}-x')U(x'-X_m). \end{aligned} \tag{C.13}$$

The accompanying shifted versions of $U(x)$ serve to explicitly specify that $x_m \leq x' < x_{m+1}$. In the expression for $p_{\overline{x''}}(\overline{X''})$, similar functions would appear corresponding to $x_n \leq x'' < x_{n+1}$. In the sections to follow, joint and conditional pdf's involving both $\overline{x'}$ and $\overline{x''}$ will be presented. Whenever there are at least two arrivals between x' and x'', the following inequality applies: $-\infty < x_m \leq x' < x_{m+1} < x_n \leq x'' < x_{n+1}$. When there is one arrival between x' and x'', $-\infty < x_m \leq x' < x_{m+1} = x_n \leq x'' < x_{n+1}$. When there are no arrivals between x' and x'', $-\infty < x_m = x_n \leq x' \leq x'' < x_{m+1} = x_{n+1}$. Multiplication by a set of appropriately shifted $U(x)$ incorporates these inequalities explicitly, but in the following derivations they are left out to simplify notation.

C.2 The Sandwiched Arrival

Consider a point x_s which is the s^{th} of k points between x' and x''. The pdf of x_s is extremely useful in the derivation of the correlation function of the facet process.

$$p_{x_s|N(x'')-N(x')=k}(X_s|N(x'')-N(x')=k) = \frac{p_{x_s,N(x'')-N(x')=k}(X_s, N(x'')-N(x')=k)}{Pr[N(x'')-N(x')=k]} \tag{C.14}$$

$$\begin{aligned} &= \frac{\frac{d}{dX_s}(1-Pr[x_s > X_s, N(x'')-N(x')=k])}{Pr[N(x'')-N(x')]=k} \\ &= -\frac{d}{dX_s}\frac{\sum_{i=0}^{s-1} Pr[N(X_s)-N(x')=i, N(x'')-N(x')=k]}{Pr[N(x'')-N(x')=k]} \\ &= -\frac{d}{dX_s}\frac{\sum_{i=0}^{s-1} Pr[N(X_s)-N(x')=i]Pr[N(x'')-N(X_s)=k-i]}{Pr[N(x'')-N(x')=k]} \\ &= -\frac{d}{dX_s}\left[\sum_{i=0}^{s-1}\frac{[\lambda_r(X_s-x')]^i}{i!}\frac{[\lambda_r(x''-X_s)]^{k-i}}{(k-i)!}\frac{k!}{[\lambda_r(x''-x')]^k}\right]. \end{aligned} \tag{C.15}$$

After differentiation and a change of index on one of the two resulting sums, one gets:

$$
\begin{aligned}
&p_{x_s|N(x'')-N(x')=k}(X_s|N(x'')-N(x')=k) \qquad \text{(C.16)}\\
&= \sum_{i=0}^{s-1} \frac{k!(x''-X_s)^{k-i-1}(X_s-x')^i}{i!(k-i-1)!(x''-x')^k} - \sum_{i=1}^{s-1} \frac{k!(x''-X_s)^{k-i}(X_s-x')^{i-1}}{(i-1)!(k-i)!(x''-x')^k}\\
&= \frac{k!(x''-X_s)^{k-s}(X_s-x')^{s-1}}{(s-1)!(k-s)!(x''-x')^k},
\end{aligned}
$$

where the last line is obtained by a change of index on the second sum. The resulting pdf is referred to as the *sandwiched arrival* pdf. In the case of a single event between x' and x'', $s = k = 1$, the pdf of x_s is uniform on the interval $(x', x'']$.

C.3 Joint Conditional Densities for $\overline{x'}$, $\overline{x''}$, and $(\overline{x'}, \overline{x''})$ given $N(x'') - N(x')$

The joint conditional densities are derived for three seperate cases: (i) $N(x'') - N(x') = 0$, (ii) $N(x'') - N(x') = 1$, and (iii) $N(x'') - N(x') > 1$.

C.3.1 Case (i): $N(x'') - N(x') = 0$

When there are no arrivals between x' and x'', $x_m \equiv x_n$ and $x_{m+1} \equiv x_{n+1}$. The pdf for $\overline{x'}$ conditioned on there being no arrivals between x' and x'' is thus the product of the pdf's for x_m (lying before x') and x_{m+1} (lying after x'') by indepent increments.

$$
p_{\overline{x'}|N(x'')-N(x')=0}(\overline{X'}|N(x'')-N(x')=0) = \lambda_r^2 e^{-\lambda_r(X_{m+1}-x'')} e^{-\lambda_r(x'-X_m)}. \qquad \text{(C.17)}
$$

Knowledge of $\overline{x'}$ fixes x_n and x_{n+1}. Therefore,

$$
p_{\overline{x''}|\overline{x'},N(x'')-N(x')=0}(\overline{X''}|\overline{X'}, N(x'')-N(x')=0) = \delta(X_n - X_m)\delta(X_{n+1} - X_{m+1}). \qquad \text{(C.18)}
$$

The above two relations are combined using Eq. C.4.

$$p_{\overline{x'},\overline{x''}|N(x'')-N(x')=0}(\overline{X''},\overline{X'}|N(x'')-N(x')=0)= \tag{C.19}$$
$$\delta(X_n - X_m)\delta(X_{n+1} - X_{m+1})\lambda_r^2 e^{-\lambda_r(X_{n+1}-x'')}e^{-\lambda_r(x'-X_m)}.$$

C.3.2 Case (ii): $N(x'') - N(x') = 1$

In this case, $x_{m+1} \equiv x_n$. By independent increments, the pdf for $\overline{x'}$ conditioned on there being a single arrival between x' and x'' is the product of the pdf for $x_{m+1} \equiv x_n$ (lying between x' and x''), and for x_{n+1} (lying after x''). Using the sandwiched arrival formula,

$$p_{\overline{x'}|N(x'')-N(x')=1}(\overline{X'}|N(x'')-N(x')=1) = \lambda_r \frac{e^{-\lambda_r(x'-X_m)}}{(x''-x')}. \tag{C.20}$$

Only the x_n component of $\overline{x''}$ is fixed; x_{n+1} is an independent increments arrival occuring after x''. Therefore,

$$p_{\overline{x''}|\overline{x'},N(x'')-N(x')=1}(\overline{X''}|\overline{X'},N(x'')-N(x')=1) = \delta(X_n - X_{m+1})\lambda_r e^{-\lambda_r(X_{n+1}-x'')} \tag{C.21}$$

Combining these two relations using Eq. C.4,

$$p_{\overline{x'},\overline{x''}|N(x'')-N(x')=1}(\overline{X''},\overline{X'}|N(x'')-N(x')=1) = \frac{\delta(X_n - X_{m+1})}{(x''-x')}\lambda_r^2 e^{-\lambda_r(x_{n+1}-x'')}e^{-\lambda_r(x'-x_m)}. \tag{C.22}$$

C.3.3 Case (iii): $N(x'') - N(x') > 1$

In this case, all the vertices are distinct from one another. By independent increments, the pdf for $\overline{x'}$ will be the product of the pdf for x_m which lies below x' and that for x_{m+1}, a sandwiched point being the first of k arrivals between x' and x''. Using the

sandwiched arrival formula,

$$p_{\overline{x'}|N(x'')-N(x')=k}(\overline{X'}|N(x'')-N(x')=k)=k\lambda_r e^{-\lambda_r(x'-x_m)}\frac{(x''-X_{m+1})^{k-1}}{(x''-x')^k}. \quad \text{(C.23)}$$

This equation applies for $k>0$; it reduces to Eq. C.20 when $k=1$. The pdf for $\overline{x''}$ given $\overline{x'}$ is the product of the pdf for x_{n+1} which lies beyond x'' and that for x_n, a sandwiched arrival being the last of $k-1$ arrivals between x_{m+1} and x''. Relying once more on the sandwiched arrival formula,

$$p_{\overline{x''}|\overline{x'},N(x'')-N(x')=k}(\overline{X''}|\overline{X'},N(x'')-N(x')=k)=(k-1)\lambda_r e^{-\lambda_r(X_{n+1}-x'')}\frac{(X_n-X_{m+1})^{j-2}}{(x''-X_{m+1})^{j-1}} \quad \text{(C.24)}$$

Combining these two relations using Eq. C.4,

$$p_{\overline{x'},\overline{x''}|N(x'')-N(x')=k}(\overline{X''},\overline{X'}|N(x'')-N(x')=k)= \quad \text{(C.25)}$$
$$k(k-1)\lambda_r^2 e^{-\lambda_r(X_{n+1}-x'')}e^{-\lambda_r(x'-X_m)}\frac{(X_n-X_{m+1})^{j-1}}{(x''-x')^k}.$$

Armed with the pdf's in this section, it is now possible to proceed with the evaluation of the expectations in Eq. C.6.

C.4 The correlation function of $h(x)$

The major analytical challenge in obtaining $R_{hh}(x',x'')$ resides in the evaluation of the terms within the three expectation operators in Eq. C.6. It will be helpful to make use of the fact that for an arbitrary vector $\overline{y}$,

$$\mathcal{E}[f(\overline{y})]=\int d\overline{Y}\,f(\overline{Y})p_{\overline{y}}(\overline{Y}). \quad \text{(C.26)}$$

To simplify notation, we define

$$F(\overline{x'})=\frac{x'-x_m}{x_{m+1}-x_m} \quad \text{(C.27)}$$

and

$$G(\overline{x''}) = \frac{x'' - x_n}{x_{n+1} - x_n}. \tag{C.28}$$

Term 1 is:

$$\mathcal{E}\left[F(\overline{x'})|N(x'') - N(x') = k\right], \tag{C.29}$$

Term 2 is:

$$\mathcal{E}\left[G(\overline{x''})|N(x'') - N(x') = k\right], \tag{C.30}$$

and Term 3 is:

$$\mathcal{E}\left[F(\overline{x'})G(\overline{x''})|N(x'') - N(x') = k\right]. \tag{C.31}$$

In the following subsections, each term will be analyzed separately.

C.4.1 Term 1

The analysis for Term 1 has two components, one for $k = 0$ and one for $k > 0$. Starting with $k > 0$ and using Eqs. C.23 and C.26,

$$\begin{aligned}
\mathcal{E}\left[F(\overline{x'}|N(x'') - N(x') = k\right] &= \int d\overline{X'} F(\overline{X'}) p_{\overline{x'}|N(x'')-N(x')=k}(\overline{X'}|N(x'') - N(x') = k) \\
&= \int_{-\infty}^{x'} dX_m \int_{x'}^{x''} dX_{m+1} k\lambda_r \frac{(x'' - X_{m+1})^{k-1}}{(x'' - x')^k} \frac{(x' - X_m)}{(X_{m+1} - X_m)} e^{-\lambda_r(x' - X_m)} \\
&= \frac{k!e^a}{a^k} \left\{ \left[\frac{a^{k-1}e^{-a}}{(k-1)!} \right] * E_2(a) \right\},
\end{aligned} \tag{C.32}$$

where $a \equiv \lambda_r(x'' - x')$, $*$ denotes convolution,

$$f(t) * g(t) \equiv \int_{-\infty}^{\infty} f(\tau) g(t - \tau) d\tau, \tag{C.33}$$

and $E_n(x)$ is the n-th order exponential integral for $x \geq 0$:

$$E_n(x) = \begin{cases} \int_1^\infty e^{-xu} u^{-n} du, & x \geq 0 \\ 0, & x < 0. \end{cases} \tag{C.34}$$

The convolution is left in uncalculated form because it involves definite integrals for which an analytical solution is not available in today's integral tables. The case $k = 0$ yields:

$$\begin{aligned} \mathcal{E}\left[F(\overline{x'})|N(x'') - N(x') = 0\right] &= \int d\overline{X} F(\overline{X'}) p_{\overline{x}|N(x'')-N(x')=k}(\overline{X}|N(x'') - N(x') = 0) \\ &= \int_{-\infty}^{x'} dX_m \int_{x''}^{\infty} dX_{m+1} \lambda_r^2 e^{-\lambda_r(X_{m+1}-x'')} e^{-\lambda_r(x'-X_m)} \frac{x' - X_m}{x_{m+1} - x_m} \\ &= e^a E_3(a). \end{aligned} \tag{C.35}$$

C.4.2 Term 2

The procedure for Term 2 is analogous to that for Term 1 and gives:

$$\mathcal{E}[G(\overline{x''})|N(x'') - N(x') = k] = \begin{cases} \frac{k!e^a}{a^k} \left\{ \left[\frac{a^{k-1}e^{-a}}{(k-1)!} \right] * [aE_1(a)] \right\}, & k > 0 \\ e^a \left\{ e^{-a} - E_3(a) \right\}, & k = 0. \end{cases} \tag{C.36}$$

C.4.3 Term 3

The analysis for Term 3 has three components, one for $k = 0$, one for $k = 1$, and one for $k > 1$. Starting with $k > 1$,

$$\begin{aligned} &\mathcal{E}[F(\overline{x'})G(\overline{x''})|N(x'') - N(x') = k] = \\ &\int d\overline{X'} F(\overline{X'}) \int d\overline{X''} G(\overline{X''}) p_{\overline{x'},\overline{x''}|N(x'')-N(x')=k}(\overline{X'}, \overline{X''}|N(x'') - N(x') = k) \\ &= \int_{-\infty}^{x'} dX_m \int_{x'}^{x''} dX_{m+1} \int_{X_{m+1}}^{x''} dX_n \int_{x''}^{\infty} dX_{n+1} \times \\ &k(k-1) \frac{\lambda_r^2 e^a}{(x'' - x')^k} e^{-\lambda_r(X_{n+1}-X_m)} (X_n - X_{m+1})^{k-2} F(\overline{X'}) G(\overline{X''}) \\ &= \frac{k!e^a}{a^k} \left\{ \left[\frac{a^{k-2}e^{-a}}{(k-2)!} \right] * [aE_1(a)] * E_2(a) \right\}. \end{aligned} \tag{C.37}$$

For $k = 1$,

$$\begin{aligned}
&\mathcal{E}[F(\overline{x'})G(\overline{x''})|N(x'') - N(x') = 1] \\
&\quad = \int d\overline{X'}F(\overline{X'}) \int d\overline{X''}G(\overline{X''})p_{\overline{x'},\overline{x''}|N(x'')-N(x')=1}(\overline{X'}, \overline{X''}|N(x'') - N(x') = 1) \\
&\quad = \int_{-\infty}^{x'} dX_m \int_{x'}^{x''} dX_{m+1} \int_{x''}^{\infty} dX_{n+1} \frac{\lambda_r^2 e^{-\lambda_r(X_{n+1}-x'')}}{x'' - x'} e^{-\lambda_r(x'-X_m)} F(\overline{X'}) \frac{x'' - X_{m+1}}{X_{n+1} - X_{m+1}} \\
&\quad = \frac{e^a}{a} \{[aE_1(a)] * E_2(a)\} \qquad \text{(C.38)}
\end{aligned}$$

Finally, for $k = 0$,

$$\begin{aligned}
&\mathcal{E}[F(\overline{x'})G(\overline{x''})|N(x'') - N(x') = 0] \\
&\quad = \int d\overline{X'}F(\overline{X'}) \int d\overline{X''}G(\overline{X''})p_{\overline{x'},\overline{x''}|N(x'')-N(x')=0}(\overline{X'}, \overline{X''}|N(x'') - N(x') = 0) \\
&\quad = \int_{-\infty}^{x'} dX_m \int_{x''}^{\infty} dX_{m+1} \lambda_r^2 e^{-\lambda_r(X_{m+1}-x'')} e^{-\lambda_r(x'-X_m)} \frac{(x' - X_m)(x'' - X_m)}{(X_{m+1} - X_m)^2} \\
&\quad = e^a E_4(a). \qquad \text{(C.39)}
\end{aligned}$$

C.4.4 Final Substitution to Form $R_{hh}(x', x'')$

Substituting Eqs. C.32, C.35, C.36, C.37, C.38, and C.39 into Eq. C.6 yields a function which depends on a alone:

$$\begin{aligned}
R^*_{hh}(a) &= (2E_4(a) - e^{-a})(R_{zz}[0] - R_{zz}[1]) + (\{aE_1(a)\} * \{E_2(a)\})(2R_{zz}[1] - R_{zz}[2] - R_{zz}[0]) \\
&\quad + \sum_{k=0}^{\infty} \frac{a^k e^{-a}}{k!} R_{zz}[k] + \sum_{k=1}^{\infty} \left\{ \frac{a^{k-1} e^{-a}}{(k-1)!} \right\} * \{E_2(a)\} (R_{zz}[k-1] - R_{zz}[k]) \\
&\quad + \sum_{k=1}^{\infty} \left\{ \frac{a^{k-1} e^{-a}}{(k-1)!} \right\} * \{aE_1(a)\} (R_{zz}[k+1] - R_{zz}[k]) \qquad \text{(C.40)} \\
&\quad + \sum_{k=2}^{\infty} \left\{ \frac{a^{k-2} e^{-a}}{(k-2)!} \right\} * \{aE_1(a)\} * \{E_2(a)\} (2R_{zz}[k] - R_{zz}[k+1] - R_{zz}[k-1]).
\end{aligned}$$

In the above, the fact that $R_{zz}[1] = R_{zz}[-1]$ was used. The correlation function of $h(x)$ is related to $R^*_{hh}(a)$ through:

$$R_{hh}(x', x'') = R_{hh}(x'' - x') = R^*_{hh}(\lambda_r(x'' - x')), \tag{C.41}$$

where $\chi = x'' - x'$. The fact that $R_{hh}(x', x'')$ depends only on the separation between the two observation points χ proves that the process $h(x)$ is wide-sense stationary. Also, note that it is now possible to generalize to the case $x' > x''$ simply by repeating the analysis in this section after interchanging the definitions of x' and x''. This leads to the final result

$$R_{hh}(x', x'') = R_{hh}(\chi) = R^*_{hh}(\lambda_r \chi), \tag{C.42}$$

where $\chi = |x'' - x'|$.

C.5 The Power Spectral Density of $h(x)$

To evaluate the power spectral corresponding to $R_{hh}(\chi)$, the Laplace transform of $R^*_{hh}(a)$ is found first. The Laplace transform of $p(a)$ is defined as:

$$P(s) = \mathcal{L}[p(a)] = \int_0^\infty p(a) e^{-as} da. \tag{C.43}$$

Two useful properties of the Laplace transform are

$$\mathcal{L}[ap(a)] = -\frac{d}{dx} P(s), \tag{C.44}$$

and

$$\mathcal{L}[p(a) * q(a)] = P(s)Q(s). \tag{C.45}$$

The recursive property of the exponential integral functions is also useful:

$$E_n(a) = \frac{1}{n-1}\left(e^{-a} - aE_{n-1}(a)\right), E_0(a) = \frac{e^{-a}}{a}. \tag{C.46}$$

Also, note that

$$E_1(a) = \int_{-a}^{\infty} \frac{e^{-t}}{t} dt. \tag{C.47}$$

From Ref. [10], two useful Laplace transforms are:

$$\mathcal{L}[E_1(a)] = \frac{\ln(1+s)}{s}, \tag{C.48}$$

and

$$\mathcal{L}\left[\frac{a^k e^{-a}}{k!}\right] = \frac{1}{(1+s)^{k+1}}. \tag{C.49}$$

Using the above relations, it is possible to build the remaining unknown Laplace transforms appearing in Eq. C.40. The Laplace transform of $aE_1(a)$ is readily obtained from Eq. C.48 using Eq. C.44:

$$\mathcal{L}[aE_1(a)] = \frac{\ln(1+s)}{s^2} - \frac{1}{s(1+s)}. \tag{C.50}$$

It is then easy to calculate

$$\mathcal{L}[E_2(a)] = \mathcal{L}[e^{-a} - aE_1(a)] = \frac{1}{s} - \frac{\ln(1+s)}{s^2}. \tag{C.51}$$

A similar usage of the recursive relation for the exponential integrals yields the Laplace transforms of $E_3(a)$ and $E_4(a)$,

$$\mathcal{L}[E_3(a)] = \frac{(s-2)}{2s^2} + \frac{\ln(1+s)}{s^3} \tag{C.52}$$

and

$$\mathcal{L}[E_4(a)] = \frac{(2s^2 - 3s + 6)}{6s^3} - \frac{\ln(1+s)}{s^4}. \tag{C.53}$$

It is now an easy matter to substitute the above relations at their appropriate destinations in Eq. C.40. The final result is:

$$\begin{aligned} L_{hh}(s) \;=\; & \sum_{k=0}^{\infty} \frac{R_{zz}[k]}{(1+s)^{k+1}} + \left(\frac{2s^2 - 3s + 6}{3s^3} - \frac{2\ln(1+s)}{s^4} - \frac{1}{1+s}\right)[R_{zz}[0] - R_{zz}[1]] + \\ & \sum_{k=1}^{\infty} \frac{1}{(1+s)^k}\left(\frac{1}{s} - \frac{\ln(1+s)}{s^2}\right)[R_{zz}[k-1] - R_{zz}[k]] + \\ & \sum_{k=1}^{\infty} \frac{1}{(1+s)^k}\left(\frac{\ln(1+s)}{s^2} - \frac{1}{s(1+s)}\right)[R_{zz}[k+1] - R_{zz}[k]] + \\ & \left(\frac{\ln(1+s)}{s^2} - \frac{1}{s(1+s)}\right)\left(\frac{1}{s} - \frac{\ln(1+s)}{s^2}\right)[2R_{zz}[1] - R_{zz}[2] - R_{zz}[0]] + \\ & \sum_{k=2}^{\infty} \frac{1}{(1+s)^{k-1}}\left(\frac{\ln(1+s)}{s^2} - \frac{1}{s(1+s)}\right)\left(\frac{1}{s} - \frac{\ln(1+s)}{s^2}\right) \times \\ & [2R_{zz}[k] - R_{zz}[k+1] - R_{zz}[k-1]]. \end{aligned} \tag{C.54}$$

The power spectral density of $R_{hh}(\chi)$ is

$$S_{hh}(\omega) = \int_{-\infty}^{\infty} R_{hh}(\chi) e^{-\chi\omega} d\chi. \tag{C.55}$$

It is related to the Laplace transform of $R^*_{hh}(a)$ as follows:

$$S_{hh}(\omega) = \frac{2}{\lambda_r} \mathrm{Re}\left[L_{hh}(\frac{s}{\lambda_r})\right]_{s=j\omega}. \tag{C.56}$$

C.6 Variance and Correlation Length

C.6.1 Variance

The variance is $\sigma_{hh}^2 = \mathcal{E}[h(x)^2]$, and is given by the value of the correlation function at $\chi = 0$ from Eq. C.40. Note that the convolution terms are 0 for $a = 0$.

$$\sigma_{hh}^2 = R_{hh}(0) = \frac{1}{3}(2R_{zz}[0] + R_{zz}[1]). \tag{C.57}$$

C.6.2 Correlation Length

The definition of correlation length used in this thesis is:

$$l_c = \sqrt{\frac{2\mu_2}{\mu_0}} \tag{C.58}$$

where

$$\mu_0 = 2\int_0^\infty R_{hh}(\chi)d\chi = \frac{2}{\lambda_r}\int_0^\infty R_{hh}^*(a)da, \tag{C.59}$$

and

$$\mu_2 = 2\int_0^\infty \chi^2 R_{hh}(\chi)d\chi = \frac{2}{\lambda_r^3}\int_0^\infty a^2 R_{hh}^*(a)da. \tag{C.60}$$

Note that for a Gaussian spectrum with variance σ_g^2 and scale parameter l_g,

$$S_{hh}^G(\omega) = \sqrt{\pi}\sigma_g^2 l_g e^{-\frac{\omega^2 l_g^2}{4}}, \tag{C.61}$$

the chosen definition of correlation length yields $l_c = l_g$. In order to find the correlation length for $h(x)$, two more Laplace transform relations are introduced. First, note that

$$\int_0^\infty p(a)da = P(0). \tag{C.62}$$

Second,

$$\int_0^\infty a^2 p(a) da = \frac{d^2}{ds^2} P(s)|_{s=0}. \tag{C.63}$$

Thus, the derivation of l_c depends directly on evaluating the limit as $s \to 0$ of Eq. C.54 and its second derivative, a task undertaken in the following two sections.

C.6.3 $\lim\ s \to 0\ L_{hh}(s)$

The limit of many of the terms in Eq. C.54 are easily evaluated. The others lead to the form $\frac{0}{0}$ and are obtained by applying l'Hopital's rule:

$$\lim_{s\to 0} \mathcal{L}[aE_1(a)] = \frac{1}{2}, \tag{C.64}$$

$$\lim_{s\to 0} \mathcal{L}[E_2(a)] = \frac{1}{2}, \tag{C.65}$$

and

$$\lim_{s\to 0} \mathcal{L}[E_4(a)] = \frac{1}{4}. \tag{C.66}$$

The final result is:

$$\mu_0 = \frac{2}{\lambda_r} \lim_{s\to 0} L_{hh}(s) = \frac{1}{\lambda_r} \left[\frac{1}{2}(R_{zz}[1] - R_{zz}[0]) + 2 \sum_{k=0}^{\infty} R_{zz}[k] \right]. \tag{C.67}$$

C.6.4 $\lim\ s \to 0\ \frac{d^2}{ds^2} L_{hh}(s)$

It is noted from Eq. C.54 that the terms making up $L_{hh}(s)$ are composed of products of any two of following four basic functions:

$$a(s) = \frac{1}{(1+s)^j};\ b(s) = \mathcal{L}[E_2(a)];\ c(s) = \mathcal{L}[aE_1(a)];\ d(s) = \mathcal{L}[E_4(a)]. \tag{C.68}$$

Term	$\lim_{s\to 0} f(s)$	$\lim_{s\to 0} f'(s)$	$\lim_{s\to 0} f''(s)$
$a(s)$	1	$-j$	$j(j+1)$
$b(s)$	1/2	$-1/3$	1/2
$c(s)$	1/2	$-2/3$	3/2
$d(s)$	1/4	$-1/5$	1/3

Table C.1: Limit values for terms in the second derivative of $L_{hh}(s)$.

The second derivative operation introduces three product terms for each product term in $L_{hh}(s)$. For example,

$$(ab)'' = (a'b + b'a)' = a''b + 2a'b' + b''a. \tag{C.69}$$

The limit as $s \to 0$ of the second derivative of the Laplace transform can thus be obtained by finding $\lim_{s\to 0}$ for each of a, a', a'', b, b', etc. Table C.1 shows the limit values for each of these quantities, obtained through repetitive uses of l'Hopital's rule. Using these results, it is lengthy although straightforward to show that

$$\mu_2 = \frac{2}{\lambda_r^3} \lim_{s\to 0} \frac{d^2}{ds^2} L_{hh}(s) = \frac{1}{\lambda_r^3} \left(-\frac{11}{9} R_{zz}[0] + \frac{2}{9} R_{zz}[1] - \frac{1}{3} R_{zz}[2] + 2 \sum_{k=0}^{\infty} (k+1)(k+2) R_{zz}[k] \right) \tag{C.70}$$

C.6.5 Final Substitution for l_c

Combining Eqs. C.58, C.67 and C.70, the correlation length for the Facet process is

$$l_c = \frac{\sqrt{2}}{\lambda_r} \left(\frac{-\frac{11}{9} R_{zz}[0] + \frac{2}{9} R_{zz}[1] - \frac{1}{3} R_{zz}[2] + 2 \sum_{k=0}^{\infty} (k+1)(k+2) R_{zz}[k]}{\frac{1}{2}(R_{zz}[1] - R_{zz}[0]) + 2 \sum_{k=0}^{\infty} R_{zz}[k]} \right)^{\frac{1}{2}}. \tag{C.71}$$

C.7 Ideas for The 2-D Facet Process

The one-dimensional profiles studied here are fruitful for the numerical study of scale structure in the next Chapter, as the computational requirements of obtaining wide-band time-domain simulations are then possible on today's machines. Although the

insights provided lead to a new way of looking at the ARSRP data, the decision to focus on the one-dimensional case comes at the cost of being able to fully explain these data. This thesis is an essential link in the chain of ideas that may one day provide a full understanding. As an introduction to that future moment, I now introduce a generalization of the Facet model to the two-dimensional case. The combination of Poisson and Gaussian processes has up to now been successful in satisfying two objectives: (i) Power-law decay of the power spectral density and (ii) feature-like appearance of realizations. It is then natural to continue with these two processes as building blocks in the two-dimensional case. The first step, as always, is the generation of vertices. The horizontal co-ordinates are given by pairs $\{(r_i, \theta_i)\}$ where the $\{r_i\}$ are the abcissae of the process

$$Pr[N(r) = k] = \frac{[r\lambda_r r]^k}{k!} e^{-r\lambda_r r}, \tag{C.72}$$

and the $\{\theta_i\}$ are realizations from a uniform distribution on $[-\pi, \pi)$, or some from some non-uniform distribution that captures anisotropy. The vertex heights $\{z_i\}$ are zero-mean and Gaussian as before. The linking of the vertices, which was a simple matter in the two-dimensional case is now more complicated as there are many ways to link arbitrary points in the 2-D plane. One method which yields a unique result for a given set of points is the Thiessen triangulation [57] [56] [1] [2]. In the Thiessen triangulation, the smallest circle enclosing each triangle must not include more than the three datapoints defining the vertices of the triangle or, if this cannot be satisfied, the minimum angle of adjacent triangles must be maximal. The derivation of the correlation function and power spectral density appear quite challenging, but numerical estimates from Monte-Carlo realizations could readily be obtained.

Appendix D

The Helmholtz-Kirchhoff Integral for Scattering From Finite Surfaces

The exact solution used in this thesis for scattering from finite-length rough surfaces is based on the direct numerical solution of the Helholtz-Kirchhoff integral equation. In practice, the domain of integration used is the finite-length surface itself. This is necessarily an approximation since the Helmholtz-Kirchhoff equation involves an integral over a *closed* surface S bounding a volume V of interest. This Appendix shows two different approximations that result in a domain of integration over the scattering surface only. First, the derivation of the general Helmholtz-Kirchhoff equation is presented.

D.1 Derivation of the Helmholtz-Kirchhoff Equation

Let the acoustic field be $p(\mathbf{r})$ and let V be a simply-connected closed compact set of finite diameter in $\mathcal{R}^3$. The surface S enclosing V constitutes the boundary between V and its complement with respect to $\mathcal{R}^3$, V^*. Let the field be non-trivial yet have no sources within V. It is then necessarily generated by sources located in the complement V^*. The derivation of the Helmholtz-Kirchhoff equation is divided into two

steps; the first is for field points within V and the second is for field points outside V, or inside V^* where sources reside.

D.1.1 The Field Inside V

Consider the free space Green's function $G(\mathbf{r}, \mathbf{r}')$ satisfying

$$\nabla^2 G(\mathbf{r}, \mathbf{r}') + k^2 G(\mathbf{r}, \mathbf{r}') = \delta(\mathbf{r} - \mathbf{r}'). \tag{D.1}$$

Since $p(\mathbf{r}')$ is source-free for $\mathbf{r}' \epsilon V$, it satisfies the homogeneous Helmholtz equation

$$\nabla^2 p(\mathbf{r}') + k^2 p(\mathbf{r}') = 0, \, \mathbf{r}' \epsilon V. \tag{D.2}$$

Multiplying Eq. D.1 by $p(\mathbf{r}')$ and subtracting Eq. D.2 multiplied by $G(\mathbf{r}, \mathbf{r}')$ yields

$$p(\mathbf{r}')\nabla^2 G(\mathbf{r}, \mathbf{r}') - G(\mathbf{r}, \mathbf{r}')\nabla^2 p(\mathbf{r}') = p(\mathbf{r}')\delta(\mathbf{r} - \mathbf{r}'). \tag{D.3}$$

Integrating over the volume V leads to

$$\int_V d\mathbf{V}' \left(p(\mathbf{r}')\nabla^2 G(\mathbf{r}, \mathbf{r}') - G(\mathbf{r}, \mathbf{r}')\nabla^2 p(\mathbf{r}') \right) = \begin{cases} p(\mathbf{r}), & \mathbf{r} \epsilon V \\ 0, & \mathbf{r} \epsilon V^*. \end{cases} \tag{D.4}$$

The zero result for $\mathbf{r} \epsilon V^*$ is due to the fact that integration is over V and that since $\mathbf{r}'$ ϵV, the delta function is not picked up by the integral. Using Green's second formula, the volume integral is transformed into an integral over the surface S enclosing V:

$$p(\mathbf{r}) = \int_S d\mathbf{S}' \cdot \left(p(\mathbf{r}')\nabla G(\mathbf{r}, \mathbf{r}') - G(\mathbf{r}, \mathbf{r}')\nabla p(\mathbf{r}') \right), \; \mathbf{r} \epsilon V. \tag{D.5}$$

Carrying out the dot product gives

$$p(\mathbf{r}) = \int_S \left\{ p(\mathbf{r}') \frac{\partial G(\mathbf{r}, \mathbf{r}')}{\partial \mathbf{n}'} - G(\mathbf{r}, \mathbf{r}') \frac{\partial p(\mathbf{r}')}{\partial \mathbf{n}'} \right\} dS', \; \mathbf{r} \epsilon V, \tag{D.6}$$

where $\mathbf{n}'$ is the outward surface normal on S. Eq. D.6 is represented symbolically as

$$p(\mathbf{r}) = \Upsilon_S(\mathbf{r}, \mathbf{r}')p(\mathbf{r}') \tag{D.7}$$

D.1.2 The Field Outside V

Since the field is non-trivial yet has no sources within V, it necessarily results from sources located in V^*. Thus,

$$\nabla^2 p(\mathbf{r}') + k^2 p(\mathbf{r}') = S(\mathbf{r}'),\ \mathbf{r}' \in V^* \tag{D.8}$$

where $S(\mathbf{r}')$ is some source distribution. Multiplying Eq. D.1 by $p(\mathbf{r}')$ and subtracting Eq. D.8 multiplied by $G(\mathbf{r}, \mathbf{r}')$ yields

$$p(\mathbf{r}')\nabla^2 G(\mathbf{r}, \mathbf{r}') - G(\mathbf{r}, \mathbf{r}')\nabla^2 p(\mathbf{r}') = p(\mathbf{r}')\delta(\mathbf{r} - \mathbf{r}') - S(\mathbf{r}')G(\mathbf{r}, \mathbf{r}'). \tag{D.9}$$

Integrating over the volume V^* leads to

$$\int_{V^*} d\mathbf{V}' \left(p(\mathbf{r}')\nabla^2 G(\mathbf{r}, \mathbf{r}') - G(\mathbf{r}, \mathbf{r}')\nabla^2 p(\mathbf{r}')\right) = p(\mathbf{r}) - \int_{V^*} d\mathbf{V}' S(\mathbf{r}')G(\mathbf{r}, \mathbf{r}') \tag{D.10}$$

for $\mathbf{r} \in V^*$. Using Green's second formula, the first volume integral can be transformed into an integral over a surface enclosing V^*. Note that if V is some set of finite diameter, V^* has infinite diameter and thus the surface which encloses it is the union of S and S_∞ where S_∞ is a sphere of infinite radius. Thus,

$$\int_{S+S_\infty} d\mathbf{S}' \cdot (p(\mathbf{r}')\nabla G(\mathbf{r}, \mathbf{r}') - G(\mathbf{r}, \mathbf{r}')\nabla p(\mathbf{r}')) + \int_{V^*} d\mathbf{V}' S(\mathbf{r}')G(\mathbf{r}, \mathbf{r}') = p(\mathbf{r}). \tag{D.11}$$

The integral over S is transformed into an integral over V by applying Green's second formula in reverse:

$$\begin{aligned}
&\int_S d\mathbf{S}' \cdot (p(\mathbf{r}')\nabla G(\mathbf{r},\mathbf{r}') - G(\mathbf{r},\mathbf{r}'\nabla p(\mathbf{r}'))) \\
&\quad = \int_V d\mathbf{V}' \left(p(\mathbf{r}')\nabla^2 G(\mathbf{r},\mathbf{r}') - G(\mathbf{r},\mathbf{r}')\nabla^2 p(\mathbf{r}')\right), \ \mathbf{r}'\epsilon V, \ \mathbf{r}\epsilon V^*. \\
&\quad = 0 \text{ from Eq. D.4.}
\end{aligned} \tag{D.12}$$

Then, Eq. D.11 becomes

$$p(\mathbf{r}) = \int_{V^*} d\mathbf{V}' S(\mathbf{r}') G(\mathbf{r},\mathbf{r}') + \int_{S_\infty} d\mathbf{S}' \cdot (p(\mathbf{r}')\nabla G(\mathbf{r},\mathbf{r}') - G(\mathbf{r},\mathbf{r}')\nabla p(\mathbf{r}')), \ \mathbf{r} \epsilon V^*. \tag{D.13}$$

For fields which satisfy the Sommerfeld radiation condition,

$$\lim_{r\to\infty} r \left[\frac{\partial p(\mathbf{r})}{\partial r} - ikp(\mathbf{r})\right] = 0, \tag{D.14}$$

the integral over S_∞ vanishes. It is useful to note that plane waves, which do not satisfy the Sommerfeld radiation condition, satisfy

$$\Upsilon_{S_\infty}(\mathbf{r},\mathbf{r}')p_{inc}(\mathbf{r}') = p_{inc}(\mathbf{r}), \tag{D.15}$$

and

$$\Upsilon_{S_a}(\mathbf{r},\mathbf{r}')p_{inc}(\mathbf{r}') = \begin{cases} p_{inc}(\mathbf{r}), & \mathbf{r} \epsilon V_a \\ 0, & \mathbf{r} \epsilon V_a^*. \end{cases} \tag{D.16}$$

for S_a a sphere of finite radius a enclosing V_a. The general rule to be retained from these derivations is that when the sources are outside the volume of interest V, the field inside V is represented by a non-vanishing integral over the enclosing surface S and a vanishing integral over V. Conversely, the field inside V^* is represented by a vanishing integral over S and a non-vanishing integral over V^*. If there were nonvanishing sources inside and outside V, both integrals would be non-vanishing in

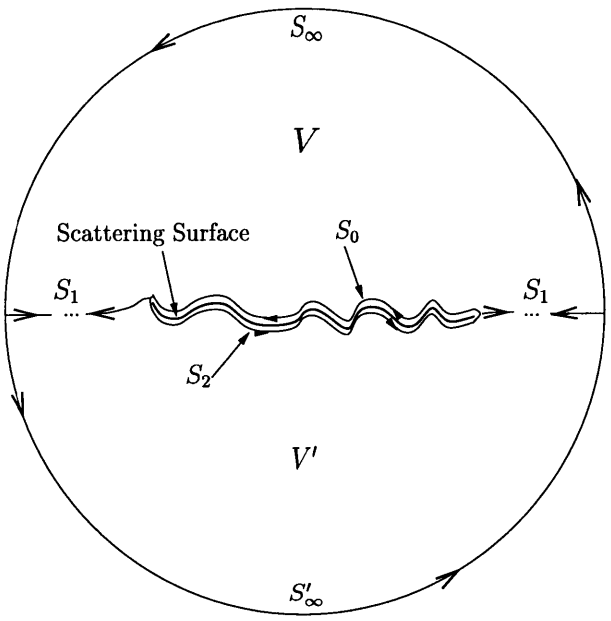

Figure D-1: Integration paths for the Helmholtz-Kirchhoff integral equation as used to compute the scatter from a finite-length rough surface.

V and in V^*.

D.2 Two-dimensional Surface Scattering

Figure D-1 depicts a scattering surface, a set of bounding surfaces and two volumes V and V'. S_0 is congruent with the scattering surface, S_1 extends to $x = \pm\infty$ from the edges of the scattering surface, S_∞ is a semi-circular contour in the upper-half plane with radius $r \to \infty$ and S_∞ is a semi-circular contour in the lower-half plane with radius $r \to \infty$. Finally, S_2 is a segment that starts from the edges of S_0 and runs behind the scattering surface, an infinitesimally small distance away from it. The direction of integration along each contour is as indicated in Fig. D-1. The inside of the surface is defined to be the region to the left as one is traversing the contour. We now consider the total field $p(\mathbf{r})$ to be the sum of an incident and a scattered field,

$$p(\mathbf{r}) = p_{inc}(\mathbf{r}) + p_{scat}(\mathbf{r}). \tag{D.17}$$

The scattered field results from interactions of the incident field with the scattering surface, located outside V and V'. The incident field emanates from loci outside V and V'. The region of interest for the total field is V. The objective is to change the integration path in Eq. D.6 to include only S_0. This is achieved by making approximations to an initially correct expression of Eq. D.6. The initial contours must be closed to satisfy exactness and must include S_0. There are two such paths:

Case (i) $S = S_0 + S_1 + S_\infty$

Case (ii) $S = S_0 + S_2 + S_\infty + S'_\infty$

Each of these cases is explored separately in the following sections. In Case (i), the integrand of the final result involves $p_{scat}(\mathbf{r})$, and in Case (ii) it involves $p(\mathbf{r})$.

D.2.1 Case (i)

When $S = S_0 + S_1 + S_\infty$, we have

$$\begin{aligned} p(\mathbf{r}) &= \Upsilon_{S_0+S_1+S_\infty}(\mathbf{r},\mathbf{r}')p(\mathbf{r}') = \Upsilon_{S_0+S_1+S_\infty}(\mathbf{r},\mathbf{r}')p_{inc}(\mathbf{r}') + \Upsilon_{S_0+S_1+S_\infty}(\mathbf{r},\mathbf{r}')p_{scat}(\mathbf{r}') \\ &= p_{inc}(\mathbf{r}) + \Upsilon_{S_0+S_1+S_\infty}(\mathbf{r},\mathbf{r}')p_{scat}(\mathbf{r}') \end{aligned} \tag{D.18}$$

where the last step results from the fact that the sources for $p_{inc}(\mathbf{r})$ lie outside the contour S. Since $p_{scat}(\mathbf{r})$ is composed of outgoing waves from the scattering surface, the Sommerfeld radiation condition applies and results in a vanishing contribution of the scattered field over the semi-circular contour at infinity:

$$\Upsilon_{S_\infty}(\mathbf{r},\mathbf{r}')p_{scat}(\mathbf{r}') = 0. \tag{D.19}$$

Eq. D.18 then becomes

$$p(\mathbf{r}) = p_{inc}(\mathbf{r}) + \Upsilon_{S_0+S_1}(\mathbf{r},\mathbf{r}')p_{scat}(\mathbf{r}'). \tag{D.20}$$

In order to simplify Eq. D.20 further, approximations are necessary. First, the Kirchhoff approximation is made along the contour S_1: $p_{scat}(\mathbf{r}') = R(\mathbf{r}')p_{inc}(\mathbf{r}')$, where

$R(\mathbf{r}')$ is a local reflection coefficient. When a *plane wave* incident field is assumed, this implies $\partial p_{scat}(\mathbf{r}')/\partial n' = -R(\mathbf{r}')\partial p_{inc}(\mathbf{r}')/\partial n'$. By fixing $R(\mathbf{r}')$ to be identically zero on S_1, these approximations yield

$$\Upsilon_{S_1}(\mathbf{r}, \mathbf{r}')p_{scat}(\mathbf{r}') = 0. \tag{D.21}$$

Substituting this result in Eq. D.20 leads to

$$p(\mathbf{r}) = p_{inc}(\mathbf{r}) + \Upsilon_{S_0}(\mathbf{r}, \mathbf{r}')p_{scat}(\mathbf{r}'), \tag{D.22}$$

which involves integration over S_0 only as desired.

D.2.2 Case (ii)

When $S = S_0 + S_2 + S_\infty + S'_\infty$, we have

$$p(\mathbf{r}) = \Upsilon_{S_0+S_2+S_\infty+S'_\infty}(\mathbf{r}, \mathbf{r}')p(\mathbf{r}'). \tag{D.23}$$

Because $S_0 + S_2$ forms a closed contour and there are no sources of p_{inc} within this contour, Eq. D.16 states that

$$\Upsilon_{S_0+S_2}(\mathbf{r}, \mathbf{r}')p_{inc}(\mathbf{r}') = 0. \tag{D.24}$$

Use of Eq. D.15 gives

$$p_{inc}(\mathbf{r}) = \Upsilon_{S_\infty+S'_\infty}(\mathbf{r}, \mathbf{r}')p_{inc}(\mathbf{r}'). \tag{D.25}$$

The Sommerfeld radiation condition for the scattered field gives

$$\Upsilon_{S_\infty+S'_\infty}(\mathbf{r}, \mathbf{r}')p_{scat}(\mathbf{r}') = 0. \tag{D.26}$$

Thus,

$$p(\mathbf{r}) = p_{inc}(\mathbf{r}) + \Upsilon_{S_0+S_2}(\mathbf{r}, \mathbf{r}')p(\mathbf{r}') \tag{D.27}$$

In order to obtain an integral over S_0 alone, the assumption is made that

$$p(\mathbf{r}) = \frac{\partial p(\mathbf{r})}{\partial n} \equiv 0 \tag{D.28}$$

behind the surface. This infinite-frequency approximation states that the field behind the surface is completely shadowed. In reality, it will be non-zero due to diffraction but for surfaces much longer than the wavelength the field is negligible except near the edges. Eq. D.28 causes the integral over S_2 to vanish, leaving

$$p(\mathbf{r}) = p_{inc}(\mathbf{r}) + \Upsilon_{S_0}(\mathbf{r}, \mathbf{r}')p(\mathbf{r}'), \tag{D.29}$$

another form involving integration along S_0 only. Eqs. D.22 and D.29 are identical, except for the appearance of the scattered field in Eq. D.22 versus the total field in Eq. D.29. Since different assumptions were made in arriving at the two equations, they are *not* equivalent. The form used in this thesis is that of Eq. D.29. Since the surfaces used were always much larger than the wavelength, potential inaccuracies in neglecting the integral over S_2 only exist within a few wavelengths of the edges. These edge effects are attenuated by using tapered incident fields.

Appendix E

Wavelets

E.1 The Wavelet Transform

Methods for performing space-scale localization existed before the development of wavelet theory. These methods, still in use today, are based on the Fourier transform. The Short-Time Fourier Transform uses complex exponential eigenfunctions which are windowed in space to limit their duration. One particular case is the Gabor transform, in which a Gaussian window is used. A disadvantage of these techniques is that a single window width must be chosen for the analysis. For analysis of a low-wavenumber content function, it is often desirable to consider long segments. Conversely, for high-wavenumber phenomena, short segments are preferred. While windowed Fourier transform techniques do not provide this desired flexibility, wavelets automatically include it. That is, short wavelets resolve high wavenumbers and long wavelets resolve low wavenumbers.

Scale in wavelet analysis is the counterpart to the reciprocal of wavenumber in Fourier analysis. Each eigenfunction, called a *wavelet*, is an oscillatory function of short duraction, as seen in Fig. E-1. The projection of a sharp feature onto a wavelet is energetic only if the two overlap in space. By shifting the wavelet horizontally over the function to be analyzed, features comparable in size to the wavelet are detected in sequence. Features of different size are detectable by *scaling* the wavelet. Wavelets analysis is a particular case of multiresolution analysis in which a father wavelet $\phi(x)$

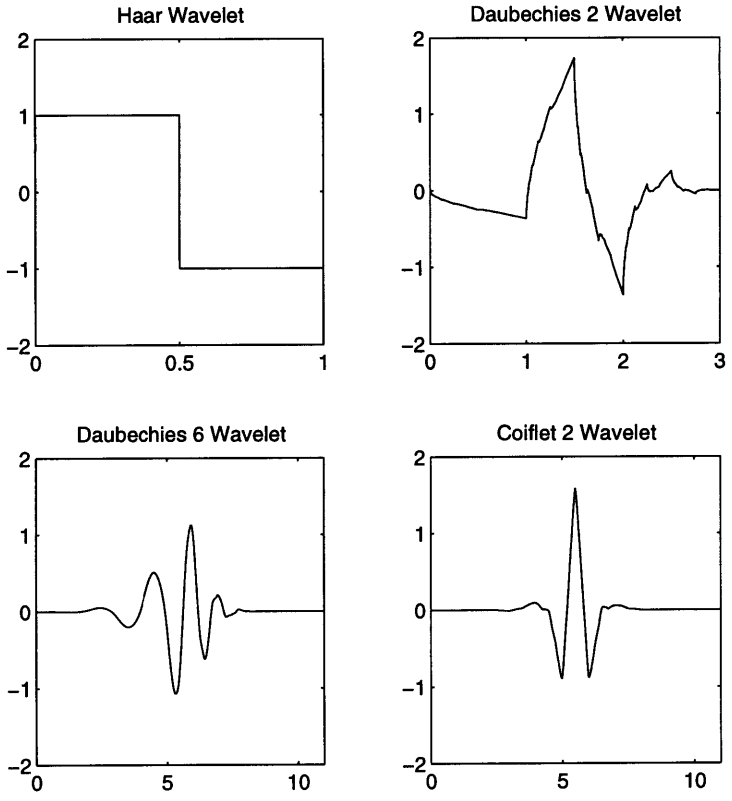

Figure E-1: Example wavelets.

is used to generate a set of nested subspaces V_i. The father wavelet and the subpaces are such that

1. $\cdots \subset V_{-2} \subset V_{-1} \subset V_0 \subset V_1 \subset V_2 \subset \cdots$;
2. $\cap_{i \in \mathcal{Z}} V_i = \{0\}$, $\overline{\cup_{i \in \mathcal{Z}} V_i} = L^2(\mathcal{R})$;
3. $f \in V_i$ if and only if $f(2\cdot) \in V_{i+1}$;
4. $f \in V_0$ implies $f(\cdot - j) \in V_0$ for all $j \in \mathcal{Z}$;
5. There exists a function $\phi \in V_0$ such that the set $\{\phi_{0,j} = \phi(\cdot - j), j \in \mathcal{Z}\}$ constitutes an orthonormal basis for V_0.

The first property indicates that each subspace V_i is a subset of the next higher subspace V_{i+1}. The second part of Property 2 indicates that all the subspaces taken

together span the space of square integrable functions on the real axis, $L^2(\mathcal{R})$. The first part of Property 2 indicates that each higher subspace is larger than all previous subspaces. Property 3 states that the particular multiresolution considered is a *dyadic* one, that is, each higher subspace spans all the functions in the previous subspace, *plus* those that have twice the resolution. Properties 3, 4 and 5 together imply that the basis for each V_i is $\phi_{i,j} = 2^{i/2}\phi(2^i \cdot -j)$. The $2^{i/2}$ normalization is required to preserve an orthonormal basis at each level i. A new set of subspaces W_i are defined to be the span of the basis functions included in V_{i+1} but *not* in V_i, i.e.

$$V_i = V_{i-1} \oplus W_{i-1}, \tag{E.1}$$

where the operator $\oplus$ is the orthogonal sum of two subspaces. The subspaces $\{W_i\}$ are orthogonal to each other. *Wavelets* $\psi_{i,j}$ are the basis functions of the subspaces W_i:

$$W_i = \text{span}\{\psi_{i,j},\ j \in \mathcal{Z}\}. \tag{E.2}$$

The analog of the father wavelet ϕ that generates all $\phi_{i,j}$ is the *mother wavelet* ψ, which generates all $\psi_{i,j}$:

$$\psi_{i,j} = 2^{i/2}\psi(2^i \cdot -j). \tag{E.3}$$

Let the projection of a function f in $L^2(\mathcal{R})$ on the subspace V_i be defined as $P_V^i f$. This is an approximation to f which grows increasingly accurate as i is increased; each new level includes finer details. The projection of f on the subspace W_i, P_W^i, gives the *details* in passing from the approximation at level i to the next higher-resolution approximation at level $i+1$:

$$P_V^{i+1} f = P_V^i f + P_W^i f. \tag{E.4}$$

From the discussion so far, we conclude that the index i satisfies the intuitive concept

of "scale". Suppose that a multiresolution analysis is begun with a coarse approximation of f as its projection on V_0. This approximation plus all higher-resolution details give f exactly:

$$f = P_V^0 f + \sum_{k=0}^{\infty} P_W^k f. \tag{E.5}$$

The above equation is equivalent to stating that

$$L^2(\mathcal{R}) = \text{span}\{\phi_{0,j}, \psi i, j\},\ i \geq 0. \tag{E.6}$$

The *wavelet transform* of f is simply the set of coefficients $w_{i,j}$ resulting from the projection of f on each subspace:

$$w_{i,j} = \int_{-\infty}^{\infty} f(x)\psi_{i,j}(x)dx. \tag{E.7}$$

For a given resolution level i, $w_{i,j}$ gives the details of f localized about $x = j/2^i$ at scale i. These details are introduced in passing from the representation of f in V_i to its finer representation in V_{i+1}. The wavelet coefficients over all i and j span $L^2(\mathcal{R})$, but in practice there is some upper bound on scale (lower bound on i) that is considered in the analysis. Defining the lowest level to be $i = 0$, a complete decomposition should also include the approximation coefficients $c_{0,k}$ corresponding to $P_V^0 f$, where

$$c_{i,j} = \int_{-\infty}^{\infty} f(x)\phi(x)dx. \tag{E.8}$$

E.2 The Continuous Wavelet Transform

With the continuous wavelet transform, the analyzing wavelets are scaled and shifted in a continuous instead of discrete manner:

$$\psi_{a,b}(x) = |a|^{-/frac12}\psi(\frac{x-b}{a}). \tag{E.9}$$

The transform is:

$$\mathcal{W}_{a,b}f = \int dx f(x)|a|^{-\frac{1}{2}}\overline{\psi(\frac{x-b}{a})}. \tag{E.10}$$

The resulting decomposition contains redundant information in that the discretely scaled and shifted basis functions already formed a complete and orthonormal set; the projection of $f(x)$ onto $\psi_{a,b}(x)$ for all other values of a and b than $a = 2^i$ and $b = 2^{-i} - j$ is fully recoverable from the discrete values.

To explore how the continuous wavelet transform might be useful, we show in Fig. 5-12 the continuous wavelet transform of each realization of Fig. 5-11 as a two-dimensional contour plot. The color intensity is proportional to the logarithm of the magnitude ot the wavelet transform at each spatial co-ordinate (x-axis) and scale parameter (y-axis). The realizations of Fig. 5-11 are overlaid. Some interesting observations can be made. $f_2(x)$ and $f_3(x)$ have complicated bifurcating line patterns that grow in number as scale decreases. These are indicative that with each reduction in scale, additional structure is introduced; these functions exhibit fractal behavior. $f^1(x)$, on the other hand, shows extensive black areas at the finer scales, starting at around $a = l_c$. The analyzing wavelet is a Daubechies 2 wavelet which has zero projection on constant and linearly-increasing functions. Thus, when the width of the analyzing wavelet becomes smaller than a facet, a zero is introduced. Clearly, the wavelet transform makes the task of distinguishing $f^1(x)$ from the other two easy. Unfortunately, this is not a useful contribution because it was already easy to distinguish it just from the realizations. It was to distinguish between $f^2(x)$ and $f^3(x)$ that we hoped the wavelet transform would be helpful but alas they have similar-looking wavelet transforms. In sum, these deterministic wavelet transforms have not added much to our ability to detect hidden scale structure. More sophisticated methods are required which are based on statistical analyses of the wavelet transform.

E.3 Wavelet Statistics

Uncovering the scale structure of random functions requires an analysis of the statistics of the coefficients $w_{i,j}$ or of the continuous wavelet transform. The goal for introducing wavelets was to provide a means of distinguishing between functions having the same second-moment statistics but different scale structure. A second moment analysis of the wavelet transform is not sufficient. For example, the correlation function of the continuous wavelet transform of a wide-sense stationary function $f(x)$ is:

$$\begin{aligned} R_{\mathcal{W}\mathcal{W}}(a,a',b,b') &= \mathcal{E}\left[\mathcal{W}_(a,b)f\overline{\mathcal{W}_(a,b)f}\right] \\ &= \mathcal{E}\int dx f(x)|a|^{-\frac{1}{2}}\overline{\psi}(\frac{x-b}{a})\int dx'\overline{f}(x')|a'|^{-\frac{1}{2}}\psi(\frac{x'-b'}{a'}) \\ &= \int\int dxdx' R_{ff}(x'-x)\psi(\frac{x'-b'}{a'})\overline{\psi}(\frac{x-b}{a}). \end{aligned} \tag{E.11}$$

Clearly, if two functions f and g have identical correlation function, their wavelet transforms have identical correlation functions. It is interesting to note that $R_{\mathcal{W}\mathcal{W}}$ is a wide-sense stationary function of b and b' for a given scale. Setting $a = a'$, Eq. E.11 becomes

$$\mathcal{E}\left[\mathcal{W}_(a,b)f\overline{\mathcal{W}_(a,b)f}\right] = R_{zz}(b'-b) * |a|^{-\frac{1}{2}}\psi(\frac{b'-b}{a}) * |a|^{-\frac{1}{2}}\overline{\psi}(\frac{b'-b}{a}). \tag{E.12}$$

where $*$ is the convolution operator:

$$f(b) * g(b) = \int_{-\infty}^{\infty} dx f(x-b)g(x). \tag{E.13}$$

It is clear from Eq. E.12 that $R_{\mathcal{W}\mathcal{W}}(a,a,b,b') = R_{\mathcal{W}\mathcal{W}}(a,a,b'-b)$, proving wide-sense stationarity.

E.4 Statistically Self-Similar Processes

The following definitions and theorems are taken from Ref. [71]. A random process $f(x)$ defined on $-\infty < x < \infty$ is said to be *statistically self-similar* if its statistics are invariant to dilations and compressions of the waveform in time. More specficially, a random process $f(x)$ is statistically self-similar with parameter H if for any real $a > 0$ it obeys the scaling realtion

$$f(x) \stackrel{\mathcal{P}}{=} a^{-H} f(ax) \tag{E.14}$$

where $\stackrel{\mathcal{P}}{=}$ denotes equality in a statistical sense. $Wide-sense$ self-similarity is defined as similarity in second order statistics:

$$M_f = \mathcal{E}[f(x)] = a^{-H} M_f(ax) \tag{E.15}$$

$$R_{ff}(x', x'') = \mathcal{E}[f(x')f(x'')] = a^{-2H} R_{ff}(ax', ax''). \tag{E.16}$$

In Ref. [71], a special class of stochastic processes is studied: $1/f$ processes. Loosely, these are processes whose power spectral density is proportional to $1/f^{\alpha}$, for some alpha. In Ref. [71], they are explicitly defined as follows:

Definition *A wide-sense statistically self-similar zero-mean random process $f(x)$ is said to be a $1/f$ process if there exist k_0 and k_1 satisfying $0 < k_0 < k_1 < \infty$ such that when $f(x)$ is filtered by an ideal bandpass filter with wavenumber response*

$$B_1(k) = \begin{cases} 1, & k_0 < |k| < k_1 \\ 0, & otherwise, \end{cases} \tag{E.17}$$

the resulting process $g_1(x)$ is wide-sense stationary and has finite variance.

This Definition is justified by the following Theorem:

Theorem *A $1/f$ process $f(x)$, when filtered by an ideal bandpass filter with frequency*

response

$$B(k) = \begin{cases} 1, & k_L < |k| < k_U \\ 0, & \textit{otherwise}, \end{cases} \tag{E.18}$$

for arbitrary $0 < k_L < k_U < \infty$*, yields a wide-sense stationary random process* $g(x)$ *with finite variance and having power spectum*

$$S_g(k) = \begin{cases} \sigma_f^2/|k|^\alpha, & k_L < |k| < k_U \\ 0, & \textit{otherwise}, \end{cases} \tag{E.19}$$

for some $\sigma_f^2 > 0$*, and where the spectra exponent* α *is related to the self-similarity parameter* H *according to* $\alpha = 2H + 1$.

Bibliography

[1] Hiroshi Akima. ALGORITHM 526: Bivariate interpolation and smooth surface fitting for irregularly distributed data points. *ACM Transactions on Mathematical Software*, 4(2):160–164, June 1978.

[2] Hiroshi Akima. A method of bivariate interpolation and smooth surface fitting for irregularly distributed data points. *ACM Transactions on Mathematical Software*, 4(2):148–159, June 1978.

[3] Jonathon M. Berkson and J. E. Matthews. Statistical characterization of seafloor roughness. *IEEE Journal of Oceanic Engineering*, OE-9(1):48–52, January 1984.

[4] M. A. Biot and I. Tolstoy. Formulation of wave propagation by normal coordinates with an application to diffraction. *Journal of the Acoustical Society of America*, 29:381–391, 1957.

[5] Jerald W. Caruthers and Jorge C. Novarini. Modeling bistatic bottom scattering strength including a forward scatter lobe. *IEEE Journal of Oceanic Engineering*, 18(2):100–107, April 1993.

[6] Dezhang Chu. Impulse response of density contrast wedge using normal coordinates. *Journal of the Acoustical Society of America*, 86(5):1883–1896, November 1989.

[7] C. S. Clay and Wayne A. Kinney. Numerical computations of time-domain diffractions from wedges and reflections from facets. *Journal of the Acoustical Society of America*, 83(6):2126–2133, June 1988.

[8] C.S. Clay, Dezhang Chu, and Saimu Li. Specular reflections of transient pressures from finite width plane facets. *Journal of the Acoustical Society of America*, 94(4):2279–2286, October 1993.

[9] Ingrid Daubechies. *Ten Lectures on Wavelets.* Society for Industrial and Applied Mathematics, Philadelphia, PA, 1992.

[10] Prof. D'Eleuterio. Control systems. Course notes, 1991. University of Toronto Institute for Aerospace Studies.

[11] L. Bruce Palmer Devid Meloy Fromm, John P. Crockett. BiRASP - the Bistatic Range-dependent Active System Prediction Model. Technical Report NRL/FR/7140–95-9723, Naval Research Laboratory, September 1996.

[12] Yevgeniy Yakov Dorfman. *Bistatic scattering of acoustic waves from a rough ocean bottom.* PhD thesis, Massachusetts Institute of Technology, Department of Ocean Engineering, 1997.

[13] Ira Dyer, Arthur B. Baggeroer, Henrik Schmidt, J. Robert Fricke, Nazan Ozluer, and Dominique Giannoni. Discrete backscatter can be dominant in rough bottom reverberation. In D. D. Ellis, J. R. Preston, and H. G. Urban, editors, *Ocean Reverberation*, pages 51–57. Kluwer Academic Publishers, 1993.

[14] Pierre Elisseeff. ARSRP 93: Acoustic shape estimation of a linear towed array. MIT Ocean Engineering report submitted to Arthur Baggeroer, 1995.

[15] Kenneth Falconer. *Fractal Geometry: Mathematical Foundations and Applications.* John Wiley and Sons, New York, 1990.

[16] Efi Foufoula-Georgiou and Praveen Kumar, editors. *Wavelets in Geophysics*, volume 4 of *Wavelet Analysis and its Applications.* Academic Press, Boston, 1994.

[17] Christopher G. Fox and Dennis E. Hayes. Quantitative methods for analyzing the roughness of the seafloor. *Reviews of Geophysics*, 23(1):1–48, February 1985.

[18] J.A. Goff and B. E. Tucholke. Multiscale spectral analysis of bathymetry on the flank of the Mid-Atlantic Ridge: modification of the seafloor by mass wasting and sedimentation. *Journal of Geophysical Research*, 102(B7):15447–62, July 1997.

[19] John A. Goff and Thomas H. Jordan. Stochastic modeling of seafloor morphology: Inversion of sea beam data for second-order statistics. *Journal of Geophysical Research*, 93(B11):13589–13608, November 1988.

[20] John A. Goff and Thomas H. Jordan. Stochastic modeling of seafloor morphology: Resolution of topographic parameters by sea beam data. *IEEE Journal of Oceanic Engineering*, 14(4):326–337, October 1989.

[21] I. S. Gradshteyn and I. M. Ryzhik. *Table of Integrals, Series, and Products.* Academic Press, Inc., fifth edition, 1994.

[22] Robert J. Greaves and Ralph A. Stephen. Seafloor acoustic backscattering from different geological provinces in the atlantic natural laboratory. *Journal of the Acoustical Society of America*, 101(1):193–208, January 1997.

[23] Frederic J. Harris. On the use of windows for harmonic analysis with the distrete fourier transform. *Proceedings of the IEEE*, 66(1):51–83, 1978.

[24] Ute C. Herzfeld, Isaac I. Kim, and John A. Orcutt. Is the ocean floor a fractal? *Mathematical Geology*, 27(3), 1995.

[25] R. L. Holford. Scattering of sound waves at a periodic, pressure-release surface: An exact solution. *Journal of the Acoustical Society of America*, 70(4):1116–1128, October 1981.

[26] Stephane Jaffard and Yves Meyer. Wavelet methods for pointwise regularity and local oscillations of functions. *Memoirs of the American Mathematical Society*, 123(587), September 1996. Published by the American Mathematical Society.

[27] Gary M. Jebsen and Herman Medwin. On the failure of the Kirchhoff assumption in backscatter. *Journal of the Acoustical Society of America*, 72(5):1607–1611, November 1982b.

[28] J. C. Novarini Jerald W. Caruthers, E. F. Yoerger. Modeling low-frequency reverberation near the mid-atlantic ridge and comparison with ARSRP data. *Journal of the Acoustical Society of America*, 101(5, Pt. 1):2555, May 1997.

[29] Wayne A. Kinney and C. S. Clay. The spatial coherence of sound scattered from a wind-driven surface: Comparison between experiment, Eckart theory, and the facet-ensemble method. *Journal of the Acoustical Society of America*, 75(1):145–148, January 1984.

[30] Wayne A. Kinney and C. S. Clay. Insufficiency of surface spatial power spectrum for estimating scattering strength and coherence: Numerical studies. *Journal of the Acoustical Society of America*, 78(5):1777–1784, 1985.

[31] Wayne A. Kinney, C. S. Clay, and Gerald A. Sandness. Scattering from a corrugated surface: Comparison betwen experiment, Helmholtz-Kirchhoff theory, and the facet-ensemble method. *Journal of the Acoustical Society of America*, 73(1):183–194, January 1983.

[32] P. G. Lemarie. *Les Ondelettes en 1989.* Springer-Verlag, New York, 1990.

[33] Dan Li. *Unknown.* PhD thesis, Massachusetts Institute of Technology, Department of Ocean Engineering, 1997.

[34] Saimu Li, Dezhang Chu, and C. S. Clay. Time domain reflections and diffractions from facet-wedge constructions: Acoustic experiments including double diffractions. *Journal of the Acoustical Society of America*, 96(6):3715–3720, December 1994.

[35] Saimu Li and C. S. Clay. Sound transmission experiments from an impulsive soure near rigid wedges. *Journal of the Acoustical Society of America*, 84(6):2135–2143, December 1988.

[36] Vincent H. Lupien, Joseph E. Bondaryk, and Arthur B. Baggeroer. Acoustical ray-tracing insonification software modeling of reverberation at selected sites near the Mid-Atlantic Ridge. *Journal of the Acoustical Society of America*, 98(5, Pt. 2):2987, November 1995b.

[37] Vincent H. Lupien and J. Robert Fricke. Coregistration of received signals with bathymetry using ARTIST. *Journal of the Acoustical Society of America*, 96(5, Pt. 2):3345, November 1994.

[38] Vincent H. Lupien and J. Robert Fricke. Seafloor insonification near the Mid-Atlantic Ridge. *Journal of the Acoustical Society of America*, 95(5, Pt. 2):2828, May 1994.

[39] N. C. Makris. Imaging ocean-basin reverberation via inversion. *Journal of the Acoustical Society of America*, 94:983–993, 1993.

[40] N. C. Makris, Lilimar Z. Avelino, and Richard Menis. Deterministic reverberation from ocean ridges. *Journal of the Acoustical Society of America*, 97(6):3547–3574, June 1995.

[41] N. C. Makris and Jonathan M. Berkson. Long-range backscatter from the Mid-Atlantic Ridge. *Journal of the Acoustical Society of America*, 95(4):1865–1881, April 1994.

[42] Nicholas C. Makris. The effect of saturated transmission scintillation on ocean acoustic intensity measurements. *Journal of the Acoustical Society of America*, 100(2, Pt. 1):769–783, August 1996.

[43] H. Medwin. Shadowing by finite noise barriers. *Journal of the Acoustical Society of America*, 69(4):1060–1064, April 1981b.

[44] H. Medwin and J. C. Novarini. Backscattering strength and the range dependence of sound scattered from the ocean surface. *Journal of the Acoustical Society of America*, 69(1):108–111, January 1981a.

[45] Herman Medwin, Emily Childs, and Gary M. Jebsen. Impulse studies of double diffraction: A discrete Huygens interpretation. *Journal of the Acoustical Society of America*, 72(3):1005–1013, September 1982a.

[46] Herman Medwin, Emily Childs, Edgar A. Jordon, and Robert A. Spaulding, Jr. Sound scatter and shadowing at a seamount: Hybrid physical solutions in two and three dimensions. *Journal of the Acoustical Society of America*, 75(5):1478–1490, May 1984.

[47] Jorge C. Novarini and Herman Medwin. Computer modeling of resonant sound scattering from a periodic assemblage of wedges: Comparison with theories of diffraction gratings. *Journal of the Acoustical Society of America*, 77(5):1754–1759, May 1985.

[48] Scientific Party of ARSRP 1993. Initial report of aRSRP acoustics experiment: 5-26 july 1993. Technical report, Scripps Institution of Oceanography, La Jolla, CA, 1993.

[49] R. Todd Ogden. *Essential Wavelets for Statistical Applications and Data Analysis.* Birkhauser, Boston, 1997.

[50] J. A. Ogilvy. *Theory of Wave Scattering from Random Rough Surface.* IOP Publishing, 1991.

[51] V. V. Ol'shevskii. *Characteristics of Sea Reverberation.* Consultants Bureau, New York, 1967.

[52] Ayse Nazan Akman Ozluer. Refraction effects on vertical line array beamforning. Master's thesis, Massachusetts Institute of Technology, Department of Ocean Engineering, 1992.

[53] Athanasios Papoulis. *Probability, Random Variables, and Stochastic Processes.* McGraw-Hill, Inc., New York, 3 edition, 1991.

[54] Emanuel Parzen. *Stochastic Processes.* Holden-Day, San Francisco, 1962. p. 128.

[55] Lord Rayleigh. *The Theory of Sound.* Dover, New York, 1945.

[56] R. J. Renka and A. K. Kline. A triangle-based c1 interpolation method. *Rocky Mountain Journal of Mathematics*, 14(1):223–237, winter 1984.

[57] Robert J. Renka. Algorithm 624: Triangulation and interpolation at arbitrarily distributed points in the plane. *ACM Transactions on Mathematical Software*, 10(4):440–442, December 1984.

[58] Kevin B. Smith and William S. Hodgkiss. Propagation and analysis issues in the prediction of long-range reverberation. *Journal of the Acoustical Society of America*, 99(3):1387–1404, March 1996.

[59] Gilbert Strang and Truong Nguyen. *Wavelets and Filter Banks.* Wellesley-Cambridge Press, Wellesley, MA, 1996.

[60] Eric I. Thorsos. The validity of the Kirchhoff approximation for rough surface scattering using a Gaussian roughness spectrum. *Journal of the Acoustical Society of America*, 83(1):78–92, January 1988.

[61] Eric I. Thorsos. Acoustic scattering from a Pierson-Moskowitz sea surface. *Journal of the Acoustical Society of America*, 88(1):335–349, July 1990.

[62] Eric I Thorsos. Studies of rough surface scattering using integral equation simulations. Presented at the Massachusetts Institute of Technology, December 1997.

[63] I. Tolstoy. Acoustic scatter from a slightly rough boundary between a fluid and an elastic solid. *Journal of the Acoustical Society of America*, 78(5):1727–1734, November 1985.

[64] I. Tolstoy. Diffraction by a hard truncated wedge and a strip. *IEEE Journal of Oceanic Engineering*, 14(1):4–16, January 1989a.

[65] I. Tolstoy. Exact, explicit solutions for diffraction by hard sound barriers and seamounts. *Journal of the Acoustical Society of America*, 85(2):661–669, February 1989b.

[66] Claude Tricot. *Curves and Fractal Dimension.* Springer-Verlag, New York, 1995.

[67] Brian E. Tucholke, W. Kenneth Stewart, and Martin C. Kleinrock. Long-term denudation of ocean crust in the central North Atlantic Ocean. *Geology*, 25(2):171–174, February 1997.

[68] Dr. Brian Tucholke. Private discussions. Woods Hole Oceanographic Institution, Fall 1997.

[69] Yazhen Wang. Jump and sharp cusp detection by wavelets. *Biometrika*, 82(2):385–397, 1995.

[70] H. Weinberg. Generic Sonar Model. Technical report, Naval Underwater Systems Center, New London, CT, June 1985.

[71] Gregory W. Wornell. *Signal Processing with Fractals.* Prentice Hall, Upper Saddle River, NJ, 1996.